Transient 2D-IR Spectroscopy

Towards Ultrafast Structural Dynamics of Peptides and Proteins

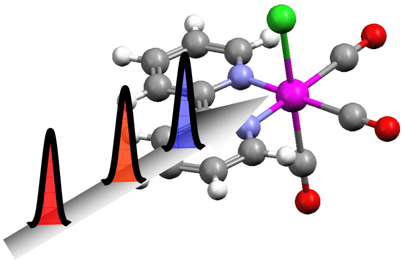

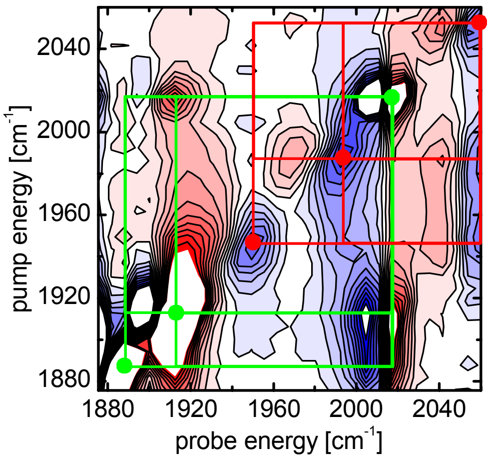

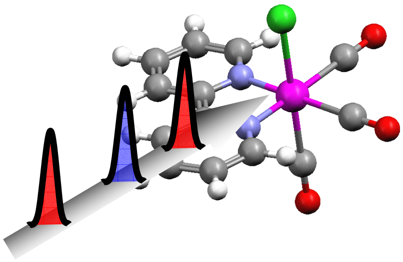

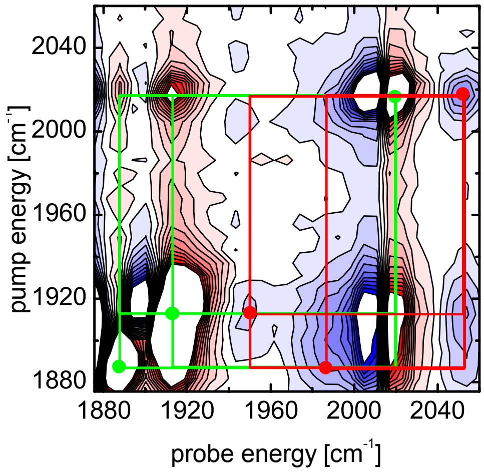

Dissertation 2005

Jens Bredenbeck

Transient 2D-IR Spectroscopy

—

Towards Ultrafast Structural Dynamics of Peptides and Proteins

Dissertation
zur
Erlangung der naturwissenschaftlichen Doktorwürde
(Dr. sc. nat.)

vorgelegt der
Mathematisch-naturwissenschaftlichen Fakultät
der
Universität Zürich

von
Jens Bredenbeck
aus
Deutschland

Promotionskomitee
Prof. Dr. Peter Hamm (Vorsitz, Leitung der Dissertation)
Prof. Dr. Stefan Seeger
Prof. Dr. Jürg Hutter
Prof. Dr. Majed Chergui

Zürich, 2005

Lux per se pulchra est quia eius natura simplex est, sibique omnia simul.[1]

In *Hexaëmeron*, Robert Grosseteste (ca. 1168-1253)

---

[1] Light itself is beautiful as its nature is simple and at the same time contains everything.

2D spectroscopy fascinates by its conceptual simplicity and its general applicability. It seems to open one further dimension to the spectroscopist. (...) Applications are conceivable in electron spin resonance, nuclear quadrupole resonance, in microwave rotational spectroscopy, and possibly in laser infrared spectroscopy.

In *Two dimensional spectroscopy. Application to nuclear magnetic resonance* [1], Richard R. Ernst *et al.* (1976)

The research carried out in the context of this dissertation has resulted in contributions to following publications, some of which are reproduced in this manuscript:

Peer Reviewed Publications

- P16: Peter Hamm, Jan Helbing and Jens Bredenbeck.
  Stretched versus compressed exponential kinetics in protein folding
  Chem. Phys., in press.

- P15: Jens Bredenbeck, Jan Helbing, and Peter Hamm.
  Two-dimensional IR spectroscopy of transient species.
  In Takayoshi Kobayashi, editor, *Ultrafast Phenomena XIV*, Chemical Physics. Springer, in press.

- P14: Jens Bredenbeck, Jan Helbing, and Peter Hamm.
  Solvation dynamics: Beyond the two-point frequency fluctuation correlation function.
  Phys. Rev. Lett., submitted.

- P13: Jens Bredenbeck, Jan Helbing, Janet R. Kumita, G. Andrew Woolley, and Peter Hamm.
  α-Helix formation in a photo-switchable peptide tracked from picoseconds to microseconds by time resolved IR spectroscopy.
  Proc. Natl. Acad. Sci., 102:2379-2384, 2005.

- P12: Valentina Cervetto, Jan Helbing, Jens Bredenbeck, and Peter Hamm.
  Double-resonance versus pulsed fourier transform 2D-IR spectroscopy: An experimental and theoretical comparison.
  J. Chem. Phys., 121:5935–5942, 2004.

- P11: Jens Bredenbeck, Jan Helbing, and Peter Hamm.
  Continuous scanning from picoseconds to microseconds in time resolved linear and nonlinear spectroscopy.
  Rev. Sci. Instrum., 75:4462–4466, 2004.

- P10: Jens Bredenbeck, Jan Helbing, and Peter Hamm.
  Transient two-dimensional IR spectroscopy - exploring the polarization dependence.
  J. Chem. Phys., 121:5943–5957, 2004.

- P9: Jan Helbing, Harald Bregy, Jens Bredenbeck, Rolf Pfister, Peter Hamm, Robert Hubert, Josef Wachtveitl, Luca De Vico, and Massimo Olivucci.
  A fast photoswitch for minimally perturbed peptides: Investigation of the trans→cis photoisomerization of N-Methylthioacetamide.
  J. Am. Chem. Soc., 126:8823–8834, 2004.

- P8: Jan Helbing, Luigi Bonacina, Ruth Pietri, Jens Bredenbeck, Peter Hamm, Frank van Mourik, Frédéric Chaussard, Alejandro Gonzalez-Gonzalez, Majed Chergui, Cacimar Ramos-Alvarez, Carlos Ruiz, and Juan López-Garriga.
  Time-resolved visible and infrared study of the cyano complexes of myoglobin and of hemoglobin I from Lucina pectinata.
  Biophys. J., 87:1881–1891, 2004.

- P7: Jens Bredenbeck, Jan Helbing, and Peter Hamm.
  Transient two-dimensional infrared spectroscopy - towards measuring ultrafast structural dynamics.
  In Monique M. Martin and James. T. Hynes, editors, *Femtochemistry and Femtobiology*, Ultrafast Events in Molecular Science, pages 387–390. Elsevier, 2004.

- P6: Wolgang Zinth, Arne Sieg, Tobias Schrader, Sebastian Spörlein, Peter Hamm, Jens Bredenbeck, Jan Helbing, Christian Renner, Luis Moroder, Heiko Carstens, Paul Tavan, and Josef Wachtveitl.

Ultrafast conformational dynamics in light triggered cyclic peptides.
In Monique M. Martin and James. T. Hynes, editors, *Femtochemistry and Femtobiology*, Ultrafast Events in Molecular Science, pages 373–379. Elsevier, 2004.

- P5: Jens Bredenbeck, Jan Helbing, and Peter Hamm.
  Labeling vibrations by light — ultrafast transient 2D-IR spectroscopy tracks vibrational modes during photoinduced charge transfer.
  J. Am. Chem. Soc., 126:990–991, 2004.

- P4: Jens Bredenbeck, Jan Helbing, Raymond Behrendt, Christian Renner, Luis Moroder, and Peter Hamm.
  Transient 2D-IR spectroscopy – snapshots of the non-equilibrium ensemble during the picosecond conformational transition of a cyclic peptide.
  J. Phys. Chem. B, 107:8654–8660, 2003.

- P3: Jens Bredenbeck and Peter Hamm.
  Peptide structure determination by 2D-IR spectroscopy in the presence of homogeneous and inhomogeneous broadening.
  J. Chem. Phys., 119:1569 – 1578, 2003.

- P2: Jens Bredenbeck and Peter Hamm.
  Versatile small volume closed cycle flow cell system for transient spectroscopy at high repetition rates.
  Rev. Sci. Instrum., 74:3188–3189, 2003.

- P1: Jens Bredenbeck, Jan Helbing, Arne Sieg, Tobias Schrader, Wolfgang Zinth, Christian Renner, Raymond Behrendt, Luis Moroder, Josef Wachtveitl, and Peter Hamm.
  Picosecond conformational transition and equilibration of a cyclic peptide.
  Proc. Natl. Acad. Sci., 100:6452–6457, 2003.

Talks at Conferences

- Jens Bredenbeck, Jan Helbing, and Peter Hamm.
  Two-dimensional IR spectroscopy of transient species.
  Ultrafast Phenomena XIV, Niigata, Japan, July 25.-30., 2004.

- Jens Bredenbeck, Jan Helbing, and Peter Hamm.
  Transient 2D-IR spectroscopy.
  227th ACS National Meeting, Anaheim, USA, March 28.- April 1., 2004.

- Jens Bredenbeck, Jan Helbing, Arne Sieg, Tobias Schrader, Wolfgang Zinth, Christian Renner, Raymond Behrendt, Luis Moroder, Josef Wachtveitl, and Peter Hamm.
  Light-triggered conformational transition of a cyclic peptide monitored by ultra-fast vibrational spectroscopy.
  Conference of the German Physical Society (DPG), Dresden, Germany, March 24.-28., 2003.

- Jens Bredenbeck, Jan Helbing, and Peter Hamm.
  Light-triggered conformational transition of a cyclic peptide monitored by ultra-fast vibrational spectroscopy - towards measuring ultrafast structural dynamics.
  The 1st Symposium on Multidimensional Vibrational Spectroscopy, Korea University, Seoul, Korea, October 21.-23., 2002.

Posters at Conferences

- Jens Bredenbeck, Jan Helbing, and Peter Hamm.
  Conformational dynamics of peptides by transient IR spectroscopy - α-helix formation from picoseconds to microseconds.
  Minerva-Gentner Symposium on Optical Spectroscopy of Biomolecular Dynamics, Banz, Germany, March 21. - 25., 2004.

- Jens Bredenbeck, Jan Helbing, Josef Wachtveitl, and Peter Hamm.
  Transient 2D-IR spectroscopy: Towards measuring ultrafast structural dynamics.
  Femtochemistry VI, Paris, France, July 6.-10., 2003.

- Jan Helbing, Jens Bredenbeck, Peter Hamm, Luigi Bonacina, Frank van Mourik, Frédéric Chaussard, Alejandro Gonzalez-Gonzalez, Majed Chergui, Ruth Pietri, Cacimar Ramos-Alvarez, Carlos Ruiz, and Juan López-Garriga.
  Ultrafast UV-visible and infrared study of the cyano complexes of myoglobin and haemoglobin I from Lucina pectinata.
  Femtochemistry VI, Paris, France, July 6.-10., 2003.

- Jens Bredenbeck, Jan Helbing, Josef Wachtveitl, and Peter Hamm.
  Transient 2D-IR spectroscopy: Towards measuring ultrafast structural dynamics.
  11th International Conference on Time Resolved Vibrational Spectroscopy TRVS XI, Castiglione della Pescaia, Italy, May 24. - 29., 2003.

- Jan Helbing, Jens Bredenbeck, Harald Bregy, Rolf Pfister, Peter Hamm, Christian Renner, Raymond Behrendt, Luis Moroder, Wolfgang Zinth, Josef Wachtveitl, Janet R. Kumita, and G. Andrew Woolley.
  Ultrafast triggering and probing of conformational dynamics in peptides using transient infrared absorption.
  11th International Conference on Time Resolved Vibrational Spectroscopy TRVS XI, Castiglione della Pescaia, Italy, May 24. - 29., 2003.

- Jens Bredenbeck, Jan Helbing, Harald Bregy, Rolf Pfister, Peter Hamm, Christian Renner, Raymond Behrendt, Luis Moroder, Wolfgang Zinth, Josef Wachtveitl, Janet R. Kumita, and G. Andrew Woolley.
  Conformational dynamics in peptides: Ultrafast triggering and transient two dimensional infrared spectroscopy.
  Ultrafast Science with X-rays and Electrons, Montreux, Switzerland, April 9. - 12., 2003.

Contents

Abstract

While it has long been known that peptides and proteins are dynamic structures, the paramount importance of dynamic effects for biological function became clear only during the last few decades. As a result, intense effort is currently made to investigate the dynamics of peptides and proteins in their native environment in the context of such different phenomena as protein folding, motor proteins, catalysis, allosteric regulation or ligand binding in general. The picture beginning to emerge is that of a continuum of timescales governing peptide and protein motion from seconds or longer down to the sub-picosecond regime. For the dynamics on a millisecond and slower timescale there is NMR as a powerful structure resolving method at our hands. For the faster processes in the liquid phase, there is clearly a need for a method offering high time resolution and, at the same time, a sufficient structure sensitivity. Nonlinear two-dimensional femtosecond infrared spectroscopy (2D-IR), demonstrated for the first time in 1998 by Hamm, Lim and Hochstrasser [2], combines useful structure sensitivity in the liquid phase with high time resolution. The potential of this method has been demonstrated by the determination of the backbone dihedral angles of a tripeptide with a time resolution of 1 ps [3, 4]. So far, however, 2D-IR has been applied only to systems in equilibrium, where the high time resolution has been used to distinguish fast interconverting conformations. The extension of 2D-IR to the non-equilibrium regime and the investigation of transient structures seems very promising, not only for polypeptide dynamics but for the investigation of molecular dynamics in general. To this end the technique of transient 2D-IR spectroscopy (T2D-IR) is introduced here.

The present dissertation consists of two loosely connected parts contributing to the understanding of polypeptide dynamics and to the field of 2D-IR spectroscopy: In Part I *'Phototriggered Peptide Dynamics and Secondary Structure Formation'* new tools for time resolved IR spectroscopy are developed that allow to investigate non-equilibrium conformational dynamics of polypeptides in unprecedented detail. Built-in molecular photoswitches are employed to trigger and control dynamics. Two peptide model systems are discussed. The first is a cyclic peptide that is formed from the thioredoxin reductase active site fragment via backbone cyclization with the photoswitch moiety. Its transient absorption shows so called logarithmic oscillations. The oscillations are discussed in terms of relaxation on a rugged energy landscape. The second peptide can be triggered by its built-in photoswitch to fold into an α-helix. The observed folding kinetics are in contradiction to the kinetic zipper model often used to rationalize helix folding. A detailed analysis shows that helix folding is better modelled by conformational diffusion on a rugged energy landscape with only a relatively small gradient. Part II *'Principles and Applications of Two-Dimensional and Transient Two-Dimensional IR Spectroscopy'* starts with a comparison of current 2D-IR approaches. 2D-IR structure determination is explained and its scalability to larger peptides is investigated. The experimental and theoretical groundwork of transient 2D-IR spectroscopy (T2D-IR) is developed, opening up the important field of non-equilibrium dynamics for 2D-IR spectroscopy. Different types of T2D-IR experiments are investigated with respect to their information content and are demonstrated for a metal carbonyl model system undergoing metal-to-ligand charge transfer. The developments of Part I and II are merged by applying T2D-IR to the conformational transition of a photoswitchable peptide. The technical appendix *'A Transient 2D-IR Spectrometer'* describes the experimental setup. An emphasis is made on the extension from 2D-IR to T2D-IR and on the innovations necessary for the investigation of photoswitchable peptides. A setup for nonlinear spectroscopy based on two synchronized femtosecond systems is developed that allows to scan time delays from 1 ps to 40 μs. A temperature controlled flow cell system is designed for the use with photoswitchable peptides, allowing for time resolved measurements of sample volumes down to 200 μl.

A few words for orientation: This dissertation is based on selected publications. Each of the two parts is accompanied by a general Introduction and a Conclusions and Outlook chapter. The main chapter of each part consists of the publications as well as manuscripts in preparation for publication.

Zusammenfassung

Schon lange ist bekannt, dass die Struktur von Peptiden und Proteinen einer gewissen Dynamik unterliegt. Die Bedeutung dynamischer Effekte für die biologische Funktion dieser Moleküle wurde jedoch erst im Verlauf der letzten Jahrzehnte deutlich. Gegenwärtig wird daher mit Nachdruck an der Dynamik von Peptiden und Proteinen geforscht, unter anderem im Zusammenhang mit Proteinfaltung, Motorproteinen, Katalyse, allosterischer Regulation und der Bindung von Liganden im Allgemeinen. Es beginnt sich abzuzeichnen, dass Peptid- und Proteindynamik auf einem Kontinuum von Zeitskalen stattfindet, das sich von Sekunden oder länger bis in den Subpicosekundenbereich erstreckt. Dynamik im oberen Millisekundenbereich oder langsamer kann mit Hilfe der NMR Spektroskopie untersucht werden, einer Methode die gleichzeitig eine sehr detaillierte Strukturanalyse ermöglicht. Für die schnelleren Prozesse in flüssiger Phase existieren bisher keine Methoden die sowohl hohe Zeitauflösung als auch eine ausreichende Strukturempfindlichkeit bieten. Nichtlineare zweidimensionale Femtosekunden-Infrarotspektroskopie (2D-IR), erstmalig realisiert 1998 von Hamm, Lim und Hochstrasser [2], vereint hohe Zeitauflösung mit einer gewissen Strukturempfindlichkeit. Die Aussagekraft dieser Methode wurde durch die Bestimmung der Backbone-Diederwinkel des Tripeptides Trialanin mit einer Zeitauflösung von einer Pikosekunde unter Beweis gestellt [3, 4]. Bisher wurde 2D-IR nur auf Systeme im Gleichgewicht angewandt. Die hohe Zeitauflösung diente hier der Unterscheidung sich schnell ineinander umwandelnder Zustände. Eine Erweiterung der 2D-IR Spektroskopie auf Systeme im Nichtgleichgewicht sowie die Untersuchung transienter Strukturen und Zustände erscheint unter diesen Voraussetzungen sehr vielversprechend—nicht nur im Hinblick auf Peptiddynamik sondern zur Untersuchung von Moleküldynamik im Allgemeinen. Diesem Zweck dient die hier vorgestellte transiente 2D-IR Spektroskopie (T2D-IR).

Die vorliegende Dissertation besteht aus zwei lose verknüpften Teilen, die Beiträge sowohl zum Verständnis der Dynamik von Polypeptiden als auch zum Gebiet der 2D-IR Spektroskopie leisten: Im Teil I *'Phototriggered Peptide Dynamics and Secondary Structure Formation'* werden neue Verfahren zur zeitaufgelösten Infrarotspektrosopie entwickelt, die eine detaillierte Untersuchung der Nichtgleichgewichtsdynamik von Polypeptiden ermöglichen. Integrierte molekulare Photoschalter werden eingesetzt um Dynamik zu initiieren und zu kontrollieren. Zwei Peptidmodellsysteme werden diskutiert. Beim ersten handelt es sich um ein zyklisches Peptid, das aus dem aktiven Zentrum des Proteins Thioredoxin Reduktase durch Zyklisierung mit der photoschaltbaren Gruppe synthetisiert wurde. Die transiente Absorption dieses Peptides weist sogenannte logarithmische Oszillationen auf, die im Zusammenhang mit Relaxation auf einer rauhen Energiefläche diskutiert werden. Das zweite Peptid kann mittels des eingebauten Photoschalters veranlasst werden sich zu einer α-Helix zu falten. Die hierbei beobachtete Faltungskinetik steht im eklatanten Widerspruch zu den Vorhersagen des 'kinetic zipper models' zur Helixfaltung. Eine detaillierte Analyse der Faltungskinetik ergibt, dass Helixfaltung besser als ein Konformationsdiffusionsprozess auf einer rauen Energiefläche mit nur geringem Gradienten beschrieben werden kann. Der Teil II *'Principles and Applications of Two-Dimensional and Transient Two-Dimensional IR Spectroscopy'* beginnt mit einem Vergleich experimenteller Ansätze zur 2D-IR Spektroskopie. 2D-Strukturbestimmung wird erläutert und ihre Skalierbarkeit hin zu grösseren Peptiden wird untersucht. Die experimentellen und theoretischen Grundlagen für die transiente 2D-IR Spektroskopie (T2D-IR) werden geschaffen und so der wichtige Bereich der Nichtgleichgewichtsdynamik für die 2D-IR Spektroskopie erschlossen. Verschiedene T2D-IR Experimente werden hinsichtlich ihres Informationsgehaltes untersucht und an einem Metallcarbonyl-Modellsystem demon-

striert. Die in den Teilen I und II vorgestellten Entwicklungen finden ihre Vereinigung im zuletzt vorgestellten Experiment—der Untersuchung der Konformationsdynamik eines photoschaltbaren Peptides mithilfe der T2D-IR Spektroskopie. Der technische Anhang *'A transient T2D-IR Spectrometer'* beschreibt den experimentellen Aufbau. Dabei wird besonderen Wert gelegt auf die Erweiterung von 2D-IR zu T2D-IR sowie die zur Untersuchung photoschaltbarer Peptide nötigen Neuerungen. Zu diesem Zwecke wurde ein experimenteller Aufbau für nichtlineare Spektroskopie im Zeitbereich von 1 ps bis zu 40 μs entwickelt. Eine Durchflusszelle mit Temperaturregelung, die transiente Spektroskopie mit kleinen Probenvolumina bis zu weniger als 200 μl ermöglicht, wurde speziell für photoschaltbare Peptide konstruiert.

Part I

Phototriggered Peptide Dynamics and Secondary Structure Formation

Chapter 1

Introduction

The investigation of the relation between structure, dynamics and function of peptides and proteins is of growing importance. The relevance of the three-dimensional structure for protein function has been recognized early: In 1894 Emil Fischer proposed his Lock-and-Key Principle for an enzyme binding a substrate in his work '*Einfluss der Configuration auf die Wirkung der Enzyme*' [5]. It has also long been known that peptides and proteins are dynamic structures, but the paramount importance of dynamic effects for biological function became clear only during the last decades. The role of dynamics is quite obvious in the case of so-called motor proteins such as the ATP-driven microtubule-based dynein and kinesin motors or the actin-based myosin motor [6, 7]. Also for the folding of a protein into its functional state the dynamics of the polypepide chain clearly is of importance. Much less apparent is the role of dynamics in the catalytic function or in the allosteric regulation of enzymes which is becoming more and more evident [8, 9, 10]. As a result there is currently an intense effort to investigate the dynamics of peptides and proteins in their native environment, be it liquid phase or membrane. The picture beginning to emerge is that of a continuum of timescales governing peptide and protein motion over many orders of magnitude from seconds down to the sub-picosecond regime. For millisecond and slower dynamics there is NMR as a powerful structure resolving method at our hands [11, 12]. For the faster processes in the liquid phase, taking place on the sub-millisecond to sub-picosecond time scale, there is clearly a need for an experimental method offering both high time resolution and a sufficient structure sensitivity at the same time. This is the field addressed in in this dissertation. In the present Part I, novel techniques for time resolved IR absorption spectroscopy are introduced that are particularly suited to probe conformational dynamics and folding events over a large time range from 1 ps onwards. They are applied to study the dynamics of two model peptides in the course of secondary structure formation, addressing some problems in the context of protein folding.

Section 1.1 of the present chapter gives a brief and necessarily very incomplete introduction to protein folding with a strong bias towards time resolved studies. Secondary structure formation and dynamics, as studied in this dissertation by means of model peptides, is a crucial part of the folding process. Furthermore, many aspects of the complex dynamics of polypeptide chains can be studied already in small systems undergoing secondary structure formation. A short overview of experiments on secondary structure formation and dynamics is given. Different points of view on how experimentally obtained folding kinetics might relate to a microscopic picture are reviewed. Open questions and their implications for the design of experiments are highlighted. In Section 1.2 the design of the experiments in Part I is outlined.

1.1 The Protein Folding Problem—In Search for the Native State

A great challenge in the field of protein dynamics is to understand how proteins acquire their three-dimensional structure, the prerequisite for their biological function. This question has gained additional significance in the last two decades through the discovery of so-called prion-proteins—proteins that, in a misfolded state, cause diseases

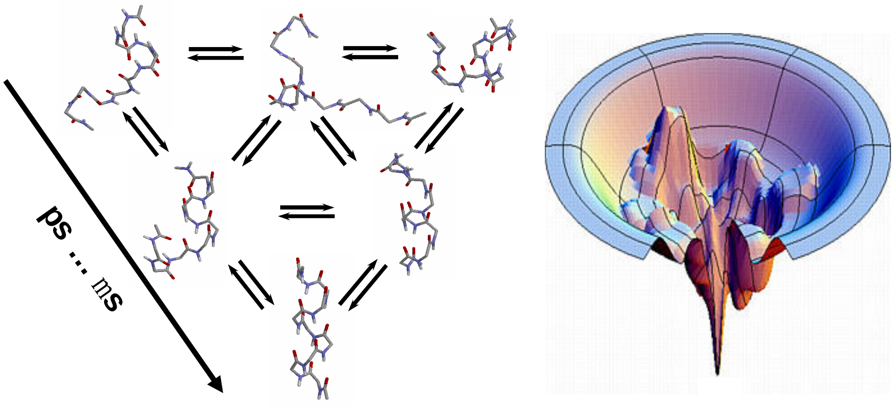

Figure 1.1: Schematic view of the formation of a small α-helix from an unfolded ensemble via conformational diffusion. The folding ensemble is believed to move on a funnel shaped free energy landscape[3] towards the global minimum.

like the bovine spongiform encephalopathy (BSE) or the Creutzfeld-Jakob disease (CJD). The cellular environment contains many factors that are involved in the process of folding during and after the protein synthesis at the ribosomes [13]. However, the work of Christian Anfinsen and others in the 1950s and 60s demonstrated that most proteins can refold spontaneously into their native structure after denaturation without any support of an *in vivo* surrounding [14, 15]. They concluded "that the information ... for the assumption of the native secondary and tertiary structures is contained in the amino acid sequence itself" [14] and that the native state of a protein is the global minimum on the Gibbs free energy surface. That is, the native conformation is determined by the totality of interatomic interactions and hence by the amino acid sequence, in a given environment. This statement has been called the 'thermodynamic hypothesis' [15].

Levinthal countered in 1969 with his well known estimate that a random search for the global minimum—proposed to be the native state—in the conformation space of even a small protein would take longer then the age of the universe [16][1]. This estimate misses the experimentally determined folding times by some dozens orders of magnitude—a discrepancy that has later been termed 'Levinthal's Paradox'. Levinthal's original argument [16] starts from the assumption that finding the global minimum requires an extensive random search in conformation space that is inconsistent with the fast time scales of folding observed by experiment. It led Levinthal to speculate that the biologically active state is a kinetically stabilized metastable state [17, 16] that is reached via a distinct sequence of events, a so called folding pathway. Levinthals picture of a series of distinct conformational events leading "from the unfolded random coil to a uniquely folded metastable state" [17] is in a way a paradox itself: if the denatured state was as random as Levinthal assumed, there could be no unique 'pathway'. However, his suggestion that the search has to be biased in some way to explain the high speed of folding remains correct.

1.1.1 A 'New View' on Folding

A widely accepted solution to Levinthal's 'paradox' has been provided by what is known as the 'new view' of protein folding [18, 19, 20, 21]. In the new view, folding is envisioned as a diffusion-like process. The folding ensemble moves on a funnel-shaped free energy landscape towards the native state, which is the global minimum in free energy as suggested by Anfinsen (see Fig. 1.1) [22][4]. Thus the 'search' in conformation space is biased,

---

[1] The original formulation [16] of what later became known as 'Levinthal's Paradox' is frequently miscited as [17].

[3] Energy landscape picture taken from Ken Dill's homepage, http://www.dillgroup.ucsf.edu/energy.htm

[4] One has to be careful about the representation of the energy landscape. Sometimes free energy is plotted against a set of reduced coordinates as in the present case [20], sometimes energy is plotted against configurational entropy to visualize the collapse of the polypeptide chain with reduced energy [23].

explaining the experimental finding of fast folding without the need to invoke distinct sequential folding pathways (but also without excluding them). The new view, sometimes termed ‘energy landscape perspective’, stresses the statistical mechanics perspective of a fluctuating structural ensemble [24]. It goes beyond the reaction path picture inherited from chemistry, which describes a reaction in terms of a few uniquely defined structural intermediates connected by mass-action kinetics equations.

The new view originated from general theoretical considerations and simplified generic lattice simulations borrowed from the fields of spin glasses [25, 26] and polymer theory [27, 28, 29]. Thus, although the funnel picture led a way out of the Levinthal dilemma, it cannot provide information on the actual energy surface for a certain real protein [21], as the funnel landscapes are constructed based on statistical mechanics considerations using a few parameters like ruggedness, the gradient towards the native state and the conformational entropy [22, 23]. Those funnels lack detailed specific features of a certain polypeptide sequence. Mapping out the complete energy landscape of a protein by realistic all-atom MD simulations including solvent degrees of freedom is still far beyond today’s computer power [30]. However, the funnel shape of the free energy landscape has been verified for simplified lattice peptide models that mimic the chain dynamics by including self avoidance and a certain topology of native contacts [19, 31, 32]. While the topology of the distribution of hydrophobic and hydrophilic residues is surely an important factor, there is strong experimental evidence for the crucial role of single ‘key-residues’ [33, 34, 35] and their specific interactions, that determine the outcome of the folding process and thus seem to affect the energy landscape fundamentally. The mechanisms for this control are still poorly understood. In this respect, new view and funnel picture are only weakly linked to experiments.

In a more direct connection to experiments, models have been suggested that employ a hierarchical view of the dynamics, often paralleling the structural hierarchy of primary, secondary, tertiary and quarternary structure. These models assume a separation of timescales, which greatly simplifies the description and thus allows for the prediction of folding sequences and rates. However, evidence is accumulating that questions the separation of time scales and consequently the general applicability of hierarchical models. A hotly debated controversy, for example, is that about the interplay between hydrophobic collapse, secondary structure formation and tertiary structure formation [36, 37, 38]. Folding of polypeptides containing tertiary structure elements can extend to milliseconds or even seconds and longer [8]. The formation of *isolated* secondary structure elements in *smaller model polypeptides* occurs between 120 ns and a few microseconds [39, 40, 41, 42, 43, 44, 45, 46, 47, 48, 49, 30, 50, 51, 46, 52, 53, 54]. While secondary structure formation was found to be quite fast in smaller peptides, the situation in a protein might be much more complicated. It is easy to imagine both, situations where secondary structure formation is assisted by the rest of the protein environment and situations where it is impeded. A large number of experiments for various proteins exists that are contradictory in respect to the relative importance of hydrophobic collapse, secondary structure formation and the formation of tertiary contacts. This experiments led to the formulation of various folding models proposing different types of hierarchies, such as the framework model, the diffusion-collision model, the nucleation-condensation model and the hydrophobic collapse model [55, 36]. However, the more experiments on different molecules are carried out, the larger seems the variety of scenarios. The balance between collapse, secondary structure formation and the guiding role of tertiary contacts thus is very likely to vary considerably from one protein to the other [38, 37]. The recent search for a ‘speed limit’ of protein folding led to the discovery of proteins with folding rates in the low microsecond range, overlapping with the timescales of secondary structure formation in small model peptides [56, 57, 58, 59] (see Reference [60] for a review). This finding raises further doubt on the separation of time scales assumed in hierarchical protein folding models. In principle, energy landscape theory can interpolate between all kinds of proposed folding models, including pure pathway models. However, there is strong disagreement on how much complexity of the energy landscape is really required to build folding models with predictive power—in the worst case one would have to carry out all-atom MD simulations for each polypeptide one would like to predict the folding mechanism for. Generally speaking there is a mismatch between the microscopic complexity of folding suggested by many theoretical papers and the simple, in many cases single exponential, kinetics found by most experiments. The question arises if the experiments are to insensitive to provide relevant model-generating information on the energy landscape or if theoreticians failed so far to distill the essential unifying themes out of the simulations.

1.1.2 Secondary Structure Formation and Peptide Dynamics

Much of the complexity found in protein folding can also be observed in the dynamics of smaller polypeptides that undergo secondary structure formation [46, 61, 54, 62]. Such small systems are the subject of the present dissertation. Related processes as in proteins, like solvation, hydrophobic collapse, breaking of nonnative contacts, hydrogen bond formation, ion pair formation or side-chain packing have been discussed in the literature. Similarly as in proteins the question of a separation of timescales arises, as well as the contradiction between microscopic complexity found in simulations and simple experimental kinetics. Like for proteins, phenomenological two-state models, hierarchical models, progress variables and the energy landscape perspective have been used to understand, describe and predict folding kinetics. The study of secondary structure formation in polypeptides thus is not only interesting because secondary structure formation might play a crucial role in the early stages of protein folding as discussed above. Those systems also offer the possibility to learn about the interplay of various processes occurring on different time and length scales in polypeptide dynamics. In contrast to large proteins, comparison of experiment and computer simulation is within reach due to the smaller size and the faster equilibration, even when considering the need for collecting sufficient statistics from a bundle of trajectories [50, 63], and one can hope to address some of the points raised in the present section.

Timescales of Peptide Dynamics. The folding and unfolding relaxation of isolated secondary structures in polypeptides of a length up to 39 residues [41] has been observed to occur between 120 ns and 3.5 μs. Various detection methods have been used to monitor secondary structure dynamics such as single channel IR absorption [44, 41], fluorescence quenching [47], UV Raman [39], and triplet-triplet energy transfer [64]. Typically a nanosecond temperature jump (T-jump) has been used to trigger the dynamics, which leads to unfolding of the secondary structure in almost all cases. Relaxation of α-helical peptides after an unfolding perturbation has been found between 120 ns and 420 ns [65, 39, 40, 41, 42, 43, 44, 45, 46, 47, 49, 30, 50, 51]. Unfolding relaxation of β-hairpins occurs between 300 ns to 3.5 μs [46, 52, 53, 54]. Except in a few experiments [48, 66] information on folding has been inferred indirectly from unfolding experiments. To this end, however, a certain folding model has to be assumed, which in most cases was a simple two-state model. Folding of secondary structure subsequent to a perturbation has so far only been observed for a cold denatured α-helix within 1.2 μs [48]. The reversible photoswitch approach pursued in this dissertation will offer increased control on the nature of the perturbation and selection of folding or unfolding at wish.

Secondary structure folding and unfolding has to be the consequence of underlying faster conformational dynamics. Several T-jump experiments have provided hints on those faster processes observing an ‘instantaneous’ component, where instantaneous means faster than about 10-20 ns in experiments published so far [44, 46, 52, 67, 68, 49, 56, 42, 41]. The origin of the instantaneous component, however, is not clear yet. An important factor for secondary structure formation is the rate at which intra-chain contacts can form. Contact formation in glycine rich random coil peptides by intra-chain diffusion has been measured by triplet-triplet energy transfer [64]. Contact formation took place within 20 ns for residues separated by 3 peptide bonds and within 200 ns at a separation of 9 peptide bonds. Somewhat surprising is the finding of 90 ns for a separation of 21 peptide bonds in an alanine rich peptide [69][5]. Molecular dynamics simulations suggest that polypeptides can undergo considerable structural changes within 1 ns or less [70, 50, 30, 51, 71]. Hummer *et al*. [72] found the formation of the first α-helical turn within 0.1-1ns in their simulations of helix nucleation in short Ala and Gly based peptides. Daura *et al*. [50, 73] simulated equilibrium folding/unfolding of a β-heptapeptide with a realistic force field at the melting point to obtain statistics on the populations of the folded and unfolded states. Several folding/unfolding events were observed in a 50 ns trajectory, where the actual transitions from unfolded to folded conformations could be as fast as 50 to 100 ps. The fast end of the time scale of backbone dynamics is marked by the fluctuations of dihedral angles about their equilibrium position that have been found to occur on a sub-picosecond to picosecond timescale by femtosecond 2D-IR spectroscopy [74]. The time resolution of the folding experiments planned here will allow to detect the presence of such fast processes, should they show up in the kinetics at early times.

---

[5] Alanine chains are thought to be less flexible than glycine chains, thus slower contact formation would have been expected.

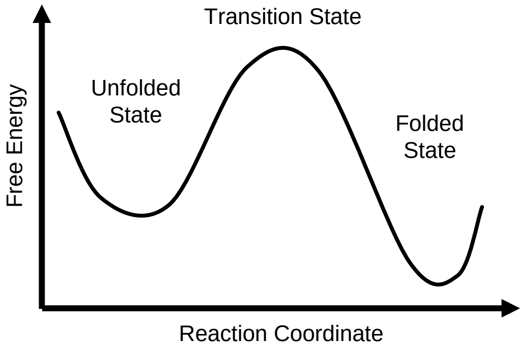

Figure 1.2: Kramers description of a two-state folder.

1.1.3 Can Folding be Mapped onto a Two-State Process?—Reduced Landscapes and What Might be Learned About Them From Time Resolved Folding Experiments

Experiments seem to suggest that many polypeptides are two-state folders. During folding a myriad of conformational steps has to occur that lead to the overall change of the structure. A multiplicity of timescales for those internal motions exists as pointed out above. This microscopic complexity has been revealed by simulations and by experiments on smaller subsystems. However, most experiments that probe the overall folding/unfolding process yielded single exponential kinetics within the experimental accuracy for larger single domain proteins [75] as well as for a number of smaller model polypeptides forming isolated α-helices [76, 47, 48] and β-structures [46, 52, 53, 54, 77]. In many cases the temperature dependence of the rate has been found to simply follow Arrhenius' law ($\ln k \propto 1/T$). Is the reason for the failure to detect complex kinetics the limited sensitivity of the experiments? Or are there more fundamental reasons for this observation? From chemical kinetics it is well known, that single exponential relaxation occurs when the system has to surmount a single high barrier (high compared to $k_\mathrm{B}T$). For gas phase reactions, this is the realm of transition state theory. In solution phase, Kramers theory is a more adequate description. For Kramers theory to be valid, it is required that a single reaction coordinate with a rate limiting free energy barrier of several times $k_\mathrm{B}T$ exists. The remaining degrees of freedom can be expressed in terms of the free energy profile along the reaction coordinate [78, 79]. While such a 1D projection describes the thermodynamic equilibrium properties correctly, the dynamics are properly described only when the relaxation of all other degrees of freedom is fast compared to the motion along the reaction coordinate. If this separation of timescales holds, folding can be described as a diffusive motion on this free energy profile (see Figure 1.2). The system then contains effectively only two macroscopic states (unfolded and folded), separated by the barrier region that is virtually unpopulated. The observation of single exponential folding kinetics in polypeptides, often in combination with an Arrhenius-like temperature dependence, displays a deceptive similarity to small-molecule reactions that has led many people to the conclusion that folding is such a two-state process and the multidimensional energy landscape can effectively be reduced to a one dimensional free energy curve with a high free energy barrier like in Figure 1.2. As a result, polypeptides that fold with single exponential kinetics often are indiscriminately termed *two-state folders* in literature, which implies that no intermediates can be observed. The use of two-state models to fit kinetics of polypeptides is thus widespread. The existence of the required barrier is typically rationalized by assuming a rate limiting step, invoking some kind of folding model. In case of protein folding, the rate limiting step could be, for example, the formation of secondary structure, as it is assumed in the framework model. In α-helix formation, the so-called zipper model is often cited with the argument that helix-nucleation—the formation of the first helical turn—should be rate limiting (as we will see below, the zipper model does not necessarily imply single exponential kinetics).

If folding was a two-state process—what could be learned from a time resolved folding experiment? During folding, the population of the conformations in the barrier region and in particular of the transition state is neg-

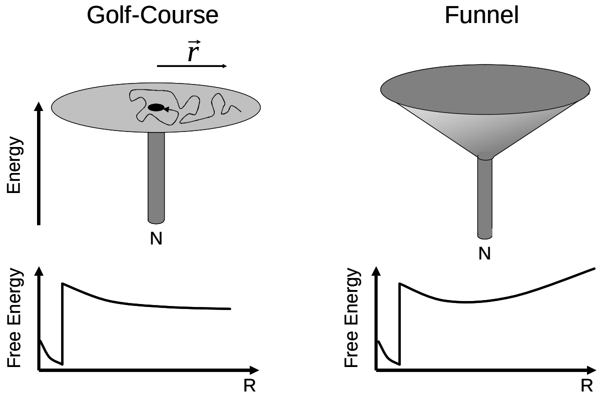

Figure 1.3: Golf-course and funnel landscape and their projection on the distance $R = |\vec{r}|$ from the native state N as a reaction coordinate. The resulting potential of mean force (free energy) features an entropic barrier that can give rise to single exponential kinetics (adopted from Reference [84]).

ligible. All that can be probed by the experiment is the vanishing of the unfolded state and the appearing of the folded state. The observed signals then are just weighted averages of the states on each side of the barrier. As intermediates are not populated, nothing can be learned about the reaction coordinate and the transition state[6]. Thus any experimental observable that can distinguish unfolded and folded state will yield the same single exponential kinetics. Also the strength and kind of the perturbation defining the starting ensemble does not matter as the relaxation within the wells is very fast compared to the barrier crossing. In particular, the direction in which the experiment is carried out (folding or unfolding) is not crucial, as the folding and unfolding rates can be easily calculated from the observed relaxation rate[7]. This is very convenient as in most cases unfolding is much easier to achieve experimentally than folding. Thus the design of the experiment is very uncritical in the case of two-state folding. The enthalpic contribution to the barrier can be inferred from measurements at various temperatures using Arrhenius' law.

However, it is wrong to generally conclude from the observation of single exponential relaxation and Arrhenius-like temperature dependence that the underlying process is two-state. While a one dimensional reaction coordinate with a high barrier leads to exponential relaxation, the observation of exponential relaxation does not necessarily imply the existence of a single transition state acting as a barrier. This was discussed by Hagen for a simple hydrophobic collapse model where relaxation occurs downhill on a 1D harmonic free energy profile [81]. The simulations showed that "downhill" folding in a 1D barrierless potential can be almost perfectly exponential, however, the apparent relaxation time then depends strongly on the experimental observable. Also the observation of a temperature depend rate that can be fit by Arrhenius' law is not sufficient to safely conclude that a single barrier is present. Thermal activation can also arise from the diffusion on a rugged energy landscape, leading to a so called super-Arrhenius temperature dependence ($\ln k \propto 1/T^2$) [82, 83]. Distinguishing Arrhenius temperature dependence from super-Arrhenius or other forms that may arise from different microscopic processes is difficult, as often the temperature in a polypeptide folding experiment can be varied only in a comparably narrow range.

Funnel landscapes and apparent two-state folding. Folding on a complex energy landscape clearly can generate heterogeneous kinetics. However, it has been shown by Zwanzig and others that a funnel shaped energy landscape, as it is typically discussed for folding, can generate single exponential kinetics for the formation of the native state [85, 84, 31, 86, 81], also in the absence of energy barriers. This has been discussed by Bicout and Szabo in a very instructive paper [84]. They have shown that folding on a completely flat and smooth golf-course Levinthal-energy-landscape (Figure 1.3) is essentially single exponential, if the native state region is sufficiently

---

[6] Information on the transition state structure in the two-state limit could be obtained for example by analyzing the effect of mutations that are designed to affect the transition state as done in Fersht's Φ-value analysis [80].

[7] For a two-state relaxation process, $k_{\mathrm{obs}} = k_{\mathrm{f}} + k_{\mathrm{u}}$, $K_{\mathrm{eq}} = k_{\mathrm{f}}/k_{\mathrm{u}}$

small. This can be rationalized using the simple centrosymmetric model of conformational diffusion in Fig. 1.3. The distance $R = |\vec{r}|$ to the native state is defined as a reaction coordinate and conformation space is projected onto this one dimension. In this reduced dimensionality the narrowing of the conformation space close to the native state shows up as an entropic barrier in the potential of mean force (Fig. 1.3). In this way the Levinthal 'paradox' can be reformulated in 1D as being the result of a high entropic barrier to folding. In a similar fashion, folding on a smooth, funnel shaped landscape can become single exponential (Fig. 1.3). In a spherical model the definition of a reaction coordinate is straight forward due to symmetry. In a real molecule it might be impossible to find a meaningful reaction coordinate in terms of molecular structure[8], however, the reasoning that the narrowing of conformation space close to the native state introduces an entropic barrier still remains valid. Now, what about the thermal activation? In case of a purely entropic barrier there is no activation enthalpy, or, in case of the funnel, the activation enthalpy is even negative. However, introducing sufficient ruggedness of the energy landscape renders the process thermally activated and can easily lead to apparent Arrhenius behavior in a certain temperature range [84]. Thus, in an experiment, relaxation on a rugged funnel landscape could appear like a two-state process at first glance.

In a real two state process, however, no intermediates and transition states could be observed. In the case of a funnel landscape, the situation is different. As a consequence of the entropic barrier, even on a multidimensional funnel shaped, essentially barrier-free energy landscape something like a transition state can exist. However, this has not much in common with the transition state of a simple chemical reaction associated with a well defined molecular structure. In the case of folding it might be more adequate to call it a transition state ensemble. In a microscopic picture, the rate limiting effect of the transition state ensemble can be understood by considering that it is more likely for a more unfolded structure to make a new native contact and proceed down the funnel than it is for a near native structure, because the majority of conformations that are accessible to a near native structure are uphill and more unfolded. Zwanzig has called such near-native structures 'gateway' structures [85]. The gateway structures act like transition states in the way that they are obligatory on the way to the native state and rate limiting. But in contrast to the transition state in a chemical reaction they are not high in energy and not improbable—in contrast they are highly populated compared to other microstates [86]. The gateway states might be structurally not much different from many other neighboring unfolded states. However, the gateway states might be quite different among each other. Therefore it is not very helpful to treat them as a single transition state, if one is interested in the structural mechanisms behind the folding process. Thus, even in the case where one could construct a 1D free energy projection, this might be not be very helpful for learning something about the structural events driving the folding process. While in a simple chemical reaction the connection between the macroscopic Kramers description and the microscopic states behind it is straight forward (microscopic and macroscopic pathways pretty much coincide), it is not at all clear what the phenomenological two-state description in terms of Kramers means for the microscopic structures involved in folding. However, in many folding experiments this is exactly what is used to interpret the data.

In contrast to the transition state of a chemical reaction, the gateway states can be highly populated, thus they might be observed using appropriate experimental techniques. This is demonstrated in a simulation by Ozkan *et al.* [31] using a two-dimensional 16-mer G$\bar{\text{o}}$ model (Figure 1.4). In a G$\bar{\text{o}}$ model, peptide units are modelled as connected beads that hop on a lattice with only pairwise native interactions contributing to the potential. Thus, the G$\bar{\text{o}}$ model is generates a very smooth funnel landscape[9]. Already this small system, that contains a comparable number of residues as the systems studied in this dissertation, but much less degrees of freedom and interactions, can teach us a lot about the effects to be expected. Ozkan *et al.* found the formation of the native state to be almost perfectly single exponential. However, as shown in Figure 1.4, parallel intermediates are occurring during folding so that the term two-state folding is completely out of place despite single exponential formation of the native structure. Such intermediates have been called hidden intermediates, as their existence is not obvious from

---

[8] Typical attempts include the number of native contacts, the number of native dihedral angles, rms deviation from the native structure or the radius of gyration.

[9] However, even the G$\bar{\text{o}}$ model is not free of frustration as the protein chain is self-avoiding. Thus there are conformations that cannot reach the native state without breaking already formed native contacts.

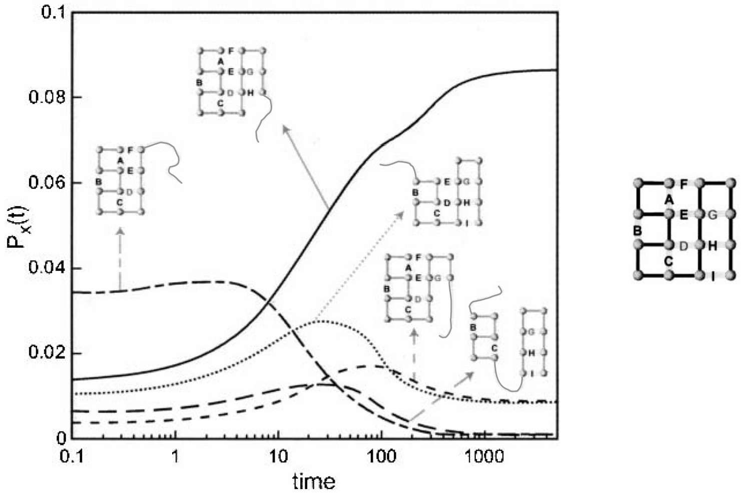

Figure 1.4: Folding of a two-dimensional Gō lattice model. The time course of the population of certain states P_x is shown. In this Gō model, the native state (right) was shown to form with exponential kinetics. However, different intermediates are populated in parallel or sequentially during folding. Reproduced from: S. B. Ozkan *et al.*, *Protein Sci.*, 11:1958-1970, 2002.

the single exponential folding kinetics with which the native state is formed [31]. However, hidden intermediates might be observed using appropriate selective time resolved techniques. Thus, despite the apparent two-state kinetics, much more details than implied by a two-state model will be accessible experimentally for folding on a funnel landscape. Using selective techniques with high structure sensitivity and high time resolution we have in principle the chance to find out about the nature of the gateway states and the structural changes in the course of the process in contrast to a real chemistry-like two-state process.

Nucleation-propagation models. Nucleation-propagation models, sometimes called zipper models, have been very successful in describing thermodynamic properties of secondary structure formation. In particular in the case of α-helices they have been used to predict secondary structure content, melting curves, etc. [87, 88, 89, 90]. With the advent of time resolved experiments on secondary structures such models where adopted also for the description of kinetics and applied to the helix-coil transition [76, 47, 48], β-hairpin kinetics [46, 91] and also the formation of a non-peptide helix [92]. Assumptions that are typically made in such kinetic models include that for each residue there is an equilibrium between a random coil conformation and a native conformation, that the transition from random coil to native is associated with a reduction of entropy, that interactions can only occur between native residues that are connected by a stretch of native residues and thus non-native interactions such as wrong hydrogen bonds or hydrophobic interactions are ignored. This setting gives rise to a system of coupled rate equations (master equation approach). To reduce the number of states it is often assumed that only a single stretch of native structure can exist in a molecule at a time, the so-called single sequence approximation. Such nucleation-propagation models are characterized by a competition between entropy loss as random coil residues become native and energy gain as native contacts are formed, leading to a more or less pronounced nucleation barrier and a certain cooperativity of the transition.

In the case of the helix-coil transition, native hydrogen bonds are formed between peptide units i and i+3. Thus, in order to form a helix, initially 3 residues must undergo the entropically costly transition from coil to helix, leading to an entropic *nucleation* barrier. Only then the helix motif can *propagate*, the so-called zipping process, driven by the enthalpic gain of hydrogen bond formation. The helix zipper model can be projected onto a 1D free energy surface like the one in Figure 1.5 where the reaction coordinate is given by the number of native hydrogen bonds. It has been shown that simulation of a diffusion process on this 1D free energy surface, using a constant

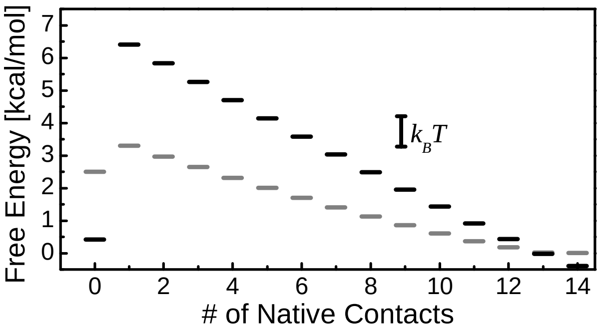

Figure 1.5: Free energy surface of the zipper model projected onto a single reaction coordinate given by the number of native contacts. The surfaces stem from a fit of the melting curve of the helical peptide investigated in this dissertation. Black bars — single sequence approximation, grey bars — without single sequence approximation.

diffusion coefficient over the hole range of the reaction coordinate, gives essentially the same results as exactly solving the coupled rate equations, even in case of a heteropeptide [93]. If the single sequence approximation is applied, the nucleation barrier is very high (Figure 1.5). Kinetics is then is single exponential. However, when abandoning the single sequence approximation, the barrier is lowered[10] and deviations from single exponential behavior are expected.

Such non-exponential kinetics have been detected recently by Gai and coworkers for the unfolding of an α-helix forming 19mer [49]. They also observed a variation of the kinetics depending on the location of the spectroscopic probe in the sequence using IR absorption spectroscopy in combination with site specific isotope labeling. Furthermore they found a dependence of the kinetics on final *and initial* temperature of their T-jump experiment. This is in strong disagreement with a two-state picture and is in contrast to many previous studies that have shown that the helix-coil transition follows single exponential kinetics that are independent of the initial temperature. While Gai and coworkers rationalized the finding of the dependence on initial temperature employing the funnel picture, Doshi and Muñoz showed in detailed simulations, that the kinetics found by Gai can be reproduced using a zipper model [94]. However, a detailed model for the IR absorption and the abandoning of the single sequence approximation is then required.

While the zipper model is very well established for the description of thermodynamics, it is not a priory clear, that it also will give a good description of the kinetics. As described above, it is always possible to make a projection on a selected reaction coordinate (for example the number of hydrogen bonds in the zipper model) that gets the equilibrium properties right. However, other coordinates might be rate limiting to the relaxation after a perturbation. In contrast to what is predicted by the zipper model, significant enthalpic barriers, that have to be overcome in the folding process, where found experimentally as well as in several simulations. Simulations suggest that these barriers arise from non-native interactions that are non-local in sequence. There is increasing evidence, that the unfolded state of proteins and even of small peptides is by no means random as assumed in the statistical models. Instead, the existence of more or less specific nonnative contacts and remaining native contacts in the unfolded state was demonstrated. This would mean the breakdown of important assumptions made in the zipper model.

Interestingly, deviations from single exponential kinetics found in experiments so far always led to a ‘stretching’ of the kinetics, i. e. a fit with a stretched exponential function ($e^{-(t/\tau)^\beta}$ [95]) reveals $\beta < 1$. In paper **P16** it is shown for the zipper model that after a strong perturbation ‘compressed’ kinetics ($\beta > 1$) should be obtained due to its high downhill driving force. Such strong perturbations can be realized by the photoswitch approach employed in this dissertation, providing a test of the zipper model. In case of the photoswitchable α-helix, helicity can be

---

[10] Allowing for multiple helical stretches in a molecule increases the number of possible species with a low number of hydrogen bonds. Thus nucleation becomes more likely.

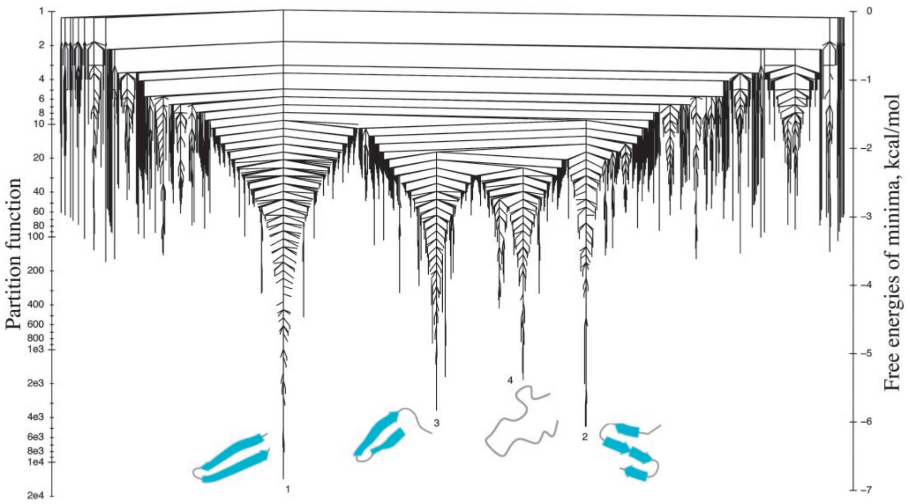

Figure 1.6: Free energy disconnectivity graph of a β-hairpin. From: S. V. Krivov and M. Karplus, *Proc. Natl. Acad. Sci.*, 101:14766-14770, 2004.

changed from about 30 % to 90 %.

Projection-free representations of the energy landscape advise caution with reduced descriptions. In general, a multidimensional dynamical problem cannot be exactly reduced to a one-dimensional one. However, given any reaction coordinate, it is always possible to obtain the free energy along this coordinate using equilibrium statistical mechanics. Given such a potential, the simplest approximate treatment of stochastic dynamics that is consistent with the equilibrium properties is to assume that the system diffuses along the reaction coordinate in the presence of this potential [84]. Typical reaction coordinates used in the context of polypeptide folding are the number of native contacts, the number of H-bonds, the number of native dihedral angles, rms deviation or radius of gyration. The obtained projections typically result in very simple and smooth funnels. However, doubts have been raised by Karplus that these reduced descriptions do obscure parts of the complexity of the full problem that are relevant for the kinetics [61]. Recently, potential energy [96] and free energy [97] *disconnectivity graphs* have been introduced as projection free representations of multidimensional energy landscapes. To construct a free energy disconnectivity graph, states are grouped into free energy minima *not* according to any geometrical characteristics (such as the number of native contacts) but according to the equilibrium dynamics. To this end, an equilibrium trajectory is used to estimate the relative free energies of the states and the rates of the transition between the states which are used to estimate the free energy barriers. An example for a β-hairpin is shown in Figure 1.6. While the formation of the native state was found to be single exponential in agreement with previous simulations and with the experimentally motivated zipper model of Muñoz *et al.* [46], the underlying free energy landscape is very complex (Figure 1.6). Apart from the funnel 1 leading to the native state, a denatured basin exists that has a number of deep subbasins which are not evident in projected surfaces published before [98]. This result contrasts with the standard funnel picture which assumes a single large basin that directs folding to the native state. Karplus comments on the kinetic measurements [46] of β-hairpin kinetics: “That the available experimental data can be parameterized in terms of a 1D Kramers-like model may tell us more about the limitations of the measurements than the underlying phenomenon” [61].

1.2 Design of the Experiments

In the case of a real two-state process, the experimental design is not very critical as pointed out above. The observable must be able to distinguish folded and unfolded, the perturbation must be just strong enough to see some response, the direction of the experiment—folding or unfolding—does not matter and the time resolution must be just sufficient to resolve the barrier-limited process. Thus, often a nanosecond T-jump has been used to perturb the equilibrium, which leads to unfolding of the secondary structure in almost all cases. If in addition measurements of the equilibrium constants are available, folding and unfolding rates can be calculated from the observed relaxation rate in the two state framework. All of this does not hold if the energy landscape is more complicated. Then, the type and strength of the perturbation in a relaxation experiment matter. Looking at Figure 1.6 it clearly becomes important where the starting ensemble is prepared on the energy landscape. Very interesting would be the preparation of non-thermal localized ensembles. Ensembles might be prepared high up on the energy landscape or in a specific subbasin. Intelligently designed phototriggers open up a way to this kind of starting ensembles. To resolve the relaxation of such an ensemble, high time resolution for the preparation as well as for the detection is required. The way an observable maps the conformational dynamics also becomes important when leaving the two-state limit. Different types of observables have been utilized in experiments on fast (ns) folding dynamics of polypeptides, such as single channel infrared absorption, UV Raman, circular dichroism, fluorescence quenching and Triplet quenching. Cases are accumulating, where different kinetics are obtained by using different observables [99, 100, 101], resulting in different folding models as demonstrated for example in the review by Winkler [100] on cytochrome c folding. The view we obtain from a particular experiment is likely to be strongly biased, as the subensemble we observe as ‘a state’ is very much defined by the experimental observable used. Using very selective observables, it might be possible to detect hidden intermediates predicted by simulations, such as in work of Ozkan *et al.* described before (Figure 1.4). However, if the kinetics depends on the experimental observable, this is already a strong hint for conformational heterogeneity during the folding process [102, 81] and a support for the energy landscape perspective.

Trying to experimentally address the issues highlighted above and extract information on the energy landscape beyond a two state picture thus places high demands on time resolution, structure resolution and the specificity of the trigger event preparing the starting ensemble. The technical developments and experiments discussed in this dissertation will hopefully contribute to a more detailed knowledge about polypeptide dynamics. The progress described here lies mainly in the following points:

- **Picosecond time resolution and scanning over 8 orders of magnitude in time.** Higher time resolution allows to observe the ensemble in regions higher up on the energy landscape, starting ‘before the Levinthal paradox is solved’, where the multiplicity of routes is most evident [103]. The combination of femtosecond laser technology and polypeptides with built in ultrafast photoswitches allows to monitor complete conformational transitions from one picosecond to tens of microseconds. Such continuous data is a prerequisite for a detailed analysis of the whole transition. The time resolution is four or more orders of magnitude higher then in most previous experiments on secondary structure formation. In particular it will allow to resolve the so-called instantaneous phase of previous T-jump experiments [44, 46, 52, 67, 68, 49, 56, 42, 41] and permit a much more precise discrimination of exponential and nonexponential kinetics.

- **Polypeptides with built in photoswitches.** High time resolution is only one benefit of the photoswitches. While in a T-jump only thermal starting ensembles can be used, the photoswitch can be designed to control the starting ensemble in different ways. It can, for example, restrict the ensemble to a certain region of conformation space and then release it [104] or steer the molecules to a certain area in conformation space [105], allowing to observe the equilibration starting from this point. In particular, folding kinetics can be observed directly and do not have to be extracted indirectly from unfolding experiments as it has to be done in most T-jump experiments. Strong perturbations become possible that allow more rigorous tests of folding models. Artifacts associated with the temperature rise in a T-jump experiments are avoided, providing a complementary view.

- **Spectrally dispersed multichannel IR detection.** Spectrally dispersed IR detection is used for the first time in fast folding experiments. IR spectroscopy is a well established tool in structural biology and is particularly sensitive to secondary structure[11]. In previous folding experiments either only single observables have been used (e. g. IR absorption at one wavelength or fluorescence lifetime), or different, subsequent experiments have been merged [67, 68]. Spectrally dispersed IR detection allows to monitor multiple observables simultaneously which helps to discriminate between different mechanisms, in particular between two-state folding and more complicated processes. The amide I band of polypeptides reports on the folding process in an averaged way. Site selective isotope labeling can be used to follow the dynamics at specific backbone sites. The signal of the isotope labeled residues thus is much more sensitive to the kinetic heterogeneity that might be hidden by apparent two-state kinetics. Also other IR chromophores, e. g. amino acid side chains, can be monitored simultaneously.

- **2D-IR spectroscopy** (discussed in Part II). Nonlinear 2D-IR spectroscopy can measure the coupling between oscillators. As the coupling depends on distance and orientation, structural parameters can be obtained with $\approx$1 ps time resolution. Contact formation between specific residues leads to strongly increased coupling and could be resolved by site directed isotope labeling. Furthermore, 2D-IR can peer behind the ensemble average in a holeburning-like fashion, separating inhomogeneous and homogeneous contributions to the spectrum. This allows for measurements of the ensemble inhomogeneity. The homogeneous linewidth measured by 2D-IR is sensitive to structure fluctuations on a picosecond timescale and thus to the very local properties of the energy landscape. **Transient 2D-IR** allows for 2D-IR measurements on the transient ensemble after a conformational transition has been triggered and will be applied to a photoswitchable peptide in Part II.

The first three ingredients, **high time resolution and continuous scanning**, **photoswitchable peptides** and **spectrally dispersed detection and isotope labeling** will be used in the remainder of **Part I**. The last point, **2D-IR spectroscopy** and its extension to **Transient 2D-IR**, will be treated in **Part II** of this dissertation on a broader basis, discussing in detail the spectroscopic background and the application to very simple metal carbonyl model systems.

1.2.1 Triggering Peptide and Protein Dynamics

Among the most widespread methods for triggering conformational changes in peptides and proteins are *rapid mixing* techniques [116] (demonstrated time resolution 70 μs), *pressure jump* employing piezo devices [117] (demonstrated time resolution 50 μs) as well as *laser induced pH-jump* employing photoacids [118] (here, time resolution has been limited in most cases by the use of nanosecond pump lasers or slow detection, however, the fundamental limit is set by the equilibration of the exited state of the photoacid with the bulk and the polypeptide). *Laser induced T-jump* is the method that provided most of the information on secondary structure formation to date. The T-jump changes the equilibrium between folded and unfolded state. In most cases elevating the temperature leads to unfolding of the molecules, however, for cold denatured samples, folding can be observed [119]. In principle, T-jump experiments could be performed with quite high time resolution, limited only by the thermal equilibration of the bulk solvent on a time scale of tens of picoseconds [120]. However, usually the T-jump is achieved by pumping a vibrational overtone of D_2O at about 1.9 μm with a Raman-shifted nanosecond Nd-YAG laser which limited the time resolution to about 3 ns [68]. Furthermore, the detection schemes usually employed have a time resolution $>$10 ns. In the Papers **P1**, **P4**, **P6**, **P9**, **P13** and **P16** of this dissertation we advance a different approach for triggering based on *photoswitchable peptides* (Figure 1.7) to achieve subpicosecond time resolution.

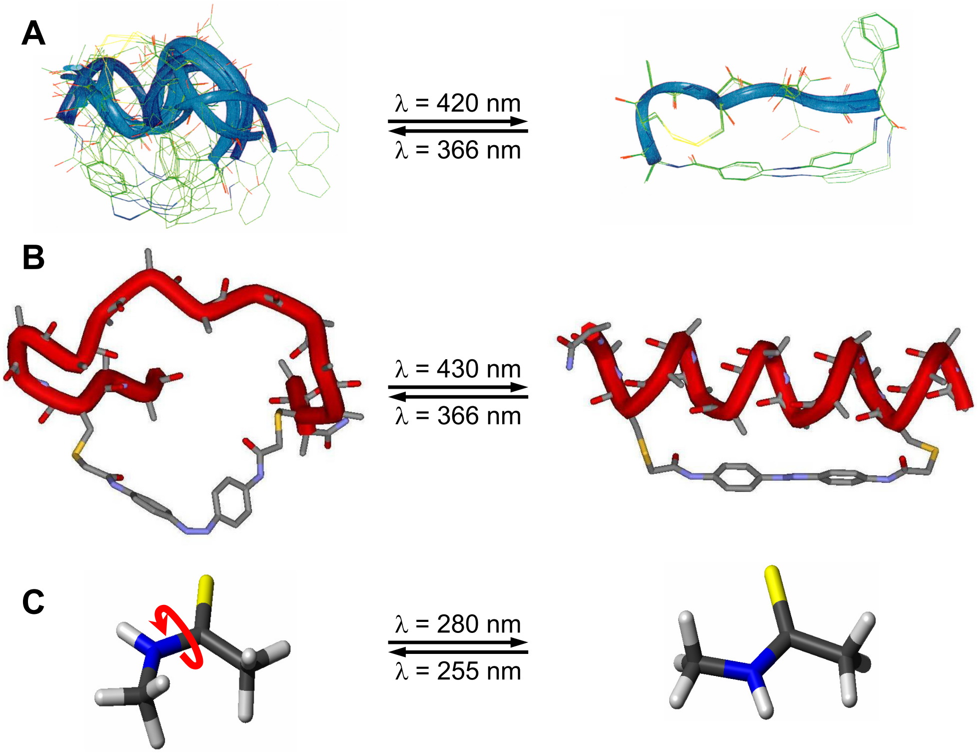

Figure 1.7: A—The cyclic peptide cycAMPB was designed by Moroder and coworkers and is investigated in Papers **P1**, **P4** and **P6**. B—Photoswitchable α-helix FK11X designed by Woolley and coworkers, investigated in **P13** and **P16**. C—N-Methylthioacetamide, investigated in **P9**.

Photoswitchable Peptides

A variety of phototriggers for the investigation of peptide and protein dynamics has been suggested. In many cases, the trigger process is ultrafast ($<$1 ps), and therefore does not overlap anymore with potentially interesting timescales of the peptide. Here is an overview of the most promising approaches including those employed in the present dissertation:

- *Photocleavable linkers*: The polypeptides are forced into a nonnative conformation by a chemically introduced linker. Upon photocleavage of the linker the molecules are released to explore their conformation space freely and folding can be observed. This approach could allow to impose a significant perturbation on the system and, to some extend, to select the starting point on the energy landscape by biochemical engineering of the educt. Time resolved spectroscopy of such molecules was pioneered by the group of Robin Hochstrasser using artificial disulfide bridges formed by thiotyrosine derivatives [104, 121]. Their model peptide was designed to fold into an α-helix after photocleavage, however, geminate recombination of the biradicals was too fast and occurred before secondary structure formation could be observed. Recently, the group of Chan put forward a more promising approach based on 3',5'-dimethoxybenzoin bromoacetylate for linking a cysteine residue with the N-terminus of the peptide [115]. Upon cleavage, a benzofuran linked to the N-terminus and a carboxymethylcysteine are formed which are inert to further chemistry. This resulted in a high quantum yield for cleavage and secondary structure formation in the refolding of a β-sheet.

---

[11] Besides IR techniques, a large variety of detection methods has been used in the context of protein folding (See Ref. [106, 107]): pulsed deuterium labeling in combination with NMR [108, 109] or mass spectroscopy [110], NMR spectroscopy [111], CIDNP techniques [112], circular dichroism (CD) [113], fluorescence quenching [64], resonance Raman [39], Small Angle X-Ray Scattering (SAXS) [114], photoacoustic calorimetry [115] and many more.

However, folding was monitored by photoacoustic calorimetry with a time resolution of 30 ns to occur with a time constant of 40 ns, one to two orders of magnitude faster than observed by other techniques.

- *Photoinduced dipole change of a prosthetic group*: Gai and coworkers linked a Ruthenium tris-bipyridyl complex to the N-terminus of a helix forming peptide [66]. This complex undergoes metal-to-ligand charge transfer upon photoexcitation, thereby increasing its dipole moment by 5-9 D. Helix formation is assisted and triggered by this dipole. The authors observed folding on a 300 ns timescale. A great advantage is that this switching is fully reversible. Drawbacks of this approach are strong vibrational Stark effects that make the interpretation of spectral shifts more difficult. Also, the electronic relaxation of the complex perturbs the folding kinetics.
- *Photoisomerizable azobenzene based* ω*-amino acids*: The *cis-trans* isomerization of azobenzene is widely used for photoswitching. Isomerization is ultrafast ($<$ 1 ps) [122, 123] with a high quantum yield (up to 50%). In most azobenzene derivatives, the *trans*-state is thermally stable, so that *trans-cis* isomerization is thermally reversible, typically on a time scale of minutes to hours. A crucial advantage of most azobenzene based compounds is the spectral separation of *cis* and *trans* absorption bands that allows to select the direction of isomerization. The groups of Moroder [124, 125, 126] and Chmielewski [127] achieved photomodulation of the 3D structure of cyclic peptides by directly incorporating azobenzene into the peptide backbone in form of an ω-amino acid derivative. In Papers **P1**, **P4** and **P6** of this dissertation we employed femtosecond transient IR absorption spectroscopy, as well as femtosecond 2D-IR and T2D-IR spectroscopy to investigated the dynamics of a peptide of this type (cycAMPB, see Figure 1.7a for the structure).
- *Photoisomerizable azobenzene cross linker*: Andrew Woolley and coworkers have achieved control over the helical content of various peptides using an azobenzene cross-linker that connects two cysteine side chains [128, 105, 129, 130]. One peptide (FK11X) out of their series has recently been studied by nanosecond optical rotary dispersion yielding a time constant of 55 ns for phototriggered α-helix unfolding [40]. In Papers **P13** and **P16** of this dissertation we study α-helix folding of FK11X (structure in Figure 1.7b) by femtosecond IR absorption spectroscopy. The main spectral change associated with α-helix formation occurred with a time constant of 270-2500 ns depending on temperature, but in addition much faster processes where resolved with the help of site specific isotope labeling and spectrally dispersed detection.
- *Thioamides*: The least invasive way of photoswitching, avoiding all prosthetic groups, would be to use the photoisomerizing properties of the peptide unit (the -CONH- unit) itself. The peptide unit can be isomerized from the energetically favored *trans* isomer to *cis* by exciting the $\pi\pi^*$ transition at 186 nm [131]. However, such an excitation of a polypeptide would not be site specific and would lead to random isomerization at different residues. Site specific substitution of the amide oxygen by sulfur (thioxylation) leads to a thioamide, that still undergoes photoisomerization but exhibits a significantly red shifted $\pi\pi^*$ transition at 255 nm. It has been shown that the original secondary structure is almost unperturbed in thioxylated peptides [132, 133] rendering thioxylation the least invasive way of making a peptide photoswitchable. This approach for photocontrol of peptide structure has been demonstrated in the group of Seebach [134] as well as by Fischer and coworkers [135] in steady state experiments. In Paper **P9** of this dissertation we investigated the photophysics of the photoswitchable N-Methylthioacetamide unit itself by time resolved IR spectroscopy (see Figure 1.7c for the structure).

1.2.2 IR Spectra Provide Structure Information

IR spectroscopy as a method for secondary structure determination of polypeptides has been explored since the 1950s [136] (for reviews see [137, 138]). The IR spectrum of peptides and proteins features nine vibrations associated with the peptide groups of the backbone, usually called amide A, amide B and amide I-VII in order of decreasing frequency [139]. By far most of the research has focused on the amide I band (1600-1700 cm^{-1}) as it is particularly sensitive to secondary structure and it is spectrally well separated from most of the other vibrational

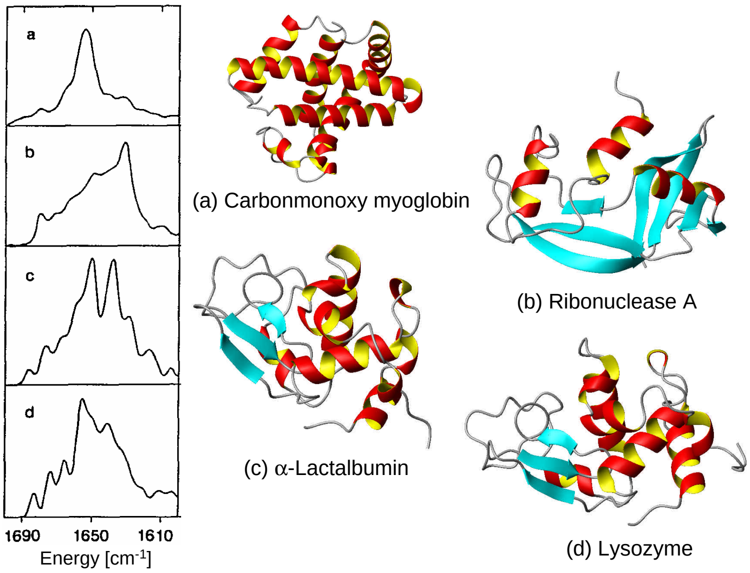

(a) Carbonmonoxy myoglobin

(b) Ribonuclease A

(c) α-Lactalbumin

(d) Lysozyme

Figure 1.8: Amide I spectra of proteins with different secondary structure content. The spectra are already weakly deconvoluted. Spectra are taken from Torii and Tasumi [140] and references therein. Structures 1MBC, 7RSA, 1ALC, 2LYM are taken from the RCSB Protein Data Bank, figures are prepared with the program MOLMOL [141].

modes. The amide I mode is mainly a CO stretching vibration with minor contributions from antiphase CN stretching, CCN deformation and the NH in plane bending. The NH contribution is responsible for the sensitivity of the amide I mode to N-deuteration of the backbone. The amide I bands of an *N*-deuterated backbone can be red shifted up to 10 cm^{-1} and are often termed amide I'.

The experimental determination of secondary structure content from IR absorption spectra typically involves band fitting, often assisted by resolution enhancement techniques such as Fourier-deconvolution [142], fine-structure enhancement [143], derivation techniques or similar. The component bands obtained by fitting are then assigned to secondary structures using empirical databases. The analysis of secondary structure content based on IR spectra requires great cautiousness as there are several severe conceptual problems associated with decomposing 1D spectra into component bands: Above all, the band overlap is severe; most methods rely on the additivity of different parts of the structure, however coupling between neighboring secondary structure elements can lead to new spectral features; spectra depend on the dimension of the structure (length of the helix, etc.); Spectra depend on charge distribution and polarizability of the surrounding, that can change from the core of a protein to its surface—just to name a few of the problems. For a critical assessment of secondary structure determination by IR spectroscopy see references [144, 145]. Despite those problems IR spectroscopy, if applied carefully, has proven useful in estimating the secondary structure of peptides and proteins. (See Figure 1.8 for amide I spectra of proteins with different secondary structure content.)

Due to its high structure sensitivity IR absorption spectroscopy is particularly suited to observe small structural changes by taking difference spectra [138]. Even if the structural origin of the signal is not completely clear, time resolved difference spectroscopy is still very useful to establish the time scales of structural changes. The intrinsic time resolution given by the vibrational lifetime is fast, typically on the order of 1 ps. In paper **P13** of Chapter 2 we monitor the folding of an α-helix by time resolved difference spectroscopy. Here, we can resolve the 'random coil' signature decreasing and the α-helix signature growing in. Isotope labels are used to follow the dynamics of specific residues. In the α-helix we also where able to spectrally resolve the contribution of Glu side chains, however, the structural origin of their response is not yet understood.

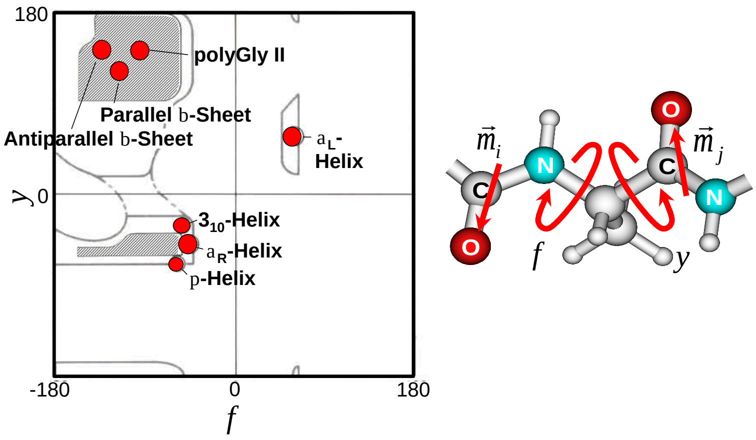

Figure 1.9: Ramachandran plot of common periodic secondary structures (adapted from reference [146]). Two neighboring peptide units, their transition dipole moments $\vec{\mu}$ and the dihedral angles ϕ and ψ describing their relative orientation.

How the spectrum depends on backbone conformation—Transition dipole coupling provides a basic theoretical description of amide I structure sensitivity. The success of IR spectroscopy in peptide and protein structure determination triggered theoretical investigations of the structure sensitivity and attempts to calculate amide I spectra quite early: In 1960 Miyazawa considered the peptide backbone as being built out of NMA (N-methylacetamide) monomers and devised a perturbative approach for the calculation of vibrational eigenstates of the peptide chain composed by the NMA monomers [147]. However, the coupling formulas in his approach where quite complicated and the physical background of the various coupling terms was not very obvious. Krimm and Abe in 1972 proposed *transition dipole coupling* (TDC) as the main mechanism coupling the amide I modes of the different peptide units [148, 149, 139]. Like Miyazawa they treated the amide I subspace of vibrational states as decoupled from the rest of vibrations. In their model, delocalized molecular vibrations arise from coupling between the site states that are localized on the single peptide units. This gives rise to the one-exciton Hamiltonian in the basis of site states $|i\rangle$ that describes the absorption spectrum

$$H^{(1)} = \sum_{i}^{n} \varepsilon_i |i\rangle\langle i| + \sum_{i\neq j}^{n} \beta_{ij} |i\rangle\langle j|. \tag{1.1}$$

Here, ε_i are the vibrational eigenenergies of the uncoupled site states and β_{ij} are the couplings between the two site states $|i\rangle$ and $|j\rangle$. The β_{ij} arise from transition dipole coupling according to

$$\beta_{ij} = \frac{1}{4\pi\varepsilon_0} \frac{\vec{\mu}_i \cdot \vec{\mu}_j}{r_{ij}^3} - 3\frac{(\vec{r}_{ij} \cdot \vec{\mu}_i)(\vec{r}_{ij} \cdot \vec{\mu}_j)}{r_{ij}^5}, \tag{1.2}$$

where $\vec{\mu}_i$ are the transition dipole moments of the site states $|i\rangle$ and the r_{ij} are the distances between their transition dipoles. The dependence of the amide I band on backbone conformation enters via the relative orientation and distance of the transition dipoles. The relative orientation of two peptide units depends on the dihedral angles ϕ and ψ, which are the main degrees of freedom of the polypeptide backbone. Figure 1.9 shows the dihedral angles as well as the location of common periodic secondary structures in ϕ/ψ-space in a Ramachandran plot. Using the TDC model (or one of the more sophisticated models discussed in **Part II**) one can map the coupling parameter β_{ij} on combinations of dihedral angles. The TDC model was successful in explaining qualitatively the change of the amide I with structure and the various spectral features resulting from different secondary structures and was used by many authors for the simulation of peptide and protein spectra [140, 150, 151, 152, 153, 154, 155, 156]. In the description of 2D-IR spectra the coupling and the relative orientation of the transition dipoles also plays an important role as discussed in **Part II**.

1.2.3 Technical Developments for Folding Experiments with Photoswitchable Peptides.

The details of the experimental setup are described in the technical appendix. Here just an overview of the main technological developments is given. To make full use of the ultrafast trigger event provided by the photoswitches we use femtosecond UV-pump IR-probe spectroscopy as described in Paper **P1**. In standard femtosecond pump-probe setups the scanning range is limited to about 10 ns by the use of optical delay lines. To cover the whole time scale of peptide dynamics we designed a system of two synchronized femtosecond laser systems as described in Paper **P11** in the technical appendix 7.3. In this setup, the delay is scanned electronically, circumventing the limitations of optical delay lines in terms of delay range, scanning speed and beam pointing stability. This setup is applied in the investigation of the photoswitchable α-helix in Papers **P13** and **P16**. For the first time in fast time resolved folding experiments we use spectrally resolved multichannel infrared detection. This allows us to monitor spectral shifts in unprecedented detail (**P1**) and to follow simultaneously multiple spectroscopic observables such as the amid I' band, side chains and isotope labels (**P13**). Furthermore, multichannel detection is a prerequisite for the T2D-IR experiments as described in **Part II**. An important development is the thermostated flow cell for micro amounts of sample (Described in Paper **P2** in the technical appendix 7.4). This flow cell allows us to work with a few hundred micrograms of sample, and made the time resolved experiments on the specially designed photoswitchable peptides possible.

1.2.4 Outline of the Publications

Following Publications are reproduced in the next Chapter:

Paper **P1** discusses the cyclic peptide cycAMPB (Figure 1.7a) derived from the thioredoxin reductase active site fragment H-Ala^1-Cys^2-Ala^3-Thr^4-Cys^5-Asp^6-Gly^7-Phe^8-OH via backbone cyclization with the photoswitchable (4-aminomethyl) phenylazobenzoic acid [125]. This peptide undergoes a transition from an unordered state to an ordered state that comes close to the conformation of the active site in the natural thioredoxin reductase. Thereby a photomodulation of the redox potential and the enzymatic activity of the fragment can be achieved [157].

Paper **P13** reports on the photoswitchable α-helix in Figure 1.7b. The molecule is designed in a way that helix formation can be triggered and studied directly. The perturbation imposed by the photoswitch is strong, leading to a change in helicity of about 60 %, much more than in a typical T-jump experiment.

Paper **P16** analyzes the kinetics of the α-helix experiment in some detail. Kinetics of a zipper model, a golf-course landscape and of a funnel shaped landscape are compared with the experimental results. The role of the experimental observable is discussed. Due to the strong perturbation and the investigation of folding, rather than unfolding, the experiment allows some strong conclusions on the shape of the energy landscape.

Paper **P9** examines a different type of photoswitch suitable for triggering polypeptide dynamics. The least invasive photoswitch is actually already build into a polypeptide: the peptide bond itself undergoes *trans-cis*-isomerization upon 190 nm excitation. In a polypeptide such excitation would not be selective and change the conformation of arbitrary peptide bonds. However, substituting the carbonyl oxygen by sulfur shifts the absorption to the red and the so obtained thiopeptide bond can be selectively addressed by an excitation pulse.

Chapter 2

Dynamics of Photoswitchable Peptides —The Publications

2.1 P1 – Picosecond Conformational Transition and Equilibration of a Cyclic Peptide

Jens Bredenbeck, Jan Helbing, Arne Sieg, Tobias Schrader, Wolfgang Zinth, Christian Renner, Raymond Behrendt, Luis Moroder, Josef Wachtveitl, and Peter Hamm,
Proc. Natl. Acad. Sci., 100:6452–6457, 2003

2.1.1 Abstract

Ultrafast IR spectroscopy is used to monitor the non-equilibrium backbone dynamics of a cyclic peptide in the amide I vibrational range with picosecond time resolution. A conformational change is induced by means of a photo-switch integrated into the peptide backbone. While the main conformational change of the backbone is completed after only 20 ps, the subsequent equilibration in the new region of conformational space continues for times $>$16 ns. Relaxation and equilibration processes of the peptide backbone occur on a discrete hierarchy of time scales. Albeit possessing only a few conformational degrees of freedom compared to a protein, the peptide behaves highly non-trivially and provides new insights into the complexity of fast protein folding.

2.1.2 Introduction

Protein dynamics occurs on a large range of time scales, which can coarsely be related to various length scales of proteins: Dynamics of tertiary and quaternary structure extends from milliseconds to seconds and even longer, while formation of secondary structure has been observed between 50 ns and a few microseconds [43, 44, 45, 46, 47, 48, 49, 30, 50, 51, 64]. Nevertheless, several experiments have provided strong hints for the relevance of even faster processes from the observation of large instantaneous signals, which could not be time-resolved [44, 158, 49]. For example Huang *et al*. [49] indirectly concluded that helix nucleation might occur on a sub-nanosecond time scale, while Thompson *et al*.[47] estimated a ”zipping time” for a 21-residue α-helix of 300 ps at 300 K. Also molecular dynamics (MD) simulations suggest that peptides and proteins can undergo considerable structural changes within 1 ns or less [70, 50, 30, 51, 71]. Hummer *et al*. [72] found the formation of the first α-helical turn within 0.1-1ns in work on helix nucleation in short Ala and Gly based peptides. Daura *et al*. [50, 73] simulated equilibrium folding/unfolding of a β-heptapeptide at the melting point and above to obtain statistics on the populations of the folded and unfolded states. Several folding/unfolding events were observed in a 50 ns trajectory, where the actual transitions from unfolded to folded conformations could be as fast as 50 to 100 ps. Time-dependent 2D-IR-spectroscopy has recently been applied to focus directly on single bond dynamics in a peptide backbone, revealing that fluctuations of dihedral angles occur in less than a picosecond [74]. These elementary conformational steps represent the lowest hierarchical level of protein dynamics. Due to a lack of appropriate techniques, however, little is known from experiment about intermediate times between about 1 ps and 10 ns. It is the aim of the present study to bridge this gap.

Conformational transitions of peptides and proteins are most commonly triggered by changing the environment of the molecule, thereby shifting the equilibrium constant of the process under investigation (see Refs. [43, 46, 45, 48, 49] and Refs. [36, 106, 159, 160] for recent reviews). Among these methods only temperature jump experiments have been shown to allow for a sub-nanosecond time resolution [120]. Even faster triggering with a possible sub-picosecond time resolution can be achieved with a molecular switch incorporated in the peptide chain [104, 161, 125, 162]. Ultrafast light-induced changes of the switching molecule [122] initiate structural dynamics of the peptide on the picosecond time scale by changing a conformational restraint [162]. The peptide then starts from its old conformation to sample the conformational space now accessible under the rule of the modified potential.

The system studied here is a cyclic octapeptide with an azobenzene photoswitch embedded in its backbone (cycAMPB, Fig. 2.1b) [125]. The azobenzene unit can be reversibly switched between the *cis* and *trans* conformation using light with different wavelengths, thereby predetermining the conformation of the backbone of the cyclic peptide. According to NMR investigations [125], the *cis* state of cycAMPB is a frustrated system with many close lying conformational energy minima, leading to an ensemble of structures with different backbone geometries. The standard deviation (rmsd) of the nuclei positions of the backbone is 1.54 Å (Fig. 2.5). Upon switching to the *trans* conformation, the backbone structure is much better defined with a significantly reduced rmsd value of 0.19 Å (Fig 2.5). The *cis* → *trans* transition, which is studied here, thus runs from a broad ensemble into one with a narrow distribution in conformational space. The photoreaction of this [125] and a very similar molecule [124] has been analyzed recently by probing the electronic response of the photoswitch itself by visible spectroscopy [162, 163]: The *cis* → *trans* isomerization of the azobenzene unit has been found to be finished within less than a picosecond with a quantum efficiency of about 50% [164]. A transient signal extending up to 1 ns -with significant contribution in the 50 ps range- has been observed which has been attributed to residual stress exerted by the peptide backbone onto the photoswitch. The time scale of these processes could be reproduced using MD simulations. Different concepts to photo-modulate the conformation of small peptides using an azobenzene moiety have been reported in Refs. [127, 128].

Here, we monitor directly the dynamics of the peptide backbone applying ultrafast transient vibrational spectroscopy of the amide I band, rather than the indirect effect of backbone dynamics on one spectroscopic degree of freedom as in Ref. [162]. The amide I band originates mainly from the C=O stretch vibration of the peptide units and has proven to be a sensitive probe of backbone structure [139]. It is therefore expected that the amide I band monitors much more directly the complicated structural dynamics. We find that stretching of the peptide backbone is essentially completed after only

20 ps, while the subsequent equilibration in the new region of the conformational space continues for times >16 ns.

2.1.3 Material and Methods

We investigated the cyclic octapeptide formed from the thioredoxin reductase active site fragment H-Ala^1-Cys^2-Ala^3-Thr^4-Cys^5-Asp^6-Gly^7-Phe^8-OH via backbone cyclization with the photoswitchable (4-aminomethyl) phenylazobenzoic acid (cycAMPB, see Fig. 2.1b) [125], as well as its linear precursor molecule (linAMPB, see Fig. 2.1a), which was used as a reference molecule. Both samples were dissolved in anhydrous dimethylsulfoxide (DMSO) with the concentration adjusted to an absorbance of about 0.1 OD for the amide I band (≈ 4 mM). DMSO was used as solvent because of the good solubility of the peptides and because of its high IR transmission in the spectral range of interest. The sample was circulated through a CaF_2 flow cell in a closed cycle designed for small amounts of liquid. Its teflon spacer (thickness 100 μm) featured a small reservoir allowing for cw-irradiation and a thin channel where the flow was sufficient to completely exchange the sample between subsequent laser pulses. No indications of sample degradation during the measurements were found from visible and stationary FTIR spectroscopy.

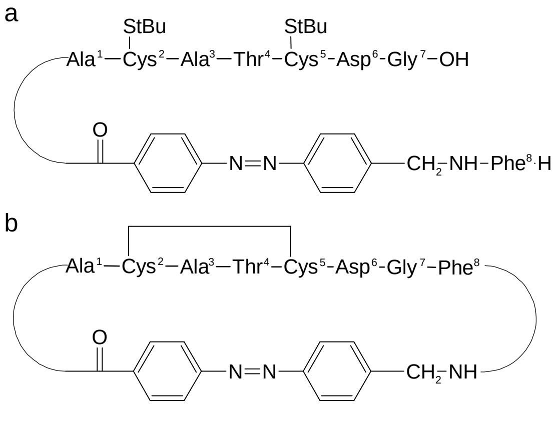

Figure 2.1: Structure sketch of (a) the S-*tert*-butylthio-protected linear precursor peptide linAMPB and (b) the disulfide-bridged cyclic peptide cycAMPB.

The dark adapted peptide molecules are in the *trans*-azo conformation at room temperature [125]. Before applying the short switch pulse, the population was shifted to *cis* by continuous UV irradiation of the *trans* $\pi \rightarrow \pi^*$ band with an Ar-Ion laser (Coherent "Innova 100", 363 nm, 200 mW). Using the absorption cross sections at 363 nm and isomerization quantum yields of the *cis* and *trans* isomers, the thermal back-reaction rate [161, 124, 125], and the transmission of the cw UV laser, we estimated that >90% of all molecules in the closed cycle system are in the *cis*-azo conformation after about 1/2 h of irradiation. The transition from *cis* to *trans* was then initiated by a short 420 nm laser pulse (energy 8.5 μJ/pulse) obtained from a frequency doubled 1 kHz Ti:Sapphire-laser/amplifier system (Spectra-Physics, Spitfire). In order to avoid unwanted nonlinear effects in the sample cell windows (such as white light generation or the formation of color centers in the sample cell windows [104]), the pump pulses were stretched to 700 fs by guiding them through 25 cm fused silica.

The evolution of the peptide backbone after photoswitching the azobenzene unit was monitored by transient IR spectroscopy of the amide I band. IR probe pulses (center frequency 1650 cm^{-1}, bandwidth 240 cm^{-1} FWHM, 100 fs) were generated using a white light seeded two-stage BBO-optical parametric amplifier, the signal and idler pulses of which were difference frequency mixed in a $AgGaS_2$ crystal [165]. The IR beam was split into a probe and a reference pulse which were focused into the sample with a $f = 10$ cm off-axis parabolic mirror, yielding a spot size of 70 μm. Both probe and reference beam were frequency dispersed in a spectrometer and imaged onto a 2×32 pixel HgCdTe detector array which enables us to measure low noise transient spectra on a single shot basis with a resolution of 4 cm^{-1}.

Time scans with parallel and perpendicular pump pulse polarizations were recorded simultaneously by changing the polarization of the pump beam every 400 laser shots in order to correlate drifts in both measurements. The pump pulses were delayed with respect to the probe pulses by means of an optical delay stage for the delays up to 1.7 ns. Longer delays of up to 16 ns were created by a fixed delay loop, therefore no transients are available in this time range. In addition, a transient spectrum at a delay of 1 ms spectrum was recorded using two subsequent laser pulses of the Ti:Sapphire-amplifier with a larger focus of the 420 nm pump pulses and a reduced flow rate of the sample. Stationary *cis-trans* difference spectra were measured in a FTIR spectrometer (resolution 4 cm^{-1}) after irradiation with a spectrally filtered high power xenon lamp.

2.1.4 Experimental Results and Assignments

Steady-State Spectroscopy

The absorption spectra of the cyclic peptide cycAMPB in the *trans* configuration, as well as that of its linear precursor linAMPB, show a broad amide I band centered at 1675 cm^{-1} with only little structure (Fig. 2.2 and Fig. 2.3, top). As the peptide chain contains 8 amino acids and the C=O group of the azobenzene moiety, in total 9 amide I vibrators, which are not spectrally resolved, lie underneath this band. The band at 1720 cm^{-1} originates from the carboxyl groups of the aspartic acid and (in the case of linAMPB) the C-terminal group. The difference spectra between the *trans* and *cis* conformation obtained under steady state illumination in a FTIR spectrometer, on the other hand, reveal a very different response for the two samples (Fig. 2.2 and Fig. 2.3, bottom). In these difference spectra, negative signals originate from the depleted start (*cis*) conformation and positive signals from the generated (*trans*) conformation. The linear precursor molecule linAMPB exhibits only a small response upon *cis* → *trans* isomerization of the azo switch. In the open chain-like form of the molecule the conformation of the AMPB chromophore does not impose a severe restraint on the backbone structure of the linear peptide. In contrast, the difference spectrum of cycAMPB reveals a blue shift of the amide I band since the backbone is forced to adopt a new conformation.

It is well established that the amide I band is a sensitive probe of protein secondary structure, and is for example commonly used to distinguish between α-helical and β-sheet structure motives in large proteins [144]. The structure sensitivity is attributed mainly to the distance and angle dependence of the coupling between individual amide I vibrators [139, 140]. This coupling was originally introduced by Krimm and coworkers as transition dipole coupling. However, since the size of the peptide unit is about the same as the distance between adjacent groups, the dipole approximation is crude, and more sophisticated approaches using *ab initio* quantum-chemistry calculations have been developed recently [150, 166]. Applying the model outlined in Ref. [140] to the *cis* and *trans* structures of cycAMPB derived from NMR spectroscopy [125], the experimentally observed blue shift can be reproduced. Hence, we conclude that the blue shift directly reflects the stretching of the peptide backbone upon *cis*→*trans* isomerization.

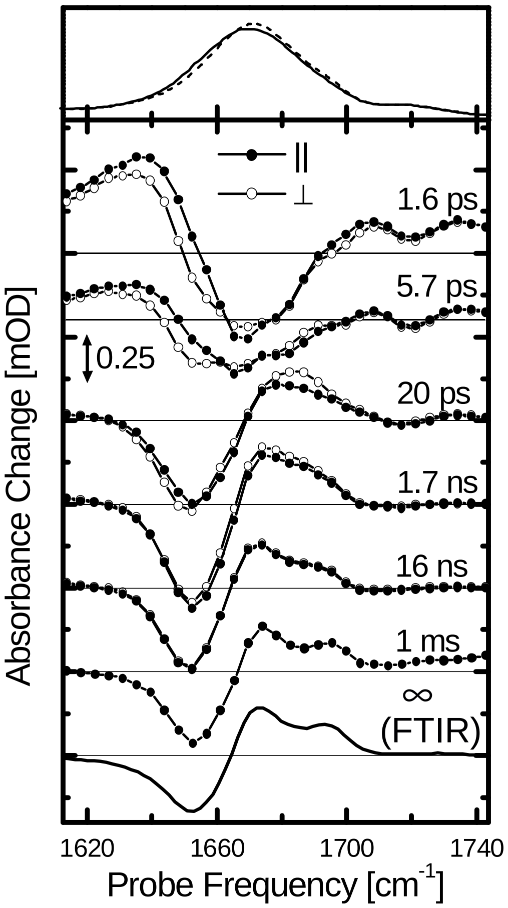

Figure 2.2: Absorption spectra of the *cis* (top, solid line) and *trans* confomer (top, dashed line), transient difference spectra at selected delay times (middle) and stationary *cis*-*trans* difference spectrum measured in the FTIR spectrometer (bottom) of the cyclic peptide cycAMPB. The FTIR difference spectrum and the absorption spectrum have be scaled to facilitate direct comparison with the time resolved spectra. The transient responses with both parallel (filled circles) and perpendicular (open circles) polarization of pump and probe pulses are shown (both have been measured simultaneously and have not been scaled with respect to each other, see Material and Methods). The scale of the time resolved spectra is the same as in Fig. 2.3

Transient Spectroscopy

The time evolution of both AMPB peptides on their way from the start to the end conformation is investigated by transient IR spectroscopy (Fig. 2.2, Fig. 2.3 and Fig. 2.4). Two main phases can clearly be distinguished from the experimental data:

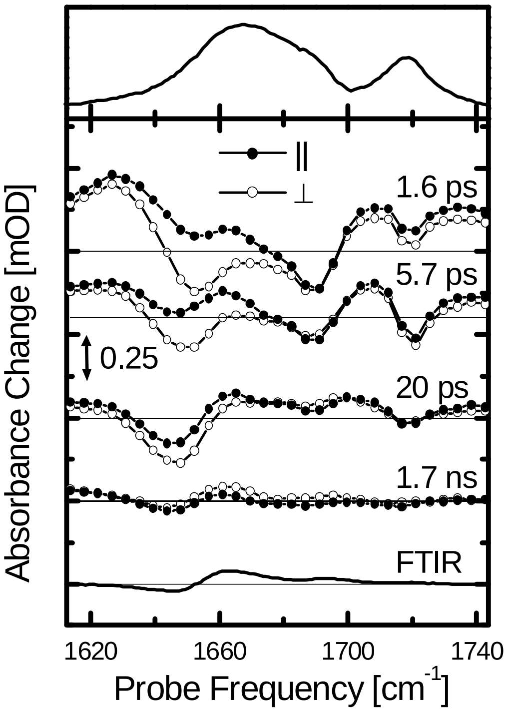

Figure 2.3: Absorption spectrum (top), transient difference spectra at selected delay times (middle) and stationary *cis-trans* difference spectrum measured in the FTIR spectrometer (bottom) of the linear precursor peptide linAMPB. The responses with both parallel (filled circles) and perpendicular (open circles) polarization of pump and probe pulses are shown (both have been measured simultaneously and have not been scaled with respect to each other, see Material and Methods). The FTIR difference spectrum and the absorption spectrum have be scaled to facilitate direct comparison with the time resolved spectra. The scale of the time resolved spectra is the same as in Fig. 2.2

Fast Phase, 0 - 20 ps (*driven* and *cooling* phase): Immediately after photo-switching of the azobenzene unit from *cis* to *trans*, a transient red shift of the amide I band of the peptide is observed (Fig. 2.2, 1.6 ps), which decays on a 4 ps time scale and vanishes within 14 ps (Fig. 2.4a). Test measurements on the linear precursor molecule linAMPB, as well as on a compound containing only one amino acid attached to the photoswitch (data not shown), revealed an almost identical red shift at early times (Fig. 2.4a). In view of this universal response we attribute this red shift to a heating, or non-thermal vibrational excitation, of low-frequency modes that are anharmonically coupled to the amide I vibrations. A similar response has been observed for pure azobenzene and has been analyzed in detail in Ref. [167].

A somewhat slower process leads to the transient blue shift observed after 20 ps (Fig. 2.2). We used a global exponential fit to separate this process from the heat signal and obtained a time constant of 6 ps for the formation of the blue shifted signature. The intensity and peak positions in the difference spectrum reached after 20 ps is almost equivalent to that observed in the 1 ms time difference spectrum. Since the blue shift of the amide I band can be directly related to the change of backbone structure (see above), we conclude that stretching of the peptide conformation is, in a coarse sense, completed after *only* 20 ps.

The linear reference molecule linAMPB shows a response comparable to that of cycAMPB up to about 20 ps (Fig. 2.3 and Fig. 2.4ab). In particular the bleach signal at 1644 cm^{-1} around 20 ps (Fig. 2.4b) indicates a significant change of the linear molecules backbone structure, even though the backbone is not closed to a loop. Apparently, friction fixes the open end of the linear peptide on a short time scale and thus allows the flipping photoswitch to indeed perturb the conformation of the peptide backbone. In contrast to cycAMPB, however, this bleach decays within $\approx$ 100 ps (Fig. 2.4b). As expected, and as confirmed by the steady state FTIR difference spectra, the conformation of the azo-switch has no significant long-lasting influence on the backbone structure of the linear molecule. Apparently, conformational diffusion of the backbone quickly reestablishes its initial structure.

Interestingly, the early 1.6 ps spectrum of the linear peptide linAMPB is stronger modulated than the corresponding cycAMPB spectrum. It shows the bleach and heating of 2 bands at 1650 cm^{-1} and 1690 cm^{-1} (Fig. 2.3), which we tentatively assign to the peptide units directly attached to the azobenzene unit, since these are expected to receive most of the dissipated energy during isomerization. In contrast, a broad response throughout the whole amide I band is observed in the cyclic peptide, indicating that essentially all units of the cyclic peptide are perturbed instantaneously by pulling apart both ends of the peptide chain.

Slow Phase, $>$20 ps (*biased diffusion* phase): While stretching of the peptide backbone is essentially finished after 20 ps in cycAMPB, it is clear from the further evolution of the transient spectra that the system is not yet in equilibrium (Fig. 2.2 and Fig. 2.4c-e). Most prominent is the formation of a shoulder at the blue side of the product band (1695 cm^{-1}) after 16 ns, the onset of which is visible already after 1.7 ns. As this shoulder develops into a well separated band in the 1 ms spectrum, we conclude that equilibration of the system is not completed after 16 ns. On the 1 ms time scale, however, the transient and FTIR difference spectra are identical, indicating that the system is now entirely relaxed.

An additional measure of internal motion of the peptide backbone is obtained from the time evolution of the polarization dependence of the transient signals. The negative part of the signal at 20 ps is only weakly polarization dependent, in agreement with the broad distribution of the orientations of the C=O groups in the various *cis* structures with respect to the electronic transition dipole of the azobenzene unit (Fig 2.5). In contrast, the anisotropy $\alpha = (\Delta A_{\parallel} - \Delta A_{\perp})/(\Delta A_{\parallel} + 2\Delta A_{\perp})$ of the product band at 1670 cm^{-1} is initially close to 0 but decreases until 200 ps to $\alpha \approx -0.2$ (Fig. 2.4d). As the anisotropy measures the angle ϕ between pumped and probed transition through $\alpha = 1/5(3\cos\phi - 1)$, the negative anisotropy is consistent with the perpendicular orientation of most amide I transition dipoles to the electronic transition dipole of the azobenzene unit, in agreement with the NMR structure for the *trans* conformation (Fig. 2.5) [125]. In other words, the alignment of the peptide units still changes between 20 ps and 200 ps. However, it should be noted that the strong overlap of *cis* and product *trans* band might overstate the anisotropies. On a longer time scale, rotational diffusion of the entire molecule blurs the effect of internal motion and diminishes the anisotropy after about 200 ps. The time scale of that anisotropy decay matches the rotational correlation time of 1.5 ns obtained from NMR relaxation experiments [125].

The dynamics of the equilibration process is governed by a complex hierarchy of time scales. This becomes directly evident from the transient at the quasi-isosbestic point at 1661 cm^{-1} (Fig. 2.4c), which is very sensitive to minor shifts of sub-states of the amide I band induced by the underlying conformational dynamics. These frequency shifts might originate directly from rearrangements of the individual C=O groups and/or from the opening and closing of intramolecular hydrogen bonds as a result of such rearrangements (intermolecular hydrogen bonds to the solvent should play a minor role in DMSO). At least five phases can be distinguished during the first 1.7 ns of equilibration. To illustrate the complexity of the response, we attempted a global exponential fit of the cycAMPB data at all probe frequencies and for delay times up to 1.7 ns (the time range for which we were able to measure transients, see Material and Methods). A reasonable fit is obtained when including 5 time constants of 2.2 ps, 6.2 ps, 17 ps, 430 ps and 1 ns for the magic angle signal, while somewhat different values are obtained when fitting the data with either parallel or perpendicular polarization of pump and probe pulse. A singular value decomposition of the same data sets, on the other hand, suggests the presence of at least six linearly independent dynamical contributions between 0 ns and 1.7 ns. The further evolution of the signal between 1.7 ns and 16 ns, which is not included in this analysis, requires even more kinetic components for a complete temporal description of the conformational dynamics.

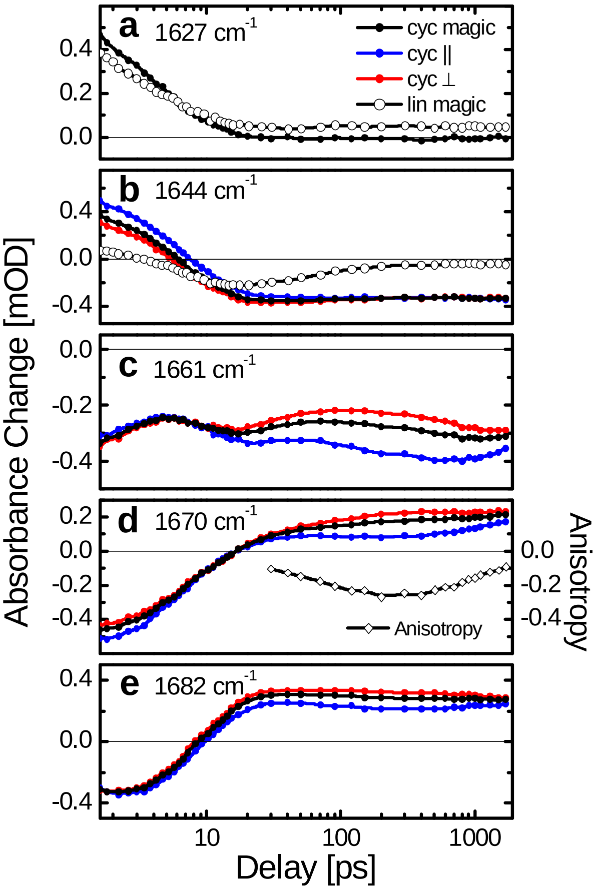

Figure 2.4: Polarization dependent (parallel, perpendicular and magic angle) transient absorbance change of the cyclic (cyc) and linear (lin) AMPB-peptide at selected probe frequencies. An example of the anisotropy is shown for 1670 cm^{-1}.

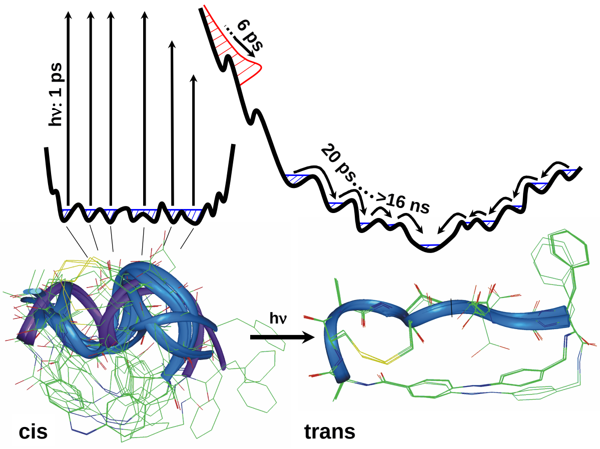

Figure 2.5: Ensemble of structures with the azobenzene unit in the *cis* (bottom, left) and *trans*-conformation (bottom, right), as obtained from a NMR structure analysis [125]. After photo-isomerizing the built-in azobenzene unit, the random distribution of *cis* structures is projected onto a new potential energy surface. During the *driven* phase (in red) the ensemble relaxes very quickly on a 6 ps time scale and entirely floods the bottom area of the potential energy surface. During the subsequent *biased diffusion* phase, the system equilibrates on a discrete hierarchy of time scales, extending from 20 ps to $>$ 16 ns, toward the much better defined global minimum of the *trans* conformation.

We cannot rule out that part of the complexity of the response is due to the 50% of molecules which do not undergo *cis*→*trans* isomerization but relax back to the original *cis*-conformation after electronic excitation of the azo-compound (i.e. the 50% quantum efficiency of the *cis*→*trans* isomerization). However, we expect that the $<$ 1 ps lifetime of the electronically excited state of the azoswitch is too short to significantly deform the *cis* structures so that the excess energy is not converted into directional motion but into heat, that is dissipated within 10 ps.

The dynamics might also be influenced by the use of the relatively slow solvent DMSO. Indeed, experiments have shown that the solvation response of DMSO contains a small (10%) component with a 10 ps time constant [168], significantly slower than water. However, solvation dynamics is still fast enough to not perturb the dynamics of the equilibration process (>20 ps), but it might slow down slightly the driven phase.

2.1.5 Discussion

Combining all experimental observations, the course of the conformational transition can be sketched as shown in Fig. 2.5. The reaction starts from the *cis* state of cyc-AMPB which is a frustrated system with many close lying conformational energy minima. The *cis*→ *trans* isomerization transfers the peptide to a modified potential surface by changing the conformational restraint. The area where the molecular ensemble is launched on the modified surface is determined by the region of the conformational space occupied by the equilibrium ensemble before the arrival of the switch pulse. Starting from the broad distribution of *cis* structures, the conformational distribution on the modified surface directly after switching are expected to be similarly inhomogeneous with many possible downhill pathways. Furthermore, a good fraction of huge excess energy pumped into the photo-switch (420 nm $\hat{=}$290 kJ/mol!) is certainly expected to remain in the molecule as heat and/or strain within the early phase. Hence, the potential energy surface in the vicinity of the well defined global minimum of the *trans* conformation might be entirely flooded even when the downhill pathways were homogeneous. In any case, we expect to find a broad distribution of structures after the initial driven phase. In other words, the peptide is forced into an almost stretched configuration at the end of the driven phase but the backbone is not yet in the most favorable conformation and the dihedral angles have yet to adjust to the elongated structure. The initial phase may be imagined as an essentially barrierless process on the steep part of the energy surface, driven by a large amount of excess energy. This is by far the fastest large scale peptide backbone motion ever observed directly, which exceeds previous results [43, 44, 45, 46, 47, 48, 49, 30, 50, 51, 64] by 2-3 orders of magnitudes. The subsequent much slower phase at the bottom of the funnel is diffusion controlled. The potential energy landscape is still biased in this region due to the rest of strain not yet released, but solvent driven conformational fluctuations will now be necessary in order to escape from traps on the way to the final state.

It is instructive to compare the present results with related experiments by Hochstrasser and coworkers [104], who have investigated a cyclic peptide closed by a disulfide bridge. After breaking the disulfide bridge using a short UV pulse, the liberated molecules either underwent geminate recombination or diffused apart to allow the peptides to change conformation. However, no significant shift of the amide I band, which would be indicative for a conformational change of the backbone, has been detected during the first 2 ns. In our case, a notable fraction of the energy pumped into the azobenzene unit is converted into a directional force, driving the peptide backbone far away from the new equilibrium conformation within an extremely short time. The subsequent relaxation of the non-equilibrium ensemble hence includes very fast processes.

One would expect a two state kinetics if the peptides reach the *trans* state directly by a smooth and steep funnel. In contrast, the observed conformational transition is surprisingly complex. This becomes particularly clear at the quasi-isosbestic point at 1661 cm^{-1} (Fig. 2.4c) which emphasizes that relaxation and equilibration of the backbone occurs on multiple time scales. However, it is important to note that we observe discrete processes with alternating signs of the change of the absorption signal near the quasi-isosbestic point, so that the signal oscillates on the logarithmic time scale (used in Fig. 2.4c). Logarithmic oscillations have been suggested by Jortner and coworker to be indicative for a *discrete hierarchy* of relaxation processes on a *rugged energy landscape* [95]. The more traditional picture of protein dynamics starts from the assumption of a continuum of time scales, leading to a non-exponential but monotonic decay, which commonly is modelled by stretched exponentials or power-laws [169, 104, 170, 119, 78]. The latter response is frequently observed in much larger systems, in particular at low temperatures, and emphasizes the glass-like behavior of proteins [43, 44, 45, 46, 47, 48, 49]. In view of the small size of the peptide studied here, its complex response seems surprising. However, we apply a sharp trigger on a small system and directly probe the backbone dynamics with high time resolution. The amide I band, consisting of in total 9 spectroscopic states, can sense very directly even minor rearrangements of the C=O groups. Hence, we are able to monitor details of the backbone dynamics that are obscured in larger systems due to averaging over too many spectroscopic states, or when using a more indirect, i.e. electronic probe.

Protein folding is an inherently very difficult problem. Microscopic all atom MD simulation, albeit being a powerful tool, encounters great difficulties to reach the time scales of protein folding with present computer power [30]. Therefore, simplifying models have been proposed, which try to describe protein folding with kinetic models employing a more macroscopic description of the molecule [46, 47, 48]. Depending on whether one is interested in secondary or tertiary structure, macroscopic states could be, for example, either native or non-native conformations of each peptide unit [46, 47, 171] or contacts between whole α-helical strands which themselves are treated as building blocks [172]. The number of degrees of freedom needed to describe the state of the system is thereby reduced dramatically. It is hoped that dynamics of the system can be understood without having to consider a microscopic level. However, these approaches intrinsically assume a separation of time scales of the fast internal motion within each macroscopic state and the much slower kinetic transitions between them. The peptide studied here is too small to form any distinct secondary structure. Nevertheless, the dynamics of this small fragment shows a series of processes overlapping in time, which extend well into the $\gg$10 ns range; much longer than individual steps in the formation of, for example, an α-helix, which have been proposed to occur within less than 1 ns [47, 49, 48, 50, 71]. In other words, equilibration of a small peptide fragment can be considerably slower than kinetic transitions in simplified, macroscopic protein folding models [172, 171, 46, 47, 48]. In view of this result it seems questionable whether a separation of time scales is possible, that would allow the discussion of protein dynamics on certain length scales without having to consider a microscopic atomic level [78].

2.1.6 Conclusion

We have studied the backbone response of a small cyclic peptide after *cis*→*trans* isomerisation of a built-in photoswitch applying ultrafast vibrational spectroscopy. The experiments show that important conformational changes of peptide fragments can be extremely fast (i.e. a few picoseconds) when a sufficiently strong force is driving it. The subsequent relaxation of the peptide ensemble far away from equilibrium is governed by a *discrete hierarchy* of time scales, extending from about 20 ps to $\gg$16 ns. This indicates that the potential energy surface, on which the *trans* ensemble equilibrates, is rugged and contains *hierarchical* energy barriers [95]. The system studied here is small enough to allow resolving many of the entangled processes involved in its conformational transition directly by ultrafast vibrational spectroscopy all the way from the start to the very end. Furthermore, the system is still within the scope of thorough all atom MD simulation [162], which can be connected directly to the experiment and at the same time have the capability to reveal a microscopic picture of the underlying processes. Nevertheless, albeit possessing only a few conformational degrees of freedom compared to a protein, the peptide behaves highly non-trivially and provides new insights into the complexity of protein dynamics on short time scales and small length scales.

The work was partially supported by the Swiss Science Foundation and the Deutsche Forschungsgemeinschaft (SFB 533 A8 and B8).

2.2 P13 – α-Helix Formation in a Photo-Switchable Peptide Tracked from Picoseconds to Microseconds by Time Resolved IR Spectroscopy.

Jens Bredenbeck, Jan Helbing, Janet R. Kumita, G. Andrew Woolley, and Peter Hamm,
Proc. Natl. Acad. Sci., 102:2379–2384, 2005

2.2.1 Abstract

Photo-triggered α-helix formation of a 16 residue peptide featuring a built-in conformational photoswitch is monitored by time resolved IR spectroscopy. A new experimental approach with 2 ps time resolution and a scanning range up to 30 μs is used to cover all timescales of the peptide dynamics. Experiments are carried out at different temperatures between 281 K and 322 K. We observe single exponential kinetics of the amide I′ band at 322 K on a timescale comparable to a recent T-jump folding experiment. When lowering the temperature, the kinetics become slower and nonexponential. The transition is strongly activated. Spectrally dispersed IR measurements provide multiple spectroscopic probes simultaneously in one experiment by resolving the amide I′ band, isotope labelled amino acid residues and side chains. We find differing relaxation dynamics at different spectral positions.

Conformational dynamics of peptides and proteins range from sub-picosecond fluctuations of backbone dihedral angles [74] to collective motions of large regions of the molecule, extending to milliseconds and longer [8]. Attempts to model dynamics of peptides and proteins often adopt a hierarchical view. This implies a separation of timescales generating classes of events that can be treated separately. The lower, faster hierarchical levels are typically handled in a collective statistical fashion leading to a transition state theory like picture [78]. This is justified if the coupling of the processes, occurring on different time and length scales, allows the selection of a reaction coordinate with a well defined barrier for a simplified description [78, 102]. However, the overlap of timescales often questions the applicability of hierarchical models and leads to controversies, such as about the interplay between hydrophobic collapse, secondary structure formation and tertiary structure formation in protein folding [37, 36]. In the present paper we report on stretched kinetics, overlapping dynamics of different spectroscopic probes and oscillations of the transient absorption during α-helix formation. These results indicate that even such simple phenomena as the formation of a single stretch of secondary structure are governed by multiple processes and a separation of their timescales is not given.

Except in a few cases [48, 66, 104], the kinetics of helix folding has been inferred indirectly from thermal unfolding experiments [44, 76, 47, 67, 68, 49, 56, 42] which requires a number of assumptions. If one aims to enter a regime where these approximations are likely to break down, it is clearly preferable to start from a largely unfolded ensemble and observe the relaxation into a helical state. Helix formation has been achieved previously by T-jumping a cold denatured peptide [48]. Also photo excitation of a ruthenium complex attached to a peptide chain has been used as a trigger [66]. While the complex is electronically excited, its large dipole moment promotes helix formation. A drawback of this approach is the perturbation of the peptide dynamics by electronic relaxation. Vibrational stark effects make the interpretation of spectral shifts difficult. A nonreversible approach for triggering is photocleavage of a disulfide cross-linking group that prevents helix formation in its bridged form [104]. However, most of the sulfide biradicals recombine before secondary structure formation can take place.

Our present approach features three main ingredients to provide a detailed picture of folding dynamics.

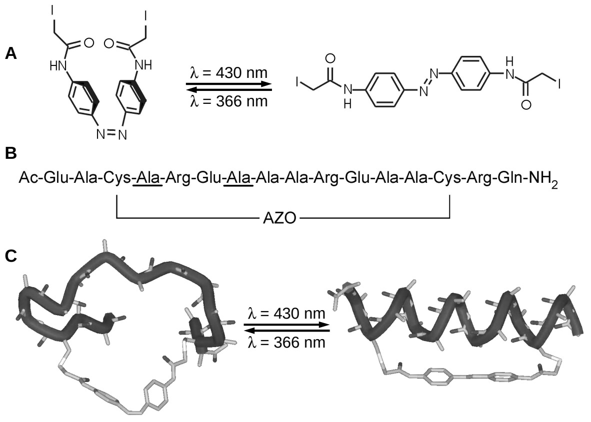

Figure 2.6: A — Cross-linker in *cis* (left) and *trans* (right) conformation. B — FK11X sequence, showing the positions of the ^{13}C labels (underlined residues) and the attached cross-linker. C — Schematic models of *cis* FK11X (left) and *trans* FK11X (right), illustrating the conformational transition induced by the photoswitchable linker. Hydrogens and side chains are omitted for clarity.

- To trigger folding, we use an azobenzene-based *ultrafast reversible photoswitch* that is covalently linked to the peptide and can be switched back and forth using light of different wavelengths [128, 105, 173, 174, 162, 175] (Fig. 2.6).

- To cover the whole range of dynamics, we employ a setup based on *two synchronized femtosecond laser systems* [176]. In the present version, the delay can be continuously scanned up to 30 μs with a time resolution of 2 ps.

- The importance of using multiple spectroscopic probes to discriminate different relaxation mechanisms has been stressed previously [102, 81]. *Spectrally dispersed multi channel detection* of broadband femtosecond IR pulses provides multiple spectroscopic probes in a single experiment: The amide I$'$ band reports on the dynamics of the whole backbone. Isotope labelling reveals the dynamics at specific backbone sites [67]. In the present work, we also resolve the dynamics of amino acid side chains. If folding was a simple two-state process, all observables must follow the same dynamics, yielding the same single exponential rate constant. We will see that this is not the case here.

We designed FK11X for strong helix propensity, starting from the general sequence Ac-(EAAAK)$_3$-A-NH$_2$ [177, 178], which is stabilized by interactions between the Glu and Lys side chains of opposite charge. In FK11X, Lys has been replaced by Arg to further increase helicity [179] and a Gln residue is used for C-terminal capping [180]. Capping has been observed not only to stabilize the helix but also to speed up folding [41]. Two alanines at positions 3 and 14 have been replaced by Cys to allow for the attachment of the photoswitchable linker. Switching the linker between *cis* and *trans* modifies the energy landscape of the peptide and allows for larger changes in helicity than typically achieved in T-jump experiments. Three helical turns are required to form an α-helix out of the 12 residues bridged by the linker. These three turns do not fit well into the distance spanned by the linker in the *cis* form, thus helicity is greatly reduced when the linker is in this conformation (CD yields 34% helicity at 5°C as described below). Only upon stretching the linker by switching it to *trans* can the α-helix fold properly (93% helicity at 5°C). Ultrafast *cis*→*trans* isomerization of the linker therefore projects the unfolded ensemble onto an energy landscape which favors the folded state and folding can be observed as the dominant kinetic contribution. For isotope labelling we chose two residues with a $i, i+3$ spacing, as vibrational coupling between their amide I$'$ modes should change considerably upon transition from extended to helical structure [181].

The complementary process of *trans*→*cis* isomerization has been investigated recently by Chen *et al.* using time resolved optical rotary dispersion with a time resolution of 16 ns [40]. Chen *et al.* determined a time constant of 55 ns for the relaxation that is dominated by unfolding. Note, that though in Ref. [40] the same molecule has been investigated, the results cannot be compared directly as *trans*→*cis* isomerization is followed by equilibration on the *cis* energy landscape, while we investigate dynamics on the *trans* landscape.

2.2.2 Material and Methods

Peptide Synthesis. The 16-residue peptide Ac-EAC$\underline{\text{A}}$R-E$\underline{\text{A}}$AAREAACRQ-NH$_2$ (underlined residues are ^{13}C labelled in FK11X(iso)) was prepared using standard FMOC-based solid phase peptide synthesis methods [105]. The two cysteine residues were cross-linked with the photo-isomerizable linker (Fig. 2.6a) [128, 105] to obtain the isotope labelled and unlabelled photoswitchable peptides FK11X(iso) and FK11X (Fig. 2.6b).

Time Resolved IR Spectroscopy. Most time resolved measurements were performed on FK11X(iso). 700 μg FK11X(iso) were dissolved in 260 μl deuterated phosphate buffer (10 mM, pD 7.0). The sample was circulated through a closed cycle CaF$_2$ flow cell (pathlength 50 μm) [182]. The closed cycle was thermostated to ±1°C.

The dark adapted FK11X(iso) is in the *trans*-azo conformation ($c_{cis} < 1\%$ [105]) which favors helical conformation of the peptide (Fig. 2.6). To monitor folding, the initial *cis* (unfolded) state was prepared by continuous UV irradiation of the *trans* $\pi \rightarrow \pi^*$ band of the linker with an Ar-Ion Laser (Coherent ”Innova 100”, 363 nm, 200 mW). The transition from *cis* (unfolded) to *trans* (helical) was initiated by a short (700 fs) 425 nm laser pulse.

The evolution of the peptide after photoswitching the linker was monitored by time resolved IR spectroscopy. To investigate the whole range of the dynamics with 2 ps time resolution up to 30 μs, a setup of two synchronized 1 kHz Ti:sapphire-oscillator/regenerative amplifier femtosecond laser systems was used [176]. System 1 was frequency doubled to generate pulses at 425 nm for switching the linker. System 2 pumped an OPA with a difference frequency mixing stage to obtain IR probe pulses (100 fs, center frequency 1620 cm^{-1}, bandwidth 240 cm^{-1} FWHM) [165]. The delay of the pulses was controlled electronically. The IR beam was split into a probe and a reference beam which were focused into the sample with a spot size of 80 μm. The probe beam was centered in the 425 nm pump spot (140 μm), the reference beam passed the flow cell 1 mm upstream. Probe and reference beams were frequency dispersed in a spectrometer and imaged onto a 2×32 pixel HgCdTe detector array.

Circular dichroism measurements. Circular dichroism measurements were performed on a Jasco Model J-710 spectropolarimeter. Helix content was calculated using $[\theta]_{222}$ of FK11X dissolved in 50 % TFE at 5 °C as 100 % helical [178].

2.2.3 Experimental results and assignments

Steady-state IR spectroscopy. The IR absorption spectrum of *trans*-FK11X shows a broad amide I$'$ band centered at 1638 cm^{-1} (Fig. 2.7, upper panel) as commonly observed for small α-helical peptides in D$_2$O [155, 183].

Between 1520 cm^{-1} and 1620 cm^{-1} we find several bands that exist both in FK11X(iso) and FK11X. They belong to the side chains of Glu (1563 cm^{-1}, antisymmetric carboxylate [184]) and Arg (1583 cm^{-1} and 1600 cm^{-1}, symmetric and antisymmetric $CN_3H_5^+$ [184]). A ring mode of azobenzene causes a tiny absorption at 1601 cm^{-1}, which can be better seen in the transient spectra at picosecond delays (see below). The band of the two isotope labels is not clearly resolved as it is obscured by the absorption of the six side chains. It leads to an increased absorption around 1590 cm^{-1} in FK11X(iso), which is the position expected for a doubly labelled helix, with the labelled amino acids separated by two unlabelled residues [155].

Steady-state FTIR difference spectra were obtained by subtracting the *cis* (unfolded) from the *trans* (helical) spectrum (Fig. 2.7, lowest plot). We observe a red shift of the amide I′ band with a decreased absorbance at 1665 cm^{-1} (‘random coil’ frequency [68, 44, 183]) and an increase at 1633 cm^{-1} (Pos. 9) (solvent exposed α-helix in D_2O [68, 183]). At 1590 cm^{-1} (Pos. 10) we find that FK11X(iso) differs from FK11X as expected for an isotope labelled α-helix [155]. Side chain absorption at 1560 cm^{-1} is also slightly changed by helix formation.

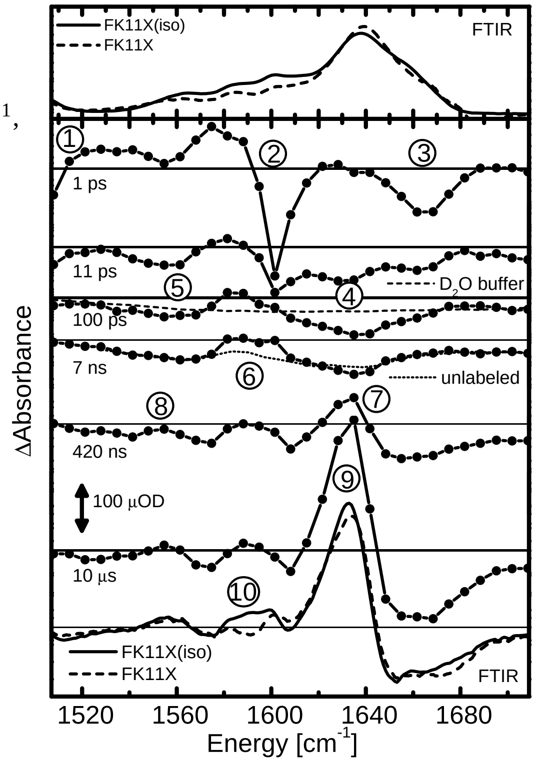

Figure 2.7: upper panel—FTIR absorption spectra of *trans* FK11X(iso) and FK11X. lower panel—Transient difference spectra of FK11X(iso) at different delays, magic angle polarization. Steady state FTIR difference spectra of FK11X(iso) and FK11X. All measurements at 20 °C. See text for discussion of numbered peaks.

Overview of the transient spectral features. The time resolved measurements discussed here were carried out for FK11X(iso). At early times (1 ps) the signal is dominated by the response of the linker (Fig. 2.7), that is heated by absorption of the UV photon and subsequent ultrafast electronic relaxation of the azobenzene moiety [167, 173, 175]. The local heating leads to a red shift and broadening of the vibrational bands of the linker [167]. By comparison with other molecules [173], we can assign the signals at 1 ps to N=N stretching of azobenzene (Fig. 2.7, Pos. 1), a ring-mode of azobenzene (Pos. 2) and the C=O stretching of the amide groups of the linker that are conjugated with the azobenzene moiety (Pos. 3)(see Fig. 2.6 for the linker structure). The heat signal decays within a few ps as the local excess energy is rapidly dissipated [173].

Accordingly the heat signature is greatly reduced in the 11 ps spectrum. Already on this very short timescale we observe a bleach at the position of the amide I′ band (Pos. 4), as well as at the position of the Glu side chains (Pos. 5), indicating a perturbation of the peptide backbone by the stretching of the photoswitch.

The amide I′ bleach is growing and shifting slightly until about 100 ps, reflecting small changes in the backbone at this early time. The heat is fully dissipated into the buffer after about 20 ps, inducing a temperature rise of about 10 mK. This causes a small background signal of the deuterated phosphate buffer (dashed line at 100 ps delay, measured by exciting the 1550 cm^{-1} band of D_2O and scaled accordingly), 2 to 3 orders of magnitude smaller than in typical T-jump measurements. This background stays constant for longer delays. It is essentially flat, thus the structure in the signal clearly originates from peptide dynamics.

Between 100 ps and 7 ns, only minor changes of the signal are observed at the position of the isotope labels (Pos. 6). Comparison of FK11X(iso), unlabelled FK11X (dotted line) and the buffer background shows that the difference signal around 1590 cm^{-1} (Pos. 6) in FK11X(iso) is due to the isotope labelled residues. The details of the dynamics in this spectral range are shown in Fig. 2.9a-c and will be discussed below.

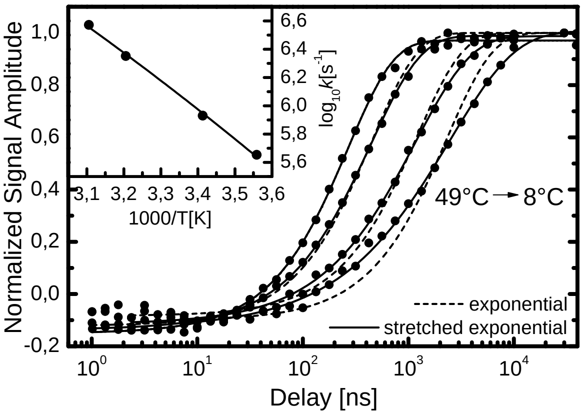

Figure 2.8: Time dependent amplitude of the amide I′ difference signal at different temperatures and exponential and stretched exponential fits. Inset: dots — Arrhenius plot of the rates (taken from exponential fits). solid line — fit using Eq. 2.2 assuming a non-Arrhenius (quadratic in $1/T$) behavior. Within the small temperature intervall we cannot distinguish an Arrhenius (linear in $1/T$) from a quadratic dependence on $1/T$.

The spectrum after 420 ns shows the signature of helix formation. The red shift of the amide I′ band is now clearly visible (Pos. 7) and also the rising absorption at the Glu side chain position (Pos. 8). Folding is largely finished after about 10 μs at 20°C (2 μs at 49°C, see Fig. 2.8) and the transient spectrum then closely resembles the steady state difference spectrum.

Amide I′ dynamics and their temperature dependence. The main signal reporting on helix formation is the amide I′ difference signal. Fig. 2.8 shows the dynamics of the unlabelled amide I′ band at different temperatures. The amplitude (ΔA(1635 cm^{-1}) - ΔA(1662 cm^{-1})) is plotted and its maximum is normalized to one for better comparison. Exponential ($e^{-t/\tau}$) as well as stretched exponential ($e^{-(t/\tau)^{\beta}}$ [95]) fits are shown. Lowering the temperature from 49°C to 8°C slows down equilibration by an order of magnitude. Moreover, with lower temperature the kinetics become more and more stretched. This is measured by the exponent β varying from $\beta = 1.00$ at 49°C to $\beta = 0.69$ at 8°C (see Table 2.1). We cannot completely rule out a small contribution to the signal from the reverse *trans*→*cis* process. However, we estimate it to be 5 % at most, which is too small to explain the observed values of β.

Dynamics at selected spectral positions. During the first nanoseconds we observe spectral changes mainly at the position of the labelled residues (Pos. 6 in Fig. 2.7). This is highlighted in Fig. 2.9a and b showing selected transient spectra and in Fig. 2.9c showing the dynamics at selected spectral positions. After the first 20 ps that are dominated by heat dissipation and deflection of the backbone by the linker, the absorption at the position of the isotope labels around 1590 cm^{-1} first rises until about 0.5 ns (see Fig. 2.9c, isotope labelled transient). It subsequently decreases from 0.5 ns to 18 ns, while there is no comparable change in the amide I′ band of the unlabelled residues at 1638 cm^{-1} (Fig. 2.9a). Fig. 2.9b and Fig. 2.9c show how the decrease at the labelled position continues up to 100 ns. However, after 18 ns, the signal of the unlabelled amide I′ band now grows in, leading to a rising absorption at 1638 cm^{-1}. At the isotope position, the absorption begins to rise towards its final value only after 100 ns. The oscillating transient absorption at the position of the isotope labels and its shift against the unlabelled amide I′ band clearly show that different processes overlap in time during relaxation.

T [°C]	Helicity [%]	τ [μs] $e^{-t/\tau}$	τ [μs] $e^{-(t/\tau)^{\beta}}$	β
8	93	2.2	2.4	0.69
20	86	1.2	1.2	0.82
39	71	0.44	0.44	0.91
49	64	0.27	0.27	1.00

Table 2.1: Helicities in the *trans* state and parameters for the fits in fig. 2.8.

The side chain signal (Fig. 2.7, Pos. 8) around 1555 cm^{-1} shows a similar time dependence as the amide I′ band at 1638 cm^{-1} (Pos. 4): at short times we observe a bleach (Pos. 5) and at longer times we observe a positive signal (Pos. 8) rising together with the amide I′ band (Pos. 7) as is shown in greater detail in Fig. 2.9b. The transients in Fig. 2.9c indicate that the side chain dynamics may be slightly faster than the rise of the amide I′ band. Fits with stretched exponentials yield time constants of 810 ns versus 1150 ns, respectively.

2.2.4 Discussion

To understand the action of the photoswitch on the peptide backbone, it is instructive to compare the results on FK11X with our previous work on a cyclic octapeptide, where we observed dynamics to be faster by several orders of magnitude [173]. The small, strained, cyclic peptide features a photo-isomerizable azobenzene-based

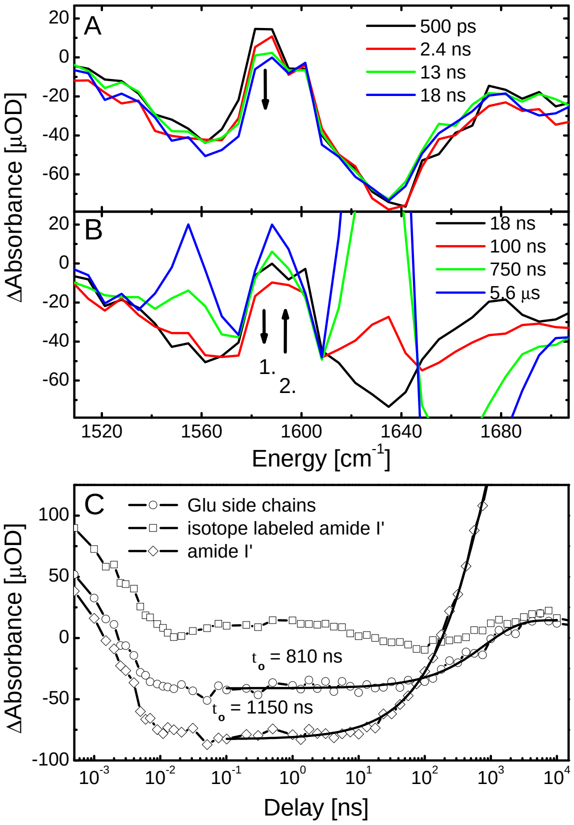

Figure 2.9: Dynamics of selected spectral positions in the early nanosecond range at 20 °C. A—Decreasing absorption at the isotope position. B—Decrease at the isotope position continues until 100 ns by which time build up at the amide I′ and Glu position already has begun. Only after 100 ns also the absorption at the isotope position rises. (C) Dynamics at selected spectral positions. The solid lines are fits with stretched exponentials.

ω-amino acid as a rigidly linked part of its backbone. Thus, stretching of this switch exerts strong forces on the rest of the backbone. Already after 20 ps, we observed a transient signal closely resembling the steady state difference spectrum showing that the major part of the conformational transition takes place on this ultrafast time scale. This is in strong contrast to FK11X, where the time scale of linker-isomerization in the range of a picosecond [185] is very much separated from the major changes of amide I′ absorption that report on α-helix formation. Therefore we conclude that the bias imposed by the photoswitch in FK11X is soft and changes the energy landscape globally without introducing strong gradients driving the system towards the final state. Molecular mechanics calculations show that the linker in the *cis* state prefers distances between the cysteine sulfur atoms of 6.2 Å to 14.6 Å while in the *trans* state, the favored distances are between 17.0 Å and 18.6 Å[130], better matching the distance expected for an α-helical conformation. This change between *cis* and *trans* is small compared to the length of the peptide chain bridged by the linker, which would measure ≈ 40 Å in extended conformation. Switching the linker thus leads to a comparably slight deflection of the backbone which is reflected by the small bleach in the amide I′ band occurring on the timescale of tens of picoseconds (see Fig 2.7). Furthermore, the four flexible single bonds on each side of the linker provide a soft coupling between the backbone and the more rigid conjugated part of the azobenzene moiety. Unlike in the cyclic octapeptide, the linker does not force the molecule into a certain secondary structure. A more adequate picture of the switching in FK11X is that stretching the linker opens up a new part of conformational space for the backbone. The system is transferred from the *cis* to the *trans* energy landscape where it folds in a diffusion controlled way on timescales that are comparable to those obtained by a recent T-jump α-helix folding experiment [48].

A striking observation in FK11X is the stretching of amide I′ kinetics at lower temperatures (Fig. 2.8). The high time resolution reveals these kinetics without being affected by the instrument response. It is well known from chemical kinetics that if the system has to surmount a single high barrier (large compared to k_bT), the kinetics is single exponential. In this case, the system is effectively a two-state system. The observed non-exponentiality implies that a single pronounced barrier does not exist and that the free energy surface is relatively flat (since, in addition, the equilibrium constants do not deviate much from one). A large body of theoretical work and simulations predict that the folding kinetics of polypeptides should become non-exponential at lower temperature [19, 23, 186, 187, 102, 188]. So far, despite a systematic search for this effect [75], experimental support for this kind of temperature dependence is sparse [189], and it has only been observed for a synthetic (phenylacetylene) helical oligomer [92]. Sabelko *et al.* investigated refolding of two cold denatured proteins with kinetics that in contrast became *more* exponential as the temperature was lowered [119]. However, one has to keep in mind that in the cold denaturation regime the stability of the native state as well as the surface roughness is reduced with lower temperature [119]. If the reason for non-exponentiality is the stability of the folded relative to the unfolded state, our observations do in fact comply with those of Sabelko *et al.*. With increasing stability of the folded state, any rate limiting dominant barrier might be flattened out and folding becomes a downhill process with kinetics governed by surface roughness [57]. This conclusion has been confirmed by simple lattice dynamics models [187, 186] which revealed stretching factors $\beta < 1$ with decreasing temperature. The kinetic effect of helix stabilization was investigated by Wang *et al.* [41]. For 19-mer peptides (length comparable to FK11X) the use of stabilizing capping residues resulted in acceleration and stretching of the kinetics. For proteins, it has been shown that reducing the folding barrier by mutagenesis may result in non-exponential kinetics as well [190].

We find helix folding to be a strongly thermally activated process (Fig. 2.8, inset) in agreement with the T-jump experiment by Werner *et al.* [48]. This finding is corroborated by more indirect conclusions from unfolding experiments [47, 68, 191, 41]. Previously, the strong temperature dependence has often been interpreted in terms of a two state model, where unfolded and folded state are separated by a large enthalpic barrier. Fitting the temperature dependence of the rates by an Arrhenius law,

$$k(T) = k_0 e^{-\frac{\Delta H^{\ddagger}}{k_B T}}, \tag{2.1}$$

would yield an apparent activation enthalpy of $\Delta H^{\ddagger} = 9.3$ kcal/mol and a large pre-exponential factor of $k_0 = 6.9 \times 10^{12}\ \mathrm{s}^{-1}$. However, a single rate-limiting barrier much larger than $k_B T$ would lead to strictly single exponential kinetics. This is inconsistent with the observation of stretched exponentials (unless the large activation enthalpy is compensated by a large activation entropy resulting in a relatively flat free energy barrier). Instead of relating the observed thermal activation to a single dominant barrier, it can also be attributed to multiple local barriers between misfolded microstates, or, in other words, to an activated diffusion process on a rugged energy landscape. It has been shown that for a random distribution of barrier heights the diffusion constant depends more strongly on temperature [82, 83],

$$D(T) = D_0 e^{-\frac{\langle \Delta H^2 \rangle}{(k_B T)^2}}. \tag{2.2}$$

Within the small temperature range of Fig. 2.8, fits based on Eq. 2.1 and Eq. 2.2 both work equally well, thus we cannot distinguish Arrhenius (linear in $1/T$) from non-Arrhenius (quadratic in $1/T$) behavior. Yet, Eq. 2.2 yields a much more realistic number for the average barrier heights (roughness) ($\Delta H^{=}$1.7 kcal/mol), which agrees well with what is expected for hydrogen bond breaking [192]. The pre-exponential factor is $3 \times 10^{9}\ \mathrm{s}^{-1}$ in this case.

Indeed, there is increasing evidence from both experimental work and simulations that the so-called unfolded state of proteins and even of small peptides is by no means random, as assumed in statistical models of helix-coil relaxation [35, 193, 194, 195, 196, 197, 198, 199, 72]. Only in recent years has it become possible to simulate peptide dynamics in atomic detail using force fields that allow for a realistic description of native and nonnative interactions [196, 197]. Simulations show that the unfolded state of peptides comprises vastly less conformations than one would expect based on the number of conformational degrees of freedom present, and that those states are stabilized by more or less specific nonnative contacts [196, 197, 198, 199, 72, 200]. Significant enthalpic barriers in the folding process arise from the breaking of nonnative contacts, such as nonlocal hydrogen-bonds of the backbone and of the side chains as well as interactions between hydrophobic side chains [72, 199, 201, 202], rendering the energy landscape rugged. Chowdhury *et al.* [202] found rapid nucleation of the helix within a nanosecond in their simulations of a hexadecapeptide in agreement with the simulations of Hummer *et al.* [72]. However, instead of subsequent rapid helix propagation driven by the formation of backbone hydrogen bonds, as envisioned in the statistical ‘kinetic zipper model’ of helix coil relaxation [76], they found that folding is hampered by nonnative contacts, whose breaking determines the rate of helix formation. They concluded that helix nucleation does not trigger quick formation of the entire helix. Similar results are obtained by Bertsch *et al.* [201], who observe the frequent inhibition of helix propagation by nonnative hydrogen-bonds.

Fig. 2.10 shows the sketch of a rugged energy landscape model inspired by the work of Bicout and Szabo [84]. It can qualitatively account for all our experimental observations (i.e. the temperature dependence of the overall rate, equilibrium constant and stretching factor). It contains a distinguished folded state, a largely flat, but rugged conformational space of unfolded states, and a relatively small barrier separating both regions. The barrier is entropic, reflecting the narrowing conformational space in the vicinity of the folded state [84]. If the overall rate k_{eq} connecting unfolded states was much faster than the rate k_{fold} towards the folded state, the folding

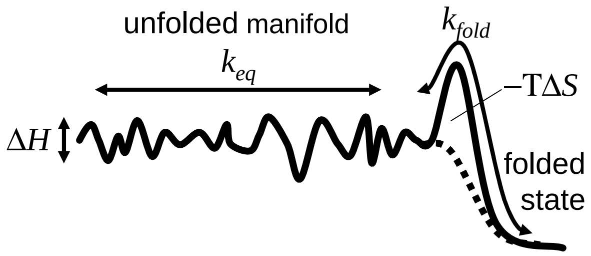

Figure 2.10: A simple model explaining the experimental observations. The solid line is a free energy surface, while the dotted line represents the enthalpic contribution only. The roughness of the unfolded manifolded is characterized by ΔH.

kinetics would be exponential, since all unfolded states would be in equilibrium among each other at any time. In this case, one could view them as one unified ensemble of unfolded states, and a two-state picture would be appropriate. However, if both rates are of the same order of magnitude (or if $k_{fold} > k_{eq}$), non-exponential folding kinetics is expected. In this case, we indeed find $\beta \approx 0.7$ in simple kinetic simulations. Hence, the diffusion on the rugged energy surface becomes rate limiting, and might even dominate the barrier connecting to the folded state. In order to obtain a situation where the non-exponentiality increases with lowering temperature, k_{eq} should decrease quicker with temperature than k_{fold}. Diffusion on a rugged energy surface supports a large variation of k_{eq} with temperature (Eq. 2.2) while an entropic barrier will render k_{fold} temperature independent. An additional negative activation enthalpy for this barrier may further assist the large variation of the stretching factor β within a relatively small temperature range as observed in this work.

The model shown in Fig. 2.10, while certainly not unique, explains all the experimental observations in a physically reasonable manner [84]. Several alternative models we tested in simulations, including initiation-propagation models, produce stretching factors $\beta > 1$ (contrary to what we observe) when starting as far away from equilibrium as in the present case. A discussion of this finding would go beyond the scope of the present paper and will be published elsewhere.

The time resolved amide I′ spectra of FK11X(iso) provide no hints for the existence of distinct intermediates resulting from traps or wells on the rugged landscape. However, the amide I′ absorption measures the peptide conformation averaged over all residues and therefore is relatively insensitive to the underlying heterogeneity. The isotope labels in FK11X(iso) avoid this averaging and allow measurement of dynamics at a specific backbone site. The high time resolution reveals oscillations of the isotope signal on a logarithmic timescale (Fig. 2.9c). Such logarithmic oscillations have been found to be indicative for relaxation processes on a rugged energy landscape [95] and clearly discard a simple two-state folding model. It is very likely, that other residues would show a similar behavior if labelled and that the smooth but non-exponential kinetics of the unlabelled amide I′ band is just the average of local processes of similar complexity. However, extended labelling studies are needed to obtain a more detailed picture.

Uncertainty exists in the literature as to the origins of the so-called instantaneous component, a fast component beyond the time resolution ($\geqslant$ 10 ns) of previous approaches, that has been observed in most T-jump experiments on helical systems [44, 67, 68, 49, 56, 42, 41]. It often has the same or even larger amplitude than the slower component attributed to the actual α-helix folding/unfolding dynamics. Two origins have been discussed: an instantaneous spectral shift due to changes in solvation due to the T-jump [44, 49, 191, 42], or a very fast conformational change [67, 49, 191]. We observe a rapid bleach of the amide I′ band during the first 20 ps that changes until about 100 ps and then stays constant to the early nanosecond range. With the buffer background subtracted, its amplitude is only 15 % of the final amplitude of the difference signal, much less than the instantaneous component typically observed in T-jump experiments. In our case, the T-jump and its influence on the peptide spectrum is negligible and we attribute this rapid bleach to a deflection of the backbone by the linker, as described above. Arguing along the lines of the kinetic zipper model it has been presumed that the instantaneous component is due to the fast redistribution of helix lengths (’zipping’). However, in our spectrally resolved measurements the phase up to 10 ns does not show any spectral signature of the helical state. In the light of the present observations it seems likely that the instantaneous component in T-jump experiments is, to a large extent, caused by a change in solvation.

2.2.5 Conclusion

The fast isomerization of the azobenzene photoswitch on the timescale of a picosecond is decoupled from the backbone dynamics during folding. Our folding rates compare well to those obtained from T-jump experiments confirming that triggering with a built-in photoswitch can be designed for essentially unperturbed folding dynamics. The high time resolution of the experiment enables discussion of deviations from exponential behavior without ambiguities introduced by overlap with the instrument response. We observed increasingly stretched kinetics of α-helix formation with lower temperature. Spectrally dispersed multi channel detection revealed kinetic heterogeneity of amide I′ band, isotope labelled amide I′ oscillators and amino acid side chains, which clearly shows the presence of different processes overlapping in time. While the amide I′ band only provides averaged information on the backbone secondary structure, circumventing this averaging by isotope labelling in combination with the high time resolution reveals logarithmic oscillations of the transient absorption. This highlights the complexity of the transition on a local level. In agreement with previous studies we find folding of a small α-helix to be considerably thermally activated. However, this does not necessarily require the existence of a pronounced rate limiting barrier. Large thermal activation can also arise from an activated diffusion process on a rugged energy landscape, which is more consistent with our observations of nonexponentiality, kinetic heterogeneity and strong temperature dependence of β.

The present results call for further investigation of the cause of nonexponentiality in α-helix formation. A key role of nonnative contacts in secondary structure formation as suggested by recent all-atom MD simulations would question simple statistical kinetic models, as folding then strongly depends on nonlocal interactions within the peptide sequence. The present experimental approach is well suited to further address these questions: more detailed isotope labelling studies can access events at different backbone sites and side chains. The possibility of tailoring the action of the photoswitch should be further explored to drive the system to certain locations on the modified energy landscape: An α-helical peptide where the photoswitch bridges only four residues has already been reported [105]. In this peptide switching to *cis* preforms one helical turn. If helix nucleation was a rate limiting event in folding, switching would mean a jump right onto this free energy barrier, which should lead to a speed up of the folding kinetics.

Acknowledgement. We thank Martin Volk for valuable discussions. The work has been supported by the Swiss National Science Foundation (2100-067573/1).

2.3 P16 – Stretched *versus* compressed exponential kinetics in α-helix folding

Peter Hamm, Jan Helbing and Jens Bredenbeck
Chem. Phys., in press.

2.3.1 Abstract

In a recent paper (Bredenbeck *et al.*, *Proc. Natl. Acad. Sci USA*, 102:2379–2384, 2005), we have investigated the folding of a photo-switchable α-helix with a kinetics that could be fit by a stretched exponential function $\exp(-(t/\tau)^{\beta})$. The stretching factor β became smaller as the temperature was lowered, a result which has been interpreted in terms of activated diffusion on a rugged energy surface. In the present paper, we discuss under which conditions diffusion problems occur with stretched exponential kinetics ($\beta < 1$) and under which compressed exponential kinetics is obtained ($\beta > 1$). We show that diffusion problems do have a strong tendency to yield stretched exponential kinetics, yet, that there are conditions under which compressed exponential kinetics would be expected instead. We discuss the kinetics on free energy surfaces predicted by simple initiation-propagation models (zipper models) of α-helix folding, as well as by folding funnel models. We show that our recent experiment has been performed under condition for which models with strong downhill driving force, such as the zipper model, would predict compressed, rather than stretched exponential kinetics, in disagreement with the experimental observation. We therefore propose that the free energy surface along a reaction coordinate that governs the folding kinetics must be relatively flat and has a shape similar to a 1D golf course. We discuss how this conclusion can be unified with the thermodynamically well established zipper model by introducing an additional kinetic reaction coordinate.

2.3.2 Introduction

The current concepts of protein folding focus on the shape of the free energy surface on which the protein is evolving [23, 203, 204, 24, 84, 32]. With the help of kinetic experiments a wealth of information may be obtained about details of the free energy surface, such as its roughness and the existence of potential folding barriers. Nevertheless, despite of extensive experimental and theoretical work, a generally accepted view on the folding of even the smallest peptides, that form secondary structures (α-helices, β-hairpins), has not yet been found.

Most time resolved experimental studies of α-helix folding so far used the technique of temperature jumps [44, 76, 47, 67, 68, 49, 42, 58]. In such an experiment, an ensemble of peptides is suddenly heated by some 10°C with the help of a short laser pulse that vibrationally excites the solvent water. As a result, the peptides suddenly are in a non-equilibrium situation and partially unfold. While important insight about α-helix folding have been gained from temperature jump experiments, they suffer from two limitations: (i) Except of a few examples [205, 119], these experiments try to infer the folding kinetics indirectly from an unfolding experiment, since the temperature can only be risen, not lowered on the required fast timescale, and (ii) the perturbation from equilibrium that can be initiated with the help of a temperature jump is relatively small (change in helicity typically 10% to maximal 20% [58]). If α-helix folding were a two-state problem, these points would be no limitation. However, there is increasing experimental and theoretical evidence that α-helix folding is not a two-state problem.

We have recently investigated folding of a small α-helix applying a new experimental concept that circumvents the problems listed above [206]. A photo-isomerizable compound (azobenzene) connects the two cysteine side chains of the polypeptide Ac-EACAREAA-AREAACRQ-NH_2 which has a high helix propensity. The position of the cysteine's was designed such that three helical turns fit in between the azo-linker, when the latter is in the *trans* configuration (see Fig. 2.11a). In the *cis* configuration, on the other hand, the end-to-end distance of the azo-linker is too small for these three helical turns, thus helicity is greatly reduced. According to CD measurements, the helicity changes form 34% helicity at 5°C in the *cis* configuration to 93% helicity in the *trans* configuration. This jump in helicity is larger than that typically achieved in a temperature jump experiment. The azo-compound can be switched in both directions by the choice of the laser excitation wavelength. In Ref. [206] we have investigated α-helix folding by initiating the *cis-trans* transition. The photo-isomerisation of the azo-compound itself occurs on an ultrafast subpicosecond timescale [122, 162], so that our approach poses no limitation to the time resolution of the experiment (another novelty of the experiment in Ref. [206] for α-helix folding).

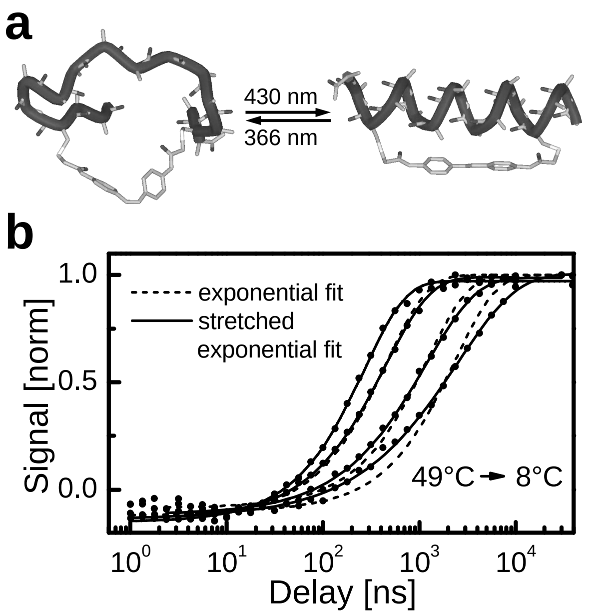

Figure 2.11: (a) The photo-switchable α-helix. (b) Rise of the amide I′ band as a result of α-helix folding after photo-isomerisation of the built in azo-compound at 430 nm. The folding kinetics is fit to an exponential ($e^{-t/\tau}$, dotted lines) as well as a stretched exponential ($e^{-(t/\tau)^\beta}$, solid lines) function. Adapted from Ref. [206]

Fig. 2.11b summarizes the most important results of Ref. [206]: α-Helix folding is an activated process, as seen from the strong temperature dependence of the main amide I′ signal, which reflects helix folding. More important in the context of the present paper, however, is the observation that helix folding becomes more and more non-exponential as the temperature is lowered. Fig. 2.11b shows fits to the folding kinetics using exponential ($e^{-t/\tau}$, dotted lines) as well as stretched exponential ($e^{-(t/\tau)^\beta}$, solid lines) functions. A stretched exponential is a commonly used phenomenological fitting function to account for the derivation from exponential relaxation behavior. In our experiment, the stretching factor β varied from 0.69 at 8°C to 1.0 at 49°C

Stretched exponential kinetics has been observed in numerous studies of protein folding before: in α-helix unfolding [49, 41], in unfolding of a synthetic (phenylacetylene) helical oligomer [92], in unfolding of proteins with reduced folding barrier (by mutagenesis) [190], in folding of cold denatured proteins [119], in the disulphide recombination of a photo-cleavable cyclized peptide [104, 170], as well as in folding of equine lysozyme in a stop-flow experiment [207]. It is well known from chemical kinetics that if the system has to surmount a high barrier (large compared to k_bT), the kinetics is single exponential. This would be the situation of a two-state folder with a dominant folding barrier. Non-exponential relaxation, on the other hand, strongly implies that such a folding barrier does not exist and that the overall free energy surface is relatively flat. Note that the inversion of this argument is not valid, and exponential kinetics does not necessarily imply a dominant folding barrier [81].

In the present paper, we investigate what can be learned from the experiment about the shape of the free energy surface on which folding of the α-helix in Ref. [206] proceeds. First we not that performing an experiment in a folding or in an unfolding direction might yield different kinetics [24], and that it is not possible to determine the folding kinetics from an unfolding experiment (except when it is a two-state system with single exponential relaxation kinetics). All observations so far, including ours, yielded stretching factors $\beta \leqslant 1$. We show in the present paper, that diffusion problems have a strong tendency to reveal $\beta \leqslant 1$. However, for certain commonly discussed protein folding models there are experimental conditions under which compressed kinetics with $\beta \geqslant 1$ are expected. In contrast to most previous investigations, our experiment has been performed under such conditions (in the folding direction, strong perturbation from equilibrium), which is why the observation of a stretching factor $\beta < 1$ allows us to draw relatively strong conclusions on the shape of the free energy surface.

2.3.3 Theoretical Background

Rate Equation System

In the following section we briefly review the mathematical treatment of the relaxation of a system of discrete microstates that are connected trough certain relaxation channels. The discussion is complimentary to a recent paper of Bicout and Szabo [84] who have obtained similar results in a continuous representation of the free energy surface.

The dynamics of a system of discrete microstates is described by a rate equation

$$\dot{\rho} = K \times \rho \tag{2.3}$$

were the relaxation matrix K_{ij} contains the rate constants for the transition from microstate j to microstate i (with $i \neq j$). To ensure particle conservation (no sinks or sources), we have for the diagonal elements $K_{ii} = -\sum_{j \neq i} K_{ji}$. Detailed balance furthermore requires

$$\frac{K_{ij}}{K_{ji}} = e^{\frac{G_i - G_j}{k_B T}}. \tag{2.4}$$

If the connectivity of states is one-dimensional, K adopts a tridiagonal form:

$$K = \begin{pmatrix} -k_1^{(f)} & +k_1^{(b)} & & 0 \\ +k_1^{(f)} & -k_2^{(f)} - k_1^{(b)} & +k_2^{(b)} & \\ & +k_2^{(f)} & -k_3^{(f)} - k_2^{(r)} & \ddots \\ 0 & & \ddots & \ddots \end{pmatrix}, \tag{2.5}$$

with a forward $k_i^{(f)}$ and a backward $k_i^{(b)}$ rate between adjacent microstates.

Eq. 2.3 and 2.5 describe a system of discrete microstates. However, they also can be viewed as a discretised version of a continuous Smoluchowski equation:

$$\frac{\partial \rho}{\partial t} = D \left[\frac{\partial}{\partial x} \left(\frac{\partial G}{\partial x} \rho \right) + \frac{\partial^2}{\partial x^2} \rho \right] \tag{2.6}$$

which can be seen easily by discretizing the x-derivatives. The diffusion constant D in Eq. 2.6 is connected to Eq. 2.5 through

$$\begin{aligned} k_i^{(f)} &= k^{(0)} e^{-\frac{G_{i+1} - G_i}{2k_B T}} \approx k^{(0)} \left(1 - \frac{G_{i+1} - G_i}{2k_B T} \right) && (2.7) \\ k_i^{(b)} &= k^{(0)} e^{+\frac{G_{i+1} - G_i}{2k_B T}} \approx k^{(0)} \left(1 + \frac{G_{i+1} - G_i}{2k_B T} \right) && (2.8) \end{aligned}$$

with $k^{(0)} = D/\Delta x^2$. For clarity, the diffusion constant D is assumed independent on position x in Eq. 2.6. A x-dependent diffusion constant could readily be introduced. We concentrate here on the discretized version of the Smoluchowski equation, since it is convenient for numerical calculations. Eq. 2.3 can be viewed as an expansion of the Smoluchowski equation Eq. 2.6 in a basis of site-localized states (similar to a discrete variable representation (DVR) basis in quantum mechanics) where each microstate i corresponds to a position along a continuous reaction coordinate x.

Eq. 2.3 is solved by:

$$\rho(t) = e^{Kt}\rho^{(0)} = Qe^{\Lambda t}Q^{-1}\rho^{(0)} \tag{2.9}$$

where $\Lambda = \mathrm{diag}(\lambda_0, \lambda_1, ..., \lambda_{\mathrm{n}-1})$ is a diagonal matrix containing the eigenvalues of K and Q a transformation matrix containing the corresponding eigenvectors. Particle conservation is responsible for one eigenvalue being $\lambda_0 = 0$; the corresponding eigenvector is the thermal equilibrium distribution

$$\rho_i^{(eq)} = Q_{i0} \propto e^{-\frac{G_i}{k_B T}}. \tag{2.10}$$

All other eigenvalues λ_i are negative, and we sort them according to their value (slowest rate λ_1 first, fastest rate λ_{n-1} latest).

The matrix K is not symmetric, which is why the eigenvectors Q are not necessarily orthogonal. However, one can symmetrize the problem by introducing

$$H_{ij} = K_{ij}\sqrt{\frac{K_{ji}}{K_{ij}}} = K_{ij}e^{-\frac{G_i - G_j}{2k_B T}}. \tag{2.11}$$

When $\sum_j K_{ij} q_j = \lambda q_i$ solves the eigenvalue equation of K, then $\sum_j H_{ij} e^{G_j/2k_B T} q_j = \lambda e^{G_i/2k_B T} q_i$ solves the eigenvalue problem of H. Hence, the eigenvalues of H are the same as those of K, and the eigenvectors of H are

$$Q^{(s)} = \mathrm{diag}(\mathrm{e}^{\frac{\mathrm{G_i}}{2\mathrm{k_b T}}})\mathrm{Q} \tag{2.12}$$

It is convenient to symmetrize the problem, since the eigenvectors of H are orthonormal.

Observable

Before we proceed, we need to examine how a particular experiments maps the diffusive motion onto a measurement observable. To that end, we introduce a function $f(x)$ that relates the measurement signal to the reaction coordinate x. The function $f(x)$ will depend on the particular experiment performed. For example, when measuring a CD signal of an α-helix, it is reasonable to assume that the observable is proportional to the helicity of the particular state:

$$f_i = i/(n-2) \tag{2.13}$$

where the reaction coordinate i in this case is the number of helical turns, and n is the number of residues of the polypeptide with a maximum of $n-2$ hydrogen bonds. The same assumption is made when measuring the amide I′ signal in the IR spectrum, which is a sensitive probe of the amount of helical structure [44, 67, 68, 49, 42, 41, 206]. A different observable is the Förster transfer (quenching) rate between a fluorescence donor and an acceptor group [205, 76, 47, 208]. In this case, one would view the donor-acceptor distance R as the reaction coordinate mapped by the experiment and one would get

$$f(R) = \frac{1}{1 + (R/R_0)^6}. \tag{2.14}$$

As a third example, very local contacts leading to triplet-triplet transfer between certain groups have been used as molecular labels [64]. In this case we obtain for the observable:

$$f = \begin{cases} 1 & \text{if contact} \\ 0 & \text{otherwise} \end{cases} \tag{2.15}$$

The observable $f(x)$ will turn out to be crucial in the following discussion. The result of a kinetic measurement critically depends on the choice of the observable $f(x)$.

Equilibrium Fluctuations

In equilibrium, the distribution function $\rho(t) = \rho^{(eq)}$ is time-stationary by definition. Yet, a selected single molecule (or sub-ensemble) still may undergo dynamics, which is characterized by the equilibrium fluctuation autocorrelation function:

$$C(t) = \frac{\langle \delta f(t) \delta f(0) \rangle}{\langle \delta f(0)^2 \rangle}, \tag{2.16}$$

The fluctuation autocorrelation function describes the correlation between the signal of a single selected molecule at time 0 and that at some later time t. In a continuous representation, the correlation function is defined as [209]

$$\langle f(t) f(0) \rangle \propto \int\int f(x) G(t, x|x_0) f(x_0) \rho^{(eq)}(x_0) dx dx_0, \tag{2.17}$$

where $G(t, x|x_0)$ is the conditional (joint) probability of being at x at time t given the system was at x_0 initially. In matrix representation, this translates to

$$\langle f(t) f(0) \rangle \propto \sum_{i,j} f_j G_{ji}(t) f_i e^{-\frac{G_i}{k_B T}}. \tag{2.18}$$

with

$$G_{ji} = \sum_k Q_{jk} e^{\lambda_k t} Q_{ki}^{-1}. \tag{2.19}$$

the matrix elements of the time propagation operator. Using the orthonormality of $Q^{(s)}$ one can easily show that

$$c(t) \propto \sum_{k=1} \left(\sum_i f_i Q_{ik} \right)^2 e^{\lambda_k t}. \tag{2.20}$$

Bicout and Szabo have recently obtained a similar result [84], except that Eq. 2.20 is valid for a more general form of the observable f_i. The prefactors to the individual kinetic components $e^{\lambda_k t}$ are *all positive*. The autocorrelation function initially decays with the fastest rate λ_{n-1}, and eventually with the slowest rate λ_1. Mathematically speaking, the autocorrelation function $c(t)$ is, of course, *not* a stretched-exponential function. However, if we write a stretched exponential function with $\beta < 1$ as a multi-exponential decay:

$$e^{-(\lambda t)^\beta} = \int_0^\infty g(\lambda')e^{-\lambda' t} d\lambda' \tag{2.21}$$

we obtain a continuous distribution of rates $g(\lambda) > 0$ that is positive for all λ [210]. Therefore, if we attempt to approximate (fit) the autocorrelation function $c(t)$ by a stretched exponential function, the fact that the prefactors to the individual kinetic components in Eq. 2.20 are all positive is responsible for the obtained stretching factor necessarily being $\beta \leqslant 1$. This conclusion $\beta \leqslant 1$ is independent on the particular choice of the observable f_i, although the exact form of the correlation function does, of course, depend on the observable f_i. The conclusion $\beta \leqslant 1$ is also independent on the shape of the free energy surface and is not restricted to the one-dimensional connectivity of Eq. 2.5. In an equilibrium experiment, *non-exponential* kinetics necessarily implies *stretched-exponential* kinetics (in the sense discussed above).

Non-Equilibrium Relaxation

In a non-equilibrium experiment, we start from a non-equilibrium initial distribution $\rho^{(0)} \neq \rho^{(eq)}$, and propagate it in time (in analogy to a wavepacket in quantum mechanics). The observable in such a non-equilibrium experiment will be:

$$m(t) \propto \sum_{i,j} f_j G_{ji}(t) \rho_i^{(0)}. \tag{2.22}$$

When expanding the initial condition $\rho^{(0)}$ in terms of the eigenvectors of the rate matrix K:

$$\rho_i^{(0)} = \sum_k c_k Q_{ik} \tag{2.23}$$

we obtain

$$m(t) \propto \sum_{jk} f_j Q_{jk} c_k e^{\lambda_k t}. \tag{2.24}$$

In general, there is no reason to assume that $m(t)$ has any similarity with $c(t)$, except that the 'rate spectra' of both are the same. However, determining the rate spectrum of an experimentally measured $m(t)$ would involve an inverse Laplace transformation which, although mathematically unique, is an ill-conditioned problem in the presence of noise. In principle, we are free to choose the initial condition as we wish, and hence, there is no condition for the expansion coefficients c_k. In particular, there is no condition that would ensure that all the prefactors to the various kinetic components are positive (c_k can be chosen positive or negative), as they were in the case of the equilibrium correlation function. Hence, in contrast to an equilibrium experiment, non-exponential kinetics *no longer* implies stretched exponential kinetics; in fact we will see in Sec. 2.3.4 that one often obtains *compressed exponentials* with $\beta \geqslant 1$ instead.

The detailed outcome $m(t)$ of a non-equilibrium experiment depends on three factors:

- The free energy surface of the system $G(x)$, which enters Eq. 2.24 trough the eigenvalues λ_k and eigenvectors and Q_{ij} of the rate matrix K.
- The observable f.
- The initial condition $\rho^{(0)}$, which enters Eq. 2.24 trough the expansion coefficients c_k.

Two different experiments may be compared only when all this three parameters are similar. The same free energy surface may lead to different kinetics, dependent on the initial condition and the observable.

A comparison of Eq. 2.18 with Eq. 2.22 shows that a non-equilibrium observation $m(t)$ will equal an equilibrium correlation function $c(t)$ whenever

$$\Delta\rho_i^{(0)} \propto f_i e^{-\frac{G_i}{k_b T}}. \tag{2.25}$$

where $\Delta\rho_i^{(0)}$ is the difference of the initial condition from the equilibrium distribution $\rho^{(eq)}$. We can think of two situations which fulfill this condition: (i) A small perturbation regime and (ii) applying a localized probe. Both will be discussed in the following.

Small Perturbation Regime Onsager's regression hypothesis would state that relaxation of a (small enough) non-equilibrium disturbance is governed by the same laws as the regression of spontaneous microscopic fluctuations in an equilibrium ensemble [211]. However, this conclusion is based on the linear response assumption with a restoring force that is proportional to the excursion. In other words, Onsager's regression hypothesis assumes a harmonic free energy surface. The free energy surfaces we encounter in protein dynamics typically deviate strongly from harmonic already in regions that are populated in equilibrium at k_BT. If the free energy surface of proteins were harmonic, proteins would be non-reactive and 'dead'. Hence, assuming a small perturbation $\Delta\rho^{(0)}$ solely is not sufficient to ensure $m(t) \propto c(t)$. The expansion Eq. 2.24 is linear, and a perturbation $a \cdot \Delta\rho^{(0)}$ will lead to the same time-dependence of the relaxation process independent on the value of a. Nevertheless, there are realistic scenarios for which a smallness parameter can be introduced that leads to $m(t) \propto c(t)$ in certain limits.

For example, lets assume that the non-equilibrium initial condition has been prepared by a small linear bias

$$\rho_i^{(0)} \propto e^{-\frac{G_i+\Delta G_i^{(ne)}}{k_bT}}, \tag{2.26}$$

with $\Delta G_i^{(ne)} \propto i$. If the perturbation $\Delta G_i^{(ne)}$ is small compared to k_BT, we obtain for the deviation of the initial condition from the equilibrium distribution:

$$\Delta\rho_i^{(0)} \approx \frac{\Delta G_i^{(ne)}}{k_BT} e^{-\frac{G_i}{k_bT}}. \tag{2.27}$$

When we furthermore assume that the observable f_i varies linearly with i ,as it would in the case of CD spectroscopy and IR spectroscopy of the amide I$'$ band of an α-helix (Eq. 2.13), we indeed find that an equilibrium and a non-equilibrium experiment would reveal identical results $m(t) \propto c(t)$. As in equilibrium, non-exponential dynamics would imply stretched-exponential dynamics in this case (see Sec. 2.3.4).

Along the same lines, we can discuss a temperature-jump experiment, where a non-equilibrium ensemble is generated by a sudden change of the temperature $\Delta T^{(ne)}$:

$$\rho_i^{(0)} \propto e^{-\frac{G_i}{k_b(T+\Delta T^{(ne)})}} \tag{2.28}$$

when $|\Delta T^{(ne)}/T| \ll 1$ we obtain

$$\Delta\rho_i^{(0)} \approx \frac{H_i}{k_bT} e^{-\frac{G_i}{k_bT}} \frac{\Delta T^{(ne)}}{T}. \tag{2.29}$$

If we have an approximately linear enthalpic slope H_i along the reaction coordinate i, as we do have in a helix zipper model, we again find $m(t) \propto c(t)$, given that also the observable varies linearly with the reaction coordinate.

Localized Probe If the observable is sensitive to one particular microstate, e.g. the folded state:

$$f = \begin{pmatrix} 1 \\ 0 \\ \vdots \end{pmatrix} \tag{2.30}$$

and when we choose as starting condition the same state:

$$\Delta\rho^{(0)} = \begin{pmatrix} 1 \\ 0 \\ \vdots \end{pmatrix} \tag{2.31}$$

we trivially fulfill condition Eq. 2.25, and hence get $m(t) \propto c(t)$. In contrast to the 'small perturbation' cases discussed above, this conclusion is true even when being far away from equilibrium (it doesn't involve any smallness parameter for the perturbation). However, it requires a very sharp observable and a very special initial condition. Important is that the system is leaving the state to which the observable is sensitive to. It is the situation of an unfolding experiment.

2.3.4 Protein Folding Models

Initiation-Propagation Models

Kinetic Zipper Model in the Single Sequence Approximation In the following, we apply the mathematical concepts discussed above to simple protein folding models. The most commonly used model for the folding of an α-helix is the zipper model [90, 87], which assumes that the rate limiting step in helix folding is the formation of a first helical turn (nucleation). Three amino acids in a row need to be in a specific conformation for the first helix loop to be formed, which is why helix nucleation is entropically costly. Subsequently, individual hydrogen bonds are closed ('zipping'), which is a downhill process since the enthalpic gain of each new hydrogen bond overcompensates the additional smaller entropic cost of only one amino acid. In the initial works [90, 87], only the thermodynamics of the zipper model has been discussed with the help of a partition function, but the idea has later been extended to also describe the

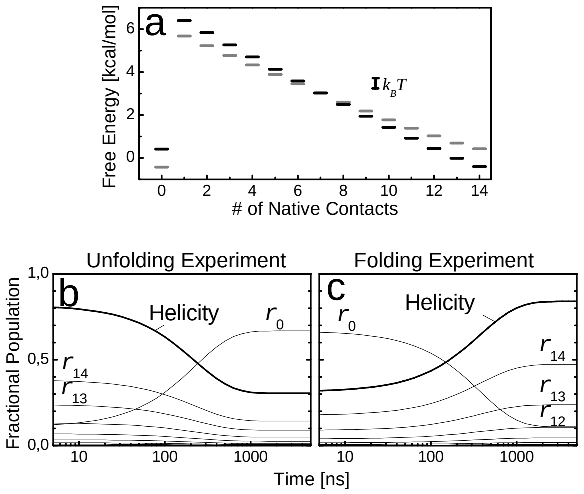

Figure 2.12: Free energy surface (a) and kinetic simulation (b,c) of the zipper model in the single sequence approximation at 8°C. Fig.(a) shows the free energy of the individual states in the unfolded (gray states) and folded (black states) conformation as calculated from Eq. 2.32. The action of the photo-switch was modelled by assuming a sudden change of the hydrogen bond enthalpy ΔH_{Hbond} from -0.49 kcal/mol (average helicity 30%, gray states) to -0.61 kcal/mol (average helicity 84%, black states) in the folding experiment or *vice versa* in the unfolding experiment. The nucleation entropy was set to $\sigma = 5 \cdot 10^{-7}$ from the fit of the melting curve. Fig.(b) shows the kinetic result of an unfolding experiment, and (c) that of a folding experiment. The population of the individual states (thin lines) is plotted together with the average helicity Eq. 2.33 (thick line).

kinetics on the in this way introduced free energy surface ('*kinetic zipper model*') [76]. The partition function reads in the single sequence approximation:

$$q = 1 + \sum_{i=1}^{n-2} \Omega_i \sigma s^i \qquad (2.32)$$

where i runs over the number of native hydrogen bond contacts, n is the number of amino acids, $\sigma = \exp(-\Delta S_{loop}/k_B)$ is an equilibrium constant describing the entropic cost of helix nucleation, $s = \exp(-\Delta H_{Hbond}/k_BT)$ an equilibrium constant describing the enthalpy gain of one step of helix propagation, and $\Omega_i = (n-i-1)$ an entropy factor describing the number of ways of putting a connected sequence of i closed hydrogen bonds units in in a chain of n residues (in the single sequence approximation). Helix nucleation is governed by entropic effects, rendering σ temperature-independent. In contrast, s reflects the hydrogen bond enthalpy and varies with temperature. The measurement signal is assumed to be proportional to the average helicity (see Eq. 2.13):

$$\langle f(t) \rangle = \frac{1}{n-2} \sum_{i=0}^{n-2} i\rho_i(t) \qquad (2.33)$$

In the experiment of Ref. [206] the molecule first is in equilibrium with the azo-switch in the *cis* configuration. An ultrashort UV pulse then isomerizes the azo-compound on a sub-picosecond timescale into its *trans* configuration, projecting the peptide onto a new free energy surface. We assume that the distribution of peptide conformations right after photo-switching is the same as the equilibrium distribution before photo-switching. We mimic this process in our model calculations (Figs. 2.12-2.17) by defining two free energy surfaces, one for the non-folding *cis* configuration (e.g. Fig. 2.12a, gray lines) and one for the folding *trans* configuration (black lines). The non-equilibrium ensemble is propagated on the free energy surface after photo-switching with an initial distribution $\rho^{(0)}$ that is the equilibrium distribution on the free energy surface before photo-switching. Furthermore, it is assumed that the action of the azo-switch works against helix formation, effectively reducing the average hydrogen bond enthalpy ΔH_{Hbond} .

Helix folding is a corporative effect as a result of the counterbalance between enthaplic gain and entropic cost of the folded state. The steepness of the melting curve fully determines the two parameters σ and s of the model. The helicity of the peptide with the azo-switch in the *trans* configuration changes by 30% between 8°C and 49°C [206, 105]. We can reproduce this behavior by setting $\sigma = 5 \cdot 10^{-7}$ and $\Delta H_{Hbond} = -0.61$ kcal/mol for the *trans* configuration. The helicity furthermore changes by 50-60% when switching the azo-compound from *cis* to *trans*, a jump that can be reproduced by setting $\Delta H_{Hbond} = -0.49$ kcal/mol in the *cis* configuration. With these parameters, the nucleation barrier $\Delta G^{\ddagger} = 6$ kcal/mol is very large (Fig. 2.12a), leading to strictly single-exponential folding kinetics in both directions (Fig. 2.12b and c). In the single sequence approximation of the zipper model, the α-helix would in fact be a two-state folder, in contrast to the experimental observation.

General Kinetic Zipper Model The single sequence approximation is a severe simplification which assumes that nucleation occurs only once in a peptide sequence.

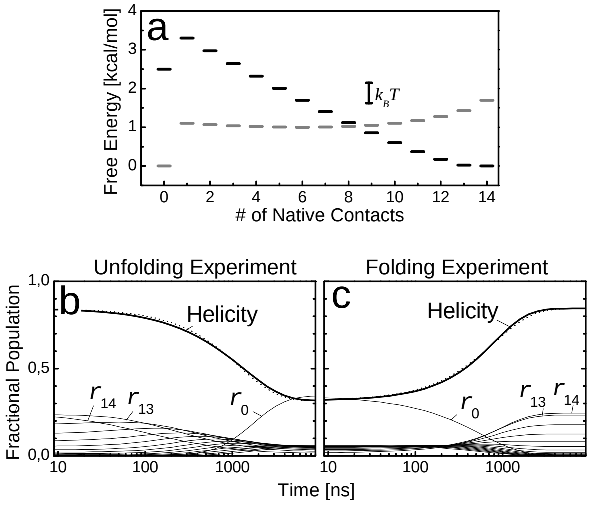

Figure 2.13: Free energy surface (a) and kinetic simulation (b,c) of the zipper model at 8°C, without single sequence approximation. Fig.(a) shows the free energy of the individual states in the unfolded (gray states) and folded (black states) conformation as calculated from Eq. 2.34. The action of the photo-switch was modelled by assuming a sudden change of the hydrogen bond enthalpy ΔH_{Hbond} from -1.4 kcal/mol (average helicity 32%, gray states) to -1.7 kcal/mol (average helicity 84%, black states) in the folding experiment or *vice versa* in the unfolding experiment. The single-bond entropy was set to $\sigma = 0.1$ from the fit of the melting curve. Fig.(b) shows the kinetic result of an unfolding experiment, and (c) that of a folding experiment. The population of the individual states (thin lines) is plotted together with the average helicity Eq. 2.33 (thick line). The dotted line shows the best exponential fit to the the average helicity.

When giving up this restriction, much flatter free energy surfaces are obtained that would indeed lead to non-exponential kinetics. The partition function in this more general form reads [88]:

$$q = 1 + \sum_{i=1}^{2^n} \sigma^{h(i)} s^{l(i)} \qquad (2.34)$$

Here, it is assumed that each amino acid may adopt two conformations: a helical-like conformation (*h*) or a non-helical (coil) conformation (*c*). The sum in Eq. 2.34 runs over all 2^n conformations of a sequence of *n* amino acids. The entropy factor $h(i)$ counts the helical-like amino acids of a particular conformation, while $l(i)$ counts helix loops that enable a closed hydrogen bond. A hydrogen bond is possible only when three helical-like elements occur in a row (..*hhh*..). For example, a sequence ..*chchhhhc*.. gives $h(i) = 5$ and $l(i) = 2$. Zimm and Bragg have worked out a complicated combinatorial expression for Eq. 2.34 [88]. Here, we chose to evaluate the 2^n conformations explicitly in the computer.

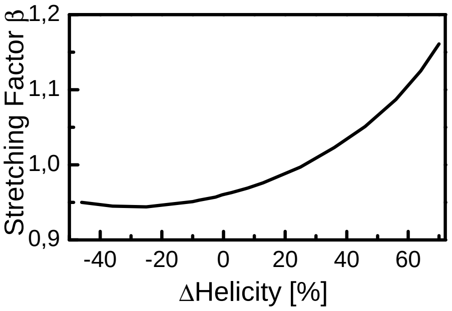

Figure 2.14: Stretching factor β as a function of the change of helicity for the zipper model. The parameters are the same as in Fig. 2.13; switching is symmetric around $\Delta H_{Hbond} = -1.47$ kcal/mol (corresponding to 50% helicity at 8°C).

The model still contains only two parameters σ and *s* that are fully determined by the steepness of the melting curve. The two parameters have the same physical interpretation as in the single sequence approximation Eq. 2.32, except that σ in Eq. 2.32 accounts for three helical amino acids in a row. However, the number of sequences with only few closed hydrogen bonds (i.e. with small $l(i)$) is significantly larger in Eq. 2.34 than the factor $\Omega_i = (n - i - 1)$ in Eq. 2.32. Since this number of sequences gives rise to an additional entropy factor, the single-bond entropy $-k_B \ln \sigma$ turns out be significantly smaller in Eq. 2.34, and mostly reflects the ratio of the areas of the helix-like conformation compared to β-sheet-like conformations in the Ramachandran plot. In other words, most of the entropy difference between folded and unfolded state in Eq. 2.34 originates from a combinatorial argument, rather than from the single-bond entropy σ. As a consequence, the nucleation barrier is much less pronounced in Eq. 2.34 and the free energy surface is much flatter (Fig. 2.13a).

Fig. 2.13b,c show kinetic simulations with $\sigma = 0.1$ and $\Delta H_{Hbond} = -1.7$ kcal/mol for the *trans* configuration and $\Delta H_{Hbond} = -1.4$ kcal/mol for the *cis* configuration. With these parameters, the temperature dependence of the average helicity - i.e. the thermodynamics - is the same as before in the single-sequence approximation. In contrast, the kinetics is different as a result of the less pronounced nucleation barrier which now renders the relaxation non-exponential. A stretched exponential fit reveals $\beta = 0.9$ for an unfolding experiment (Fig. 2.13b) and $\beta = 1.1$ for an folding experiment (Fig. 2.13c). In the latter case, the kinetics would be a compressed, rather than a stretched exponential function.

Fig. 2.14 shows the dependence of the stretching factor on the strength of the perturbation in the non-equilibrium experiment. For negative changes of helicity (unfolding experiment), the stretching factor is relatively constant with $\beta < 1$. The stretching factor still is $\beta < 1$ for a folding experiment with positive, but small changes of helicity. In this case, the system is in a small perturbation limit (Eq. 2.27), and the non-equilibrium relaxation follows the same kinetics as an equilibrium correlation function, for which $\beta < 1$ is obtained (see Sec. 2.3.3). For large positive changes of helicity, on the other hand, the zipper model predicts compressed kinetics with $\beta > 1$, in disagreement with the experimental observation of Ref. [206] (Fig. 2.11b).

Diffusion Models

Biased Funnel Model Szabo and coworkers have recently discussed biased diffusion as a minimalistic model for protein folding [84]. Contraction of diffusion in d dimensions onto an one-dimensional reaction coordinate, the distance x from the folded state, yields for the free energy surface:

$$V(x) = H(x) - (d-1)k_B T \ln(x) \tag{2.35}$$

where the first term, $H(x)$, is an enthalpic contribution with the shape of a funnel with a hole at the center:

$$H(x) = \begin{cases} -H_f, & \text{for x < a} \\ (x-a)F, & \text{for a < x < 1} \end{cases} \tag{2.36}$$

and a is the 'radius' of the folded state. The second term, $S(x) = -(d-1)k_B T \ln(x)$, is an entropic term which is related to the surface area of a d-dimensional sphere.

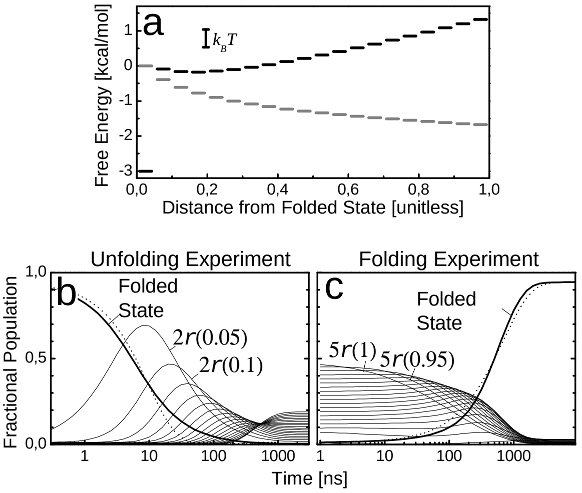

Figure 2.15: Free energy surface (a) and kinetic simulation (b,c) of the funnel model at 8°C with dimensionality $d = 2$, radius of the folded states $a = 0.05$ and folding enthalpies $H_f = 3$ kcal/mol and $F = 3$ kcal/mol, respectively. Fig.(a) shows the free energy surface as a function of the unitless distance to the folded state; the gray states show the free energy in the unfolded conformation, the black states that in the folded conformation. The action of the photo-switch was modelled by suddenly switching on (folding experiment) or off (unfolding experiment) the folding enthalpies H_f and F. Fig.(b) shows the kinetic result of an unfolding experiment, and (c) that of a folding experiment. The population of the individual states along the reaction coordinate (thin lines, scaled for better visibility) is plotted together with that of the folded state (thick line). The dotted line shows the best exponential fit to the kinetics of the folded state.

We model the action of the photo switch by assuming that the folding enthaplies, F and H_f, are suddenly switched on (or off), and that free energy in the unfolded state is governed by the entropic contribution solely. Fig. 2.15 shows a kinetic simulation of an unfolding as well as of a folding experiment using the parameters: temperature 8°C, dimensionality $d = 2$, radius of the folded states $a = 0.05$ and folding enthalpies $H_f = 3$ kcal/mol and $F = 3$ kcal/mol, respectively. Furthermore, we assume that the observable f selectively measures the folded state. Note that although the free energy surfaces in Fig. 2.15a and Fig. 2.13a seem to be similar, they are in fact reversed because the folded state is found on the left side in Fig. 2.15a (distance from the folded state $x = 0$) and on the right side in Fig. 2.13a (maximal number of native contacts).

In the case of an unfolding experiment (Fig. 2.15b), the relaxation is distinctively slower than exponential with a stretching factor $\beta = 0.77$. The unfolding experiment is in the limit described in Sec. 2.3.3 (localized probe & starting at the probed state). We therefore expect to observe the same kinetics as we would in an

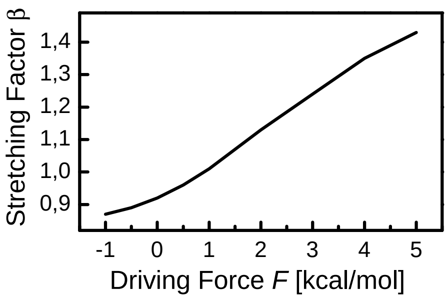

Figure 2.16: Stretching factor β as a function of the downhill driving force F for the funnel model, when performing the experiment in the folding direction. The parameters are the same as in Fig. 2.15. While varying F, the sum $F + H_f$ was kept constant (6 kcal/mol) to keep the equilibrium constant between folded and unfolded state the same.

equilibrium experiment, for which $\beta \leqslant 1$ is obtained (see Sec. 2.3.3).

While the same localized probe is used in the folding experiment (Fig. 2.15c), the probed state is no longer the starting state. As a result, the kinetics is compressed with $\beta = 1.24$. In this example, the reason for the compressed kinetics is particularly intuitive: The initial distribution $\rho^{(0)}$ is localized at relatively large distance x from the folded state and hence starts far away from the state to which the observable is sensitive to. Consequently, there is a time lag during which the build up of folded population is essentially zero, since the distribution first needs to get closer to the folded state. In other word, when the initial population of the state adjacent to the folded state is zero, the initial rate of appearance in the folded state vanishes, $\dot{\rho}_{fold} = 0$, leading to compressed exponential kinetics.

Fig. 2.16 shows the dependence of the stretching factor β on the downhill driving force F for the case of a folding experiment. The stronger the downhill force F, the larger is the expected stretching factor, and the more compressed is the kinetics.

1D Golf Course Model Fig. 2.17 shows a kinetic simulation of a golf course model in one dimension (i.e. Eq. 2.35 and 2.36 with $d = 1$ and $F = 0$). In this case, the entropic barrier vanishes and the free energy surface in the unfolded state is flat (Fig. 2.17a, gray states). As a result, the initial population in regions close to the folded state is non-zero, and hence may populate the folded state immediately after triggering, in contrast to the situation in Fig. 2.15. Consequently, the kinetics now is stretched with a stretching factor $\beta = 0.71$ also when performing the experiment in the folding direction (Fig. 2.17c). The unfolding kinetics is stretched as well with $\beta = 0.63$ (Fig. 2.17b).

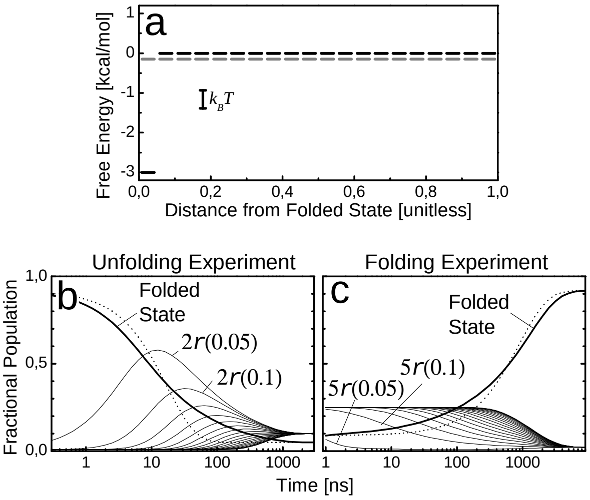

Figure 2.17: Free energy surface (a) and kinetic simulation (b,c) of the golf course model at 8°C with dimensionality $d = 1$, radius of the folded states $a = 0.05$ and folding enthalpies $H_f = 3$ kcal/mol and $F = 0$, respectively. Fig.(a) shows the free energy as a function of the unitless distance to the folded state; the gray states show the free energy in the unfolded conformation, the black states that in the folded conformation. The action of the photo-switch was modelled by suddenly switching on (folding experiment) or off (unfolding experiment) the folding enthalpy H_f. Fig.(b) shows the kinetic result of an unfolding experiment, and (c) that of a folding experiment. The population of the individual states along the reaction coordinate (thin lines, scaled for better visibility) is plotted together with that of the folded state (thick line). The dotted line shows the best exponential fit to the kinetics of the folded state.

2.3.5 Discussion

Our experiment in Ref. [206] investigated folding, rather than unfolding, of an α-helix. We have observed a stretching factor of 0.69 at 8°C, similar to the 1D golf course model of Fig. 2.17. The additional variation of the stretching factor with temperature has been explained by introducing a minor temperature dependent barrier (i.e. an entropic barrier) and a temperature dependent diffusion constant D. On a rugged free energy surface, the effective diffusion constant varies faster with temperature than an Arrhenius law [82, 83]. This model qualitatively explained all experimental observations.

To our knowledge, compressed exponentials have not been discussed in the context of protein folding. We have found only one example in literature where a peptide folding model indeed revealed $\beta \geqslant 1$, yet, this fact remained undiscussed (see Fig. 10 in Ref. [76]). We believe that compressed exponentials have escaped the attention of the protein folding community because most experiments so far have been performed either

- in a small-perturbation regime [49, 41, 92, 190, 119], in which we find that the observable $m(t)$ is approximately proportional to the equilibrium correlation function $c(t)$, for which we indeed obtain $\beta \leqslant 1$ under any circumstances (see Eq. 2.20 and Fig.2.14 for small changes of helicity),
- and/or were performed in the unfolding direction [49, 41, 92, 190, 119], which also tends to produce $\beta \leqslant 1$ (see Fig. 2.13b, Fig. 2.15b and Fig. 2.17b).

Nevertheless, compressed exponentials are not uncommon in diffusion problems. An example known to any chemist from practical courses in undergraduate education is that of biased diffusion in e.g. gel electrophoresis or HPLC. Diffusion of molecules in a column is described by a Smolukochowski equation Eq. 2.6, just like diffusion of a folding ensemble along a reaction coordinate. High resolution of these methods is guaranteed (in part) by a strong driving force (a downhill scenario), which should be larger than diffusive thermal broadening. In this case, an initial distribution remains spatially compact, or, in other words, the initial rate of appearance of a fraction at the exit of the column is low, followed a 'burst' that is compact in space and/or time (similar to Fig. 2.15c). A compressed exponential fit of this behavior would reveal $\beta \gg 1$. The larger the driving force, the larger is β (as in Fig. 2.16) and the more compacts stays the spatial distribution.

As a rule of thumb, if the experiment is performed in a way that the state to which the experimental observable is most sensitive to is *approached*, the stretching factor β will be larger than one. In this case, there is a time-lag until the first molecules appear at the final state and the initial rate of formation of the fully folded state is small (since, at $t = 0$, there is hardly any population in partially folded states, see Fig. 2.15c). On the other hand, when *leaving* the experimentally observed state, the stretching factor will be $\beta < 1$ (see Fig. 2.15b). In our experiment it is reasonable to assume that the experimental observable is sensitive to the more ordered, folded state, which is why one should expect compressed kinetics when performing the experiment in the folding direction. This conclusion is obvious in Fig. 2.15, where the observable f was assumed to be sensitive exclusively to the folded state. In the case of Fig. 2.13, on the other hand, the weighting factor i in Eq. 2.33 also renders the observable to be more sensitive to the folded state, however, the result is smeared out leading to smaller deviations of the stretching factor from 1.

The observation of stretched exponential kinetics with $\beta \leqslant 1$ in Ref. [206] (Fig. 2.11b) did not seem to be anything surprising, as it has been observed many times before [49, 41, 92, 190, 119, 207]. However, in contrast to most previous investigations of protein folding, the experiment has been performed under conditions for which most folding models would predict compressed, rather than stretched exponential kinetics:

- The experiment investigates folding, rather than unfolding
- The photo-switch perturbs the system far away from equilibrium that leads to a helicity change of ≈60%.

Hence, the observation of a stretching factor $\beta \leqslant 1$ in our experiment does in fact allow us to draw rather strong conclusions on the shape of the free energy surface on which the non-equilibrium ensemble is evolving. In particular, this observation excludes models with strong downhill scenarios, such as the zipper model in Fig. 2.13 or the funnel model in Fig. 2.15. The stretching factor $\beta \leqslant 1$ speaks for a relatively flat free energy surface for the unfolded region, while the fact that non-exponential kinetics is observed excludes any dominant folding barrier. Hence, we propose that α-helix folding proceeds on a kinetic reaction coordinate along which the free energy surface has a shape similar to a 1D golf course (Fig. 2.17a). Due to the low dimensionality of the model, however, the conformational space of the unfolded region is not vast, as it is typically discussed in the context of Levinthal's paradox with a high dimensional golf course shape.

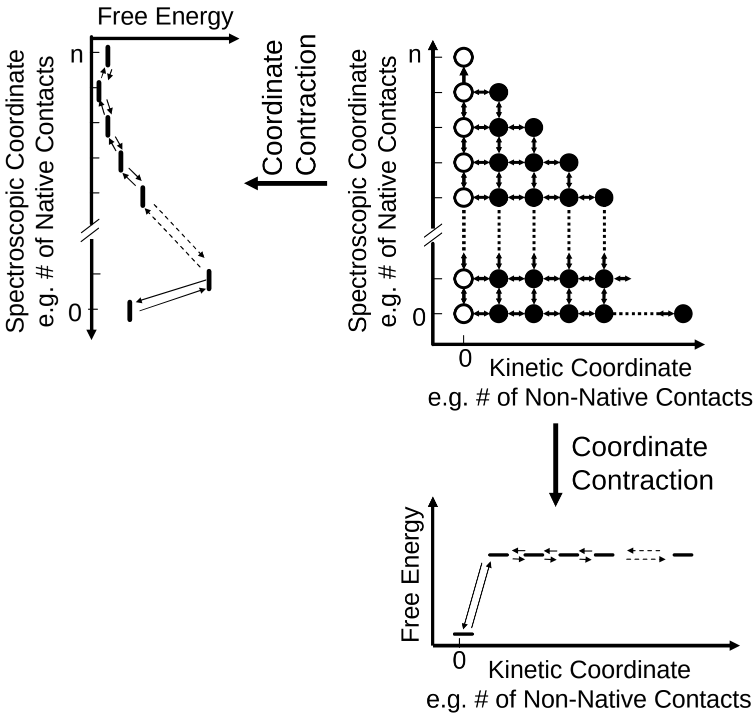

Figure 2.18: A model unifying the zipper model and the 1D golf-course model. See text for discussion.

Our experiment seems to suggest that the kinetics of α-helix folding is not governed by the zipper model. Yet, the zipper model has been established already in the late 50's [88, 87] and is well supported by a wealth of experimental work investigating the thermodynamics of folding (summarized in Ref. [90]). The - often implicitly made - extension to the *kinetic* zipper model assumes that the rate limiting step in helix folding is the formation of the entropically costly first helical turn (nucleation), while propagation of the helix is a downhill process due to the closing (zipping) of hydrogen bonds. However, there is increasing evidence from both experimental and simulation work that *nonnative* hydrogen-bond contacts are rate-limiting in the folding process. All-atom molecular dynamic (MD) simulations show that the so-called unfolded state of proteins and even of small peptides is by no means random [35, 193, 194, 195, 196, 197, 198, 199, 72], and that the unfolded state of peptides comprises vastly less conformations than one would expect based on the number of conformational degrees of freedom present. These states are stabilized by more or less specific *nonnative* contacts [196, 197, 198, 199, 72, 200]. MD simulations furthermore show that breaking of nonnative hydrogen-bond contacts cause significant enthalpic barriers in the folding process [72, 199, 201, 202]. Chowdhury *et al.* [202] as well as Hummer *et al.* [72] found rapid nucleation of the helix within a nanosecond in their simulations of a polypeptide. However, instead of subsequent rapid helix propagation driven by the formation of backbone hydrogen bonds, as envisioned in the 'zipper model', they found that folding is hampered by nonnative contacts, whose breaking determines the rate of helix formation. They concluded that helix nucleation does not trigger quick formation of the entire helix. Similar results were obtained by Bertsch *et al.* [201], who observe the frequent inhibition of helix propagation by nonnative hydrogen-bonds. Hence, the number of native hydrogen bonds, which is the reaction coordinate in the zipper model, does not seem to be the coordinate that determines the rate of α-helix folding.

Fig. 2.18 represents a suggestion of how the two models models, the zipper model (Sec. 2.3.4) and the 1D golf-course model (Sec. 2.3.4), may be reconciled. The picture starts from *two* reaction coordinates (Fig. 2.18, top right): a *spectroscopic coordinate* (e.g. the number of native contacts i) and a *kinetic coordinate* (e.g. the number of non-native contacts j) with a free energy F_{ij} in this two-dimensional coordinate space. One can eliminate either of these coordinates by a coordinate contraction, which would read for the zipper model:

$$F_i = -k_B T \ln \sum_j e^{-\frac{F_{ij}}{k_B T}} \tag{2.37}$$

and for the 1D golf course model

$$F_j = -k_B T \ln \sum_i e^{-\frac{F_{ij}}{k_B T}} \tag{2.38}$$

With respect to the thermodynamics, a free energy can always be defined in a self-consistent way for any choice of a reaction coordinate. The choice might not be very intelligent, i.e. the reaction coordinate might not be very expressive in representing the conformational transition, but the in this way defined free energy surface is correct. The number of native contacts in the zipper model is a spectroscopic reaction coordinate, since the measurement signal in an IR experiment (as well as in a CD experiment) is assumed to be proportional to that coordinate. Hence, as long as one is discussing the thermodynamics of α-helix folding in a stationary experiment, the number of native contacts appears to be a natural choice of a reaction coordinate, justifying in retro respect the zipper model.

With respect to the kinetics, however, certain reaction coordinates might be rate limiting while others might not. The *spectroscopic coordinate* is not necessarily a *rate limiting coordinate*, i.e. is not necessarily a *kinetic coordinate*. The distinction between kinetic coordinates and thermodynamic coordinates has been discussed recently by Dill and coworkers [24]. In fact, the simulation work discussed above, in combination with experimental results, seems to suggest that non-native contacts are rate limiting. The number of non-native contacts is summed out in the zipper model (Eq. 2.37), and hence, hidden in the entropy contribution to the free energy in the zipper model. If we assume in Fig. 2.18 (top right) that horizontal arrows along the number of non-native contact are slow, since enthalpic barriers have to be overcome, while vertical arrows are comparably fast, then the overall kinetics would be governed by a free energy surface of the shape of a 1D golf course (Fig. 2.18, bottom right). The free energy surface of the zipper model (Fig. 2.18, top left) is not wrong, it is just not a very expressive choice of a reaction coordinate when describing the kinetics of α-helix folding.

2.3.6 Conclusion

In the present paper, we have discussed the conditions under which diffusion problems, such as protein folding, lead to stretched exponential kinetics and under which they would lead to compressed exponential kinetics. We showed that diffusion problems have a strong tendency to yield stretched exponential kinetics: In equilibrium, non-exponential kinetics necessarily implies stretched exponential kinetics (Sec. 2.3.3), while in non-equilibrium, this conclusion is still true for certain weak perturbation regimes (Sec. 2.3.3). Compressed exponential kinetics have not yet been discussed in literature in the context of protein folding. Nevertheless, in contrast to most previous experiments, our recent experiment has been performed under conditions (investigation of folding rather than unfolding, strong perturbation from equilibrium) for which most protein folding models would predict compressed rather than stretched exponential kinetics, in disagreement with our observation [206]. We can therefore draw rather strong conclusions on the shape of the free energy surface that governs α-helix folding. We find that the free energy surface along the kinetic reaction coordinate must be relatively flat and rugged, without significant downhill driving force and without any significant folding barrier.

Acknowledgement. This work has been initiated by an extremely fruitful collaboration with Andrew Woolley (University of Toronto). We thank Andrew Woolley for valuable and inspiring discussions and for carefully reading the manuscript. The work has been supported by the Swiss National Science Foundation (2100-067573/1).

2.4 P9 – A Fast Photoswitch for Minimally Perturbed Peptides: Investigation of the Trans→Cis Photoisomerization of N-Methylthioacetamide

Jan Helbing, Harald Bregy, Jens Bredenbeck, Rolf Pfister, Peter Hamm, Robert Hubert, Josef Wachtveitl, Luca De Vico, and Massimo Olivucci.
J. Am. Chem. Soc., 126:8823–8834, 2004.

2.4.1 Abstract

Thio aminoacids can be integrated into the backbone of peptides without significantly perturbing their structure. In this paper we use ultrafast infrared and visible spectroscopy as well as state-of-the-art *ab initio* computations to investigate the photoisomerization of the trans form of *N*-Methylthioacetamide (NMTAA) as a model conformational photoswitch. Following the S_2 excitation of *trans*-NMTAA in water, the return of the molecule into the trans ground state, and the formation of the cis-isomer is observed on a dual timescale, with a fast component of 8-9 ps and a slow time constant of ≈250 ps. On both timescales the probability of isomerization to the cis form is found to be 30-40 % independently of excitation wavelength. *Ab initio* CASPT2//CASSCF photochemical reaction path calculations indicate that, *in vacuo*, the trans-cis isomerization event takes place on the S_1 and/or T_1 triplet potential energy surfaces and is controlled by very small energy barriers, in agreement with the experimentally observed picosecond timescale. Furthermore, the calculations identify one S_2/S_1 and four nearly isoenergetic S_1/S_0 conical intersection decay channels. In line with the observed isomerization probability, only one of the S_1/S_0 conical intersections yields the cis conformation upon $S_1 \rightarrow S_0$ decay. A substantially equivalent excited state relaxation results from four T_1/S_0 intersystem crossing points.

2.4.2 Introduction

While amides are usually most stable in the trans conformation, they can be converted into the cis conformation with relatively high quantum yield by photoisomerization upon π-π^* excitation.[212] In *N*-methylacetamide (NMA) the corresponding absorption band peaks at 186 nm.[213] Substitution of oxygen by sulfur in a peptide bond yields a thioamide, and leads to significantly red-shifted π-π^* and n-π^* absorption, thus lowering the excitation energy needed for photoisomerization. When a thioamide is integrated into the backbone of a polypeptide, it is therefore possible to selectively excite this unit and to photoinduce a conformational change via trans-cis isomerization at a well defined position in the peptide chain. For the thionated endorphins Tyr-ϕ[CS-N]-Pro-X-Phe-NH_2 (X=Trp or Phe) Schutkowski and coworkers have shown, that the concentration of molecules with the Tyr-Pro bond in the cis-conformation can be significantly enhanced by photoisomerization.[135] Seebach and coworkers [214] have synthesized β-thiohexapeptides with one, two and three C=S groups in the N-terminal position, and report drastic changes in the CD-spectra upon π-π^* excitation of the thionated peptide units. In very recent work, Zhao et al. report on efficient photoswitching of secondary thiopeptide bonds in α-polypeptides [215]. This is particularly interesting as the possibility to selectively introduce thio amino acids into polypeptides, which are capable of forming secondary structures, has recently been demonstrated by Miwa and coworkers [132, 133]. Both the incorporation of a thioamide linkage between the residues of a β-turn [132] and within a helical peptide [133] resulted only in minor changes to the native hairpin- and α-helical structures. As an alternative to the more widely used, but much bulkier azobenzene photoswitches [161, 124, 128] O→S substitution in a single peptide unit may thus provide a method to study the dynamics of photoinduced conformational changes in practically *unperturbed* (i.e. substantially native) peptides and proteins, provided that isomerization of the thioamide takes place on a sufficiently fast time scale.

N-methylthioacetamide (NMTAA) is among the simplest thioamides, and it has been subject to many studies of photoisomerization, using UV-Vis, Raman and NMR spectroscopy. [216, 217, 218] It has been shown that trans-cis isomerization [1] leads to significant shifts both in the electronic and the vibrational spectra, which in turn can be used to monitor the kinetics and dynamics of photoisomerization. However, these experiments, as well as similar measurements on regular amides [212, 219] provide only limited information on the underlying mechanism and the timescales involved. The best time resolution so far was achieved by resonance Raman experiments, which have put a 5 ns upper limit for the time of trans→cis isomerization of NMTAA [217]. While the high isomerization efficiency upon UV-excitation has been interpreted as a signature of a twisted π-π^* excited state in NMA and NMTAA, [212] torsional modes are not enhanced in the resonance Raman spectra of NMA, [219] indicating that isomerization may occur later in the relaxation process. Early *ab initio* calculations [220] have reported optimized structures with twisted geometry in both the n-π^*, π-π^* and the triplet excited states of NMA.

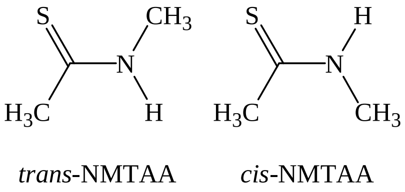

Figure 2.19: Structures of the NMTAA isomers.

Here, in order to establish the photoisomerization mechanism of NMTAA, we have used transient visible and infrared spectroscopy with high time resolution to follow the photoreaction in real time. In addition we have performed kinetic measurements of the isomerization quantum yields and photostability at different irradiation wavelengths. In order to provide a rigorous basis for the formulation of a mechanism consistent with the observed results we have performed *ab initio* CASPT2//CASSCF quantum chemical calculations to map out the intrinsic (i.e. *in vacuo*) photoisomerization path of NMTAA.

2.4.3 Methods

Experimental Setup

NMTAA was prepared from NMA employing standard procedures based on Lawesson's reagent [221] and pu-

---

[1] Since the isomerization takes place about the formally single bond C-N one should refer to *s-trans*-NMTAA and *s-cis*-NMTAA conformes. However, in order to conform to previous works, we use the labels cis or trans determined by the relative positions of the two NMTAA methyl groups.

rified by vacuum distillation. For time-resolved IR measurements, 50-250 mM solutions of NMTAA in D_2O were circulated through a flow cell made of CaF_2 windows spaced 50 μm apart at a rate sufficient to ensure complete exchange of excited sample volume between subsequent excitation pulses [182].

In order to completely avoid signals from the window material in measurements in the visible spectral range, experiments had to be performed in a jet of NMTAA, dissolved in doubly distilled water, with a thickness of about 70 μm. A high optical density of the NMTAA solution of about 100OD/mm ($c \approx 80$ mM) provided a low effective interaction pathlength between pump light and the water, to further minimize contributions from the solvent.

Femtosecond (fs) pulses for IR measurements (1 kHz, 700 μJ /pulse, 80 fs) were obtained from an amplified titanium-sapphire laser system (Spectra Physics), operating either at 840 nm or at 777 nm. UV pulses for the excitation of NMTAA at 280 nm or at 259 nm were generated by frequency tripling. The third harmonic beam was then isolated by dielectric mirrors, and the UV pulses were stretched to 1.4 ps duration by guiding them through 15 cm of fused silica. This significantly increased the threshold for the onset of undesired nonlinear effects in the sample cell, like white-light generation and/or color center formation, and allowed to excite a larger fraction of the molecules.

Mid-infrared pulses near 1400 cm^{-1} (100 fs, 1 μJ, 250 cm^{-1} bandwidth) were produced in a home-built double-stage optical parametric amplifier (OPA) followed by frequency mixing in a $AgGaS_2$ (Silver thiogallate) crystal [165]. The IR pulses were split into two parts (of $\approx$ 50 nJ each). One part (the probe pulse) was overlapped with the UV-pump pulse in the sample cell. The second part was used as a reference beam in order to correct for intensity fluctuations, and crossed the flow-cell approximately 500 μm further up-stream than the pump pulse. Both IR beams were dispersed in a spectrometer and detected with a double MCT array (2x32 pixels) on a single shot basis with 4 cm^{-1} resolution.

For transient UV-pump/Vis-probe spectroscopy a Clark MRX CPA-2001 regenerative amplifier system (1 kHz, 800 μJ /pulse, 160 fs) provided pulses with a central wavelength of 775 nm, and frequency tripling yielded UV pulses at 258 nm. The pulse energies for excitation were chosen low (between 300 nJ and 2 μJ) to minimize the formation of solvated electrons by multiphoton excitation. Transient absorbance changes in the UV-visible spectral range were recorded by a single filament white light continuum, generated in a 2 mm-thick CaF_2 plate, which covered a wavelength range from 300-1000 nm. For spectral resolution two spectrometers (for probe and reference beams) equipped with 42-diode arrays were used and operated in single shot detection.

Narrow bandwidth light for kinetic measurements was generated by passing the output of a high pressure Xe lamp through a monochromator. The UV-light was directed onto the sample, either inside an FTIR or a UV-Vis spectrometer, allowing to record spectra as a function of irradiation without having to move the sample. A flow cell allowed to introduce or exchange the sample in the FTIR spectrometer without opening the thermally equilibrated and nitrogen-flushed chamber, and guaranteed identical optical pathlengths, window absorption and scattering conditions in all experiments. All data were recorded with a liquid nitrogen-cooled MCT detector and baseline drifts were less than 1 mOD over several hours. Care was taken that the spot size used for irradiation was larger than the sample cell window. The photon flux could thus be determined from a measurement of the light power immediately behind an empty sample cell. The same excitation source was used for fluorescence measurements in combination with a photomultiplier and a photon counting system. A lower limit for the sensitivity of this home-built setup was determined from the fluorescence signal of a laser dye of identical optical density at the excitation wavelength.

^{1}H-NMR spectra in thermal equilibrium and of the photostationary state were recorded with an Avance DRX-600 MHz spectrometer. To assure full saturation of the large amount of sample needed, we irradiated with 3-6 mW UV-light from the fs-laser, while circulating the sample inside the flow cell and monitoring its UV-absorption spectrum. The saturated sample was then transferred to the NMR-spectrometer and spectra were recorded within 10 minutes after the end of irradiation.

Computational Methods

Structure optimization and relaxation path mapping have been carried out using fully unconstrained *ab initio* quantum chemical computations in the framework of the CASPT2//CASSCF strategy, with the only exception of two triplet energy minima (**Min T_1 Planar Trans** and **Min T_1 Planar Cis**) that were optimized by imposing a planarity constraint [222, 223]. Relaxation paths were computed in terms of minimum energy path (MEP) in mass-weighted coordinates, using the IRD methodology [224, 225]. The CASPT2//CASSCF strategy requires that the reaction coordinate is computed at the complete active space self-consistent field (CASSCF) level and that the corresponding energy profile is re-evaluated on the multiconfigurational second order Møller-Plesset perturbation theory level (here we used the CASPT2 method [226] implemented in MOLCAS-5) [227] to take into account the effect of electron dynamic correlation.

All computations employed the 6-31G* basis set and an active space comprising 10 electrons in 8 orbitals. This includes the full N-C-S π-system (4 electrons in 3 π-orbitals), the sulfur p lone pair (2 electrons in 1 orbital) plus the C-N and C-S bonds (4 electrons in 4 σ-orbitals). The σ/σ^* orbitals were added after test calculations because they were seen to mix with the π/π^* and lone pair systems when the geometry becomes highly pyramidalized. All geometry optimizations were carried out using the GAUSSIAN98 suite of programs [228].

When possible, energy minima and transition structures were optimized using a single root CASSCF wave function and confirmed via analytic frequency computations. However, the S_2 minimum (**Min S_2**) was located using a two roots (S_1, S_2) state-average (0.5, 0.5) CASSCF wavefunction and subsequently confirmed via a numerical frequency calculation. Similarly, due to wavefunction instability, the four S_0 transition states (**TS S_0 A1**, **TS S_0 A2**, **TS S_0 B1**, **TS S_0 B2**)were located using a two roots (S_0,S_1) state-average (0.5,0.5) CASSCF wavefunction.

The S_2, S_1, T_2, T_1 and S_0 potential energy surfaces were connected by computing five S_2/S_1, S_1/S_0 Conical Intersections (CI) [229, 230] and eight T_2/S_1, T_1/S_0 Inter System Crossings (ISC). All crossing points were optimized using the methods available in GAUSSIAN98. The optimization of both CIs and ISCs was found to be technically difficult due to the fact that the ”sloped” [231] topography of these points [224]^2 decreases the convergence efficiency. *For this reason, the reported structures represent a compromise between the quality of energy minimization on the upper state and the complete energy degeneracy between the two intersecting states*.

A S_2 MEP calculation was performed to connect the Franck-Condon point to the S_2 minimum and S_2/S_1 CI, using a two roots (S_1, S_2) state-average (0.5, 0.5) CASSCF wavefunction. An S_1 MEP connecting the S_2/S_1 CI to one of the S_1 minimum has been computed using a two roots (S_0, S_1) state-average (0.5, 0.5) wavefunction. Finally, for each S_1/S_0 CI and T_1/S_0 ISC a S_0 MEP connecting the chosen CI or ISC point to the S_0 reagent or product minimum was computed using a single root wavefunction.

As stated before, energies of stationary points, CIs, ISCs and selected points along the MEPs have been reevaluated using single point calculations performed at the CASPT2 level of theory. For each geometry, a three roots (S_0, S_1, S_2) state-average (0.33, 0.33, 0.33) CASSCF wavefunction was used as reference function for evaluating the CASPT2 energies of the singlet states, while a two roots (T_1, T_2) state-average (0.5, 0.5) wavefunction was used for the triplet states. Also, for each energy minimum on S_1 and T_1 a four roots (S_0, S_1, S_2, S_3 or T_1, T_2, T_3, T_4) state-average (0.25, 0.25, 0.25, 0.25) CASSCF wavefunction was used as reference function for evaluating the CASPT2 energies of third and forth roots.

2.4.4 Experimental Results

Steady State Absorption and Kinetic Studies

The solid lines in Figure 2.20a and 2.20c show the UV and infrared absorption spectra of *trans*-NMTAA in D_2O at room temperature. The S_2 state, which is due to a π-π^* excitation (see below), gives rise to the main UV absorption band centered at 255 nm, while a much weaker shoulder at 305 nm is due to the S_1 state (n-π^* transition). In the infrared spectrum, three prominent bands were of main interest in this study. They were assigned on the basis of a normal mode calculation on BLYP 6-31G(d) level (GAUSSIAN98), which was capable of reproducing approximate frequencies, relative intensities and energy shifts upon isomerization. The band at 1545 cm^{-1} is the amide II band, which is strongly blueshifted with respect to matrix isolation spectra of NMTAA [232] and broadened due to strong interaction with the D_2O solvent. The band at 1409 cm^{-1} and the weaker band at 1372 cm^{-1} can best be characterized as ‘symmetric’ and ‘antisymmetric’ stretch motion of the C-C-N-C backbone. Both modes also involve an umbrella-like motion of the methyl groups (The extinction coef-

---

[2] Energies and energy gaps oscillate during the geometry optimization and never converge, or if energy gap tends to converge the energy, increases endlessly. This behaviour has been found to be associated with highly sloped conical intersections.

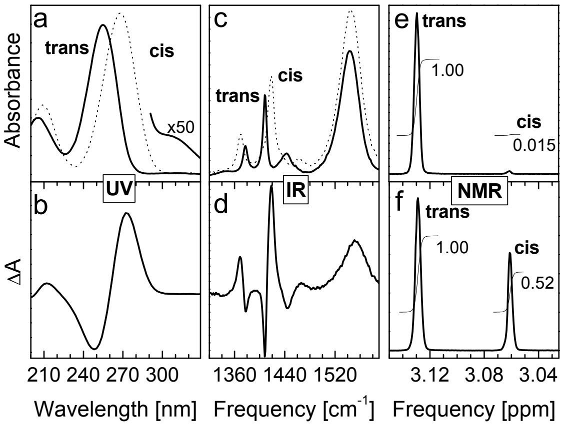

Figure 2.20: a) solid lines: UV-absorption spectrum of *trans*-NMTAA in deuterated water b) difference absorption spectrum under UV-irradiation. c) solid line: FTIR absorption spectrum of *trans*-NMTAA before irradiation d) FTIR difference absorption spectrum under UV-irradiation. The dotted lines in a) and c) show the *cis*-NMTAA absorption spectra, which were constructed from the trans the and difference spectra. e) NMR spectrum at room temperature before irradiation and f) in photo equilibrium after 256 nm irradiation. The numbers indicate the normalized peak areas.

λ/nm	c_{cis}	η_{c-t}/η_{t-c}	η_{t-c} (kinetic)	η_{t-c} (transient)
256	34% (NMR)	2.3-3.1	40%[3]	30-40%
280	4.4% (NMR)	2.1-3.5	28%	30-40%
308	$(14\pm2)\%$[4]	3-6	-	-

Table 2.2: Cis concentrations c_{cis} in photoequilibrium and quantum efficiencies of trans-cis isomerization η_{t-c} for different irradiation wavelengths obtained from kinetic and from transient absorption measurements. The ratio η_{c-t}/η_{t-c} was estimated form the concentrations in photoequilibrium and the absorption cross sections of *cis*- and *trans*-NMTAA.

ficients for *trans*-NMTAA are 12400 L mol^{-1}cm^{-1} at 255 nm and 200 L mol^{-1}cm^{-1} at 1545 cm^{-1}). The changes in UV and infrared absorption due to UV irradiation are shown in the Figure 2.20b and 2.20d. In the UV, a red-shift is observed for the π-π* absorption band and this shift obscures any changes that may occur in the region of the n-π* band. In the IR vibrational spectrum, the trans band at 1409 cm^{-1} undergoes a blue-shift, and gains in oscillator strength upon photoisomerization, while a red shift is observed for the 1372 cm^{-1} band. The amide II band of the cis species is stronger and peaks at slightly larger energies than the trans band. Kinetic measurements, based on both UV and FTIR absorption data, show an exponential decrease of the *trans*-NMTAA concentration and a simultaneous growth of the *cis*-NMTAA photoproduct. There are well-defined isosbestic points in the difference absorption spectra, which is an indication of simple two-state kinetics $\text{cis} \overset{h\nu}{\rightleftharpoons} \text{trans}$. Indeed, due to the strongly overlapping UV-absorption bands of the two isomers, the photoreaction can take place in both directions and a photoequilibrium between cis and trans species is eventually established. The *cis*-NMTAA concentration in the photostationary state under 256 nm irradiation is 34%, compared to only 1.5% in thermal equilibrium before irradiation (Figures 2.20e and 2.20f). Mainly due to the differences in the relative absorption cross sections of *cis*- and *trans*-NMTAA, their concentrations in photoequilibrium vary strongly as a function of irradiation wavelength, as shown in Table 2.2 [5]. The table also shows the ratio of the quantum efficiencies for trans→cis and cis→trans isomerization, which can be determined directly from the concentrations in photoequilibrium and the absorption cross sections. Although associated with large error bars due to uncertainties in the photon flux, the estimates for the trans→cis isomerization quantum efficiency (20-40% for π-π* excitation) from the kinetic data is very similar to the more reliable value (30-40%) obtained from our transient measurements (see below).

In previous work sample degradation and trans→cis isomerization were found to occur with equal probability and their combined quantum efficiency was estimated to be 24% [217]. In contrast, we find very little to no degradation of our NMTAA samples during the time needed to reach photoequilibrium. When irradiation was stopped in photoequilibrium the original trans-absorption spectra completely recovered due to thermal relaxation back to trans (Figure 2.21a). Only after an irradiation dose that corresponds to approximately 50 photo excitations per molecule we observed an irreversible 5% loss and a small red shoulder in the UV absorption spectrum of NMTAA after thermal relaxation (Figure 2.21b). At the same time, however, no new vibrational

---

[5] Since the irradiation wavelength can be changed without removing the sample from the FTIR spectrometer, the concentrations in photoequilibrium for different irradiation wavelengths can be determined with high accuracy (and independent of any spectrometer drifts) relative to the value at 255 nm by comparing the peak-to-peak differences in the FTIR-difference spectra shown in Fig. 2.20d).

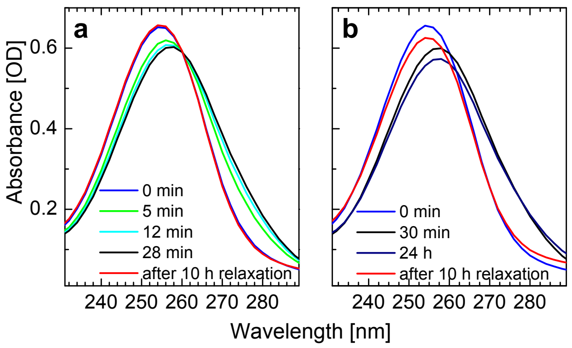

Figure 2.21: a) UV-absorption spectra of NMTAA before irradiation (blue line, 98% trans) and after 5, 12, and 28 minutes of irradiation at 255 nm. After 10 h in the dark at room temperature the original absorption spectrum has completely recovered (red line). b) irradiation for much longer than 30 minutes leads to a very slow degradation of the sample without further isomerization, and only partial recovery of the initial absorption spectrum after thermal relaxation.

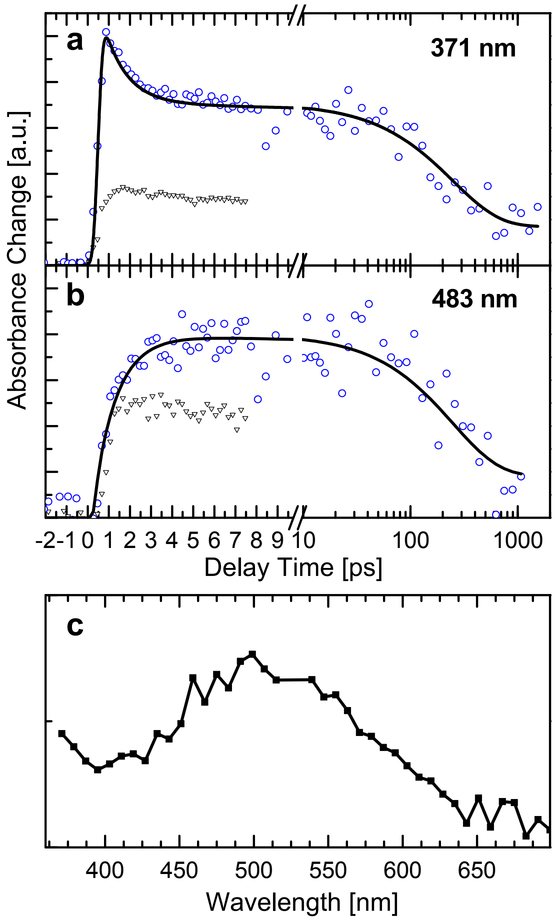

Figure 2.22: Transient absorption signals of NMTAA in H_2O (circles) and pure H_2O (triangles) at characteristic probe wavelengths of a) 371 nm and b) 483 nm, upon UV-excitation at 258 nm. The solid lines show double-exponential fits with timeconstants of 1.1 ps and 260 ps. c) Spectrum associated with the 260 ps time constant in fits to a set of transients between 350 nm and 700 nm.

bands could be detected in the FTIR spectrum. [6] Thus we conclude that NMTAA in D_2O is photostable upon π-π^* excitation with a quantum efficiency for decomposition below 0.1%. These findings are in agreement with recent measurements on small thio-substituted dipeptides [215].

Time-Resolved Measurements.

UV-Vis spectral range. Transient absorption changes of an aqueous solution of *trans*-NMTAA were recorded over a wide spectral range and compared to the contribution of the pure solvent H_2O under identical conditions. Figs. 2.22a and b show transients at two selected probe wavelengths (371nm and 483nm) after UV-excitation at 258 nm. The graphs are composed of two different data sets, one for delay times $\Delta t < 10$ ps (plotted on a linear scale) with a small temporal increment in order to facilitate detection of fast components, and one for $\Delta t > 10$ ps (plotted on a logarithmic scale). At 371 nm an absorption increase is observed for the NMTAA solution (open circles) which rises within the time resolution of the setup and decays with a fast (1.1 ps) and a slow (260 ps) time constant. Both time constants can also be observed at a probing wavelength of 483 nm. However, the fast component has a smaller relative amplitude and now appears as a rise time. Pure H_2O also shows positive transient absorption at the two wavelengths (triangles), but these signals contain no comparable fast components. This rise in solvent absorption is attributed to the photoinduced formation of solvated electrons, with a lifetime of the order of microseconds in pure liquid water [233, 234]. Their contribution to the signal of the concentrated NMTAA solution should be significantly smaller due to the high optical density and the resulting much shorter (< 15 μm) effective sample thickness. The true size of the background signal can in fact be estimated from the long-delay offset in the NMTAA data, which is much smaller than for pure H_2O.

---

[6] Note, however, that the sample can be efficiently destroyed upon irradiation with an unfiltered low-pressure Hg-lamp, which we attribute to excitation by light from the 193 nm line.

The transient measurements thus clearly identify absorption of an excited state of NMTAA with a lifetime of ≈ 250 ps. A pronounced maximum around 500 nm is found in the decay associated spectrum related with this slow time constant (Figure 2.22c), which may be interpreted as the spectral characteristics of this long-lived excited state band. Unfortunately, fast-varying solvent contributions to the signal do not allow an unambiguous identification of the spectrum associated with the 1.1 ps time constant. Overcompensatory effects by strong positive contributions from the solvated electron and the excited state absorption of NMTAA may also obscure stimulated emission signals, which could not be identified in the accessible spectral range between 300 nm and 1000 nm.

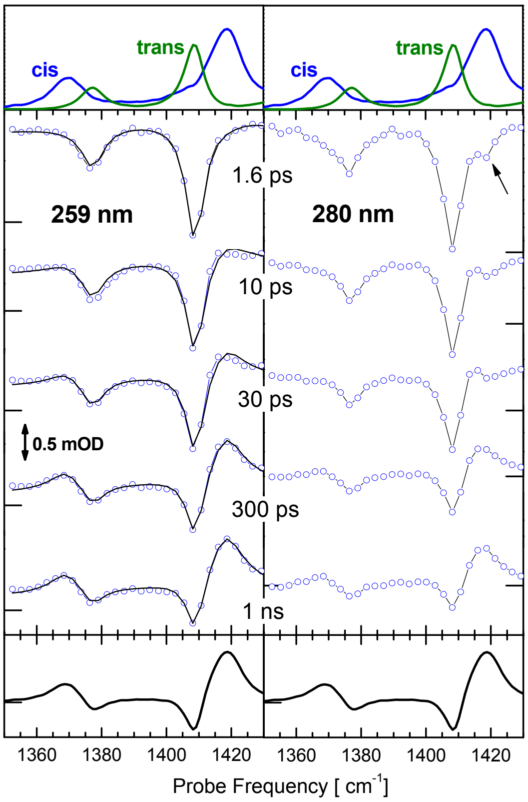

Figure 2.23: Magic angle transient infrared absorption spectra at different time delays after 259 nm (left) and 280 nm (right) excitation of NMTAA in D_2O. Thick black lines in the left column show least square fits using a linear combination of the cis and trans FTIR absorption spectra (shown on top). Horizontal ticks mark the zero-lines. The FTIR difference absorption spectrum (bottom) is also shown for comparison.

Mid-infrared spectral range. Changes in the mid-infrared absorption at different time delays after 259 nm excitation of *trans*-NMTAA are shown in the left column of Figure 2.23. Apart from a positive offset, the transient spectra at very early times after photoexcitation have the same shape as the FTIR absorption spectrum of *trans*-NMTAA. Within the first 30 ps the initial bleaching signal is reduced to little more than half of its original size, and positive absorption bands grow in at the spectral positions of the *cis*-NMTAA vibrations. This dynamics subsequently continues on a much slower timescale. After 1 ns, the difference spectra fully reproduce the FTIR difference spectrum and no further changes are observed for longer time delays.[7] These results were found to be independent of concentration in the range of 50-250 mM.

The right column of Fig. 2.23 shows transient spectra recorded for 280 nm excitation, where the *cis*-NMTAA absorption is approximately 5-10 times stronger than that of *trans*-NMTAA (Fig. 2.20). Thus, although only a small fraction of the molecules are initially in the cis-conformation ($\leqslant$2% cis at room temperature), these do contribute to the transient signal, when exciting at this wavelength. Indeed, immediately following excitation, a bleaching signal is now also observed at the cis transition energies (right column in Fig. 2.23). This signal increased during long series of measurement as a result of cis accumulation, but never exceeded 10-20% of the trans bleaching signal. Apart form the additional contribution due the excitation of *cis*-NMTAA no significant differences in the dynamics after excitation at the two wavelengths were observed. The larger change in amplitude of the signal for 280 nm excitation is due to the fact that cis→trans isomerization diminishes the trans→cis difference spectrum at long time delays. Taking this into account, we find that the trans→cis isomerization quantum yields for 280 nm and 259 nm excitation are equal within experimental error and lie in the range of 30-40%[8].

---

[7] The background underlying the NMTAA signal has two origins: A broad, unstructured positive signal, which decays to a small, constant value within approximately 10 ps is also observed for pure D_2O. The intensity of this background signal changes when the sample cell is moved, suggesting contributions from the cell windows. The main cause for the long-time background signal is, however, the temperature rise in D_2O as the excess photon energy is dissipated to the solvent. FTIR measurements show, that a small increase in temperature (1 K) leads to a positive, nearly flat difference signal in the 1300-1450 cm^{-1} region, which can be easily subtracted as a linear background from the transient data. It stays constant at delay times longer than 100 ps, indicating the end of the main energy dissipation.

[8] The isomerization quantum yields were determined in the follow-

In order to extract the relevant time scales involved in the dynamics, the magic angle signals for 259 nm excitation were analyzed using singular value decomposition (SVD). The resulting basis spectra contain no features that do not already appear in the steady state absorption spectra of *cis*- and *trans*-NMTAA. The corresponding time traces can be fit simultaneously to a bi-exponential function, yielding global timeconstants of 8.5 ± 0.5 ps and 250 ± 20 ps.

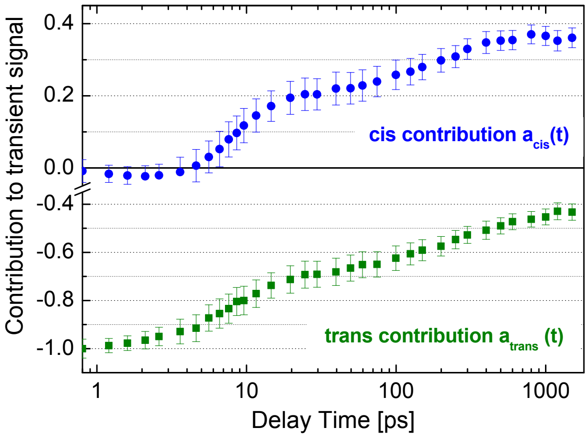

Figure 2.24: Time-dependent contributions of cis and trans absorption spectra in a least square fit $a_{cis}A_{cis}(\nu) + a_{trans}A_{trans}(\nu) +$ linear background to the magic angle transient spectra between 1350 cm^{-1} and 1450 cm^{-1}. $A_{cis}(\nu)$ and $A_{trans}(\nu)$ denote the FTIR absorption spectra, which were scaled to yield $a_{trans} = -1$ at the earliest pump probe delay. The linear term $c(t)\nu + d(t)$ was added in the fit to account for the time-dependent background signal, caused mainly by the temperature rise in the D_2O solvent. Error bars represent confidence intervals.

We could not identify any vibrational bands that may be assigned to NMTAA in an electronically excited state. The IR absorption bands of these species may either have shifted out of the spectral window used for detection, or their distribution may be so broad, that their absorption remains hidden in the unstructured background signal. A strong spectral shift could be caused by the fact that all the normal modes in the investigated spectral region include stretch motion of the central C-N bond, which have a significantly reduced bond order in the electronically excited states in which the molecule can isomerize (see below). Indeed we found that the transient spectra can be well reproduced by simply fitting the dataset with linear combinations of the cis and trans FTIR spectra (solid black lines in Figure 2.23). The quality of the fits is very good with only small deviations at intermediate delays, where there is a small red shift of the product absorption band near 1420 cm^{-1} with respect to the FTIR spectrum of *cis*-NMTAA. This redshift is maybe better seen with respect to the bleaching signal of *cis*-NMTAA in the spectra recorded upon 280 nm excitation (right column in Figure 2.23) and is a typical signature of a (cis) molecule at a more elevated temperature. It arises from anharmonic coupling of the high energy mode to low-frequency vibrations that have become excited thermally (or non-thermally) as a result of photoexcitation and energy dissipation [167]. Given the large amount of energy per normal mode that is delivered to the molecule by a 259 nm photon, the observed shifts are however surprisingly small. Our transient infrared measurements thus appear to be sensitive only to ground state molecules that have dissipated most of the excitation energy. They monitor the arrival of population in either the relaxed cis or trans conformation of NMTAA, and the observed dynamics is therefore due to the joint processes of electronic relaxation and vibrational cooling.

Figure 2.24 shows the contributions of cis and trans species to the transient spectra at different time delays, extracted from the fits using their ground state absorption spectra. It can be seen that both the recovery of the initial trans ground state and the formation of *cis*-NMTAA occur on two distinct timescales, with timeconstants compatible with those obtained from the SVD analysis (8.5 ps and 250 ps). About 30% of the initially excited trans population returns to the (cold) trans ground state within the first 20-30 ps following the 259 nm pump pulse. At the same time, another 15-20% is converted into ground-state *cis*-NMTAA. This early recovery of the IR absorption bands of cold ground state species indicates fast electronic decay and very efficient excess energy dissipation from the thioamide to the solvent. A strong interaction of NMTAA with D_2O is al-

---

ing way: The FTIR trans-absorption spectrum was fit to the magic angle transient signal at 1 ps delay (maximum bleach) by simple rescaling. This determines the amount of initially excited trans species. Next, a FTIR trans-cis difference spectrum was rescaled to fit to the 1 ns transient spectrum. The rescaled absorption spectrum A, multiplied by a variable factor $\eta_{t\to c} \leqslant 1$ can now be added to the rescaled difference spectrum D, until a smooth product-spectrum P with symmetric line shapes is obtained; $\eta_{t\to c}$ is the quantum efficiency of isomerization. This method yields $\eta_{t\to c} = 0.35 \pm 0.05$. At 280 nm, where *cis*-NMTAA is also excited the product spectrum is proportional to $D + (\eta_{t\to c} - \eta_{c\to t} n_C/n_T)A$, were n_C/n_T is the ratio of initially excited cis and trans molecules.

	sulfur lone pair	π	π	π*
	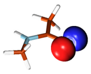	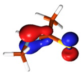	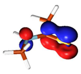	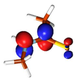
S_0	1.998	1.981	1.955	0.064
S_1	1.000	1.993	1.998	1.008
S_2	1.995	1.972	1.413	0.616

Table 2.3: Molecular orbital occupation of *trans*-NMTAA in the S_0, S_1 and S_2 states: only the p-type sulfur lone pair and the π/π* orbitals are depicted. Occupations were calculated using a three roots (S_0, S_1, S_2) state average (0.33, 0.33, 0.33) CASSCF wave function.

ready apparent from the broad amide II absorption band, that is strongly blue-shifted compared to the matrix-isolated molecule [232], and efficient energy dissipation could take place for example via dipolar coupling to the D_2O molecules of the first hydration shell as is the case of NMA in water, [235] and more directly through intermolecular hydrogen bonds. As a result, the 8-9 ps time constant very probably reflects the cooling of photoexcited NMTAA in deuterated water.

Further reduction of the initial *trans*-NMTAA bleach and the growth of the *cis*-NMTAA absorption bands take place on a much slower timescale which is comparable to the time of excited state decay in the visible measurements. Just as on the fast timescale, roughly two times more trans species than cis species are formed in the slow process. Overall, 35-40% of the excited NMTAA molecules are converted into cis, and the remaining molecules return back to the ground state in the trans conformation.

2.4.5 Photochemical Reaction Path Computations

The only energy minima located on the S_0 potential energy surface correspond to *trans*-NMTAA and *cis*-NMTAA. These are planar structures featuring C_s symmetry with the cis stereoisomer located 1.9 kcal mol^{-1} above the trans stereoisomer. Two fully asymmetric S_0 transition states (**TS S_0 A1** and **TS S_0 B1**) describe the trans→cis *thermal* isomerization reaction. They are located 24.9 and 20.7 kcal mol^{-1} above *trans*-NMTAA respectively. These values compare very well with *cis*-NMTAA concentrations of 4% at room temperature, and a free activation enthalpy of 22 kcal mol^{-1} in dilute CCl_4 solution [236]. Notice that the presence of the pyramidalized nitrogen center allows for the existence of one enantiomeric form (**TS S_0 B2** and **TS S_0 A2**) for each transition state.

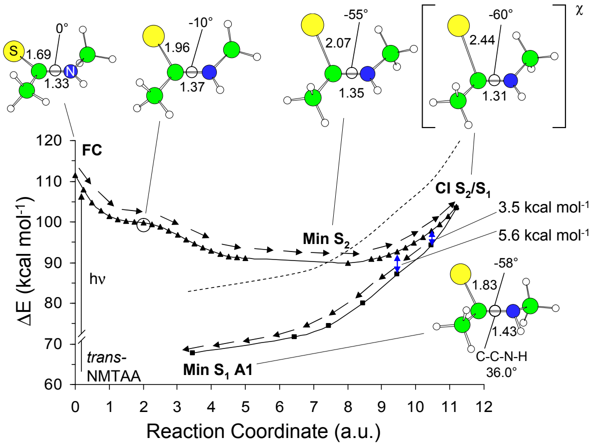

Figure 2.25: **FC** → **Min S_2** → **CI S_2/S_1** and **CI S_2/S_1** → **Min S_1 A1** paths computed at the CASPT2//CASSCF level of theory. The reaction coordinate is in mass-weighted cartesians (a.u. = amu$^{1/2}$a$_0$). Full triangles and full squares represent S_2 and S_1 energies respectively. C-S and C-N bond distances are given in Å; the S-C-N-C dihedral angle is given in degrees. For **Min S_1 A1** the C-C-N-H angle is also reported. The χ symbol indicates the CI. The dashed line represents the estimated shift in the position of the n-π* state due to solvent effects (see Section 2.4.6).

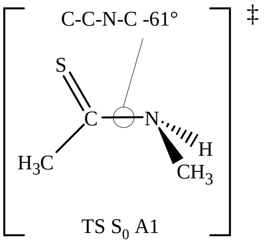

TS S_0 A1

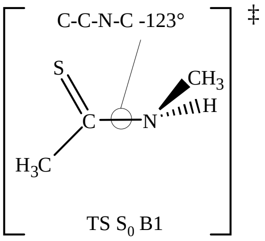

TS S_0 B1

Wavefunction analysis at *trans*-NMTAA establishes that the S_2 state corresponds to a π-π* excitation, while the S_1 corresponds to a n-π* excitation (see Table 2.3).

Excited State Relaxation

As shown in Figure 2.25, relaxation from the Franck-Condon point (**FC**) of *trans*-NMTAA is dominated by C-S bond expansion: the C-S bond passes from 1.69 Å to around 1.96 Å, while the C-N bond stretches from

1.33 Å to 1.37 Å. Later along the same relaxation path the sulfur atom is lifted out of plane as the thiocarbonyl carbon starts to pyramidalize. At **Min S_2** the C-S bond distance is 2.07 Å, while the C-N bond distance goes back to 1.35 Å; the S atom makes a -55° dihedral angle with the carbon-nitrogen frame which, in turn, remains nearly planar. A further expansion of the C-S bond of **Min S_2** leads to a S_2/S_1 conical intersection (**CI S_2/S_1**) located ca. 14 kcal mol^{-1} higher than the minimum.

Relaxation from **CI S_2/S_1** to the S_1 potential energy surface is achieved via a path dominated by back-contraction of the C-S bond length to 1.83 Å and expansion of the C-N bond distance to 1.43 Å. During the relaxation the thiocarbonyl carbon centre remains pyramidalized while the originally planar nitrogen centre pyramidalizes. The existence of two pyramidalized centers implies the existence of two diastereoisomers for the S_1 minimum. These have indeed been located and are referred to as **Min S_1 A1** (A stands for S,R) and **Min S_1 B1** (B stands for S,S). As a consequence the low-lying region of the S_1 potential energy surface is spanned by two flat ”valleys” (Path A and Path B) that originate from the diastereoisomers **Min S_1 A1** and **Min S_1 B1** respectively. Starting from **Min S_1 A1** on Path A we were able to map the entire conformational space corresponding to the torsional deformation about the central C-N bond. As shown in Figure 2.26, this path intercepts three conformational minima and three conformational transition states, in the order **Min S_1 A1** → **TS S_1 A1** → **Min S_1 A2** → **TS S_1 A2** → **Min S_1 A3** → **TS S_1 A3**. From **TS S_1 A3** the molecule goes back to **Min S_1 A1**.

Transition between Path A and Path B is possible through inversion transition states. For instance, the passage between **Min S_1 A1** and **Min S_1 B1** is driven by a transition state (**TS S_1 Pyr1** in the Supporting Information Section) located 2.6 kcal mol^{-1} higher than **Min S_1 A1**. As reported in Figure 2.26, and similar to Path A, Path B comprises three conformational minima and three conformational transition states (in the order **Min S_1 B1** → **TS S_1 B1** → **Min S_1 B2** → **TS S_1 B2** → **Min S_1 B3** → **TS S_1 B3**. From **TS S_1 B3** the molecule goes back to **Min S_1 B1**). The maximum energy difference between the entire set of minima and transition states is ca. 3.5 kcal mol^{-1}, so, at room temperature, the molecule can explore the entire conformational space of both Path A and Path B.

Relaxation to the Ground State

Decay to S_0 occurs via four different CIs. Two CIs are located along Path A (**CI S_1/S_0 A1** and **CI S_1/S_0 A2**) and two along Path B (**CI S_1/S_0 B1** and **CI S_1/S_0 B2**). All CIs are characterized by a S-C-N angle of ca. 90°. As mentioned in Section 2.4.3, these energy surface crossings are difficult to locate and therefore the structures reported are the best compromise between the requirement of stability and degeneracy. All decay channels are located in the range of 9.7-16.3 kcal mol^{-1} above **Min S_1 A1**.[9] As reported in Figure 2.26, relaxation path computations indicate that the photochemical outcome of a S_0 relaxation process depends on the specific decay channel (i.e. the specific surface crossing) prompting the relaxation. Remarkably, we found that only **CI S_1/S_0 A2** gives access to the cis product (*cis*-NMTAA), while decay at the other three CIs results in production of the initial trans molecule. One may explain this result by comparing the value of the C-C-N-C dihedral angle along a specific relaxation path to the value of the same dihedral angle for the ground state transition structures. In fact, these define the ridge between the cis and trans valleys on the S_0 potential energy surface (see Figure 2.26).

The analysis of the relaxation coordinates starting at **CI S_1/S_0 A1** and **CI S_1/S_0 B2** (C-C-N-C dihedral angles of -110° and -145° respectively) shows that the initial relaxation is dominated by replanarization of the thiocarbonyl carbon centre. As shown in Figures 2.26, after replanarization the molecule finds itself in the trans valley and goes back to the trans form. In contrast, the analysis of the relaxation coordinates starting at **CI S_1/S_0 A2** and **CI S_1/S_0 B1** (C-C-N-C dihedral angle of 55° and 30° respectively) shows that, due to the steric repulsion between the two fairly eclipsed methyl groups, thiocarbonyl carbon replanarization occurs simultaneously to a C-C-N-C dihedral angle increase of ca. 35°. For this reason, when the relaxation starts at **CI S_1/S_0 A2** the molecule achieves a dihedral angle of ca. 90° that is lower than the 123° angle of **TS S_0 A2** and right on top of the cis valley. Thus, the cis form is generated. In contrast, when relaxation starts at **CI S_1/S_0 B1**, after thiocarbonyl carbon replanarization the structure displays a dihedral angle of ca. 65° which is larger then the dihe-

---

[9] Reported energies for CIs represent the mean between the S_1 and S_0 CASPT2 energy values reported in Table 5S in Supporting Information Section. Energy degeneracy was achieved at the CASSCF level of theory, but the CASPT2 treatment split the two energies. The mean values represent a good approximation of the energy of the CI.

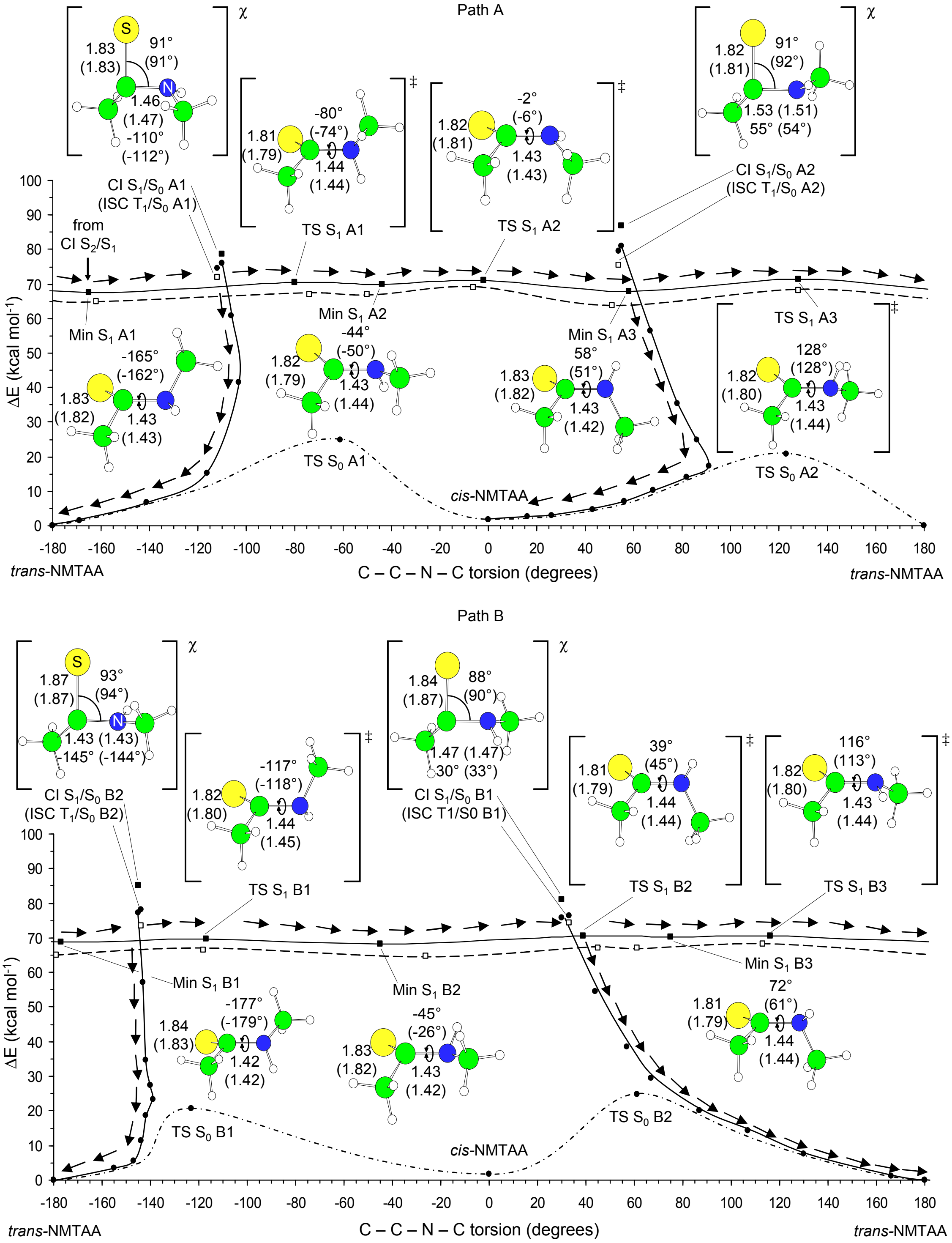

Figure 2.26: S_1 (full line), T_1 (dashed line) and S_0 (dot-dashed line) isomerization paths and $S_1(T_1) \rightarrow S_0$ relaxation paths (full line) computed at the CASPT2//CASSCF level of theory. Full circles, full squares and open squares represent S_0, S_1 and T_1 energies respectively. C-S and C-N bond distances in Å, and C-C-N-C dihedral angles in degrees. For the CIs and the ISCs the S-C-N angle is also given. Values in parentheses refer to T_1. While the C-C-N-C dihedral angle has been chosen as the internal coordinate that represents the trans-cis isomerization path, relaxation on S_0 is also characterized by planarization at the carbon and nitrogen centers. The nitrogen atoms of all structures along Path A are in the R conformation, while on Path B the nitrogens have a S conformation. The χ symbol indicates the CIs and the ISCs, the ‡ indicates the transition states.

dral angle of **TS S_0 B2** and right on top of the trans valley. *In conclusion our relaxation path analysis shows that relaxation from three out of four decay channels leads to the trans form.*

Population and Decay of the Triplet States

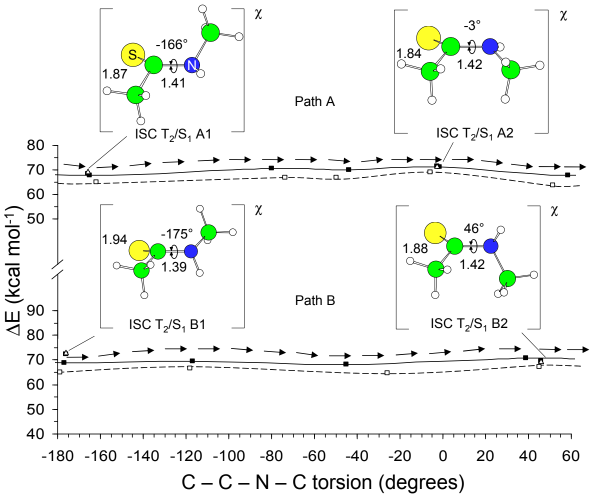

Figure 2.27: T_2/S_1 intersystem crossings computed at the CASPT2//CASSCF level of theory. Full squares, open squares and open triangles represent S_1, T_1 and T_2 energies. Geometrical parameters, symbols and lines as in Figure 2.26.

Our computations establish the existence of triplet trans-cis isomerization pathways that, ultimately, lead to the same photoproduct distribution. In fact, as shown in Figure 2.26, the structure of the T_1 energy surface is analogue to the one seen for S_1. Indeed, we have been able to locate six different T_1 conformers (three along Path A and three along Path B). These conformers may decay to S_0 via four different T_1/S_0 ISCs (two for Path A and two for Path B) featuring a geometrical structure very close to the corresponding S_1/S_0 CIs described above. Thus, substantially, ground state relaxation from T_1 may occur along the same paths already described for the S_1 relaxation. However, notice that the energy difference between the T_1 minima and the ISCs is considerably smaller then the energy difference between the S_1 minima and the S_1/S_0 CIs.

In principle efficient population of the T_1 energy surface may occur via intersystem crossing from S_1 to T_2 followed by internal conversion from T_2 to T_1. Indeed, as shown in Figure 2.27 the S_1 conformers can access the T_2 state via four different T_2/S_1 ISC channels located near the region of **Min S_1 A1**, **TS S_1 A2**, **Min S_1 B1** and **TS S_1 B2**. Following the El-Sayed rules for inter system crossings [237, 238], the T_2 state (corresponding to a triplet π-π* excitation) can be accessed quite efficiently from a degenerate singlet n-π* state. Since, in the same region, the T_2 and T_1 potential energy surfaces are substantially degenerate,[10] we assume that the T_1 state is readily accessed allowing for the efficient population of the six different T_1 conformers of Figure 2.26.

Comparison with Spectroscopic Data

In order to validate our computational strategy (see Section 2.4.3), we compare the experimental absorption and phosphorescence energies with the corresponding calculated data. Absorption maxima were calculated as the difference between the S_1 (for the $S_0 \rightarrow S_1$ transition) or S_2 (for the $S_0 \rightarrow S_2$ transition) energy and the S_0 energy at *trans*-NMTAA and *cis*-NMTAA. The resulting values are summarized in Table 2.4.

It can be seen that the π-π* absorption and the absorption red-shifts observed when passing from the trans to the cis form are well reproduced. On the other hand, there is a large discrepancy between the calculated and the observed n→π* absorption maximum, possibly because we did not consider solvent effects in our computation. Indeed, S_0, S_1 and S_2 have calculated dipole moments of 4.9 D, 2.7 D and 5.3 D respectively. Thus a polar solvent is expected to induce a similar stabilization in S_0 and S_2 (since these states have roughly the same dipole moment). On the other hand, the stabilization effect on S_1 is expected to be smaller, due to the lower dipole moment of this state. Previous works [239] showed that a quite sophisticated treatment of the solvent bulk is needed to predict n→π* excitation energies in good agreement with the experimental data.

We also tried to reproduce the phosphorescence maximum recorded in a methanol:ethanol low-temperature glass [216]. For this purpose, the phosphorescence maximum was calculated as the energy difference between T_1 (for the $T_1 \rightarrow S_0$ transition) or T_2 (for the $T_2 \rightarrow S_0$ transition) and S_0 at different structures as reported in Table 2.5.

The calculated energy differences between T_1 and S_0 at the optimized geometry of the various energy minima on T_1 are not consistent with the experimental value.

---

[10] For example, the energy difference between the T_2 and T_1 states at the T_2/T_1 ISCs is in the range 1.7 - 4.8 kcal mol^{-1}. See Table 5S in Supporting Information Section.

	Experimental			Calculated			
	n-π*	π-π*	*f*	n-π*	*f*	π-π*	*f*
absorption trans	305 (94)	255 (112)	$2.5{\cdot}10^{-1}$	366 (78)	$1.43{\cdot}10^{-2}$	257 (111)	$3.06{\cdot}10^{-1}$
absorption cis		268 (107)		374 (76)	$0.92{\cdot}10^{-2}$	267 (107)	$3.26{\cdot}10^{-1}$
fluorescence [a]						796 (36)	

[a] vertical energy difference between S_2 and S_0 energy values of **Min S$_2$**

Table 2.4: Comparison of experimental and CASPT2//CASSCF calculated absorption wavelengths and CASSCF oscillator strengths. The calculated $S_2 \rightarrow S_0$ fluorescence maximum is also reported. Data are in nm, while kcal mol^{-1} values are given in brackets.

However, since the experiment was carried out in the constrained environment of a cold glass, one can assume that the molecule had sufficient space only to relax along the stretching coordinates (e.g. it could not relax along pyramidalization coordinates), and that radiative decay was the only way for the molecule to go back to S_0. This view is supported by the fact that the calculated T_1-S_0 energy difference at the **Min T$_1$ Planar Trans** and **Min T$_1$ Planar Cis** are in good agreement with the value of λ_{max} for the observed phosphorescence.

We also investigated the possible origins of the visible transient absorption signals (Figure 2.22c). The S_1/S_2 transition being energetically out of the recorded range, we calculated the singlet forth root of each S_1 minimum and the triplet third and forth roots of each T_1 minimum. (Results are reported in Table 7S in the Supporting Information Section.) As for the n-π* excitations the computed $S_1 \rightarrow S_3$ or $T_1 \rightarrow T_3$ absorption will be shifted by a polar solvent due to the higher dipole moment of S_3 and T_3 (both π-π* states) with respect to S_1 and T_1. With the rough assumption that the energy shift would be similar to the one reported for n-π* excitations, one can estimate the absorption wavelengths of the S_1 and T_1 minima (see Table 7S in the Supporting Information Section). Remarkably these values are in the range of those reported in Figure 2.22c; in particular, at least one minimum per Path (**Min S$_1$ A3**, **Min S$_1$ B1**, **Min T$_1$ A1**, **Min T$_1$ B2**) shows an absorption wavelength in the 500 nm region, along with a not negligible calculated oscillator strength. Unfortunately this analysis cannot distinguish between S_1 or T_1 absorptions.

2.4.6 Discussion

Excited state vibrational bands do not appear in our transient infrared spectra of photoexcited NMTAA and well-defined bands are only observed at, or very near, the spectral positions of the room-temperature absorption bands of *cis*- and *trans*-NMTAA. Thus, the IR experiment provides information about the return of the photoexcited population to the two isomeric ground state minima. Two distinct timescales of approximately 8 and 250 ps are observed for both the formation of *cis*-NMTAA and the recovery of *trans*-NMTAA. On both timescales, the same branching ratio between the two isomers is found, with a cis yield of approximately 30-40%. The UV-visible measurements yield complementary information on the dynamics in the electronically excited states, revealing that the 250 ps time-constant represents the lifetime of an electronically excited state with an absorption band near 500 nm. These findings in combination with the computational results of Section 2.4.5 provide a detailed picture of the mechanism underlying the photoisomerization of *trans*-NMTAA.

Fast Relaxation Dynamics

The IR experiment shows that 50% of the exited molecules relax to the ground state of either *cis*- or *trans*-NMTAA within a few picoseconds after excitation. This implies, that isomerization and electronic relaxation from the initially excited π-π* state must take place on a faster timescale. Although our computations reveal that a S_2/S_1 conical intersection is located relatively high in energy with respect to **Min S$_2$**, suggesting a too long S_2 lifetime, the analysis of the S_2 relaxation path indicates that fast radiationless decay may still occur since:

i) The S_2 and S_1 surfaces become nearly degenerate well before the conical intersection. In fact already at a point located only 2.8 kcal mol^{-1} above **Min S$_2$** there is an energy gap of only 5.6 kcal mol^{-1} (see Figure 2.25). Thus one may assume that the non-adiabatic transition

Experimental value [216]	Calculated	Structure	Transition
485 (59)	757-945 (38-30)[a]	**Min $\mathbf{T_1}$ A1 – B3**	$T_1 \rightarrow S_0$
	605-727 (47-39)[a]	**Min $\mathbf{T_1}$ A1 – B3**	$T_2 \rightarrow S_0$
	426-448 (67-64)[a]	**Min $\mathbf{T_1}$ A1 – B3**	$T_1 \rightarrow S_0$ non-vertical[b]
	470 (61)	**Min $\mathbf{T_1}$ Planar Trans**	$T_1 \rightarrow S_0$
	462 (62)	**Min $\mathbf{T_1}$ Planar Cis**	$T_1 \rightarrow S_0$

[a] Data represent the range of the phosphorescence maximum calculated for the various minima on T_1 energy surface.
[b] These values were calculated comparing T_1 energies of the **Min $\mathbf{T_1}$ A1 – B3** minima with the S_0 energy of ***trans*-NMTAA**.

Table 2.5: CASPT2//CASSCF calculated maxima of phosphorescence for different molecular geometries, and experimental value observed in a methanol:ethanol low-temperature glass. Data are in nm, while kcal mol^{-1} values are given in brackets.

from one surface to the other starts to occur before the intersection.

ii) Both position and relative energy of **CI $\mathbf{S_2/S_1}$** are expected to be sensitive to the solvent environment, which can affect (e.g. lower or remove) the energy barrier controlling the decay. This effect is consistent with the solvent dependence of the S_1 absorption maximum discussed above and can be roughly estimated in terms of the difference between the experimental (in solution) and the calculated (*in vacuo*) n-π* excitation energies (see Table 2.4). As shown in Figure 2.25, the crossing point moves close to the S_2 minimum when the resulting energy of $\approx$ 15 kcal mol^{-1} is added to the S_1 curve (dashed line). Another considerable solvent effect has been documented in NMA, the carbonyl analogue on NMTAA, [240] where the calculated C-O and C-N bond distances for π-π* differ significantly between vacuum and solution: Indeed, *in vacuo* the C-O bond of NMA lengthens more than the C-N one, consistent with what we found for C-S versus C-N in NMTAA (see above). On the other hand, in solution the C-N bond expansion is greater than that of the C-O bond, as also indicated by Resonance Raman data [241]. This has been attributed mainly to a more elongated C-O bond in the electronic ground state due to hydrogen bonding. While the relative C-N and C-S contributions to the initial relaxation path appear to change from the gas-phase to solution and may be different in amides and thioamides, such effects clearly deserve further research efforts to be fully understood.

Notice that the prediction that initial relaxation on S_2 is dominated by C-N and C-S bond expansion (and not by torsional deformations) is consistent with the resonance Raman spectra recorded on NMA, where torsional modes are not enhanced [219]. It is also consistent with our observation that the quantum efficiency of isomerization does not depend on the irradiation wavelength (259 or 280 nm), which indicates that the initial excess energy plays no role in the trans-cis photoisomerization.

According to the above discussion the photoreaction must be determined by events occurring at lower energy. In fact, trans→cis isomerization motion is predicted to occur predominantly on the S_1 (and/or T_1) potential energy surface, where the molecule can sample all torsional angles without having to overcome significant energy barriers (see Figure 2.26). This can also explain the observation of trans-cis isomerization upon direct excitation of the S_1 state at 308 nm (n-π^* transition). From S_1 (or T_1) fast relaxation to the ground state is possible via four CIs (ISCs), that predetermine the final conformation adopted by the molecule. Indeed, if we make the rough assumption that the four different S_1/S_0 CIs have the same probability of being accessed, we can estimate a quantum yield for the trans→cis process close to 25%. This is remarkably close to the measured quantum efficiency of 30-40%. We stress that the same conclusions are drawn if one considers decay from T_1 via the four T_1/S_0 intersystem crossing points documented above. Thus the involvement of a “triplet” pathway cannot be excluded (see below).
The solvent is expected to have a similar effect on all four S1/S0 CIs (and the four T1/S0 ISCs), since the calculated dipole moments remain more or less at the value of *trans*-NMTAA along the isomerization path. This im-

plies that the energy barrier between minima and intersection points should be higher in water than calculated *in vacuo*, while there is no evidence that one decay route may become preferred.

Slow Relaxation Dynamics

Half of the photoexcited molecules follow an ultrafast relaxation pathway back to the ground state. An approximately equal fraction of NMTAA relaxes much more slowly with a time constant of 250 ps. The observation of excited state absorption with the same lifetime clearly shows that this slow dynamics is due to population trapping in an electronically excited state, which subsequently relaxes non-radiatively. However, just like in the fast process the ratio of cis and trans yield is approximately 1:2, which indicates a similar relaxation pathway on both time scales. Our computational results offer two different explanations:

i) Branching and population trapping occur on the S_2 surface, in which case the 250 ps time constant may be proportional to the time required to surmount the barrier between **Min S_2** and **CI S_2/S_1** (or a decay region close to it). Subsequent relaxation and isomerization would then be identical for temporarily trapped molecules and for the molecules that reach the $S_2 \rightarrow S_1$ decay point directly (e.g. impulsively).

In this case, however, fluorescence (predicted at a wavelength of 800 nm, see Table 2.4) should be observable from S_2, even in the presence of non-radiative relaxation with a rate of $(250 \text{ ps})^{-1}$. In agreement with earlier work [242, 217], we were not able to detect any fluorescence from NMTAA in the 300-850 nm region, which, given the sensitivity of our setup, excludes trapping in a state with an oscillator strength $\geqslant 5 \cdot 10^{-2}$ for the transition to S_0, or implies a much smaller energy difference (i.e. emission at $\lambda \geqslant 850$ nm) between excited state minimum and the ground state. Note, however, that no stimulated emission could be detected in a spectral window up to 1000 nm. Furthermore, the 1 ps risetime in the transient signal at 483 nm and the corresponding fast decay at higher energies is rather untypical for spectral dynamics due to vibrational cooling (in the S_2 state), for which one would expect a blue-shift of the excited state absorption. The 1 ps dynamics is therefore more likely due to electronic relaxation, suggesting that population trapping occurs after relaxation from S_2 to S_1.

ii) Population trapping occurs on S_1 or T_1. This implies that an initial vibrationally hot S_1 population, produced by $S_2 \rightarrow S_1$ decay, either immediately decays to S_0 (giving rise to the fast time-constant) or undergoes internal vibrational energy re-distribution and get temporarily trapped in the S_1 or T_1 excited state.

According to this scenario, competition between immediate electronic relaxation and cooling in the excited state would be at the origin of the two reaction regimes. An alternative scenario involves that branching of the S_1 population that either decays directly to S_0 via the S_1/S_0 intersections, or to T_2 via the T_2/S_1 crossings. The T_2 population would then decay to S_0 via the T_2/T_1 and T_1/S_0 crossings in a somehow slower process. Indeed, the observation of blue-green phosphorescence from NMTAA in a low-temperature glass by Tasumi et al. [216] could be an indication for the involvement of a triplet pathway. Notice that, as documented in Figures 2.26 and 2.27 respectively, there is the same number of $S_1 \rightarrow T_2$ and $S_1 \rightarrow S_0$ decay channels and that they have similar energies. It is therefore not unlikely that the S_1 population evenly decays to S_0 and T_2, which could explain why approximately one half of the molecules decay via the fast and the other half via the slow channel. In addition, very similar *cis*-NMTAA quantum yields are predicted for these two channels, since the possible relaxation pathways of the molecule upon reaching the S_0 ground state via a S_1/S_0 conical intersection or via the corresponding T_1/S_0 intersystem crossing are almost identical.

Photoequilibrium and Back Reaction

Although we could not follow the back-reaction from *cis*- to *trans*-NMTAA with time-resolved spectroscopy, we can deduce from the low cis concentrations at photo equilibrium that cis→trans isomerization must be much more efficient than the trans→cis process. The most reliable ratio of cis→trans over trans→cis isomerization efficiency was determined for 256 nm irradiation, where cis→trans isomerization is 2.3-3.1 times more likely. At the lower error limit of these measurements the sum of both quantum efficiencies may add up to unity. If confirmed by complementary measurements, this could indicate that isomerization proceeds in both directions via a common intermediate state, which then determines the outcome of the photoreaction. This is consistent with a scenario, where the same "region" of the S_1 or T_1 states are populated from either the trans or cis conformers.

In other words, in agreement with the proposed mechanism, the decay channels would always correspond to the same set of crossings.

2.4.7 Conclusion

Time resolved infrared experiments and *ab initio* CASPT2//CASSCF reaction path computations for π-$\pi*$ excitation of *trans*-NMTAA yield consistent mechanistic information on the trans→cis isomerization of NMTAA, which is summarized in Figure 2.28. The initial S_2 population (schematically represented by a gaussian wave packet) evolves on S_2 mainly via C-S bond expansion (and out-of-plane deformation) leading to efficient $S_2 \rightarrow S_1$ decay in the region of the S_2/S_1 conical intersection.

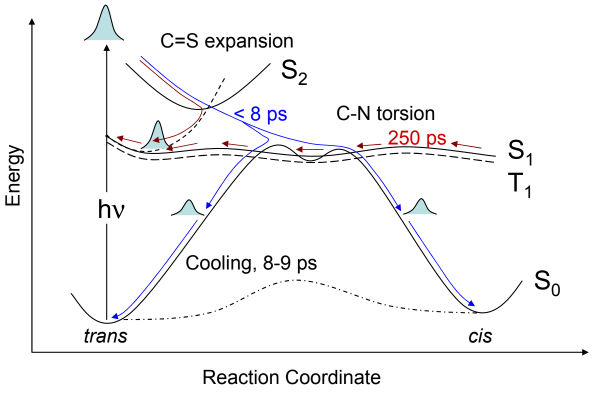

Figure 2.28: Schematic representation of the photoisomerization reaction of *trans*-NMTAA. The multiple intersections between the S_1, T_1 and the S_0 energy profiles represent the CIs and ISCs documented in Figure 2.26. See text for details.

Relaxation on S_1 delivers the system to a very flat region of the potential energy surface, characterized by multiple conformers and multiple S_1/S_0 conical intersections located a few kcal mol^{-1} above them. Decay to the ground state may then occur *directly* (blue arrows) via the S_1/S_0 CIs or *indirectly* (orange arrows). Approximately half of the excited molecules seem to follow the direct relaxation pathway, and return to the electronic ground state with a time constant of less than 7 ps. The second half of the excited molecules become temporarily trapped in an electronically excited state and reach the electronic ground state with a much longer time constant of $\approx$ 250 ps. This population trapping can either be the result of competition between vibrational energy relaxation on S_1 and $S_1 \rightarrow S_0$ electronic decay, or competition between fast $S_1 \rightarrow S_0$ decay and a somehow slower relaxation process via the triplet states. On both the fast and the slow timescale, *cis*-NMTAA is formed with a quantum efficiency of 30-40%. We have demonstrated that the final ground state conformation of NMTAA is predetermined by the molecular geometries of the S_1/S_0 CIs and T_1/S_0 ISCs and is therefore independent of the followed route, provided nearly full sampling of the torsional coordinate in S_1 and/or T_1 is possible prior to decay.

The replacement of one oxygen atom by sulfur in the backbone of a peptide is probably the least “invasive” way to render it photoswitchable. Our study indicates a thio-photoswitch is photostable and potentially capable of inducing conformational change with a high quantum yield on a sub-nanosecond timescale. This timescale is much faster than the time-resolution needed to investigate, for example, the formation of secondary structure elements in proteins. However, notice that, due to the flatness of the S_1 and T_1 isomerization paths, it is likely that a fully relaxed peptide conformation will not be perturbed by the photoexcitation of a NMTAA unit. In other words, the S_1 or T_1 force field of NMTAA may not be able to efficiently force a peptide chain out of its equilibrium conformation. On the other hand, if the peptide is exerting a certain amount of torsional strain on the NMTAA unit which is contrasted by the thioamide C-N partial double bond, then promotion to the flat S_1 or T_1 energy surfaces can act as an “unlocking event” (compare the S_0 energy profile with the S_1 and T_1 energy profiles in Figure 2.26), and allow for trans to cis isomerization. In this case NMTAA may be seen as a photoreleasable lock.

Acknowledgement

We are indebted to Prof. D. Seebach at the ETH in Zürich, who drew our attention to the potential of using thioamides in the investigation of peptide dynamics. Many thanks go to Simon Jurt and Nadja Walch from the NMR service team of the University of Zürich for their quick and competent help. Partial funding has been provided by the Università degli Studi di Siena (Progetto di Ateneo 02/04) and HFSP (RG 0229/2000-M). We also wish to thank CINECA for granting calculation time.

Supporting Information Available:

CASSCF/6-31G* absolute, CASPT2/6-31G* absolute and relative energies along with wave function reference weights and cartesian coordinates of all structures discussed in the text. Calculated and estimated absorption wavelength of the minima along S_1 and T_1 Path A and B. This material is available free of charge via the internet at http://pubs.acs.org.

Chapter 3

Conclusion and Outlook

Part I of this dissertation introduces and applies a new combination of powerful tools for the study of fast conformational dynamics of polypeptides. Ultrafast built-in photoswitches are used to trigger and control peptide dynamics and secondary structure formation. This method provides a valuable complement to traditional triggering approaches such as temperature jump or rapid mixing. The phototrigger is ultrafast and allows to prepare a starting ensemble far from equilibrium. In this way ‘non-thermal’ ensembles become accessible that could not be prepared by thermodynamic means such as temperature control or denaturant concentration. The newly developed setup of two electronically synchronized femtosecond laser systems allows to scan all relevant timescales from one picosecond onwards to the microsecond range. Therefore the complete relaxation can be followed without being limited by the time resolution. Broadband femtosecond IR detection allows to track various observables simultaneously, such as the amid-I band of the peptide backbone, sidechain bands or site directed isotope labels. Application of this new methodology to two model systems—the photoswitchable α-helix FK11X and the thioredoxin reductase active site fragment cycAMPB—revealed unexpectedly rich dynamics that would be hidden in experiments using only a single observable and low time resolution.

The cyclic peptide cycAMPB is strongly driven by the photoswitch during the first phase of the dynamics, the main part of structural change occurring within 20 ps. However, the dynamics continues to longer than 16 ns. As pointed out in the introduction, one would expect nearly single exponential kinetics, if the peptide reached its equilibrium conformation directly on a smooth funnel like energy landscape. In contrast, the transition we observe is surprisingly complex, as illustrated by the transient absorption in the rising edge of the absorption band (Figure 3.1a). We observe a repeated change of the sign of the slope, leading to an oscillatory pattern on a logarithmic time scale. Such *logarithmic oscillations* are characteristic for relaxation processes on a rugged energy landscape [95].

In the helix forming FK11X peptide the main spectral change indicating α-helix folding occurs on time scales comparable to those observed by T-jumping a cold denatured peptide [48] (270 ns to 2500 ns depending on temperature). This confirms that the photoswitch can be designed to yield largely unperturbed folding dynamics. For the first time we observe stretched exponential kinetics ($k \propto e^{-(t/\tau)^{\beta}}$, $\beta < 1$) for secondary structure formation which becomes increasingly stretched with lower temperature as predicted for relaxation on a rugged energy landscape. Due to the high time resolution, the deviation from the exponential slope can be reliably detected, in contrast to previous experiments, where overlap with the instrument response introduced a large degree of uncertainty.

While the signal of the unlabeled amide I’ band gives rise to a smooth stretched exponential, the signal of the isotope labeled sites in FK11X shows a similar behavior as the signal of the cyclic peptide, displaying *logarithmic oscillations* (Figure 3.1b). Obviously isotope labeling bypasses the averaging of the signal into a broad amide I’ band and reveals the underlying complexity of local events during the folding process. Again, like in the cyclic peptide, the oscillations span the whole time range investigated. It seems very likely, that isotope labeling at different sites will reveal a similar response. Thus the smooth amide I’ dynamics is only the result of averaging

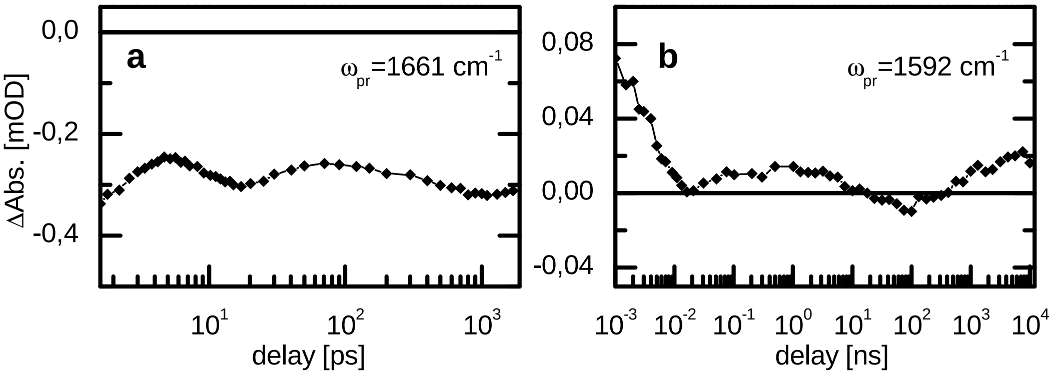

Figure 3.1: (a) Transient absorption change in the rising edge of the absorption band of cycAMPB. (b) Transient absorption change at the frequency of the isotope labels in FK11X.

over many spectroscopic observables that hides the underlying complexity. Extended isotope labeling studies recording the response for each residue should be carried out to obtain a detailed view of the processes hidden behind the concerted amide I' response.

The finding of strong Arrhenius-like thermal activation with $\log k(T) \propto -1/T$ for helix folding, as already observed by others, is usually interpreted in terms of a high free energy barrier on the order of about 10 $k_B T$. It is known from chemical kinetics that such a high barrier would lead to strictly exponential kinetics, so the observation of strong thermal activation seems to be in conflict with our observation of complex kinetics suggesting relaxation on a rugged energy landscape. However, it has been shown by Zwanzig [82] and by Bryngelson and Wolynes [83], that activated diffusion on a rugged energy landscape leads to a strong $\log k(T) \propto -1/T^2$ temperature dependence without having to introduce a high barrier. Within the small temperature window covered by our and most other experiments on helix kinetics, those two situations are virtually indistinguishable on an Arrhenius plot. However, activated diffusion on a rugged energy landscape is more consistent with our observations of nonexponentiality, kinetic heterogeneity and strong temperature dependence of the stretching parameter β.

The high time resolution allows us to zoom in on the time range faster than 10 ns, that was hidden in previous experiments in the so called 'instantaneous component' or 'burst phase'. It has been argued previously along the lines of the kinetic zipper model, that this unresolved phase observed in most helix T-jump experiments results from the fast redistribution of helix lengths after the perturbation of the equilibrium. However, in previous experiments only transients at a few single wavelengths have been discussed. In the present work, multichannel detection allows to record time resolved spectra. Those spectra do not show helix signatures on this fast time scale. Furthermore, the amplitude of the signal in our photoswitch experiments in the relevant time range is much smaller than in T-jump experiments. We therefore conclude that the instantaneous phase in T-jump experiments largely results from changes in solvation of the monitored chromophore due to the temperature change.

The kinetics of the α-helix experiment was analyzed in some detail in a separate paper to investigate how strict conclusions can be drawn about the shape of the energy landscape. Kinetics of a zipper model, a golf-course landscape and of a funnel shaped landscape as discussed in the introduction have been compared with the experimental results. The role of the experimental observables has been discussed in detail. For strong perturbations in the folding direction, such as the perturbation that is generated by the photoswitch, the zipper model was found to predict compressed exponential relaxation. This is in contradiction with our experimental observation of stretched relaxation, ruling out the zipper model for the description of the kinetics. Instead it was shown that the experimental results for the photoswitchable α-helix can be very well modelled by a 1D rugged energy landscape model with a small entropic barrier.

The zipper model is very well established for the description of α-helix thermodynamics, however, this does not a priory mean, that it also will give a good description of the kinetics. As mentioned in the introduction, it is always possible to make a 1D projection on a selected reaction coordinate (for example the number of native hydrogen bonds) that gets the equilibrium properties right. The number of native contacts used in the zipper model is a spectroscopic reaction coordinate, since the measured signal in an IR experiment (as well as in a CD experiment) is assumed to be proportional to that coordinate. Hence, as long as one is discussing the thermodynamics of α-helix folding in a stationary experiment, the number of native contacts is a natural choice for a reaction coordinate. However, other coordinates might be rate limiting in a kinetic experiment. In contrast to what is predicted by the zipper model, we found significant thermal activation which we interpret in terms of diffusion on a rugged energy landscape. This is in agreement with an number of MD simulations that suggest the existence of enthalpic barriers due to non-native contacts that have to be overcome in the folding process, adding to the ruggedness of the energy landscape. The breaking of non-native contacts thus might play an important role for the kinetics. This would not mean that the free energy surface of the zipper model is wrong, it just means that it is not a very expressive choice of a reaction coordinate when describing the *kinetics* of α-helix folding.

In summary, the Papers **P1**, **P6**, **P13** and **P16** of this dissertation show the existence of a continuum of time-scales and overlapping processes in peptide dynamics from a picosecond to microseconds, questioning a separation of time scales and the existence of a clear dynamical hierarchy. Multiple spectroscopic probes recorded simultaneously by multi channel detection yield different dynamics at different spectral positions. If folding was a two state process, all spectroscopic probes should yield the same single exponential kinetics, which is clearly not the case. While the experiments detected the kinetic complexity of the conformational transitions, more detailed studies employing isotope labeling and possibly transient 2D-IR spectroscopy are needed to attempt an interpretation on the structure level.

The switching approach was found to be a valuable complement of other initialization techniques, not only because of time resolution. It furthermore offers interesting possibilities to control the starting ensemble of the relaxation and to generate strong perturbations. As shown in Paper **P16**, going beyond the small perturbation regime is essential for a more rigid testing of folding models. The switching approach allows for increased freedom in the selection of experimental conditions. In other techniques, temperature, pH, pressure, or denaturant concentration have to be tuned to a range where jumps in the conditions lead to appropriate changes in the equilibrium between folded and unfolded states. The photoswitch approach works in a wider range of conditions. Also, photoswitching avoids artifacts due to the direct effects of the environment on the probed spectroscopic transition, that can be induced by other triggers—such as the shift of vibrational bands induced by the temperature change in a T-jump experiment. Research on other switches will extend our toolbox for selection of the suitable switch for a particular task. The thioxylated peptide unit investigated in Paper **P9** shows great promise, as we found a high quantum yield of 30-40% for *trans→cis* isomerization and a high photostability. While excitation of the $\pi-\pi^*$ transition at 280 nm leads to a biphasic isomerization with time constants of 8 ps and 250 ps, preliminary results indicate that excitation of the $n-\pi^*$ transition leads to monophasic isomerization with 250 ps.

In future experiments it will be very exciting to further explore the possibility to tailor the action of the photoswitch on the backbone. This offers the opportunity to drive the system to certain locations on the modified energy landscape and launch the folding there. An α-helical peptide, where the photoswitch bridges only four residues has already been synthesized by Woolley and coworkers [105]. In this peptide, switching preforms one helical turn. Generating a helical turn in no time by photoswitching provides the opportunity of further testing the idea of helix nucleation as a rate limiting step: In the framework of the zipper model this would mean a jump right onto the free energy barrier, which should lead to a significant speed up of the subsequent folding kinetics and the observation of downhill folding.

Another interesting target is the investigation of β-hairpin formation. As cold-denaturation for a hairpin has not been demonstrated, only hairpin unfolding has been investigated by T-jump experiments so far. A photoswitchable β-hairpin has been synthesized recently by Aemissegger *et al.* [243], that will allow to observe β-hairpin formation. In such a system, the combination with transient 2D-IR spectroscopy, described in Part II, will be particularly rewarding, as this technique in combination with isotope labeling is sensitive to contact formation on the peptide unit level.

Part II

Principles and Applications of Two-Dimensional and Transient Two-Dimensional IR Spectroscopy

Chapter 4

Introduction

Many important properties of quantum systems cannot be inferred from linear spectroscopy but have to be investigated by nonlinear techniques. Such properties include the coupling and connectivity of energy levels, the cross relaxation between levels, as well as dephasing that can be caused by various mechanisms. In NMR spectroscopy multidimensional nonlinear techniques have been extremely successful in the study of such properties [244]. The possibility to transfer the concepts of multidimensional NMR spectroscopy to IR spectroscopy has already been envisioned by Aue, Bartholdi and Ernst in the first publication on two-dimensional NMR in 1976, entitled '*Two dimensional spectroscopy. Application to nuclear magnetic resonance.*' [1]: "2D spectroscopy fascinates by its conceptual simplicity and its general applicability. It seems to open one further dimension to the spectroscopist. (...) Applications are conceivable in electron spin resonance, nuclear quadrupole resonance, in microwave rotational spectroscopy, and *possibly in laser infrared spectroscopy.*" However, the first two-dimensional IR spectrum was published only in 1998 by Hamm, Lim and Hochstrasser [2].

The terms mentioned above, *coupling and connectivity of energy levels*, *cross relaxation* and *dephasing*, refer to the quantum system under investigation. In NMR spectroscopy this quantum system is formed by the spins of the atomic nuclei, in IR spectroscopy by the molecular vibrations. However, in many cases the main interest does not lie in the quantum system itself. Instead, the focus is on the investigation of *molecular structure and dynamics* that is reflected by the properties of the quantum system. The quantum states serve as probes of molecular properties and their changes. Two-dimensional (or more generally: multidimensional) IR spectroscopy probes the energy of vibrational eigenstates, their population, couplings between vibrations and the orientation and magnitude of vibrational transition dipole moments. Furthermore, correlations between these observables and the change of their correlation in time can be inferred. In this way multipulse experiments also can peer behind the ensemble average: using for example frequency selective pulses one can pick those molecules out of an inhomogeneous ensemble that oscillate with certain frequencies at certain times when the pulses arrive. The recent literature shows, that the observables of 2D-IR spectroscopy allow us to deduce extremely valuable information about molecular structure and dynamics. Up to know, however, 2D-IR spectroscopy has been applied only to systems in equilibrium. An extension of 2D-IR to the investigation of transient molecular species in the nonequilibrium regime seems very promising due to the high time resolution of this method. This is the main objective of Part II of this dissertation, introducing the technique of transient 2D-IR spectroscopy (T2D-IR). Another topic touched on is the extension of 2D-IR structure investigation to larger molecules.

Section 4.1 of the present chapter gives an introduction to 2D-IR spectroscopy at an illustrative level, explaining the basic concept and information content of 2D-IR spectra. Important 2D-IR applications are reviewed. Sections 4.2 and 4.3 present an outline of the work in the context of this dissertation, that is described in detail in the publications reproduced in Chapter 5. The problem of extending 2D-IR structure determination to larger molecules is pointed out in Section 4.2. Theoretical as well as experimental improvements of 2D-IR structure investigation are suggested. Transient 2D-IR is introduced in Section 4.3. An overview of different T2D-IR pulse sequences and their information content is given. The publications are outlined that discuss the application of the different T2D-IR experiments to a metal carbonyl model system. Finally, the combination of the developments of Part I and II is reported—the application of T2D-IR to the conformational transition of a photoswitchable peptide.

4.1 Some Basic Concepts of 2D-IR Spectroscopy

This section gives an illustrative overview of the basic information available from a 2D-IR spectrum. To introduce the basic concepts it is instructive to start with the *double resonance* or *dynamic holeburning* implementation of 2D-IR spectroscopy[1].

The setup. A scheme of the experimental setup is shown in Figure 4.1. Broadband infrared pulses from a femtosecond source are split into a pump pulse and a probe pulse. The pump pulse is send through a computer controlled Fabry-Perot filter producing a spectrally narrow pulse with a preselected frequency. Both pump and probe pulse are reunited at the sample. Their relative timing can be adjusted by varying the delay line in the path of the pump pulse. The probe pulse still has the full spectral bandwidth and is used to measure the spectrum of the sample as it changes after the arrival of the pump pulse. To this end, the probe pulse is dispersed in a spectrometer and imaged onto a detector array. The frequency axis of the spectrometer gives one axis (probe axis) of the 2D-IR spectrum. The second axis (pump axis) is given by the frequency of the narrow band pump pulse, defined by the Fabry-Perot filter, that is scanned over the frequency range of interest. In other words: for each frequency of the narrowband pump pulse, as adjusted by the Fabry-Perot filter, a pump-probe spectrum is recorded. The set of pump-probe spectra is arranged in a 2D plot. For the details of the setup see the technical appendix.

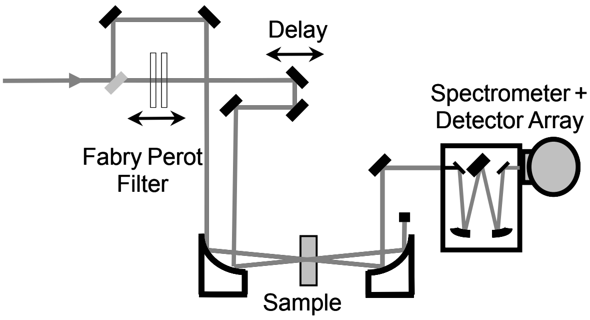

Figure 4.1: Schematic 2D-IR setup. See text for description.

2D-IR diagonal peaks. To illustrate the basic features of a spectrum recorded in this way, Figure 4.2 shows schematic 2D-IR spectra of a hypothetical molecule with two oscillators. To make the example more concrete one could imagine the oscillators being two CO oscillators of a small peptide (Figure 4.2c) as it will be discussed in Paper **P3**. In Figure 4.2a the situation of two uncoupled oscillators is depicted. For each peak in the absorption spectrum the 2D-IR spectrum shows a feature on the diagonal consisting of a negative and a positive part. This can be rationalized considering the level scheme of an anharmonic oscillator (Figure 4.2a): If the pump pulse is resonant, it prepares the oscillator in the first excited state. This gives rise to a *bleach* at the $0 \rightarrow 1$ frequency, meaning that more probe light is transmitted at this frequency. Furthermore, *stimulated emission* from $|1\rangle$ to $|0\rangle$ takes place when then probe pulse arrives, also adding light at the $0 \rightarrow 1$ frequency. Bleach and stimulated emission both contribute to the negative part on the diagonal[2]. *Excited state absorption* from $|1\rangle$ to $|2\rangle$ leads to a decrease of probe light at the $1 \rightarrow 2$ frequency, which is red shifted compared to $0 \rightarrow 1$ in the anharmonic oscillator. This gives

---

[1] For a comparison of the double resonance and the pulsed fourier transform implementation see Paper **P12**

[2] Negative and positive sign in a pump probe or 2D spectrum are subject to convention. The rationale for choosing a negative sign for the bleach was to illustrate depletion of a state by the pump pulse.

rise to the positive part of the signal. In case of an harmonic oscillator positive and negative part would cancel exactly and the signal would vanish. The 2D-IR spectrum thus provides a sensitive measure of the anharmonicity.

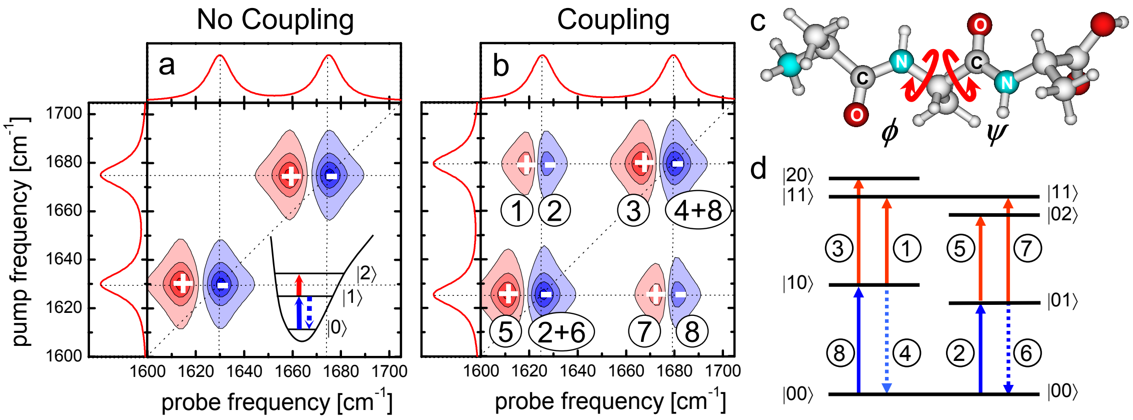

Figure 4.2: Schematic 2D-IR spectra and level scheme of a hypothetic tripeptide. See text for description.

2D-IR cross peaks and anisotropy. If we switch on coupling between the oscillators, *cross peaks* appear in the 2D-IR spectrum (Figure 4.2b). This can be rationalized using the level scheme of two coupled anharmonic oscillators (Figure 4.2d). The diagonal peaks arise in a similar manner as before: e.g. the oscillator at lower frequency makes a diagonal contribution due to bleach (Arrow 2), stimulated emission (6) and excited state absorption (5). If the oscillators are coupled, the frequency of one oscillator depends on the state of the other. Thus, the transition (7) from $|01\rangle$ to $|11\rangle$ is now at a different frequency than the transition (8) from $|00\rangle$ to $|10\rangle$. Those two transitions give rise to the lower right cross peak. In the case of uncoupled oscillators they cancel exactly which is why no cross peak is observed. Thus, the cross peaks can be used to measure the coupling between oscillators. For a comprehensive theoretical treatment describing the generation of the 2D-IR signal in terms of a quantum system of oscillators interacting with a classical light field see Paper **P12** of this dissertation.

In case we have a model of how the measured coupling depends on molecular structure we can use 2D-IR for structure determination. Another source of structure information in the 2D-IR spectrum besides coupling is the dependence of the signal on the polarization of the pump and probe pulse. This so called *anisotropy* of the cross peaks allows to determine the angle between the transition dipole moments that are involved in generating the cross peak. Both pieces of information together have been used to measure the backbone dihedral angles ϕ and ψ of the small peptide trialanine shown in Figure 4.2c [3, 4].

Dynamic 2D-IR lineshape. An important source of information in a 2D-IR spectrum is the 2D lineshape and its time dependence. From a band observed in an absorption spectrum one cannot judge if its shape results from a homogeneous broad transition or an inhomogeneous distribution of narrower lines. Such an inhomogeneous distribution can arise for example from molecules existing in different solvent environments or in different conformational substates. Information on the inhomogeneity and its time dependence is readily obtained from a 2D-IR spectrum. Figure 4.3 shows 2D-IR spectra of the amide I band of N-methylacetamide in D_2O recorded at different pump probe delay times. At early times, the 2D lineshape is tilted towards the diagonal. Thus the frequency of the 2D signal depends on the pump frequency on the y-axis. This observation implies that a distribution of absorption frequencies exists and the narrow band pump pulse selectively excites a specific subensemble (‘*holeburning*’). As the delay between pump pulse and probe pulse is increased, the lineshape becomes more and more upright. The memory of the initial excitation frequency is lost. The system samples the accessible frequency range during this time as illustrated in Figure 4.3e—a process sometimes termed spectral diffusion. In this way, 2D-IR spectroscopy provides a measure of the frequency fluctuations and their timescale. Information on the processes that are responsible for the frequency modulation can be inferred—in the case of NMA in D_2O it is the motion of the surrounding solvent molecules interacting with the solute [245]. In extreme cases, the existence of substates does

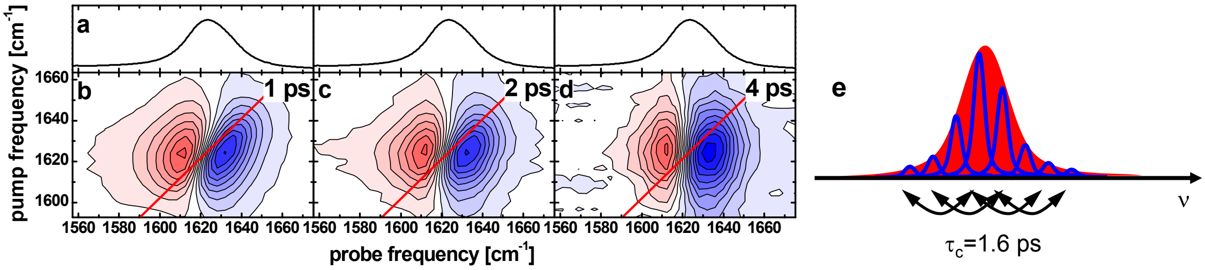

Figure 4.3: (a) IR absorption spectrum of the amide I band of N-methylacetamide in D_2O. (b-d) 2D-IR spectra at various pump-probe delay times (adapted from Reference [247]). (e) Lineshape analysis shows that different molecules sample the accessible frequency range within 4 ps (correlation time τ_c=1.6 ps).

not just broaden a band but leads to a splitting into several bands. One can then see the molecules labeled by the pump pulse not just diffusing within one band but hopping from one band to an other, provided the lifetime of the vibration is long enough. This has been demonstrated for the amide I vibration of NMA in methanol, where hydrogen bonded and non-bonded species show up as two peaks in the absorption spectrum [246]. In this system the hopping time is the hydrogen bond lifetime.

Cross-relaxation. Another useful effect is the cross relaxation between coupled vibrations. It is induced by motional processes that modulate the coupling. The population transfer leads to intensity changes, which in NMR are known as nuclear Overhauser effect (NOE) [244]. The cross relaxation rate depends on the spectral density of the modulation of the coupling induced by the motional process at the difference frequency of the two coupled states. As the typical splittings between the observed states in 2D-IR spectra are on the order of 10-100 cm^{-1}, this method is sensitive to motions on a 0.1-1 ps timescale. The population transfer can be measured by observing the cross peaks grow relative to the diagonal peaks. This method has been used to obtain the timescale of the conformational fluctuations of peptide backbone dihedral angles of the small peptide trialanine (Figure 4.2c) around their equilibrium position [74].

The above examples illustrate basic features and effects showing up in 2D-IR spectra. The next subsection reviews a number of important 2D-IR experiments mostly based on similar effects, where 2D-IR was able to provide new insight on molecular processes.

4.1.1 Important 2D-IR Applications

Structure determination of small molecules with a time resolution of $\approx$ 1 ps has been demonstrated [3, 248]. The high time resolution, at least 9 orders of magnitude faster than the typical NMR timescale, allows to ‘freeze in’ all conformational dynamics. Rapidly interconverting substates of the equilibrium ensemble, such as different conformations of a molecule, that would be averaged by slower methods, can be resolved [247]. 2D-IR spectroscopy of the amide I band has been used to determine the backbone conformation of small blocked dipeptides and tripeptides [3, 249, 4, 250, 251, 252, 247, 253]. But 2D-IR structure determination is not limited to peptides. As an ingredient it only requires molecular vibrations that show a structure-dependent coupling, which can be modelled reasonably well. For example, a coupling model for the carbonyl ligands of a metal carbonyl has been derived, that permitted to deduce the relative angles of the ligands from 2D-IR data [254]. In larger peptides and proteins a detailed structure determination in terms of all dihedral backbone angles is not feasible due to strong overlap of the amide I absorptions. However, the presence of certain structure elements like α-helices, β-sheets and turns has been shown to generate characteristic 2D band shapes in 2D-IR spectra [255, 256]. Melting curves of ribonuclease A have been recorded by 2D-IR spectroscopy, monitoring characteristic cross peaks that arise from the interstrand coupling in the antiparallel β-sheets of this protein [255]. Two-color 2D-IR, reminiscent of heteronuclear NMR, allows to correlate bands in separate wavelength regions, such as for example the amide I (mostly CO stretch, $\sim$1650 cm^{-1}) and amide A (mostly NH stretch, $\sim$3200 cm^{-1}) band. Additional information on molecular structure might be obtained from such two-color experiments [257, 258].

Apart from the advances in structure determination, a variety of **fast equilibrium processes in solution** has been studied by 2D-IR. Conformational fluctuations of the peptide backbone on a picosecond and subpicosecond time scale have been measured [74, 259, 252]. The rate of cross relaxation between coupled amide I oscillators has been used to infer the time scale of backbone fluctuations that are even faster ($\sim$100 fs) than the $\sim$ 1 ps time resolution of the actual measurement [74, 252] (A similar approach is used to infer faster time scales from NMR NOESY experiments [260]). Furthermore, the structural fluctuations of various simpler amides have been investigated, such as *N*-methylacetamide (NMA) [261], acetylproline-NH_2 [250] and formamide [262]. The dynamics of hydrogen bonds have been explored in some detail. Infrared 2D exchange spectroscopy has been used to determine a 10-15 ps hydrogen bond lifetime of NMA-methanol complexes [263]. A very detailed picture of hydrogen bond dynamics of methanol oligomers in CCl_4 has been created [264, 265, 266, 267]. Making and breaking of hydrogen bonds leads to interconversion of hydrogen bond donors, acceptors and doubly hydrogen bonded methanol species, thereby modulating the OH stretching frequency. This interconversion is revealed by spectral diffusion effects in the 2D-IR spectrum as illustrated in the previous section in Figure 4.3e [267]. The dynamics of the hydrogen bond network of water has been investigated by 2D-IR along the same lines [268]. But also the cross peaks provide additional information on spectral diffusion: it has been pointed out that correlated or anticorrelated fluctuations of two coupled vibrations lead to cross peaks of different orientation [269, 270, 271, 272]. This allows valuable conclusions on the process responsible for the frequency fluctuations, e. g. how they affect different parts of the probed species.

2D-IR spectroscopy has also been used to study various **vibrational coupling effects** in molecules and molecular crystals. The splitting of bands, that is often observed in vibrational absorption spectra, can have a variety of causes, such as Fermi resonances, the existence of conformational substates or coupling of a vibration to lattice phonons that can cause vibrational self trapping. It has been demonstrated that 2D-IR spectroscopy can discriminate between these mechanisms, and thus allows a much more detailed and reliable interpretation of IR absorption spectra [273]. In particular, the level structure of the amide I band of polypeptides has been investigated in some detail. The delocalization length of amide I vibrations in small globular proteins has been estimated to be about 8 Å [2]. Couplings between peptide units at different positions in the amino acid sequence (i,i+1, i,i+2, i,i+3) have been measured for various isotopomers of a 25 residue α-helix [274]. Such measurements allow to critically assess the accuracy of amide I coupling models that found widespread application to interpret the amide I bands of peptides and proteins in the context of secondary structure estimation by IR absorption spectroscopy (see Section 1.2.2 in Part I).

There are **various other interesting applications** of 2D-IR, and only a few can be mentioned here: Asbury *et al.* made use of its coupling sensitivity to aid *peak assignment* [275]: The appearance of a cross peak between vibrations shows that they belong to the same molecule[3]. This fact can be used to disentangle spectra of mixtures of solutes. Khalil *et al.* observed *coherence transfer* between vibrations [276]. Coherence transfer might allow for the design of pulse sequences that simplify congested 2D spectra in a similar manner as in NMR [244]. *Intermolecular couplings* can be explored, as demonstrated by Volkov and Hamm [277]. They observed cross peaks between a dipeptide with a hydrophobic anchor and a phospholipid membrane in which the peptide was embedded. Information on the localization of the dipeptide in the membrane has been obtained. Zanni *et al.* investigated the coupling between the hydrogen bonded DNA bases [278]. The same group explored *two-quantum coherences* which allows for a more accurate measurement of diagonal and off-diagonal anharmonicities from which vibrational coupling is deduced [279]. While the experiments discussed above are 3rd order experiments, additional information can be obtained from *higher order experiments* that allow for further simplification of congested spectra as described theoretically by Scheurer and Mukamel [280, 281].

The **objective of the present dissertation** is the extension of 2D-IR with all its virtues to the non-equilibrium regime. To this end the technique of transient 2D-IR spectroscopy (T2D-IR) is introduced. Another topic is the

---

[3] This holds only if the molecules are not in too close contact. The formation of aggregates thus has to be of course excluded.

extension of the 2D-IR structure determination approach to larger molecules. The following sections present an outline of the papers reproduced in Chapter 5 of **Part II** that report on progress in these directions.

4.2 Extension to Larger Structures

A crucial issue regarding the prospects of the 2D-IR structure determination approach as a tool for molecules of chemical and biological interest is its scalability to larger molecules. In this dissertation, the extension to peptides with a larger number of peptide units is discussed. So far, the 2D-IR approach has been successfully demonstrated only for the smallest possible unit of two amide I oscillators [3, 4, 282]. Attempts to determine the structure of larger peptides have failed [283, 284]. In a peptide with n amino acids, the number of backbone degrees of freedom ϕ and ψ (see Figure 4.2c) is on the order of $O(2n)$. If the peptide was not too large—like the cyclic RGB pentapeptide in Figure 4.4a—significant coupling between all amino acids could be observed, leading to cross peaks between all peptide units as shown in the calculated 2D-IR spectrum in Figure 4.4b. The number of cross peaks and therefore the number of structure relevant spectral observables would be on the order of $O(2n^2)$. Even if the peptide was larger and cross peaks could not be observed between all peptide units, the number of observables should still grow more rapidly than the number of backbone degrees of freedom. Thus the problem of inverting the spectrum to a structure should be very well defined. Unfortunately, a more realistic simulation of the 2D-IR spectrum of the pentapeptide is given by Figure 4.4c, where realistic homogenous and inhomogeneous broadening is taken into account. Here, most of the information is blurred due to significant spectral overlap, rendering the inversion problem ill-defined. In the first two papers of Part II we approach the question of how to make best use of the potential structure information content of 2D-IR spectra, both from the experimental and the theoretical side.

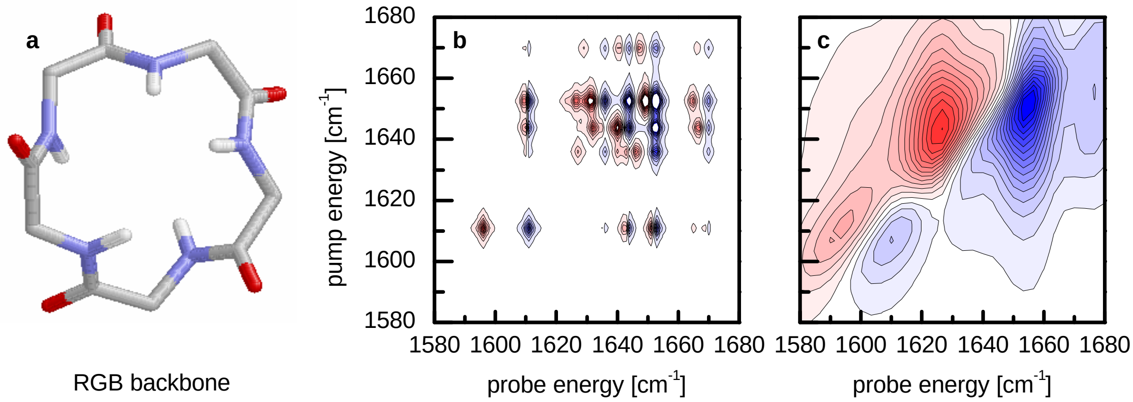

Figure 4.4: (a) Peptide backbone of the RGB model peptide investigated in Paper **P3**. (b) 2D-IR spectrum calculated with unrealistically small homogeneous and inhomogeneous broadening (single ^{13}C label). (c) 2D-IR spectrum of the same sample calculated with realistic broadening parameters.

4.2.1 Current 2D-IR Approaches and their Information Content

In Paper **P12** the two commonly used experimental 2D-IR approaches—the time domain approach (heterodyne-detected photon echo) and the frequency domain approach (double resonance spectroscopy)—are introduced. Their information content is compared, both experimentally and theoretically, with a focus on structure relevant information. The metal carbonyl model system $[Rh(CO)_2acac]$ (acac=acetylacetone) is used to demonstrate and explain various features in the 2D-IR spectra obtained by the two approaches. In the case of NMR, pulsed Fourier transform methods became much more widespread than frequency domain methods soon after their introduction, partly due to greater sensitivity because of their multiplex advantage, but also due to their greater experimental versatility. However, it is important to keep in mind that modern NMR spectroscopy works in the limit of strong fields ($\pi/2$ and π-pulses in most cases), while IR experiments work in the weak field limit. Hence in NMR—in contrast to 2D-IR spectroscopy—a simple Fourier relation between time-domain and frequency domain experiments does not exist in general. In case of 2D-IR the connections between the two domains are much closer, as explored in Paper **P12**, thus the experience gained in NMR cannot be simply transferred to 2D-IR.

The comparison shows that a disadvantage of the double resonance approach versus the pulsed Fourier transform approach is its worse spectral resolution along the pump axis. As detailed in Paper **P12** this is due to the convolution of the system's response with the IR-pump pulse in the double resonance technique. The information loss due to band overlap thus should be less critical in the pulsed FT approach. Also the theoretically achievable sensitivity of the pulsed FT experiment is higher, because the intensity of the local oscillator can be adjusted independent of the other beams, while in the double resonance approach the probe pulse simultaneously acts as a local oscillator. However, it remains to be shown that the greater complexity of the pulsed FT setup does not preclude the experimental realization of higher sensitivity.

4.2.2 Scalability of 2D-IR Structure Determination

Paper **P3** assesses the question how far we can go in the size of the structure to be determined. The computational study discusses the effects of homogeneous and inhomogeneous broadening in 2D-IR spectra and the resulting loss of structure information due to band overlap, illustrated in Fig. 4.4. To this end we start from an arbitrary target structure generated by the computer, calculate its 2D-IR spectrum using a *realistic* but not necessarily *very accurate* model, and subsequently try to reconstruct the original target structure using no other information but the calculated 2D-IR spectra of the target structure. This approach allows to investigate the structure resolution power of 2D-IR spectroscopy unaffected by all kinds of experimental uncertaincies: Firstly, the target structure, i.e. the expected outcome, is known exactly. Secondly, the models used to calculate the 2D-IR spectra during the optimization procedure can be chosen to be the same as for the calculation of the spectra of the reference structure. Hence, by construct there is no uncertainty about the accuracy of those models.

Furthermore, we investigate the potential gain in information content provided by different isotope labeling strategies, employing single ^{13}C labeling, double ^{13}C labeling, as well as mixed $^{13}C^{16}O$-$^{12}C^{18}O$ and $^{13}C^{16}O$-$^{13}C^{18}O$ labeling. The robustness of 2D-IR structure determination is assessed by employing different amide I coupling models for the calculation of the spectra of the reference structure and the calculation of the spectra of the trial structures, respectively. This mismatch is intended to mimic the mismatch between a coupling model and the coupling in the real molecule. A novel structure determination algorithm is implemented: Instead of a free optimization of all spectroscopic parameters (coupling strengths, transition dipole orientation etc.), the optimization towards the target structure is carried out in conformation space, taking into account some of the structural restraints imposed by the peptide structure. This approach greatly reduces the search space and allows more complicated problems to be tackled. It is inspired by the strategy of structure determination in NMR where a penalty function that combines experimental constrains with an MD forcefield is minimized.

The case study in Paper **P3** has been performed on the cyclic penta-peptide shown in Figure 4.4a. Cyclic penta-peptides containing the Arg-Gly-Asp-sequence (commonly termed RGD-peptides) play an important role as templates in drug design, since this sequence is a universal cell-recognition site of various extracellular proteins that interact with integrin cell-surface receptors. Despite extensive x-ray and NMR structure analysis studies over more than two decades [285, 286, 287], a controversy about the 3D structures of cyclic penta-peptides is still continuing [288, 289]. This model system has been selected, because 2D-IR is expected to reveal additional insight compared to the NMR investigations.

4.3 Extension to Transient 2D-IR Spectroscopy

In all the experiments published so far, 2D-IR is applied to an equilibrium ensemble. The main objective of Part II of this dissertation is the extension of 2D-IR with all its possibilities to the non-equilibrium regime. Here, in the investigation of transient species, the high time resolution of 2D-IR can be put to full use. To this end, the technique of Transient 2D-IR (T2D-IR) is introduced, where an additional UV pulse generates a non-equilibrium ensemble on which a 2D-IR experiment is carried out. In this way we can record time series of 2D-IR spectra of transient species by varying the delay between the UV pulse and the 2D-IR part of the experiment (see pulse sequence in Figure 4.5a).

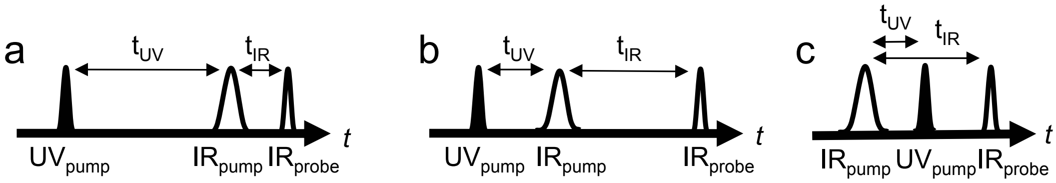

Figure 4.5: T2D-IR pulse sequences: (a) Regular T2D-IR experiment. A UV pulse generates a non-equilibrium situation. Its relaxation is monitored by 2D-IR experiments at variable delays. (b) Holeburning T2D-IR. (c) Labeling T2D-IR.

The T2D-IR experiment is a 5^{th} order experiment with two field interactions from the UV pulse and three interactions from the IR pulses. Compared to 2D-IR, we have two additional important experimental degrees of freedom to control, which are the *polarization* and the *delay* of the UV pulse relative to the IR pulses, including the possibility of changing the order of the pulses (Figure 4.5). In pulse sequence (a), termed *Regular T2D-IR*, the UV pulse arrives first and prepares the nonequilibrium ensemble. The two IR pulses constituting the 2D-IR part of the experiment arrive only after a longer delay, while the delay between them is kept short, so that relaxation of the nonequilibrium ensemble during the IR delay can be neglected. Only in this limit one can think of the T2D-IR experiment as taking a 2D-IR ‘snapshot’ of the relaxing nonequilibrium ensemble. This is typically well fulfilled for UV delays on the order of tens of picoseconds or longer, when a typical IR delay of 1 ps is used. The system then can be considered as being in quasi-equilibrium during the 2D-IR part of the experiment and normal 3^{rd} order theory can be used for modelling. Exploring the 5^{th} order characteristics of T2D-IR leads to new types of information that can not be anticipated when thinking in the 2D-IR snapshot limit. Pulse sequence (b), termed *Holeburning T2D-IR*, makes explicit use of the 5^{th} order character. In this experiment, the UV delay is comparably short and the IR delay is varied. In contrast to the snapshot limit, the nonequilibrium state prepared by the UV pulse is allowed to undergo considerable relaxation during the 2D-IR part. Information on spectral diffusion in a nonequilibrium band during relaxation is obtained. As discussed below, the holeburning T2D-IR experiment provides extended information on the solvation dynamics that cannot be obtained from 3^{rd} order spectroscopy. In pulse sequence (c), termed *Labeling T2D-IR*, the UV pulse arrives between the IR pulses. Thus, while the IR-pump pulse acts on the electronic ground state, the IR-probe pulse acts on the sample after the UV excitation. In this way sequence (c) allows to correlate vibrations before and after a UV induced process by generating cross peaks between ‘educt’ and ‘product’ vibrations. The experiment could be viewed as an IR version of NMR exchange spectroscopy under nonequilibrium conditions [290]. The *polarization dependence of T2D-IR* converges to that of a normal 2D-IR experiment only if the delay between UV and IR pulses is long compared to rotational diffusion times. For shorter delays, the additional polarization degree of freedom introduced by the UV pulse enhances the possibilities of signal manipulation and the structure information content of T2D-IR compared to 2D-IR. In summary, T2D-IR is does not only provide the information known from 2D-IR spectroscopy now for transient species, but also new types of information that also will be discussed in the following sections.

A multitude of light-induced non-equilibrium processes is conceivable that offer a wide field of applications for T2D-IR. Photoreactions, electronically excited states, photoisomerizations—all kinds of phototriggered molecular processes are possible targets[4]. As a first example in the present work we investigate *electronic excitation* or, more precisely, the metal-to-ligand charge-transfer (MLCT) of the metal carbonyl [Re(CO)$_3$(dmbpy)Cl] (Figure 4.6a). While [Re(CO)$_3$(dmbpy)Cl] exhibits interesting photophysics and has a variety of potential applications (see Paper **P10**), it is furthermore an ideal system to explore the possibilities of T2D-IR due to its straightforward and cheap synthesis and its spectroscopic properties (long lifetimes of electronic and vibrational states, large vibrational transition dipole moments, well separated bands, a well defined 3D structure and a large change of dipole moment upon electronic excitation leading to pronounced solvation dynamics). This system is studied in Papers **P5**, **P7**, **P10**, **P14** and **P15**. The second example is the investigation of the non-equilibrium conformational dynamics of one of the *photoswitchable peptides* introduced in Part I (see Figure 4.6b). This application is described in Paper **P4**. The conformational transition of the petide is triggered by a UV laser pulse via photoisomerization of a photochromic azobenzene moiety integrated into the peptide backbone. Paper **P4**, the last paper of Part II, thus unites the two main themes of this dissertation—T2D-IR spectroscopy and peptide dynamics.

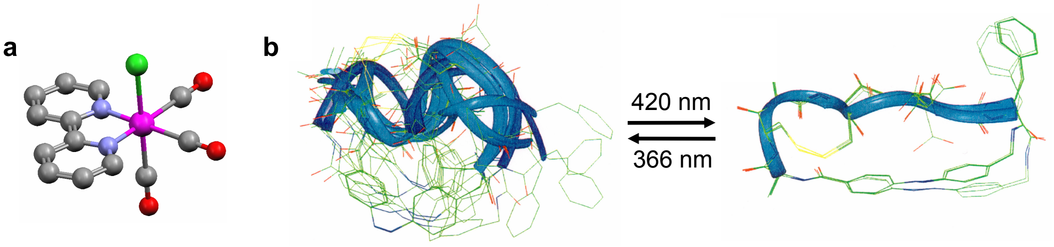

Figure 4.6: Systems studied by T2D-IR. (a) [Re(CO)$_3$(dmbpy)Cl]. (b) Photoswitchable cyclic peptide cycAMPB.

4.3.1 Polarization Dependence and Basic T2D-IR Experiments

To interpret the outcome of a spectroscopic experiment correctly, one has to take care about its polarization dependence. In fact, only by making use of the polarization dependence the maximum of information available from spectroscopic experiments can be obtained [291, 292, 293, 294]. Understanding the polarization dependence is in particular required for the determination of structure parameters from 2D-IR spectra. Paper **P10** investigates the polarization dependence of T2D-IR spectroscopy. Furthermore, all basic features of the T2D-IR spectra are explained in great detail.

In pump-probe spectroscopies, such as a normal 2D-IR experiment, only two laser pulses, having one relative polarization degree of freedom, interact with up to two transition dipole moments enclosing one relative angle (Figure 4.7a). In the T2D-IR experiment three pulses with two relative polarization degrees of freedom interact with up to three transition dipole moments whose relative orientation has to be described by three angles (Figure 4.7b). Thus the polarization dependence is more involved then in 2D-IR, however, it also allows for more versatile signal manipulation and offers more geometry information, as shown in Paper **P10**. A general expression for the polarization dependence of the T2D-IR signal is derived and its dependence on rotational diffusion is analyzed. Useful polarization conditions and magic angle like signals for all pulse sequences in Figure 4.5 are obtained. The theoretical considerations are demonstrated experimentally for MLCT in the metal carbonyl model system [Re(CO)$_3$(dmbpy)Cl]. The metal carbonyl complex features a UV transition dipole moment as well as three IR transition dipole moments of the carbonyl vibrations that are approximately perpendicular to each other, providing a rich testfield for various polarization conditions.

---

[4] Also applications are conceivable, where the trigger pulse interacts with the surrounding of the molecule under investigation. This category comprises such processes as laser induced T-jump, pH-jump employing photoacids, or the use of photolabile caged compounds, as used in time resolved studies of protein dynamics.

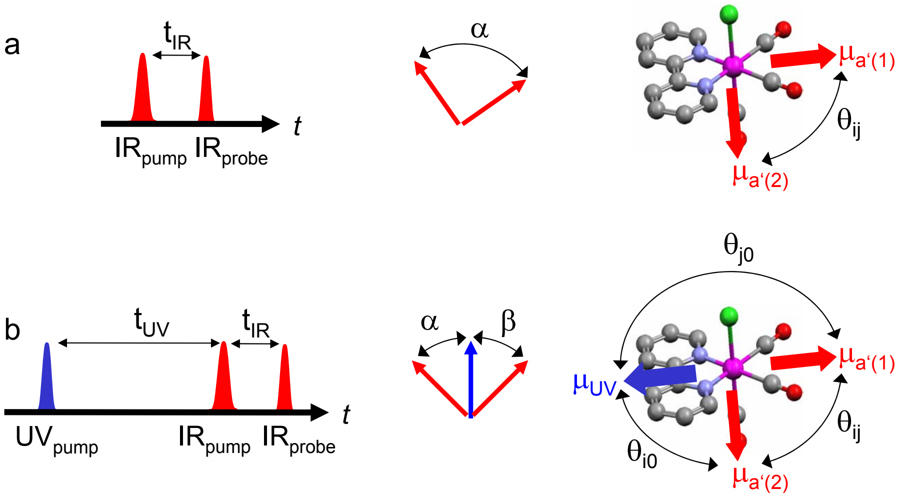

Figure 4.7: (a) The double resonance 2D-IR experiment consists of two pulses with a relative polarization α. They interact with up to two vibrational transition dipole moments enclosing an angle θ_{ij}. This is shown here for the a'(1) and the a'(2) vibration of [Re(CO)$_3$(dmbpy)Cl]. (b) The T2D-IR experiment consists of three pulses with two relative polarizations α and β. The additional UV pulse interacts with the UV transition dipole moment. To fully describe the transition dipole geometry, three angles are required.

4.3.2 Holeburning T2D-IR

The initial idea driving the development of T2D-IR was to observe structural changes in the course of the conformational transition of photoswitchable peptides: By initiating a photoreaction, the UV pulse prepares the peptide system in a non-equilibrium state. The subsequent relaxation is monitored by 2D-IR 'snapshots' in the hope to obtain structure information for the different time points. Collecting 2D-IR 'snapshots' requires the delay between the IR pulses to be short on the time scale of relaxation of the non-equilibrium situation. The system then can be considered as being in quasi-equilibrium during the 2D part and the experiment can be described as a regular 3rd order 2D-IR experiment. For many phototriggered processes, like solvation of an excited electronic state, photodissociation or isomerization of small molecules, the relaxation of the nonequilibrium situation initially prepared by the UV pulse occurs on a similar time scale or even faster than vibrational relaxation. A sufficiently long vibrational lifetime allows to carry out a true 5th order experiment, where the system undergoes considerable changes during the 2D-IR part. This experiment, shown in Figure 4.5b, can be understood in terms of dynamic holeburning spectroscopy on a non-equilibrium ensemble: After a time t_{UV}, the narrowband IR-pump pulse burns a hole into the evolving non-equilibrium spectrum. The IR-probe pulse monitors the evolution of this two-dimensional spectral hole at various delays t_{IR} during the ongoing relaxation—in contrast to the normal 2D-IR experiment, where the hole evolves in an equilibrium ensemble.

The application of T2D-IR holeburning and its information content are discussed in Paper **P14** for a solvation experiment using our model system [Re(CO)$_3$Cl(dmbpy)] as a solute in the solvent DMSO. In this solvation experiment we are not so much interested in [Re(CO)$_3$Cl(dmbpy)] itself but in the dynamics of the solvent molecules around it. Electronic excitation of the complex induces a charge transfer and thus creates a changed charge distribution within the molecule. The solvent around the complex now finds itself in a nonequilibrium situation and has to adjust to the changed charge distribution. It is well established that 3rd order spectroscopies like 2D-IR spectroscopy or vibrational photon-echoes are sensitive to the coupling between a vibrational transition, e. g. a CO mode of our carbonyl, and the surrounding solvent. They allow us to map out the spectral density of the low frequency motions of the solvent that contribute to solvation. From such 3rd order techniques it is known that in most solute-solvent systems the two-point frequency fluctuation correlation function (FFCF) of the vibration sensing the solvent motions decays on at least two time scales: (i) an ultrafast inertial component on a 100 fs time scale, and

(ii) a slower diffusive component. The reason for this general behavior of the two-point FFCF is not clear, however it shows that at least two generalized solvation modes are needed to describe the process. To learn more about the modes that give rise to the spectral density of the solvent it would be highly desirable to have an experiment at hand that is non-linear with respect to the solvent modes and thus sensitive to their coupling. 5th order Raman spectroscopy, proposed in a theoretical work by Tanimura and Mukamel [295], could in principle collect such information. However, the experimental realization turned out to be very difficult due to strong cascading 3rd order artifacts and the low Raman cross sections. Up to now, the experiment has been only demonstrated for CS_2 which has an exceptionally high Raman cross section [296, 297, 298]. As discussed in Paper **P14**, similar information can be obtained from the holeburning T2D-IR experiment. Simulations demonstrate that holeburning T2D-IR is very sensitive to higher order FFCFs in contrast to linear spectroscopy and 3rd order techniques. Correlation between a fast and a slow solvation mode shows up as a ridge in the three-point FFCF as depicted in Figure 4.8a (model 1 without correlation) and 4.8b (model 2 with correlation). Holeburning T2D-IR can sense this coupling between solvation modes and thus distinguish between the two situations in Fig 4.8a and b that are indistinguishable for a 3rd order experiment. In other words, T2D-IR allows to peer behind the spectral density of solvation modes in a similar way as 2D-IR allows to peer behind an absorption lineshape. Coupling between the fast and slow solvent motions is found to be essential to explain the T2D-IR spectra of $[Re(CO)_3Cl(dmbpy)]$ in DMSO.

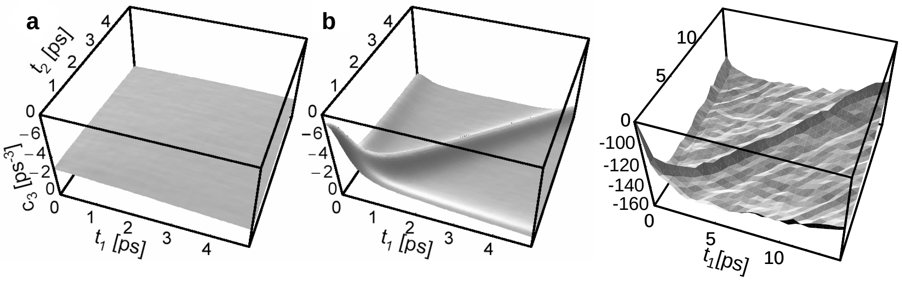

Figure 4.8: Three-point FFCFs of solvation models **1** and **2** from paper **P14** with (a) uncorrelated and (b) correlated fast and slow relaxation components. (c) Three-point FFCF of one amide I mode of trialanine obtained from an MD simulation.

From an MD simulation all orders of FFCFs are in principle available. From 3rd order experiments usually only the two-point FFCF is extracted and compared with MD, throwing away a significant part of the information available from the simulation. The T2D-IR experiment provides information on higher order FFCFs for a more complete characterization of the solvation process and a more detailed comparison with MD simulations. An example for a three-point FFCF from an MD simulation is shown in Figure 4.8c. This three-point FFCF of an amide I mode of trialanine was calculated from a 20 ps MD trajectory in water[5]. In this simulation, frequency fluctuations are due to conformational changes of the peptide backbone. Note the ridge that indicates correlation between fast and slow processes, similar as found experimentally in Paper **P14** for $[Re(CO)_3Cl(dmbpy)]$ in DMSO. The model used to calculate the instantaneous vibrational frequencies along the trialanine MD trajectory only considers effects due to conformational changes of the molecule itself. The coupled fast and slow component found in the simulation thus are directly related to those motions. The solvent only acts indirectly by driving these internal motions[6].

---

[5] The trajectory was kindly provided by Gerhard Stock.

[6] A more realistic frequency model would have to consider electrostatic effects of the solvent and hydrogen bonding.

4.3.3 Labeling T2D-IR

From an absorption difference spectrum that contains bands of reactant and product of a photoreaction, one cannot conclude which reactant bands are related to which product bands. Only in exceptionally simple cases this question can be resolved by time resolved IR absorption spectroscopy. In most cases, following the shifts of the vibrations during the reaction by time resolved absorption spectroscopy is prevented by the rapid time scale of the shifts, partial overlap of the bands and the fact that bands may shift over each other in the 1D spectrum. The situation is typically even more complicated due to the thermal broadening of the vibrational bands that is usually observed up to picoseconds after photoexcitation. Thus, in many cases it is not possible to conclude from a time series of 1D spectra which bands shift where upon a photoreaction[7]. An example is given by figure 4.9 showing the transient absorption spectra of our model system $[Re(CO)_3Cl(dmbpy)]$ after photoinduced MLCT. From the transient spectra it is not obvious which of the ground state bands shifted where in the MLCT state, as indicated by the red and green arrows. This is the type of information provided by *labeling T2D-IR*.

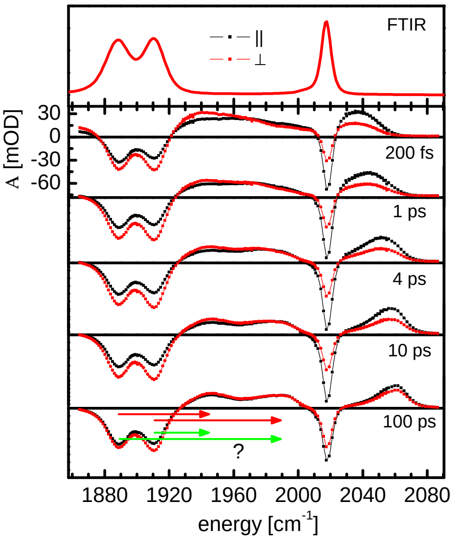

Figure 4.9: Transient 1D spectra of $[Re(CO)_3Cl(dmbpy)]$. The spectra do not allow to relate the excited state bands (positive) to the ground state bands (negative) by following them throughout the transition.

In a *regular T2D-IR* spectrum recorded with pulse sequence (c) in Fig. 4.10, the peaks shift along the diagonal upon UV excitation (scheme in Fig. 4.10a). No new information can be obtained about the shift and the new order of the bands compared to the 1D experiment depicted in the upper panel of Fig. 4.10a. However, such information is easily obtained using the *labeling T2D-IR* pulse sequence (Fig. 4.10d) introduced in Paper **P5**: this pulse sequence correlates vibrations of a molecule before and after a photoreaction by generating *cross peaks* between the reactant vibrations and the product vibrations into which they are transformed (Fig. 4.10b). In this respect the labeling pulse sequence could be regarded an infrared version of 2D NMR exchange spectroscopy (2D EXSY) under non-equilibrium conditions [290]. As compared to the regular T2D-IR pulse sequence (Fig. 4.10c), the order of the pulses is changed in the labeling sequence, so that the IR-pump pulse arrives before the UV-pump pulse (Fig. 4.10d). The spectrally narrow IR-pump pulse is tuned into resonance with the various vibrational modes and labels them by transferring population from the vibrational ground state to the first excited state. Subsequently, the UV-pump pulse triggers some kind of photoreaction that induces a shift of the vibrations. The IR-probe pulse then detects the vibrations that previously have been excited by the IR-pump pulse.

---

[7] The question of *which bands shifts where* is of course only meaningful when the character of a vibration does not change substantially, as it would e. g. by breaking a bond that is strongly involved in the vibration.

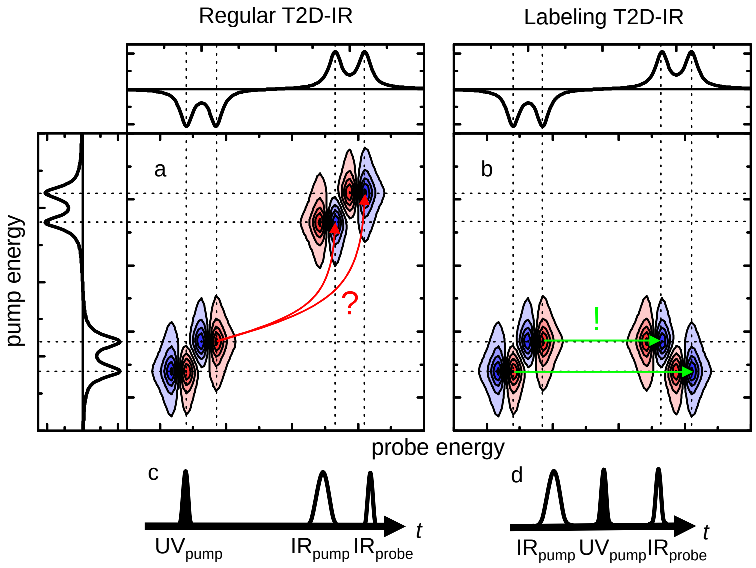

Figure 4.10: Scheme of: (a,c) Regular T2D-IR spectrum and pulse sequence. (b,d) Labeling T2D-IR spectrum and pulse sequence. While the regular T2D-IR spectrum does not allow to relate bands of reactant and product, reactant and product vibrations are correlated by the labeling T2D-IR experiment.

In Paper **P5** in the next Chapter we demonstrate the possibilities of the labeling technique for the example of MLCT in [Re(CO)$_3$Cl(dmbpy)] shown in Figure 4.9. We show that the order of the vibrational energy levels in [Re(CO)$_3$Cl(dmbpy)] is not preserved when exciting the molecule and the shift occurs according to the green arrows in figure 4.9 and not according to the red arrows as it was commonly assumed in literature [299].

In the present case of [Re(CO)$_3$Cl(dmbpy)], the observed CO modes are spectator modes - they merely change their character upon photoexcitation. The labeling experiment projects the initially excited reactant mode onto the newly generated product modes. In case of a stronger remixing of the modes, the IR excitation of a reactant mode will be distributed to several product modes. This could be used as a measure of the remixing and help to understand the change of the character of the modes.

An interesting future application will be the investigation of CO loaded myoglobin and its mutants. The difference spectrum of the myoglobin mutant in figure 4.11 features two different protein conformations resulting in two distinct CO frequencies for the bound states of CO. Photodissociation of CO leads to various product states as can be seen in the IR difference spectrum. In those states, the CO sits in different binding pockets in the myoglobin structure. Labeling T2D-IR spectroscopy will allow to follow the CO upon photodissociation and thus to map out the connectivity between the bound states and the various product states.

4.3.4 T2D-IR of a Photoswitchable Peptide

Part I of this dissertation introduced methods to investigate the nonequilibrium dynamics of polypeptides on time scales from one picosecond to microseconds by time resolved IR absorption spectroscopy. Part II so far reported on the development of 2D-IR and T2D-IR spectroscopy, also touching the aspect of structure determination. The last paper of Part II, Paper **P4**, represents a unification of the two main themes of this dissertation—non-equilibrium dynamics of polypeptides and T2D-IR spectroscopy: It reports on the application of T2D-IR on a photoswitchable peptide. The long-term objective of this combination is to measure a series of T2D-IR snapshots during a conformational transition and deduce the time dependent change of the backbones dihedral angles. Important prerequisites for approaching the task of determining transient structure parameters in photoswitchable peptides have been established in the other papers of this dissertation: The required T2D-IR setup has been constructed (see

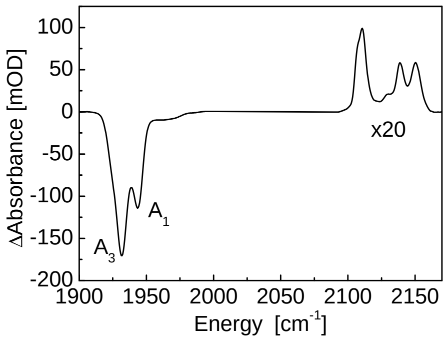

Figure 4.11: Difference spectrum of CO bands in the V68Y myoglobin mutant upon photodissociation of the CO from the heme group [300]. The protein features two conformations (A_1 and A_3) responsible for two distinct CO absorbptions for the bound states (negative contributions in the difference spectrum) and various photoproduct bands (positive contributions) indicating the migration of CO to different binding pockets. From this difference spectrum it does not become clear, which reactant band relates to which product bands. (Spectrum kindly provided by Karin Nienhaus.)

Paper **P10** and **P11** and the technical appendix). A suitable flow cell for photoswitchable peptides has been developed (Paper **P2**). The measurement of transient cross peaks required for the determination of transient structures has been demonstrated for our Rhenium carbonyl model compound (see Papers **P7** and **P10**). The polarization dependence of transient cross peaks is well understood (see Paper **P10**). Coupling models for the amide I band with sufficient accuracy have been described and advanced ways to determine the structure from 2D-IR spectra have been suggested (Paper **P3**). The techniques for triggering conformational changes of peptides on an ultrafast time scale have been established (Papers **P1**, **P6**, **P9**, **P13** and **P16**).

The first peptide investigated by T2D-IR is the cyclic photoswitchable peptide cycAMPB (see Figure 4.6b for the structure), as several milligrams of this sample were kindly provided by Luis Moroder. cycAMPB has been investigated by time resolved IR spectroscopy in Paper **P1** of Chapter 2. The peptide contains 9 peptide units and is not isotope labeled in the present version. Thus the amide I band contains contributions from 9 oscillators that overlap significantly. Already from the equilibrium 2D-IR spectrum it is obvious that this band overlap will preclude structure determination from the transient spectra. Thus for now the analysis is focused on the 2D line shape of the amide I band. As mentioned previously, 2D-IR spectroscopy allows to separate homogeneous and inhomogeneous contributions to the line shape. The homogeneous line width is related to the conformational fluctuations of the backbone on a fast (<1 ps) time scale [249, 247, 301]. Therefore, T2D-IR should be sensitive to the local properties of the potential energy surface during relaxation. Indeed we find that the fast fluctuations are more pronounced, when the peptide is far from equilibrium. With ongoing relaxation the fluctuations decrease. We tentatively attribute this observation to the increasing conformational restriction of the peptide as it approaches the minimum of the energy landscape—its equilibrium conformation. Simulations of cycAMPB that will allow to test this hypothesis on the origin of the change in the homogeneous line width during the transition are currently under way in the group of Gerhard Stock.

Paper **P4** demonstrates the feasibility of T2D-IR spectroscopy of photoswitchable peptides. In the present investigation of cycAMPB strong band overlap precludes structure determination from the T2D-IR spectra. In future, isotope labeling can provide a way out of this dilemma as shown in Paper **P3**. A next step in the investigation of cycAMPB thus could be the labeling of two peptide units, one by ^{13}C and one by ^{13}C ^{18}O, to obtain a subsystem of two coupled oscillators that can be investigated in presence of the remaining unlabeled amid I band. In this fashion, time dependent structure information can be obtained for pairs of peptide units. In the investigation of more complicated molecules the cross peak emerging from the coupling between two oscillators could be used to just report on their spatial proximity without attempting a detailed structure analysis. Such experiments could provide information about contact formation in a similar fashion as time resolved FRET or triplet-triplet energy transfer [64] but with the advantage of 1 ps time resolution and without the need of introducing bulky chromophors that might alter structure and dynamics.

4.4 Outline of the Publications

Following publications are reproduced in the next chapter:

Paper **P12** gives an introduction to 2D-IR spectroscopy. The time domain approach (heterodyne-detected photon echo) and the frequency domain approach (double resonance spectroscopy) to 2D-IR are introduced and compared, both theoretically and experimentally. The metal carbonyl model system [Rh(CO)$_2$acac] (acac=acetylacetone) is used to demonstrate and explain various features in the 2D-IR spectra obtained by the two approaches.

Paper **P3** assesses the question how far we can go in the size of the structure to be determined. The computational study discusses the effects of homogeneous and inhomogeneous broadening in 2D-IR spectra and the resulting loss of structural information due to band overlap. Isotope labeling strategies to overcome this problem are suggested. A conformational search algorithm based on simulated annealing is developed to extract structure information from the 2D-IR spectra. It makes use of the structural restrains imposed by the chemical structure of the polypeptides to narrow the search space considerably.

Paper **P10** deals with the polarization dependence of the T2D-IR experiment, where three laser pulses interact with up to three different transition dipole moments. A general expression for the polarization dependence of the T2D-IR signal is derived. Its dependence on rotational diffusion is analyzed. Useful polarization conditions and magic angle like signals for the different pulse sequences in Figure 4.5 are obtained. The theoretical considerations are demonstrated experimentally for MLCT in the metal carbonyl model system [Re(CO)$_3$(dmbpy)Cl].

Paper **P14** analyzes the *holeburning T2D-IR* experiment that employs pulse sequence *b* in Figure 4.5. The pulse sequence is applied to the solvation dynamics of DMSO with [Re(CO)$_3$(dmbpy)Cl] as a solute. The MLCT in [Re(CO)$_3$(dmbpy)Cl] leads to a charge redistribution within the complex that requires the surrounding DMSO solvent molecules to rearrange. It is shown that the 5th order holeburning is very sensitive to the coupling between fast and slow solvation coordinates and can distinguish solvation scenarios that are indistinguishable by third order techniques like photon echo or 2D-IR. In this way similar information as potentially accessible by 5th order Raman spectrosopy can be obtained by T2D-IR.

Paper **P5** explores pulse sequence *c* in Figure 4.5 called *labeling T2D-IR*. In the labeling pulse sequence, the narrowband IR-pump pulse labels a certain vibration by selectively exciting it. Then, the UV-pump pulse triggers a photoreaction that shifts the frequency of the excited vibration. The IR-probe pulse detects the frequency to which the labeled vibration has been shifted. In this way the labeling experiment correlates vibrations before and after a photoreaction by generating cross peaks between them. It can be regarded as an IR version of NMR exchange spectroscopy under non-equilibrium conditions [290]. Labeling T2D-IR is demonstrated again for MLCT in [Re(CO)$_3$(dmbpy)Cl], monitoring the shift of the CO vibrations. Surprisingly the different modes are found to change their order in the spectrum in contrast to what has been presumed in the literature so far.

Paper **P4** represents the combination of the results of several of the previous chapters: It reports on the application of T2D-IR on a photoswitchable peptide. Although band overlap in the sample under investigation precludes the extraction of structural information without isotope labeling, the work described in Paper **P4** demonstrates the feasibility of a T2D-IR experiment on peptide samples. As explained in previous chapters, 2D-IR is a nonlinear probe and can reveal details about the frequency fluctuation correlation function that cannot be obtained from linear IR spectroscopy. The spectra of the photoswitchable peptide are discussed in terms of the 2D line shape. The change of the lineshape is tentatively interpreted as resulting from changes in the local properties of the energy landscape, revealing some analogy with the transient holeburning experiments on the Rhenium complex in Paper **P14**.

Chapter 5

2D-IR and T2D-IR —The Publications

5.1 P12 – Double-Resonance Versus Pulsed Fourier Transform Two-Dimensional IR Spectroscopy: An Experimental and Theoretical Comparison

Valentina Cervetto, Jan Helbing, Jens Bredenbeck, and Peter Hamm,
J. Chem. Phys, 121:5953-5942, 2004

5.1.1 Abstract

In this study we focus on the differences and analogies of two experimental implementations of two-dimensional infrared (2D-IR) spectroscopy: double-resonance or dynamic hole burning 2D-IR spectroscopy and pulsed Fourier transform or heterodyne detected photon echo spectroscopy. A comparison is done theoretically as well as experimentally by contrasting data obtained from both methods. As an example we have studied the strongly coupled asymmetric and symmetric carbonyl stretching vibrations of dicarbonylacetylacetonato rhodium dissolved in hexane. Both methods yield the same peaks in a 2D-IR spectrum. Within certain approximations we derive an analytic expression which shows that the 2D-IR spectra are broadened in one frequency dimension in the double-resonance experiment by convolution with the pump pulse spectral width, while the spectral resolution in the other frequency direction is the same in both cases.

5.1.2 Introduction

Many important properties of quantum systems cannot be inferred from linear spectroscopy but have to be investigated by nonlinear techniques. This includes the connectivity of energy levels, the cross relaxation between levels, and the discrimination between different mechanisms of dephasing. In NMR spectroscopy multidimensional nonlinear techniques have been extremely successful in the study of such properties [244]. The transferability of the concepts of multidimensional NMR spectroscopy to IR spectroscopy has been postulated already in the earliest publications on twodimensional NMR [1], however, the first two-dimensional IR spectrum was measured only recently [2]. While this first twodimensional IR (2D-IR) experiment was a quasi frequencydomain double-resonance experiment, a technique that has been developed further [283, 3, 4, 74, 247, 252, 174, 302, 258, 303], time-domain pulsed Fourier transform IR techniques have been devised meanwhile [304, 305, 251, 250, 306, 307, 248, 308, 264, 309]. It has been shown that 2D-IR can be used to determine the structure and dynamics of small peptides on ultrafast time scales [283, 3, 252, 174, 250]. The present paper compares the frequency and time domain approaches of 2D-IR spectroscopy, concerning the potential information content as well as regarding technical issues.

Almost all nonlinear 2D-IR experiments published so far work in the small field regime, in which a power expansion of the nonlinear response in terms of the electric field of the incident pulses is very well justified [310]:

$$P^{(n)}(t) = \int_0^\infty dt_n \dots \int_0^\infty dt_1 S^{(n)}(t_n, \dots, t_1) \\ \times E_n(t-t_n) \cdot \dots \cdot E_1(t-t_n-\dots-t_1). \qquad (5.1)$$

Here, n is the order of expansion which in centrosymmetric (isotropic) samples is an odd number (in most cases $n=3$), and $S^{(n)}(t_n,\dots,t_1)$ is the nth-order response function. The emitted polarization $P^{(n)}(t)$ is *linear* with respect to the field of each interaction E_i. Therefore, at least in principle, the information content of frequency and time domain approaches are absolutely identical and are connected through Fourier transformation. We investigate in this paper to what extent this statement is true also in practice.

In the case of NMR, pulsed Fourier transform methods became much more widespread than frequency domain methods soon after their introduction, partly due to greater sensitivity because of their multiplex advantage, but also due to their greater experimental versatility. However, it is important to keep in mind that modern NMR spectroscopy works in the limit of strong fields ($\pi/2$ and π-pulses in most cases). Hence, in contrast to 2D-IR spectroscopy, a simple Fourier relation between time-domain and frequency domain experiments does in general not exist.

The principles of the two experimental implementations of 2D-IR spectroscopy are shown in Fig. 5.1, and shall be discussed briefly in the following:

a. Double-resonance spectroscopy (also called dynamic hole burning). The double-resonance experiment is essentially a conventional pump-probe experiment (Fig. 5.1a). An intense ultrashort (typically 100 fs) IR laser pulse [165], the bandwidth of which (200 cm^{-1}) covers the whole spectral range of interest, is split into a pump and a probe beam. The pump beam passes a computer controlled delay line and is spatially overlapped with the probe beam in the sample. The probe beam is frequency dispersed in a spectrometer and detected with an IR (MCT) array detector. The difference between the double-resonance experiment and a conventional pump-probe experiment is the adjustable Fabry-Perot filter which the pump beam passes before reaching the sample. It consists of two partial reflectors separated by a distance which is regulated by a feedback-controlled piezoelectric mount. It slices out a narrow-band pump pulse (typical bandwidth 5–15 cm^{-1}), the center-frequency of which is controlled by the computer. In this way two frequencies are defined, the center frequency of the pump pulse and the probe frequency. These are the frequency axes used in the 2D-IR spectrum. Hence, in a 2D-IR spectrum, each (horizontal) cut in the probe frequency direction represents a transient absorption spectrum obtained by pumping at the frequency on the pump (vertical) axis.

b. Pulsed Fourier transform spectroscopy (also called heterodyne-detected photon echo spectroscopy). The pulsed Fourier transform experiment is based on a three-pulse photon echo experiment. In this case, an intense ultrashort IR laser pulse, which spectrally covers the whole range of interest, is split into three pulses that are directed onto the sample with variable delay times. Typically, the so-called box CARS configuration is used, which allows one to separate the ingoing (k_1 , k_2 and k_3) and the two outgoing ($-k_1+k_2+k_3$ and $+k_1-k_2+k_3$) beams from each other by selecting the respective phase-matching directions. The generated third-order

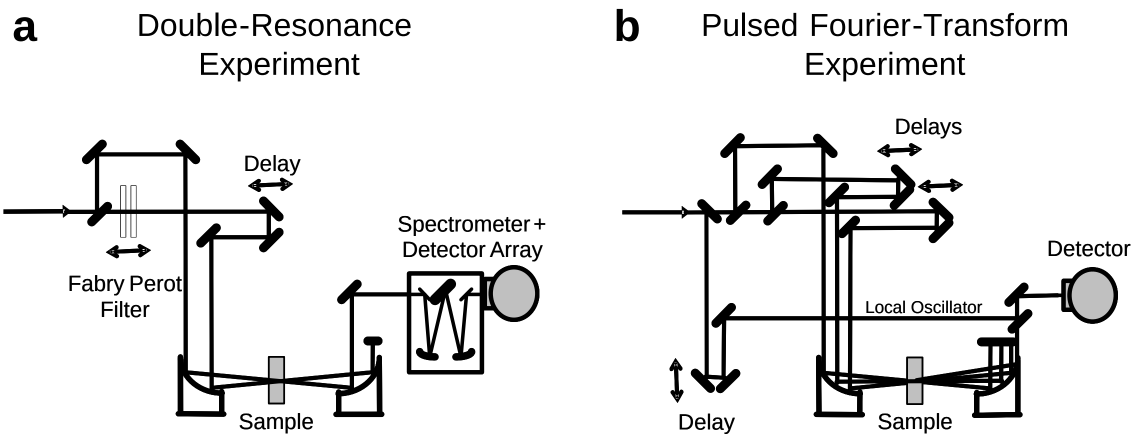

Figure 5.1: Principle of a setup for (a) a double-resonance experiment and (b) a pulsed Fourier transform experiment.

field is 2D-Fourier transformed with respect to times t_1 (the time between the first and the second pulses) and t_3 (the time after the third pulse), generating a 2D-IR spectrum as a function of two frequencies ν_1 and ν_3. In order to perform the Fourier transform, one needs to know the electric field irradiated by the third-order polarization, rather than the time-integrated intensity, which is what 'normal' square law detectors measure. The field is regained by interferometric superposition of the generated third-order field and a so called local oscillator field (heterodyning), for which a fourth replica of the initial ultrashort laser pulse is used. The interferometric superposition can be either done in the time domain (by scanning the time and phase of the local oscillator) or in the frequency domain (by spectrally dispersing both beams in a spectrograph). The outcome of the interferometric superposition depends on the optical phase between first and second pulses as well as between the third and local oscillator pulses, $(\phi_1 - \phi_2) + (\phi_3 - \phi_{LO})$, which is why the requirements on the mechanical stability of the setup and an accurate measurement of the phase are high. A scheme utilizing an intrinsic phase stabilization has been proposed recently [311].

The aim of the present paper is to compare the two techniques experimentally as well as theoretically. As an example, we investigate the symmetric (2084 cm^{-1}) and asymmetric (2015 cm^{-1}) $C{\equiv}O$ stretching vibrations of dicarbonylacetylacetonato rhodium (RDC, see Fig. 5.2) dissolved in hexane, a system which has been extensively studied by Tokmakoff and co-workers [305, 307, 248, 276]. RDC is a planar d^8 compound with two chemically equivalent terminal carbonylcarbonyl groups and a bidentate acetylacetonato ligand coordinated to the rhodium center. The molecular system has sufficiently narrow absorption bands so that all peaks in the 2D-IR spectrum are spectrally resolved.

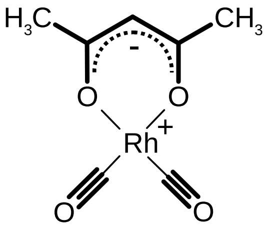

Figure 5.2: Chemical structure of dicarbonylacetylacetonato rhodium (RDC)

5.1.3 Experimental Confrontation

The double-resonance 2D-IR spectrum (Fig. 5.3a) was measured as described previously [2, 283, 3, 4, 74, 247]. The unfiltered IR pulses had a duration of $\sim$120 fs, spectral width of $\sim$150 cm^{-1}, and energy 1.5 μJ. The probe pulse was split off with a BaF$_2$ window, yielding a probe pulse energy of $\sim$40 nJ. The probe spectral resolution of the spectrometer was $\sim$4.5 cm^{-1}. The spectral width of the pump pulse was reduced to 6 cm^{-1} [full width at half maximum (FWHM)] by passing them through an adjustable Fabry-Perot filter, yielding an approximately single-sided exponential pulse shape with a falling slope of $t_{pu} = 900$ fs (see below) and a pump energy of $\sim$60 nJ. The pump-probe delay time between the rising edge of the single-sided exponentially shaped pump pulse and the probe pulse was set to 2 ps in order to minimize temporal overlap between pump and probe pulses.

The purely absorptive pulsed Fourier transform 2D-IR spectrum of RDC (Fig. 5.3b) is adapted from Ref. [307] and was made available to us by A. Tokmakoff. The experiment used 90 fs pulses with a bandwidth of 160 cm^{-1}. Each pulse had an energy of $\sim$50 nJ. The spectral resolutions in the v_1 and v_3 dimensions were 1 cm^{-1} and 1.3 cm^{-1}, respectively. The time between second and third pulses, i.e., the population time t_2 , was set to zero in the experiment in Fig. 5.3b.

Despite the apparent differences between the two measurement techniques, the 2D-IR spectra obtained from both techniques are remarkably similar (Figs. 5.3a and 5.3b with small pump probe t_{pp} or waiting time t_2 , respectively). In particular, all peaks, including the cross peaks which reveal the coupling between the two states, are present in both cases with equivalent relative intensities and splittings. The only difference is that the peaks in the double-resonance case are somewhat broader and elongated along the pump-frequency axis.

The main features in a 2D-IR spectrum can be explained in a simple way with the help of the level scheme in Fig. 5.3c. Six levels need to be considered: the ground vibrational state $|00\rangle$, two one-quantum states $|10\rangle$ and $|01\rangle$, and three two-quantum states consisting of the overtones $|20\rangle$ and $|02\rangle$ and the combination band $|11\rangle$. Each allowed vibrational transition of the molecule, depicted by an arrow in Fig. 5.3c, corresponds to a peak in the 2D-IR spectra (see labeling in Fig. 5.3c). Bleach or stimulated emission contributions (blue arrows) yield negative (blue) signals while excited state absorption signals (red arrows) yield positive (red) signals. The separation of negative and positive peaks is due to the anharmonicity of the system. For example, an excitation of the $|10\rangle$ level at 2084 cm^{-1} reduces the population of the ground state $|00\rangle$, which results in a decrease of absorption (bleach) not only at a frequency of 2084 cm^{-1} resonant with the $|00\rangle \rightarrow |10\rangle$ transition (negative diagonal peak) but also at a frequency of 2018 cm^{-1} resonant with the $|00\rangle \rightarrow |01\rangle$ transition (negative off-diagonal signal); in addition an excited state absorption signal is seen at a frequency of 2076 cm^{-1} resonant with the $|10\rangle \rightarrow |20\rangle$ transition (positive diagonal peak) and at a frequency of 1990 cm^{-1} resonant with the $|10\rangle \rightarrow |11\rangle$ transition (positive off-diagonal peak). The same happens after excitation of the $|01\rangle$ state in an analogous manner. The result is a 2D-IR spectrum with eight peaks: four diagonal peaks and four off-diagonal peaks. The offdiagonal peaks show that both transitions are connected through a common ground state. To observe a 2D-IR spectrum it is crucial that the system is anharmonic. Otherwise, if, for example, the $|00\rangle \rightarrow |10\rangle$ and $|01\rangle \rightarrow |11\rangle$ transitions had the same frequency, the positive and negative crosspeaks would appear at the same frequency and would cancel exactly.

5.1.4 Theoretical Confrontation

The explanation we just gave uses the language of double-resonance spectroscopy, which provides the more intuitive picture. However, the explanation is valid also for the pulsed Fourier transform experiment. To see this we start by noting that both experiments are third-order nonlinear spectroscopies, and as such, of course, rely on exactly the same third-order response function $S^{(3)}(t_3,t_2,t_1)$ [310]. The third-order response function is the molecular property we wish to measure. If one succeeds in measuring $S^{(3)}(t_3,t_2,t_1)$, one knows everything about the molecule that possibly can be learned with third-order spectroscopy.

Both experiments differ in the way how the third-order response is read out. In principle, in both cases, the third-order polarization $P^{(3)}$ is obtained by convoluting the third-order response function $S^{(3)}(t_3,t_2,t_1)$ with three input electric fields [310]:

$$\begin{aligned} P^{(3)}(t) = & \int_0^\infty dt_1 \int_0^\infty dt_2 \int_0^\infty dt_3 S^{(3)}(t_3,t_2,t_1) \\ & \times E_3(t-t_3)E_2(t-t_3-t_2)E_1(t-t_3-t_2-t_1). \end{aligned} \quad (5.2)$$

Here, E_1 , E_2 , and E_3 are the incident laser fields interacting with the sample at certain time points, and t_n are the time intervals in which the system evolves (Fig. 5.4) after each interaction. Time t_1 is the coherence or evolution time, t_2 is the population or waiting time, and t_3 is the detection time.

a. Double-resonance experiment. The double-resonance experiment uses a single pump pulse for the first two field interactions E_1 and E_2 , which is the pulse shaped by the Fabry-Perot filter. In the time domain, the pump pulse has an approximately single-sided exponential shape (Fig. 5.4a), which can be understood when considering the generation mechanism in the Fabry-Perot: The initial pulse is coupled into the Fabry-Perot resonator, where it bounces back and forth several times.

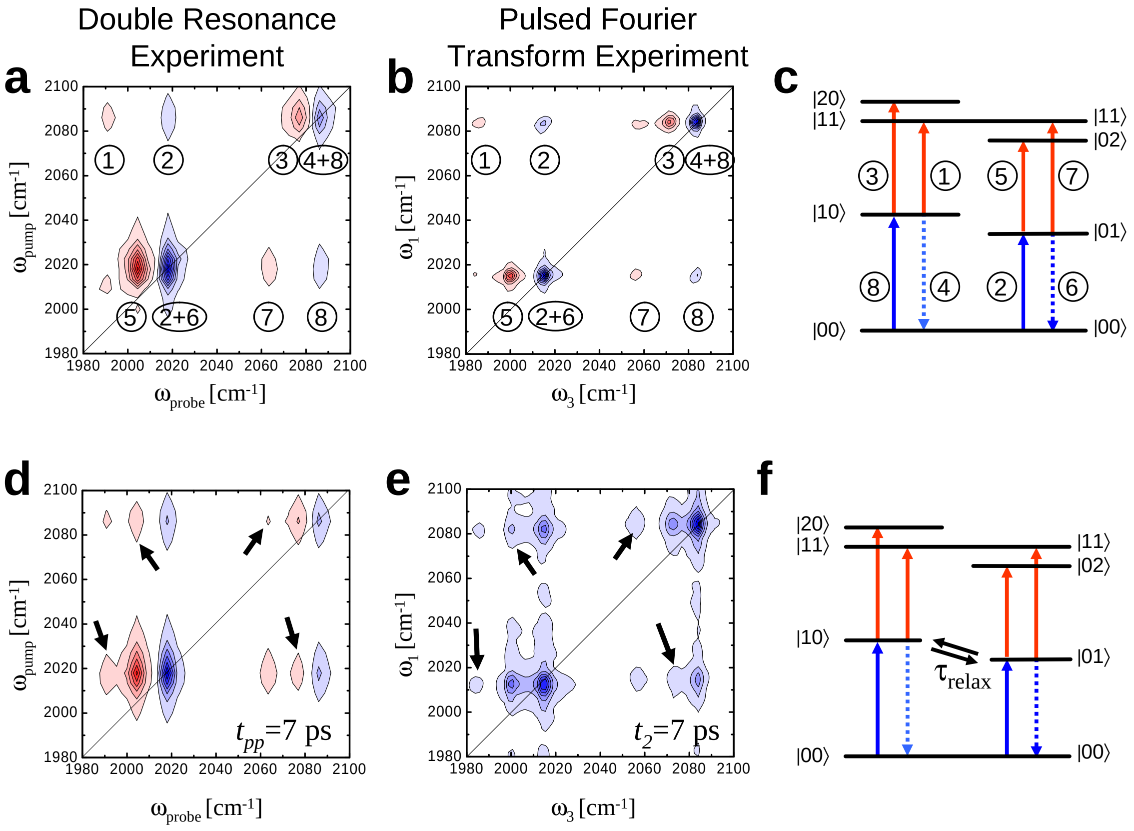

Figure 5.3: (a) 2D-IR spectrum of RDC dissolved in hexane obtained by the double-resonance experiment with a pump probe delay time of t_{pp}=2 ps. (b) Purely absorptive 2D-IR spectrum of RDC dissolved in hexane obtained with the pulsed Fourier transform experiment with $t_2 = 0$ ps. (c) Level scheme of RDC. The arrows indicate allowed transitions which give rise to the peaks in the 2D-IR spectra. Arrows and peaks are numbered correspondingly. (d–f) The same for longer waiting time t_{pp} (or t_2)= 7 ps. New peaks arise in the 2D spectra due to vibrational cross-relaxation between the two one-quantum states, which are marked by the arrows. Note that (e) is an absolute value spectrum of the rephasing term $S^{(3)}_{+}$ (Eq. 5.15). The pulsed Fourier transform 2D-IR spectra (b) and (e) are adapted from Ref. [307] and Ref. [276] and were provided by A. Tokmakoff.

Each time it hits the exit mirror, a small portion is coupled out, resulting in a sequence of pulses with exponentially decaying intensity. Since the round trip time in the resonator is shorter than the duration of the initial pulse, the pulse sequence merges into a single pulse. By fine adjustment of the distance between the two Fabry-Perot mirrors, the relative phase of the pulses in the pulse sequence is tuned, resulting in the desired narrow spectrum of the pump pulse by interferometric superposition.

We chose the arbitrary time zero to coincide with the time of the probe pulse and approximate the pump pulse in the time domain by

$$E_{\mathrm{pu}}(t) = E^{0}_{\mathrm{pu}} e^{-(t+t_{\mathrm{pp}})/\tau_{\mathrm{pu}}} \theta(t+t_{\mathrm{pu}}) \cos\omega_{\mathrm{pu}} t, \tag{5.3}$$

where t_{pu} is the pump pulse duration, ω_{pu} its carrier frequency, t_{pp} the pump-probe delay time (see Fig. 5.4a), and $\theta(t)$ is the Heaviside step function. Note that the timebandwidth product, $t_{\mathrm{pu}}\Delta\nu_{\mathrm{FWHM}}$, of a single-sided exponential pulse is $1/2\pi \approx 0.16$, which is considerably smaller than that of a Gaussian pulse.

The third field interaction E_3 is coming from the probe pulse, which is written as

$$E_{\mathrm{pr}}(t) = E^{0}_{\mathrm{pr}} e^{i\omega_{\mathrm{pr}} t} \delta(t). \tag{5.4}$$

This is the semi-impulsive limit, in which the probe pulse still has a carrier frequency ω_{pr} but its envelope is shorter than any time scale of the system and hence can be approximated as a δ-pulse.

We have written the pump pulse as a real electric field, which contains positive and negative frequencies:

$E_{\mathrm{pu}}(t) \propto (e^{-i\omega_{\mathrm{pu}}t} + e^{+i\omega_{\mathrm{pu}}t})$. The pump pulse interacts with the sample twice, once with the *bra* and once with the *ket* of the density matrix (owing to the particular phase matching condition in a pump-probe experiment). In a pump-probe experiment, we have no experimental control over which interaction comes first (in contrast to the pulsed Fourier transform experiment, see below). The third-order response function therefore contains two sets of Liouville pathways corresponding to the two possible time orderings: $S^{(3)} = S_+^{(3)} + S_-^{(3)}$. Signal $S_+^{(3)}$ relates to the rephasing Feynman diagrams and $S_-^{(3)}$ to the nonrephasing diagrams. Of the four possibilities, $e^{i\pm\omega_{\mathrm{pu}}t}S_\pm^{(3)}$, only two contribute when applying the rotating wave approximation (RWA) and we obtain for the total third-order polarization:

$$\begin{aligned} P^{(3)}(t) \quad &\propto \quad \int_0^\infty\int_0^\infty\int_0^\infty dt_1dt_2dt_3[S_+^{(3)}(t_3,t_2,t_1)e^{+i\omega_{\mathrm{pr}}(t-t_3)}\delta(t-t_3)\theta(t+t_{\mathrm{pp}}-t_3-t_2-t_1) \\ &\times \quad e^{-(t+t_{\mathrm{pp}}-t_3-t_2)/\tau_{\mathrm{pu}}}e^{+i\omega_{\mathrm{pu}}(t-t_3-t_2)}e^{-(t+t_{\mathrm{pp}}-t_3-t_2-t_1)/\tau_{\mathrm{pu}}}e^{-i\omega_{\mathrm{pu}}(t-t_3-t_2-t_1)}+S_-^{(3)}(t_3,t_2,t_1)e^{+i\omega_{\mathrm{pr}}(t-t_3)}\delta(t-t_3) \\ &\times \quad \theta(t+t_{\mathrm{pp}}-t_3-t_2-t_1)e^{-(t+t_{\mathrm{pp}}-t_3-t_2)/\tau_{\mathrm{pu}}}e^{-i\omega_{\mathrm{pu}}(t-t_3-t_2)}e^{-(t+t_{\mathrm{pp}}-t_3-t_2-t_1)/\tau_{\mathrm{pu}}}e^{+i\omega_{\mathrm{pu}}(t-t_3-t_2-t_1)}]. \end{aligned} \tag{5.5}$$

For the sake of clarity we will evaluate only the term $S_+^{(3)}$ in the following: the second term can be evaluated the same way. Since the probe pulse is a δ-pulse, the integration over t_3 can be carried out trivially:

$$\begin{aligned} P_+^{(3)}(t) \propto &\int_0^\infty\int_0^\infty dt_1dt_2S_+^{(3)}(t,t_2,t_1) \\ &\times e^{(-2t_{\mathrm{pp}}+2t_2+t_1)/\tau_{\mathrm{pu}}}e^{-i\omega_{\mathrm{pu}}t_1}\theta(t_{\mathrm{pp}}-t_2-t_1). \end{aligned} \tag{5.6}$$

At this point we make a crucial approximation: We assume that the response function is only slowly varying as a function of the waiting time t_2 (slowly compared to the pump pulse duration τ_{pu}). The system is in a population state during the time period t_2 , where it varies more slowly than during the coherence times t_1 or t_3 . For example in the Bloch picture, $S^{(3)}$ is constant during t_2 , but it oscillates with the vibrational frequency during the coherence times t_1 or t_3. $S^{(3)}$ will still be slowly varying during t_2 when spectral diffusion or population relaxation is allowed. This is the only crucial approximation in the derivation, the validity of which will be discussed further below. In this case, we can replace $S^{(3)}(t,t_2,t_1)$ by $S^{(3)}(t,t_{\mathrm{pp}},t_1)$ and obtain

$$\begin{aligned} P_+^{(3)}(t) \propto \int_0^\infty dt_1 &\underbrace{\left[e^{-t_1/\tau_{\mathrm{pu}}}e^{-(2t_{\mathrm{pp}}-t_1)/\tau_{\mathrm{pu}}}\right]\theta(t_{\mathrm{pp}}-t_1)}_{w(t_1)} \\ &\times e^{+i\omega_{\mathrm{pu}}t_1}S_+^{(3)}(t,t_{\mathrm{pp}},t_1). \end{aligned} \tag{5.7}$$

Except for the window function $w(t_1)$, Eq. 5.7 represents a Fourier transformation of the third-order response function with respect to time t_1, yielding the pump frequency axis in the 2D-IR spectrum. The second Fourier transformation with respect to time t is performed by the spectrometer in the experimental setup, yielding the probe frequency axis. Hence, we see that the 2D-IR spectrum is convoluted in the pump frequency direction by the Fourier transformation of the window function $w(t_1)$ (which weakly depends on the pump-probe delay time t_{pp}). With respect to the probe frequency, the spectral resolution is limited only by the spectrometer. Equation 5.7 becomes more intuitive when we furthermore assume that the pump-probe delay time is longer than the pulse duration $t_{\mathrm{pp}} \gg t_{\mathrm{pu}}$. In that case, the window function $w(t_1)$ reduces to a single-sided exponential, whose Fourier transform is a Lorentzian function. Hence, we obtain the following as the final result when taking into account the second set of Liouville pathways and applying the convolution theorem:

$$\begin{aligned} &P^{(3)}(\omega_{\mathrm{pu}},t_{\mathrm{pp}},\omega_{\mathrm{pr}}) \\ &\propto \frac{-1/\tau_{\mathrm{pu}}}{\omega_{\mathrm{pu}}^2+(1/\tau_{\mathrm{pu}})^2} \otimes \int_0^{+\infty}\int_0^{+\infty} dt_1dt[S_+^{(3)}(t,t_{\mathrm{pp}},t_1) \\ &\times e^{i\omega_{\mathrm{pu}}t_1}e^{i\omega_{\mathrm{pr}}t}+S_-^{(3)}(t,t_{\mathrm{pp}},t_1)e^{-i\omega_{\mathrm{pu}}t_1}e^{i\omega_{\mathrm{pr}}t}. \end{aligned} \tag{5.8}$$

In a pump-probe experiment, the third-order polarization is heterodyne detected with the probe pulse which acts as local oscillator, and only the real part of Eq. 5.8 is measured:

$$\begin{aligned} &\Delta A(\omega_{\mathrm{pu}},t_{\mathrm{pp}},\omega_{\mathrm{pr}}) \\ &\propto \frac{-1/\tau_{\mathrm{pu}}}{\omega_{\mathrm{pu}}^2+(1/\tau_{\mathrm{pu}})^2} \otimes \mathrm{Re}\int_0^{+\infty}\int_0^{+\infty} \mathrm{dt_1dt}[\mathrm{S_+^{(3)}(t,t_{pp},t_1)} \\ &\times e^{i\omega_{\mathrm{pu}}t_1}e^{i\omega_{\mathrm{pr}}t}+S_-^{(3)}(t,t_{\mathrm{pp}},t_1)e^{-i\omega_{\mathrm{pu}}t_1}e^{i\omega_{\mathrm{pr}}t}. \end{aligned} \tag{5.9}$$

Note that the relative phase between the pulses does not need to be known or controlled in this measurement, in contrast to the pulsed Fourier transform experiment (see below). For example, the probe pulse acts as third field interaction and local oscillator at the same time, so that the relative phase between both is inherently fixed.

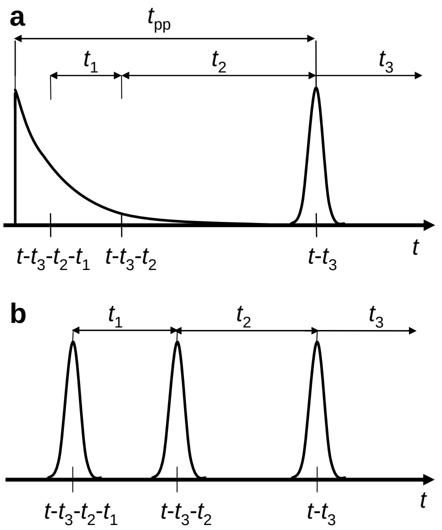

Figure 5.4: Schematic representation of the ‘pulse sequence’ in (a) the double-resonance experiment and (b) the pulsed Fourier transform experiment.

b. Pulsed Fourier transform experiment. In the pulsed Fourier transform experiment, three successive pulses are directed onto the sample. The duration of each pulse is assumed to be shorter than any time scale of the system, which is why they can be approximated as δ-pulses in the semiimpulsive limit:

$$E(t) = E^0 e^{\pm i\omega t}\delta(t). \tag{5.10}$$

Also in this case we make use of RWA and obtain, for example, for the $-k_1+k_2+k_3$ phase matching directions, i.e., for the rephasing diagram $S_+^{(3)}$:

$$\begin{aligned} P_+^{(3)}(t_3) \propto & \int_0^\infty \int_0^\infty \int_0^\infty dt_1 dt_2 dt_3 S_+^{(3)}(t_3,t_2,t_1) \\ & \times e^{-i\omega(t-t_3-t_2-t_1)}\delta(t-t_3-t_2-t_1) \\ & \times e^{i\omega(t-t_3-t_2)}\delta(t-t_3-t_2)e^{i\omega(t-t_3)}\delta(t-t_3). \end{aligned} \tag{5.11}$$

The integration can be carried out trivially when assuming δ-pulses:

$$P_+^{(3)}(t_3) \propto S_+^{(3)}(t_3,t_2,t_1). \tag{5.12}$$

The third-order polarization $P^{(3)}(t_3)$ is measured directly by interferometric superposition with the local oscillator. Finally the computer performs the 2D Fourier transform with respect to t_1 and t_3 to obtain a 2D spectrum:

$$\begin{aligned} P_+^{(3)}(\omega_3,t_2,\omega_1) \propto & \int_0^{+\infty}\int_0^{+\infty} dt_1 dt_3 S_+^{(3)}(t_3,t_2,t_1) \\ & \times e^{i\omega_1 t_1} e^{i\omega_3 t_3}. \end{aligned} \tag{5.13}$$

The 2D-IR spectrum calculated in that way is a complex valued function, and one may either plot the real part, imaginary part, or the absolute value 2D-IR spectrum. In the first two cases, however, the phase between first and second pulses as well as third and local oscillator pulses, $(\phi_1-\phi_2)+(\phi_3-\phi_{LO})$, needs to be known absolutely. This is an experimentally difficult task. The phase cannot be measured directly, which is why the spectra are ‘phased’ in the computer. To that end, the absolute phase is determined by projecting a calculated 2D-IR spectrum with the phase as free parameter onto the v_3 axis and comparing the result with a broadband-pump dispersed-probe spectrum, which, according to the projection-slice theorem, should give the same result [312]. Possible chirps of the pulses render the phasing procedure even more demanding. In contrast to the double-resonance technique, rephasing $S_+^{(3)}$ and nonrephasing $S_-^{(3)}$ diagrams can, in principle, be measured separately. This is done either by using two detectors in different phase matching directions ($-k_1+k_2+k_3$ and $+k_1-k_2+k_3$) or by using one detector and interchanging the time ordering of the first two pulses. However, it is now well established that both signals, $S_+^{(3)}$ and $S_-^{(3)}$, need to be added up to obtain *purely absorptive* 2D-IR spectra [307, 312, 313]:

$$\begin{aligned} \Delta A(\omega_3,t_2,\omega_1) \propto \mathrm{Re} & \int_0^{+\infty}\int_0^{+\infty} \mathrm{dt_1dt_3}[\mathrm{S}_+^{(3)}(\mathrm{t_3,t_2,t_1}) \\ & \times e^{i\omega_1 t_1} e^{i\omega_3 t_3} + S_-^{(3)}(t_3,t_2,t_1) \\ & \times e^{-i\omega_1 t_1} e^{i\omega_3 t_3}. \end{aligned} \tag{5.14}$$

In this case, the dispersive contributions of both signals destructively interfere in such a way that only the absorptive part remains so that the peaks become as sharp as possible. Purely absorptive 2D-IR spectra clearly provide the highest possible spectral resolution (see Fig. 5.3b). However, computing Eq. 5.14 requires that both signals are measured with exactly identical intensities (which would be difficult when using two detectors in the two phase matching directions) and are correctly phased.

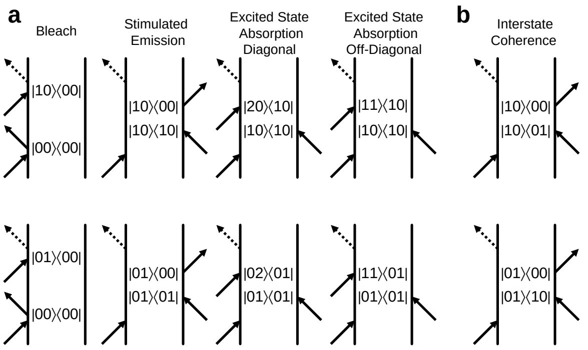

Figure 5.5: (a) Feynman diagrams which contribute to the nonrephasing third-order response function $S_{-}^{(3)}$ and give rise to both variants of 2D-IR spectroscopy. These diagrams result in a pure population state after the second field interaction. (b) Example of Feynman diagrams that result in an interstate coherence after the second field interaction. The time-order corresponds to the nonrephasing phase matching direction $+k_1 - k_2 + k_3$; a second set of Feynman diagrams exist with the time ordering of the first two pulses interchanged (the rephasing phase matching direction $-k_1 + k_2 + k_3$).

5.1.5 Discussion

Equation 5.14, i.e., the expression for purely absorptive heterodyne-detected 2D-IR spectrum, is to be directly compared with that for the double-resonance experiment, Eq. 5.9. Both expressions are equivalent except for a convolution along the pump frequency axis in the double-resonance experiment. Along the probe frequency axis, both techniques give the same result, i.e., have the same spectral resolution. This can be seen in the experimental data: All peaks are elongated along the pump frequency axis in the double resonance experiment (Fig. 5.3a), while they are circular in the pulsed Fourier transform experiment (Fig. 5.3b). However the number of the peaks and their positions are equal in both experiments. Furthermore, it should be noted that the results of Eqs. 5.9 and 5.14 are rather general. In particular, inhomogeneous broadening, spectral diffusion, and/or interstate population transfereffects which are governed by the third-order response function $S^{(3)}(t_3,t_2,t_1)$ can be observed in a similar manner by both techniques. In the specific case of RDC dissolved in hexane we demonstrate the possibility to observe interstate population transfer in Figs. 5.3d and 5.3e, where the waiting time (t_{pp} or t_2 , respectively) is increased to 7 ps (Fig. 5.3e is adapted from Ref. [276] and was made available to us by A. Tokmakoff). New peaks appear in both variants of 2D-IR spectroscopy (marked by the arrows), which are a result of cross relaxation between the two one-quantum states (Fig. 5.3f). Assume, for example, the $|10\rangle$ level is initially excited. Without cross relaxation, only the $|10\rangle \rightarrow |20\rangle$ and $|10\rangle \rightarrow |11\rangle$ transitions are possible, which give rise to the peaks labeled (1) and (3). However, when the system relaxes from the $|10\rangle$ to the $|01\rangle$ state by incoherent population transfer, the $|01\rangle \rightarrow |02\rangle$ transition becomes possible as well, resulting in the additional cross peak. The third order response function $S^{(3)}(t_3,t_2,t_1)$ consists of a sum of many possible Liouville pathways (Feynman diagrams), each of which give rise to certain peaks in the 2D-IR spectrum (see Fig. 5.5a). The Feynman diagrams of Fig. 5.5a enter both experimental techniques in the same way. They have in common that the system is in a population state after the second field interaction (i.e., $|10\rangle\langle 10|$ or $|01\rangle\langle 01|$). As such, they are relatively slowly varying as a function of t_2 ,and the approximation made to derive Eq. 5.7 is valid. However, there are additional Feynman diagrams, some examples of which are shown in Fig. 5.5b, which lead to an interstate coherence state (i.e., $|10\rangle\langle 01|$ or $|01\rangle\langle 10|$) after the second field interaction. These terms oscillate as a function of t_2 with $e^{\pm i(\omega_{|01\rangle}-\omega_{|10\rangle})t_2}$, that is, they are quickly varying on the time scale of the pump pulse duration in the double resonance experiment. The approximation made to derive Eq. 5.7 is not valid for these diagrams; in fact the t_2 integration in Eq. 5.6 results in a negligibly small contribution from these diagrams. This is the time-domain explanation for what is trivial to understand in the frequency domain: The narrowband pump pulse does not spectrally cover both resonances, and hence, may not excite any interstate coherence. Of course, interstate coherence beats can be observed in the pulsed Fourier transform experiment [276]. Hence, the pulsed Fourier transform experiment observes more Feynman diagrams, which can be good or bad, depending of what one wants to achieve. It potentially provides one with more information, but often one wants to reduce the information to obtain an easier interpretation. However, it is important to note that the reduced number of Feynman diagrams in the double-resonance experiment does not affect its ability to observe cross peaks, and hence to learn about couplings between modes. Cross peaks are generated by the Feynman diagrams in the fourth column of Fig. 5.5a, which contribute to both experimental techniques in the same way. In NMR language it is often argued that the observation of cross peaks is related to the coherence transfer between two states introduced by a mixing pulse. This statement does not apply for the present form of 2D-IR spectroscopy. Coherence transfer occurs, for example, in the simplest NMR pulse sequence, COSY, which consists of two $\pi/2$ pulses. Loosely speaking, each $\pi/2$ pulse in the strong field NMR case acts as one field interaction in the weak field IR case [313]: Both may transfer a population state (i.e., a zero-quantum coherence state) into a one-quantum coherence state and vice versa. The important difference is that a $\pi/2$ pulse may also transfer a one-quantum coherence state into another one-quantum coherence state [244], which is what the second $\pi/2$ pulse in the COSY sequence does. The same is not possible in the IR with weak field interactions. Hence, an exact equivalent to COSY does not exist in 2D-IR spectroscopy. Another way to say this is the following: In the weak field limit, a two-pulse experiment would measure the second-order response function $S^{(2)}$, which vanishes in isotropic media. The closest equivalent of our 2D-IR experiment would be NOESY in NMR (with zero mixing time) [313]. NOESY also produces J-cross peaks originating from zeroquantum coherences [244], which are unwanted in the NMR case and therefore often suppressed, but which are the exact equivalent to the cross peaks in both variants of 2D-IR spectroscopy. The present form of 2D-IR spectroscopy is in a population state (i.e., zero-quantum coherence state) after the second field interaction. However, it should be noted that variants of 2D-IR spectroscopy have been proposed and demonstrated, which indeed go through a double-quantum coherence states [313, 279, 314]. Moreover, the approximation made to derive Eq. 5.7 will be good only if the frequency fluctuation correlation function decays on well separated time scales, like in the Bloch model or when spectral diffusion is relatively slow. In that case, both variants of 2D-IR spectroscopy may observe spectral diffusion in a similar manner, since these are effects governed by the common response function $S^{(3)}(t_3,t_2,t_1)$ in Eqs. 5.9 and 5.14. Inhomogeneous broadening causes a tilt of the 2D-IR line shape [303]. However, the convolution in Eq. 5.9 will render the tilt to be smaller in the double-resonance experiment as compared to the pulsed Fourier transform experiment. The best choice for the pump pulse spectral width is to match it with the effective homogeneous width of the transition, which will yield the best compromise between spectral and temporal resolution. We cannot demonstrate this similarity with the present experiment, since RDC dissolved in hexane is hardly an inhomogeneously broadened system. Nevertheless, it has been shown in numerous previous examples that homogeneous and inhomogeneous broadening as well as spectral diffusion can be separated by the double-resonance experiment (which in principle constitutes a dynamic hole burning experiment) [247, 252, 174, 258, 303]. However, often the frequency fluctuation correlation function will decay very quickly with no clear separation of time scales. The most prominent example is the OH band in hydrogen bonded liquids such as methanol [264] or water [308, 315, 309] for which the heterodyned pulsed Fourier transform experiment certainly is superior. From the practical point of view, the double-resonance scheme is the by far the easier experiment to perform. Taking data of the sort of Fig. 5.3a takes 10 min of averaging time, and no time-consuming processing of the data is required. In the case of the pulsed Fourier transform experiment, 1–4 h of averaging time is needed, depending on the spectral resolution and signal amplitude [316]. The double-resonance experiment is essentially a pump-probe experiment without the need of any phase stabilization or knowledge about the phase. The phases between the various field interactions are inherently fixed. In the case of the pulsed Fourier transform experiment, in contrast, the biggest problem is to determine the phase (as well as any possible chirp of the pulses), which enters directly into computing Eq. 5.14 [316]. Determining the absolute phase is often avoided by plotting absolute value spectra:

$$A_{+/-}(\omega_3,t_2,\omega_1) \propto \left| \int_0^{+\infty} \int_0^{+\infty} dt_1 dt_3 S^{(3)}_{+/-}(t_3,t_2,t_1) e^{\pm i\omega_1 t_1} e^{i\omega_3 t_3} \right|, \tag{5.15}$$

in which case, however, the advantage in spectral resolution is partially forfeited and the information about the signs of the signal (whether it is bleach and stimulated emission or excited state absorption) is lost (see, e.g., Fig. 5.3e). Furthermore, the double-resonance experiment offers more flexibility in that one can, for example, measure couplings between one particular mode and the rest of the molecule without having to scan a complete 2D-IR spectrum (by adjusting the pump frequency to just that mode). This allows for longer averaging times and hence a better signal-to-noise ratio [74]. In the pulsed Fourier transform experiment, on the other hand, one has to scan the whole t_1 range before one may compute a 2D-IR spectrum and observe any coupling. However, the price one has to pay in the double resonance experiment is the reduced spectral resolution in the double-resonance experiment introduced by the convolution with the pump pulse spectral width (Eq. 5.9). Furthermore, the resonance experiment provides less experimental control over the Liouville pathways since the first two field interactions come from one laser pulse and necessarily have, for example, the same polarization. In the pulsed Fourier transform experiment, all three pulses may have different polarizations, a property which helps significantly to eliminate certain contributions to the 2D-IR spectrum in a very elegant way [251].

5.1.6 Conclusion

In the present paper, we have compared two types of 2D-IR spectroscopy: double-resonance spectroscopy and heterodyne-detected photon echo spectroscopy. We have shown experimentally and theoretically that the spectra recorded with both techniques are closely related and reveal the same peaks. Both experiments rely on the same third order response function $S^{(3)}(t_3,t_2,t_1)$, but differ in the way the laser fields read out that response function. In certain limits, both 2D-IR spectra are connected through simple convolution along one frequency axis with the pump pulse spectral width. Both techniques reveal essentially the same information, but have certain advantages and disadvantages. Generally speaking, the double-resonance experiment is the much easier and faster experiment to perform on the cost of less (spectral and temporal) resolution and less control over certain experimental parameters. It depends on the particular problem which of the technique should be chosen.

Acknowledgements We thank Andrei Tokmakoff and Munira Khalil for sending us the data of Figs. 5.3b and 5.3e, for sharing with us their results prior to publication, and for critically reading the manuscript. Illuminating discussions with Christoph Scheurer are acknowledged. The work was supported by the Swiss Science Foundation under Contract No. 2100-067573.02/1.

5.2 P3 – Peptide Structure Determination by 2D-IR Spectroscopy in the Presence of Homogeneous and Inhomogeneous Broadening

Jens Bredenbeck and Peter Hamm,
J. Chem. Phys., 119:1569 – 1578, 2003.

5.2.1 Abstract

The potential information content of 2D-IR spectroscopy of the amide-I band as a structure analysis method of small peptides is explored in a computational study, applying it to a cyclic penta peptide as an example. In the presence of realistic homogeneous and inhomogeneous broadening, the structure resolution power in the case of a non-isotope labelled molecule would be vanishingly small. However, 2D-IR spectroscopy can reveal the structure of the peptide uniquely if using a sufficiently large set of isotope labelled compounds. Design strategies for isotope labelling are developed. In the case of the cyclic penta peptide studied here, at least three single ^{13}C labelled compounds would be needed to determine the structure. While double ^{13}C labelling does not offer any advantage compared to single ^{13}C labelling, mixed $^{13}C^{16}O$-$^{12}C^{18}O$ or $^{13}C^{16}O$-$^{13}C^{18}O$ double labelling does. It is furthermore explored to what extent a structure can still be determined even under non-ideal conditions, i.e. if systematic errors in the molecular models are allowed or if the molecule is allowed to coexists in different conformations simultaneously.

5.2.2 Introduction

Recent work has shown that 2D infrared (2D-IR) spectroscopy might be a valuable experimental complement to 2D-NMR spectroscopy for studying the conformation of small peptides [2, 283, 3, 304, 4, 74, 261, 251, 313, 317, 247, 284] as well as of other molecular systems [295, 318, 319, 254, 320]. 2D-IR spectroscopy allows one to measure the coupling between certain vibrational modes of different peptide units in a similar way as 2D-NMR spectroscopy measures couplings between spin states. The vibrational modes under study are the so-called amide-I modes (mostly a C=O stretching vibration of the peptide unit) located between 1600 - 1700 cm^{-1}. Since the coupling strength is related to the relative orientation of the peptide units [139, 150, 166], one might deduce the structure from a 2D-IR spectrum. This has been demonstrated recently for the first time for trialanine [3, 4], the smallest possible peptide containing only two peptide units. The most promising potential of 2D-IR spectroscopy is its intrinsic high time resolution, which allows one to study conformational dynamics on a picosecond and even faster time scale [74].

Another aspect, also related to the fast time resolution, is the capability of 2D-IR spectroscopy to observe conformational sub-states of peptides [247]. The major degrees of freedom of the polypeptide chain are the (ϕ,ψ) dihedral angles of the two σ-bonds of each amino acid, which can rotate almost freely. A complex balance of forces results in two dominant free energy minima within the (ϕ,ψ) configuration space, corresponding to the two most important secondary structure motifs, α-helices and β-sheets [321]. The almost equal depth of these free energy minima allows for the tremendous structural diversity of proteins. However, in the case of small peptides, one expects to obtain a mixture of conformations owing to the shallow free energy potential surface, since intra-molecular hydrogen bonds that stabilize secondary structures are generally weak. Since conformational jumps between conformational sub-states occur many times on the NMR time scale ($>$1 ms), NMR techniques probe the time-averaged conformation, which does not necessarily coincide with any of the conformational sub-states. In addition, the highly nonlinear dependence of for example a NMR-NOESY signal on intermolecular distances often strongly overestimates a more compact (folded) conformation. This problem is the major reason for a lack of reliable information on the conformation of small peptides [322, 323]. The 2D-IR timescale (1 ps), on the other hand, is sufficiently fast to freeze in all conformational motion, and potentially separate them [247]. The 2D-IR spectrum of a mixture of conformations is a weighted sum of the 2D-IR spectra of the various sub-states.

In a 2D-IR spectrum, cross peaks occur whenever the two corresponding resonances on the diagonal are coupled. Two pieces of information can in principle be deduced from each cross peak: The coupling strength, given by the cross-peak amplitude, and the angle between corresponding transition dipoles on the diagonal, given by the cross peak anisotropy (see Refs. [306, 249, 252] for recent reviews). Ideally, one would want to measure couplings between each pair of amide-I states. However, this goal is seriously limited in the presence of homogeneous and inhomogeneous broadening. Both the homogeneous and the inhomogeneous line widths of amide-I modes typically are about 10 cm^{-1} [261, 247], while couplings between amide-I modes are in the same order of magnitude at most. This is why splittings of the resonances without the presence of 'chemical shifts', i.e. splittings as a result of couplings only, are hard to observe, in particular if the peptide contains more than two peptide groups. Sometimes, large chemical shifts of the intrinsic amide-I frequencies are found in very heterogeneous amino acid sequences [283], allowing one to resolve all peptide units separately. However, the more common situation is that all resonances are hidden underneath a broad amide-I band with little or no substructure [2, 259, 284]. As we shall see, the structure resolution power of a 2D-IR spectrum is essentially zero in that case already for a peptide as small as only five amino acids. One can, of course, separate certain peptide units from the main peak by site selective isotope labelling [324, 325]. The aim of this work is to explore to what extent a set of 2D-IR spectra of intelligently chosen isotopomers determines the structure of a small peptide unambiguously.

Since a measured 2D-IR spectrum certainly cannot be inverted directly into a peptide structure, some sort of optimization, or fit, algorithm is required (see Fig. 5.6a). In this approach, one would start from a random structure, calculate its 2D-IR spectra and compare them with experimental spectra. The structure subsequently would be varied using a minimization procedure until agreement is obtained. In order to verify whether the found structure is indeed the best fit, one would have to repeat the procedure many times. However, attempts to determine structures of peptides larger than trialanine have

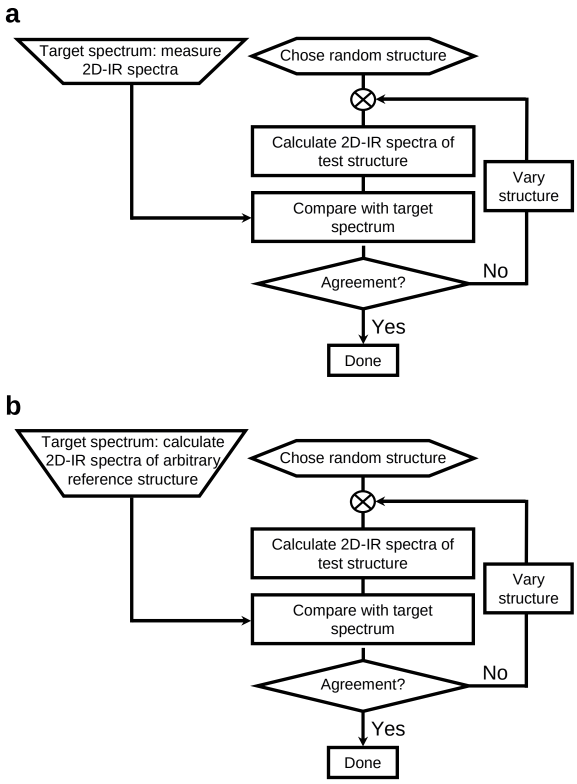

Figure 5.6: (a) Flow chart for 2D-IR structure determination of a peptide. Starting from a random structure, 2D-IR spectra are calculated, which are then compared with experimental spectra. The structure is varied using a minimization procedure until agreement is obtained. (b) Flow chart used in the present paper to short-cut the many unknowns in the approach (a). Rather than determining the structure of a real peptide, the structure of a arbitrary reference molecule is reconstructed in a computational study, testing the potential information content of 2D-IR spectra in the presence of realistic homogeneous and inhomogeneous broadening.

failed [283, 284], since this approach presently contains too many uncertainties:

(i) The structure determined in that way cannot be checked reliably since NMR structure analysis is not very expressive for the small peptides, which are potentially within the reach of 2D-IR spectroscopy. This is mostly due the fact that these small systems are not expected to be very rigid and may exist in a mixture of conformations. Since NMR spectroscopy averages very unfavorably over these conformations, a distinction of various structures is often problematic [322, 323].

(ii) The model, which relates a given peptide structure to a 2D-IR spectrum, relies on severe approximations, the quality of which is difficult to estimate.

(iii) It is not known to what extent the information content of 2D-IR spectra is blurred by homogeneous and inhomogeneous broadening.

The attempt of the present paper is to decouple these problems and tackle them separately. To this end, a computational study is presented, which starts from an arbitrary reference structure, calculates its 2D-IR spectrum using a *realistic* but not necessarily *very accurate* model, and subsequently tries to reconstruct the original reference structure using no other information but the calculated 2D-IR spectra of the reference structure (see Fig. 5.6b). This approach short-cuts the uncertainties described above. Firstly, the target structure, i.e. the expected outcome, is known exactly. Secondly, the function used to calculate the 2D-IR spectra during the optimization procedure can be chosen to be the same as that for calculation of the reference structure. Hence, by construct there is no uncertainty about the accuracy of that function. Furthermore, it allows one to critically test the sensitivity of the result of a structure determination on the accuracy of the molecular model, on which the optimization algorithm is based, i.e. it allows one to test the potential robustness of 2D-IR structure determination. The present paper focuses on the 3rd problem listed above, namely to investigate the potential structure information content of 2D-IR spectra in the presence of homogeneous and inhomogeneous broadening.

The case study has been performed on a cyclic penta-peptide, which is expected to be relatively rigid. Cyclic penta-peptides containing the Arg-Gly-Asp-sequence (commonly termed RGD-peptides) play an important role as templates in drug design, since this sequence is an universal cell-recognition site of various extracellular protein that interact with integrin cell-surface receptors. Despite extensive x-ray and NMR structure analysis studies over the last two decades [285, 286, 287], a controversy about the 3D structures of cyclic penta-peptides is still going on [288, 289].

5.2.3 Computational Methods

The molecule under investigation is a hypothetical cyclic penta peptide. Since 2D-IR spectroscopy of the amide-I band is only sensitive to the peptide backbone, and in order to avoid sterical constraints, the amino acid side chains have been replaced by hydrogen atoms, i.e. the molecule under investigation is cyc(Gly$_5$) or cyc(C$_\alpha$H$_2$-CONH)$_5$). As a simple structure model of this molecule, we consider only the dihedral angles (ϕ,ψ) of the two σ-bonds of each amino acid, which are the dominant degrees of freedom of a polypeptide chain. All other internal coordinates (i.e. bond lengths, bond angles, and dihedral angle of the peptide bond itself) are kept fixed at standard values [146].

In this stiff model, the conformation is fully determined by the four pairs of dihedral angles (ϕ_i,ψ_i) of a linear penta-peptide and hence, the dimensionality of the conformational space is 8. Of course, not every set of (ϕ_i,ψ_i) dihedral will yield a closed ring. The condition of ring-closure reduces the dimensionality of the conformational space to effectively 4, since it results in 4 constraints: the x,y,z coordinates of a dummy C$_\alpha$ atom of peptide unit #5 are forced to match those of the first C$_\alpha$ atom of peptide unit #1, and the bond angle of that C$_\alpha$ atom is forced to its standard value of 112° [146]. Starting from a given open structure described by a set of (ϕ_i,ψ_i) dihedral angles, ring-closure is achieved using a steepest descent method, which is a straight forward modification of the SHAKE algorithm common in MD simulations [326]. The fifth pair of dihedral angles (ϕ_5,ψ_5) then can be calculated. No molecular mechanics (MM) potentials have been used to discriminate structures; all structures on the 4-dimensional hyper-surface have been considered to be energetically equivalent.

The stiff character of the structure model used here might not be very realistic. It was nevertheless decided to use this approach since the aim of the present work is to explore the potential information content of 2D-IR spectroscopy *without* employing additional information from a MM force field. If one were to allow the intramolecular degrees of freedom to deviate from the idealized values, one would have to use a penalty function, which could only be a realistic MM force field. Such a force field would already drive the peptide structure into one of the few minimas of the constrained molecule, while in the present study the only driving force is the mismatch between the 2D-IR spectra of target and trial structure. Combining 2D-IR spectroscopy with a realistic force field will be discussed in a future work.

The accessible conformational space has been explored in an extensive search starting from 50.000 random open structures, which subsequently were closed to a ring (Fig. 5.7). Due to the stiff character of the model, none of the structures had overlapping atoms after ring closure. By varying the number of structures it has been verified that searching of the conformational space has converged with the 50.000 structures. It has furthermore been checked that the 4-dimensional hyper-surface is connected by testing whether each of the 50.000 conformation can be reached in a random walk with small steps (10°) on that surface.

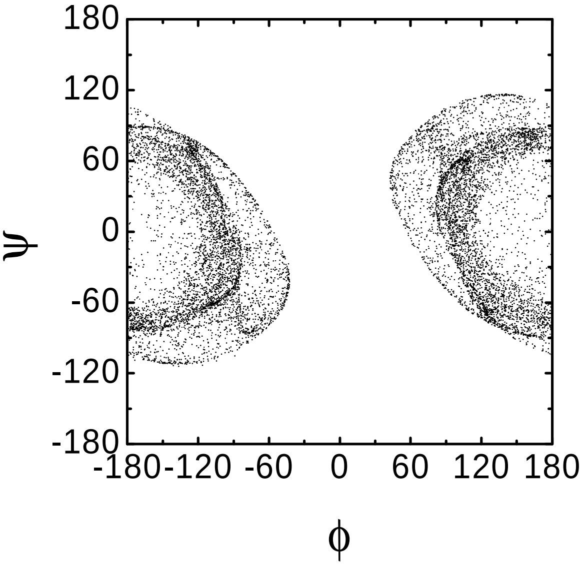

Figure 5.7: Accessible conformational space of a stiff cyclic penta-peptide sampled by 50.000 random structures closed to ring. The (ϕ,ψ) dihedral angles are allowed to vary freely while all other internal coordinates (i.e. bond lengths, bond angles, and dihedral angle of the peptide bond itself) are kept fixed to standard values. Since each group in the hypothetical cyc(Gly$_5$) molecule is identical, the accessible (ϕ_i,ψ_i) space of all site i is the same.

When not specified otherwise, the molecule shown in Fig. 5.8 is used as an arbitrary reference structure. To obtain this reference structure, the dihedral angles reported by Kessler and coworkers for cyc(RGDfV) [287] have been used as a starting point. However, since these dihedral angles do not yield a closed ring in the stiff structure model used here (since other coordinates deviate from the idealized values), the structure has subsequently been closed to a ring, yielding the structure shown in Fig. 5.8 (see also Tab. 5.1).

For a given structure, i.e. for a given set of (ϕ,ψ) dihedral angles, 2D spectra were calculated along the lines of Ref. [2]. Briefly, the one-exciton Hamiltonian

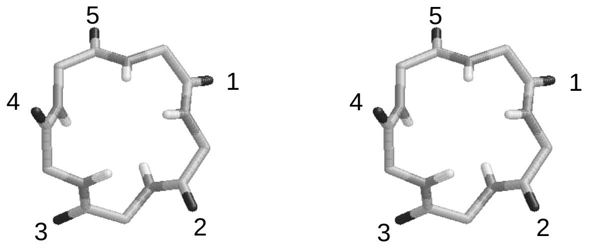

Figure 5.8: Stereo view of the reference structure (see also Tab. 5.1).

	#1	#2	#3	#4	#5
ϕ	-142.2°	120.9°	-129.8°	137.0°	-115.4°
ψ	62.4°	-48.3°	50.2°	-60.8°	-37.8°

Table 5.1: Dihedral angles of the reference molecule.

was

$$H = \begin{pmatrix} \varepsilon_1 & \beta_{12} & \beta_{13} & \beta_{14} & \beta_{15} \\ \beta_{21} & \varepsilon_2 & \beta_{23} & \beta_{24} & \beta_{25} \\ \beta_{31} & \beta_{32} & \varepsilon_3 & \beta_{34} & \beta_{45} \\ \beta_{41} & \beta_{42} & \beta_{43} & \varepsilon_4 & \beta_{45} \\ \beta_{51} & \beta_{52} & \beta_{53} & \beta_{54} & \varepsilon_5 \end{pmatrix} \tag{5.16}$$

from which the two-exciton Hamiltonian could readily be constructed [2]. Without isotope labelling, all diagonal elements ε_i of the coupling Hamiltonian, i.e. the intrinsic frequencies of the C=O groups, were equally set to 1650 cm^{-1} since the chemical environment of all C=O groups is identical in cyc(Gly$_5$). This may be considered a worst case scenario since the spectra do not resolve in separated bands (Fig. 5.9a) in this case. In a real polypeptide with different amino acids, the diagonal elements would vary due to 'chemical shifts' but these effects are commonly weak. ^{13}C-isotope labelling was taken into account by lowering the diagonal term of the corresponding peptide unit by -37 cm^{-1}. According to a Gaussian calculation [228] of N-methyl-acetamide (NMA) on the (B3LYP, 6-31+G*) level, ^{12}C^{18}O labelling yields a shift of -27 cm^{-1} (frequency scaling factor 0.95) and ^{13}C^{18}O a frequency shift of -69 cm^{-1}.

The off-diagonal terms β_{ij} of the coupling Hamiltonian depend on the structure of the molecule. When not specified otherwise, the couplings were calculated according to the transition *charge* coupling model [283, 249, 166], which is a straight forward extension of the transition *dipole* coupling (TDC) model [139, 140], but avoids the limitations of the dipole approximations. In the transition charge coupling model, Mulliken point charges and Mulliken point charge flows are assigned to each atom of a peptide unit, which, when vibrating, gives rise to an oscillating electric field, which interacts with that of a second peptide unit. The parametrization has been obtained from a Gaussian calculation of N-methyl-acetamide (NMA) on the (B3LYP, 6-31+G*) level, the smallest molecule with a peptide unit [283]. It has been verified in Ref. [166] that the transition charge coupling model reveals realistic couplings despite of its low computer costs.

The one- and the two-exciton Hamiltonian were diagonalized and the transition dipole moments between all eigenstates were calculated, yielding 2D-IR spectra in a straight forward manner [2]. The appropriate direction cosines between pumped and probe transition dipoles gave rise to the polarization dependence of the 2D-IR spectra [283, 3]. All 2D-IR spectra were calculated on a 30×30 grid with a spectral resolution of 3.3 cm^{-1}.

Homogeneous and inhomogeneous broadening have been modelled after experimental results. To account for homogeneous broadening, each transition contributing to the absorption spectrum and the 2D-IR spectra has been convoluted with a Lorentzian line shape with a width of 10 cm^{-1} (FWHM) [261, 247]. Two sources of inhomogeneous broadening have been considered: The diagonal terms of the coupling Hamiltonian vary due to interaction with surrounding solvent molecules, and the off-diagonal terms vary since the structure of the molecule fluctuates around a mean structure. To account for the first effect, each C=O frequency was distributed from a Gaussian function with standard deviation 10 cm^{-1} [261, 247] around its average value (1650 cm^{-1} for non-labelled amino acids and correspondingly lower for isotope labelled amino acids). Individual peptide units were treated as uncorrelated. In addition, an ensemble of structures around the given set of (ϕ_i, ψ_i) dihedral angles was calculated with a standard deviation of 20° [259, 74]. Deviations of different dihedral angles, as well as the resulting coupling terms, were correlated due to the subsequent ring-closure of the sample structures. Integration over the inhomogeneous distribution was performed by Monte Carlo sampling. Because of computer time limitations, the Monte Carlo integration was performed with 1000 samples for the calculation of the reference spectra and only 100 during the optimization loop. Therefore, the resulting 2D-IR spectra are noisy, limiting the accuracy of the determined structures to about 5° (see Sec. 5.2.4). We shall see that this amount of noise is not the limiting issue in the present work.

The 2D-IR spectra were the only information used to reconstruct the reference structure. The mean least square (χ^2) of all individual data points of the 2D-spectra was used as fit quality criteria:

$$\chi^2 = \frac{1}{N_{sp} \cdot N_{data}} \sum_{i=1}^{N_{sp}} \sum_{j=1}^{N_{data}} (I_{ij} - I_{ij,ref})^2 \qquad (5.17)$$

where I_{ij} is the 2D response. The index i runs over all 2D-IR spectra considered (i.e. parallel and perpendicular 2D-IR spectra of the isotopomers considered in a particular case study) while j runs over all grid points of the 2D-IR spectra. When not noted otherwise, parallel and perpendicular 2D-IR spectra were weighted equally in the fit and the absorption spectra were discarded.

As a simple and robust optimization procedure, a simulated annealing algorithm based on a downhill simplex method was employed [327]. Briefly, the algorithm uses a Metropolis Monte Carlo trajectory, where the gradient of χ^2 is estimated from a simplex. Note that one cannot calculate first derivatives of χ^2 with respect to the (ϕ_i, ψ_i) dihedral angles, limiting the applicability of most optimization algorithms. To estimate a starting and end 'temperature' in the simulated annealing algorithm, the mean χ^2 of a set of random structures and that of the reference structure was calculated. The latter was not $\chi^2 = 0$ due to the noise of the Monte Carlo integration over the inhomogeneous distribution (see above). The simulated annealing temperature was decreased exponentially with a cooling rate that was adjusted such that the algorithm found the global minimum with about 95% probability when fitting the spectra of all single ^{13}C labelled isotopomers simultaneously (i.e. the case with the best defined global minimum, see Sec. 5.2.4). Between 10 to 20 individual simulating annealing runs were performed for each case study, each starting from a random structure. One simulating annealing run typically took 3-4 hours on a 1.7 GHz pentium processor.

The quality of the result of a simulated annealing run was measured in terms of the standard deviation of all ten (ϕ, ψ) dihedral angles of the closed ring:

$$\delta\varphi = \sqrt{\frac{1}{10} \sum_{i=1}^{10} (\varphi_i - \varphi_{i,ref})^2} \qquad (5.18)$$

where φ is either ϕ or ψ. The differences $\varphi_i - \varphi_{i,ref}$ were calculated modulo 360° to account for their periodicity. Since 2D-IR spectroscopy cannot distinguish between enantiomeric pairs (i.e. a transformation $(\phi_i, \psi_i) \rightarrow (-\phi_i, -\psi_i)$ for all amino acids), the fit algorithm occasionally converged to the enantiomer of the reference structure. Hence, for each structure (ϕ_i, ψ_i), the error $\delta\varphi$ was calculated for both (ϕ_i, ψ_i) and $(-\phi_i, -\psi_i)$ and the enantiomer with the smaller error $\delta\varphi$ was considered to be the result.

5.2.4 Results

Using the ingredients described in the previous paragraph, absorption spectra (top row) and 2D-IR spectra with parallel (2nd row) and perpendicular (3rd row) polarization of pump and probe pulse have been calculated. Fig.. 5.9 shows the result for the non-isotope labelled compound as well as of all single ^{13}C labelled isotopomers of the reference molecule. The stick spectra underneath the absorption spectra indicate the positions and strengths of the individual absorption lines if no homogeneous or inhomogeneous broadening were present. The splittings of the vibrational eigenstates of the non-isotope labelled compound (Fig. 5.9a) are a result of couplings between individual C=O groups, since no 'chemical shifts' have been assumed (i.e. all diagonal elements are equal) . However, these splittings are too small to survive homogeneous and inhomogeneous broadening, so that the absorption and the 2D-IR spectra are largely structure-less. In the case of single ^{13}C labelling, however, one transition is clearly split off (Fig. 5.9b-e).

One of the improvements of 2D-IR spectroscopy over linear spectroscopy is the additional information contained in the cross peaks. If the five transitions were not coupled to each other, the parallel and perpendicular 2D-IR spectra would be identical except for an overall factor of 3. However, parallel and perpendicular polarization experiments yield different 2D-IR response, indicating that cross peaks do indeed contribute, although they are not directly evident as separate signals due to the strong homogeneous and inhomogeneous broadening. The ratio of parallel and perpendicular polarization of the diagonal peak is expected to be 3 (i.e. anisotropy 0.4), as the same transition is pumped as probed, while the off-diagonal anisotropy is in general smaller, depending on the angle between the transition dipoles of the corresponding states on the diagonal [283, 3]. To highlight the cross peak contribution, we show the weighted difference of perpendicular and parallel polar-

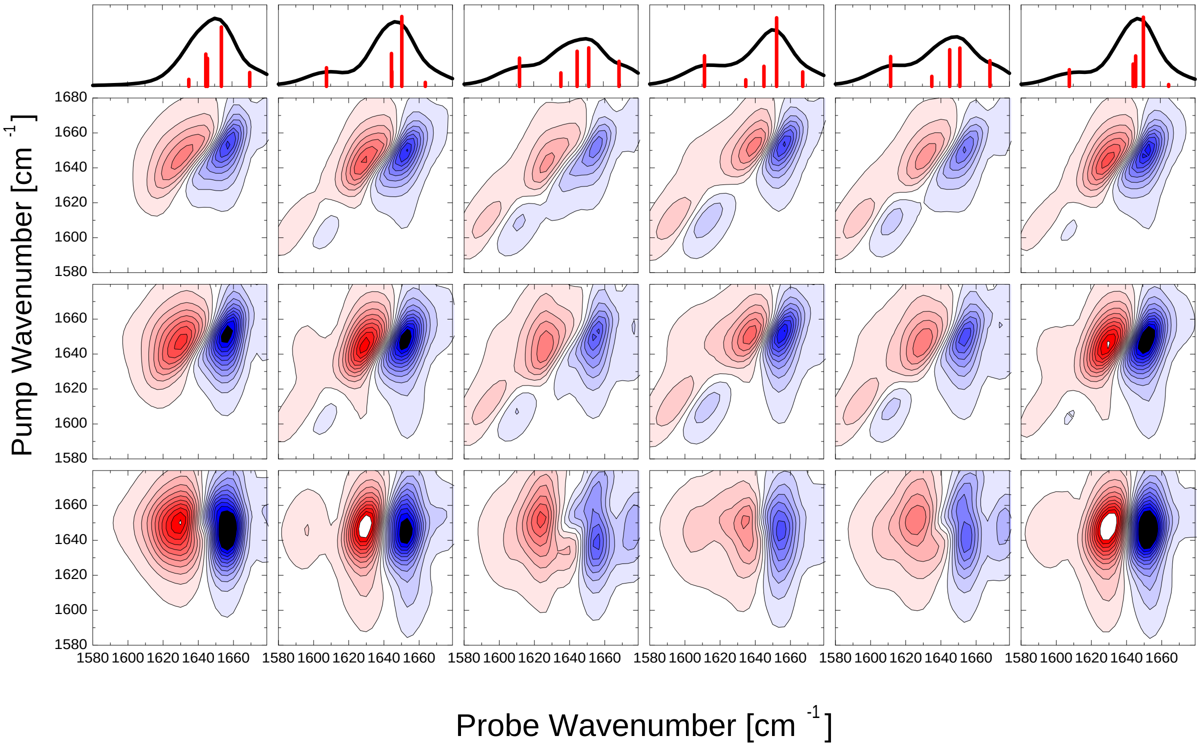

Figure 5.9: Absorption spectra (top row) and 2D-IR spectra with parallel (2^{nd} row) and perpendicular (3^{rd} row) polarization of pump and probe pulse as well as the weighted difference of both ($\perp - 1/3 \cdot \|$, bottom row). (a) Spectra of the non-labelled and (b-e) all single ^{13}C labelled isotopomers of the reference molecule shown in Fig. 5.8, respectively. The stick spectra underneath the absorption spectra indicate the position and strength of the individual absorption lines without any homogeneous and inhomogeneous broadening. The contour lines in the 2D-IR spectra represent a linear scale. Blue colors indicate negative 2D-IR response, red colors positive 2D-IR response. The scale of the spectra with perpendicular polarization is magnified by a factor 3, that of the ($\perp - 1/3 \cdot \|$) difference 2D-IR spectra by a factor of 10.

ization 2D-IR spectra ($\perp - 1/3 \cdot \|$) in Fig. 5.9 bottom row), a representation which suppresses the otherwise dominating diagonal contribution [3]. As expected, the diagonal peak of the low-frequency peak separated by ^{13}C labelling disappears, while a signal of the main band remains in the diagonal region. The latter signal reflect the (unresolved) cross peaks between the overlapping transitions that lie underneath the main band. Cross peaks between the main band and the split-off bands become clearly evident in the representation of Fig. 5.9 bottom row.

In a first step, it shall be explored whether the full set of isotopomers determines the structure of a cyclic penta-peptide unambiguously, assuming that the molecule exist only in one conformation. To this end, all single ^{13}C labelled isotopomers were fitted simultaneously. The spectra of the non-labelled compound provide no structure resolution power and hence were discarded in the fits. The penalty function χ^2 (Equ. 5.17) defines an *artificial potential energy surface*, which the molecule samples during the simulated annealing run (note again that no MM force fields have been used in the simulation). To illustrate the steepness of this potential energy surface, i.e. the definiteness of the structure determination, plots of the kind shown in Fig. 5.10 are used, where the penalty function χ^2 is plotted against the deviation from the reference structure $\delta\varphi$ (Equ. 5.18). In that way, the 4-dimensional conformational space is projected onto one dimension $\delta\varphi$. The dots in Fig. 5.10 represent all conformations sampled during the 20 independent simulated annealing runs. The dots are expected to scatter for large $\delta\varphi$ since many conformations with the same $\delta\varphi$, but not necessarily the same 2D-IR spectra, i.e. not necessarily the same χ^2, exist. For shrinking $\delta\varphi$, however, the scatter decreases since the

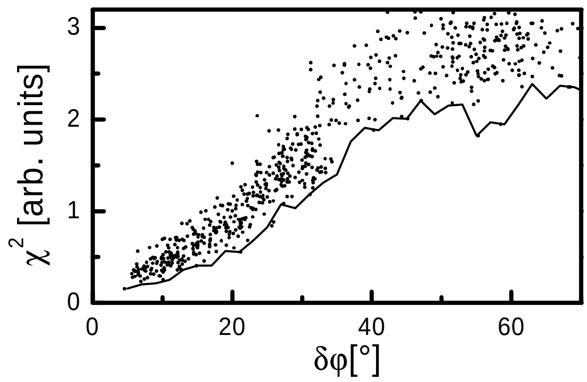

Figure 5.10: The penalty function χ^2 as a function of the deviation from the reference structure δφ. The dots represent all conformations visited during the 20 independent simulated annealing runs when fitting the 2D-IR spectra of all 5 isotopomers of the cyclic penta-peptide simultaneously. The line highlights the lowest value of χ^2 for a particular δφ.

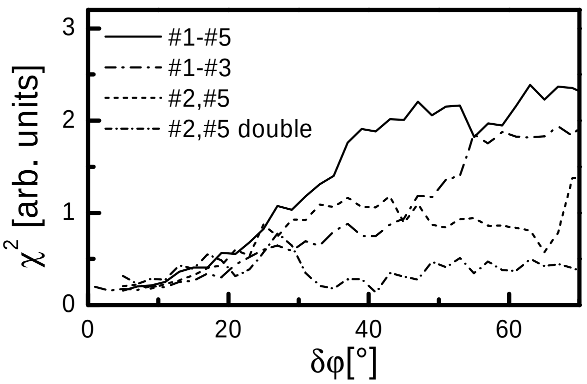

Figure 5.11: The penalty function for a simultaneous fit of isotopomer #1-#5 (solid line, as in Fig 5.10), of isotopomer #1-#3 (long dashed-dotted line) and isotopomer #2 and #5 (dotted line). The penalty function of a double ^{13}C labelled molecule at position #2 and #5 is shown as well (short dashed-dotted line).

volume of the conformational space decreases. χ^2 would be zero for $\delta\varphi = 0°$, if the calculation of the 2D-IR spectra were noise-free. The residual χ^2 still present for small δφ is a result of the noise of the Monte Carlo integration over the inhomogeneous distribution (see Sec. 5.2.3), and limits the accuracy of the structure determination to about $\delta\varphi = 5°$.

The line in Fig. 5.10 represents the lowest value of χ^2 found for a particular angle deviation δφ. This line can be understood as an *artificial 'funnel'*, on which the molecule finds its global minimum. When fitting all five isotopmers simultaneously, as in Fig. 5.10, the artificial funnel is steep with a well defined global minimum for $\delta\varphi \rightarrow 0$. No pronounced side minima exist, which would trap the optimization procedure. The global minimum has been found in 19 of 20 simulating annealing runs after typically 1000-1500 single search steps.

Variation of the Isotope Composition

It is desirable to reduce the number of isotopomers, since each isotopomer would have to be synthesized separately in a real experiment. Therefore, it shall be explored to what extent an as small as possible subset of isotopomers still would define the molecular structure sufficiently unequivocally. Fig. 5.11 compares the penalty function for the best determined problem with five single ^{13}C labelled isotopomers (solid line, as in Fig. 5.10) with that of reduced sets of isotopomers. The parameters of the simulated annealing procedure were the same in all cases. Fig. 5.11 (long dashed-dotted line) shows the result of a simultaneous fit of three single labelled peptides at position #1 to #3 (see Fig. 5.8 for the numbering). The penalty function is not as steep as in the case of fitting all five isotopomers, but it stills defines the global minimum very well and exhibits *no* side minima. All but two of the ten possible permutations of three single ^{13}C labelled isotopomers yielded a similarly well defined minimum.

However, when further reducing the number of isotopomers to two (e.g. #2 and #5, dotted line), the inversion problem starts to become ill-defined. That is, a pronounced side minimum at $\delta\varphi \approx 60°$ shows up, the energy of which is not significantly larger than that of the global minimum. This side minimum trapped the optimization procedure in 4 of 20 simulation annealing runs while the global minimum was found only in 8 cases. The remaining 8 simulation annealing runs got stuck in between where the penalty function is flat. One could of course increase the success rate of the search procedure by slowing down the cooling rate in the simulated annealing, but the result clearly demonstrates that a structure determination with only two isotopomers will be less robust. Of the ten possible permutations with two single ^{13}C labelled isotopomers, only one combination (#1 and #5) revealed a reasonably steep penalty function (Fig. 5.12, solid line). No systematic order could be identified, which would explain why exactly this combination is most expressive.

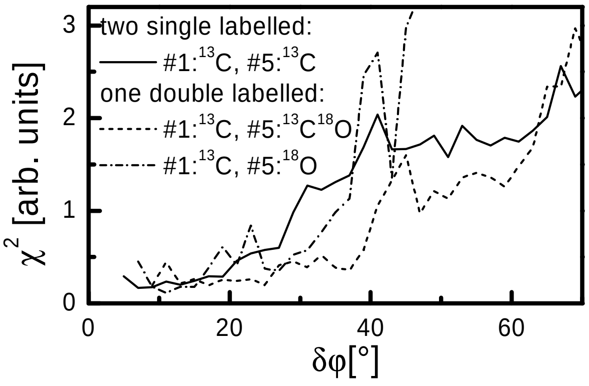

Figure 5.12: Comparison of the penalty function from a simultaneous fit of two single ^{13}C labelled isotopomers at position #1 and #5 (solid line) with that of one mixed double labelled isotopomer at the same positions. The dotted line shows the result of ^{13}C labelling at position #1 and ^{13}C^{18}O labelling at position #5, the dashed-dotted line that of ^{13}C labelling at position #1 and ^{18}O labelling at position #5. The scale of χ^2 is the same as in Fig. 5.10.

Two single ^{13}C labelled isotopomers are still significantly more expressive than one double ^{13}C labelled isotopomer (Fig. 5.11, short dashed-dotted line). In the latter case, the penalty function is essentially flat and doesn't reveal the structure anymore. Not all permutations with double ^{13}C labelled isotopomers have been checked. However, in none of the cases checked double ^{13}C labelling offered an advantage over single ^{13}C labelling.

As another approach, the usefulness of ^{18}O labelling has been investigated. The frequency shift of ^{12}C^{18}O labelling (-27 cm^{-1}) and ^{13}C^{18}O labelling (-69 cm^{-1}) is different from that of ^{13}C^{16}O labelling, and hence, one may separate two bands from the main band in a way that they do not overlap. The result of mixed ^{13}C^{16}O-^{12}C^{18}O and ^{13}C^{16}O-^{13}C^{18}O double labelling is shown in Fig. 5.12. The penalty function from a simultaneous fit of two single ^{13}C labelled isotopomers at position #1 and #5 (solid line), the only combination of two with a well defined minimum, is compared with that of both mixed double labelled isotopomer at the same positions. The penalty functions are very similar in all three cases, suggesting that the information content of the 2D-IR spectra of two single ^{13}C labelled molecules is similar as that of one mixed double labelled molecule.

Information Content of 1D-IR Spectroscopy

The structure of the molecule determines the coupling Hamiltonian Eq. 5.16, and hence, the linear absorption spectra and the 2D-IR spectra at the same time. The cross peak contribution of the 2D-IR spectra reveal information that is not contained in the linear spectra, i.e. the strength of the coupling between two sites and the angle between the corresponding transition dipoles. However, the cross peaks are weak, and one might ask whether the structure information is already contained in the dominating diagonal contribution, which would include no other information but the linear spectra alone. In order to clarify this question, we compare in Fig. 5.13 the penalty function when fitting the parallel and perpendicular spectra simultaneously (solid line, as in Fig.5.12), when fitting the $(\perp - 1/3 \cdot \|)$ difference 2D-IR spectra (dashed dotted line) or when fitting only the linear spectra (dotted line). This is done for ^{13}C isotopomers single labelled at position #1 and #5, the only combination of two isotopomers which reveals a steep, well defined minimum (see Sec. 5.2.4). When fitting the linear spectra solely (dotted line), the problem clearly is ill-defined. On the other hand, when fitting the $(\perp - 1/3 \cdot \|)$ difference 2D-IR spectra (dashed dotted line), the information content is essentially the same as when fitting both polarization spectra simultaneously (solid line), as expected. Hence, in the case of two isotopomers, it is indeed the weak cross peak contribution which adds the information content needed to determine the structure unambiguously. However, it should be noted that in the case of fitting all five isotopomers simultaneously, the problem is over-determined and the linear absorption spectra alone are sufficient.

Robustness of 2D-IR Structure Determination

The molecular model used to calculate a 2D-IR spectrum for a given structure will always be based on approximations, the quality of which is difficult to estimate. Therefore, in order to make 2D-IR spectroscopy a reliable method, it has to be robust, that is, a small systematic error in the molecular model should reveal a structure that deviates only little from the real structure. Only then one can hope to obtain increasingly more accurate structures for increasingly more sophisticated coupling models.

To test the robustness of 2D-IR structure determination, another case study has been performed. The tran-

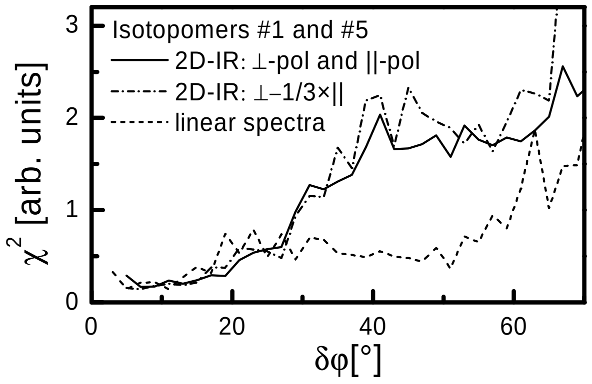

Figure 5.13: Comparison of the penalty function χ^2 as a function of the deviation $\delta\varphi$ from the reference structure when fitting the parallel and perpendicular spectra simultaneously (solid line, as in Fig.5.12), when fitting the $(\perp - 1/3 \cdot \|)$ difference 2D-IR spectra (dashed dotted line) or when fitting only the linear spectra (dotted line). Only isotopomers #1 and #5 were considered. In the case of a simultaneous fit of parallel and perpendicular spectra (solid line), the scale of χ^2 is the same as in Fig. 5.10. The scale is arbitrary in the other two cases, and has been re-normalized so that the noise of the reference structure $\delta\varphi = 0$ is equal in all three cases.

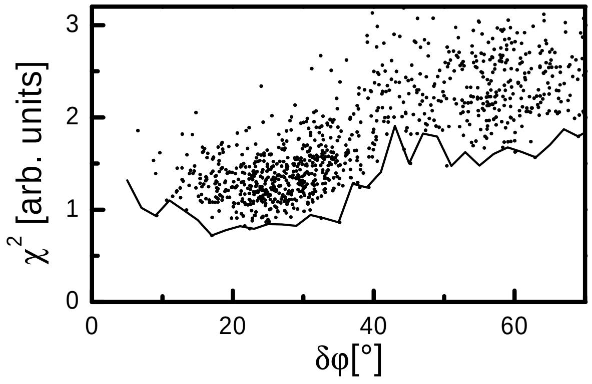

Figure 5.14: The penalty function χ^2 as a function of the deviation $\delta\varphi$ from the reference structure. The transition charge model was used during calculation of the 2D-IR spectra of the reference structure, while the more crude transition dipole model was used during the optimization loop. All five ^{13}C single labelled isotopomers were used. The scale of χ^2 is the same as in Fig. 5.10.

sition *charge* model was used during calculation of the 2D-IR spectra of the reference structure, while the more crude transition *dipole* model was used during the optimization loop. The (ϕ,ψ) dependence of the coupling of neighbors in the peptide chain predicted from both models has been compared in detail in Ref. [166]. In the (ϕ,ψ) regions accessible to the constraint cyclic pentapeptide (Fig. 5.6), the overall pattern of the coupling exhibit some similarity, but differ significantly in detail.

The resulting penalty function is shown in Fig. 5.14. In contrast to the previous cases, the reference structure $\delta\varphi \to 0$ does not correspond to a minimum of χ^2 anymore. Nevertheless, the penalty function still exhibits a well defined global minimum around $\delta\varphi \approx 20°$. Fig. 5.15 shows an overlay of the original reference structure and the minimum structure. Both structures differs only little despite the crudeness of the transition dipole model. Hence 2D-IR spectroscopy is robust in the sense of the definition given above.

The coupling terms calculated for the reference structure for both coupling models deviate by 2.2 cm^{-1} in average (rms). The deviation is even slightly larger when comparing the reference structure in the transition charge coupling model with that of the newly generated structure in the transition dipole coupling model (2.4 cm^{-1} rms). It is not solely the coupling constants which carry the structure information. A closer analysis shows that it is a combination of the coupling constants with the orientations of the transition dipoles which distinguishes the structure to which the algorithm converged. One can show that the center of gravity (i.e. the first moment) of the absorption spectrum:

$$M \equiv \frac{\sum_k |\vec{\mu}'_k|^2 \varepsilon'_k}{\sum_k |\vec{\mu}'_k|^2}. \qquad (5.19)$$

can be calculated without explicitly diagonalizing the Hamiltonian Equ. 5.16 (see Appendix):

$$M = \frac{\sum_{i\neq j} \vec{\mu}_i \vec{\mu}_j \beta_{ij} + \sum_i |\vec{\mu}_i|^2 \varepsilon_i}{\sum_i |\vec{\mu}_i|^2}. \qquad (5.20)$$

In Equ. 5.19, the transition dipoles $\vec{\mu}'_k$ and eigenvalues ε'_k are defined in the eigenstate basis, while $\vec{\mu}_i$ and ε_i are defined in the site basis in Equ. 5.20. The position of the center of gravity of the absorption spectrum relative to the diagonal elements of the coupling Hamiltonian depends on the off-diagonal coupling elements β_{ij} times the cosines of the angles between the transition dipoles in the site basis $\vec{\mu}_i\vec{\mu}_j$. In the limits of the approximations used here, both β_{ij} and $\vec{\mu}_i\vec{\mu}_j$ modify the center of gravity of the absorption spectrum when varying the structure of the molecule, but the second term $\sum_i |\vec{\mu}_i|^2 \varepsilon_i$ stays constant by construct. The shift $\sum_{i\neq j} \vec{\mu}_i\vec{\mu}_j\beta_{ij} / \sum_i |\vec{\mu}_i|^2$

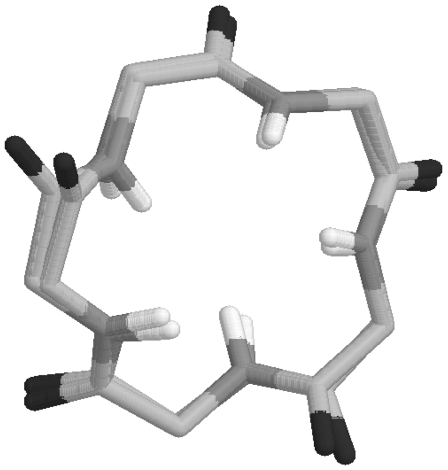

Figure 5.15: Overlay of the reference structure and the structure to which the algorithm converged, using the transition charge model for the reference molecule and the transition dipole model during the optimization. The deviation of both structures is only $\delta\varphi = 20°$, emphasizing the robustness of the structure determination with respect to the coupling model.

is +0.9 cm^{-1} for the reference structure in transition charge coupling model, -2.9 cm^{-1} for the reference structure in transition dipole coupling model and -0.5 cm^{-1} for the structure to which the algorithm converges in the transition dipole coupling model. Hence, the optimization algorithm tries to at least partially restore the shift of the center of gravity of the absorption spectrum, and consequently also that of the 2D-IR spectra.

Mixture of Conformations

Finally, in order to test the capability of 2D-IR spectroscopy to disentangle a mixture of conformations, a second reference structure with flipped turn around site #4 and #5 has been chosen (Tab. 5.2). Such flips are very likely to occur in reality [285, 286, 287, 288, 289]. 2D-IR spectra of a 80%/20% and a 50%/50% mixture of both reference structures have been calculated. Using only these 2D-IR spectra as input information, it was again attempted to reconstruct the original structures in the same way as before. This time, however, the free fit parameters were the two sets of dihedral angles for each structure as well as the mixing ratio. All five ^{13}C single labelled isotopomers were used in this case study.

In the case of a 50%/50% mixture, the penalty function is flat and does not have any defined minimum anymore (Fig. 5.16, dotted line). The information content is blurred too much by averaging over the 2D-IR spectra of two molecules and the original structures cannot be reconstructed anymore. However, in the case of a 80%/20% mixture, the conformation of the dominating species is still defined, while that of the minor species is not. Shown in Fig. 5.16 is the penalty function of the dominating species only (solid line), which exhibits a distinct minimum for $\delta\varphi \rightarrow 0$.

Table 5.2: Dihedral angles of the second reference molecule.

	#1	#2	#3	#4	#5
ϕ	-139.3°	119.5°	-139.2°	-125.4°	125.6°
ψ	67.3°	-39.2°	52.4°	54.1°	-40.4°

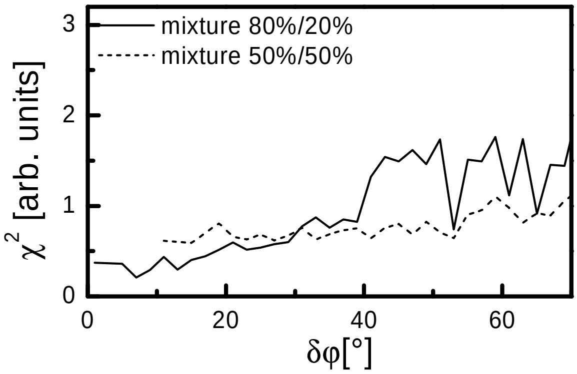

Figure 5.16: Penalty function for a 80%/20% mixture (solid line) and a 50%/50% mixture (dotted line). All five ^{13}C single labelled isotopomers were used. The scale of χ^2 is the same as in Fig. 5.10.

5.2.5 Discussion and Conclusion

The present paper explores the structure information content of 2D-IR spectroscopy of the amide I band. With the help of case studies, it is investigated to what extent 2D-IR spectroscopy of a set of isotopomers of a cyclic penta peptide can reveal its conformation unambiguously. Realistic parameters for the couplings between individual peptide units as well as for homogeneous and inhomogeneous broadening have been used. The latter severely reduce the structure information content by blurring the various cross peaks in a 2D-IR spectrum to an extent that the structure resolution power in the case of a non-isotope labelled molecule is essentially zero. However, 2D-IR spectroscopy can reveal the structure of the peptide in a unique way if using a sufficiently large set of isotopomers. Then, the structure can be determined even under non-ideal conditions, i.e. if systematic errors in the coupling model are allowed, or if the molecule exists in various conformations simultaneously. However, it will be difficult to predict beforehand, the labelling of which sites defines a structure best. In the present case it turns out to be #1 and #5, which is the only combination of two single ^{13}C labelled peptides that works. When choosing three arbitrary single ^{13}C labelled isotopomers, however, the chances are almost 100% that the structure is defined uniquely.

Double ^{13}C labelling does not offer any advantage compared to single ^{13}C labelling, since the two bands that are separated from the main band still overlap. However, mixed $^{13}C^{16}O$-$^{12}C^{18}O$ or $^{13}C^{16}O$-$^{13}C^{18}O$ double labelling is advantageous. From the practical point of view, one then would have to synthesize one isotopomer less on the expense of a more complicated synthesis, since ^{18}O labelled amino acids are more difficult to obtain (they are not available commercially) [325]. Although one mixed double labelled molecule provides the same information content as two single labelled molecules in terms of its global structure, it will still be advantageous in resolving local structure around the labels. This is since the coupling and anisotropy between two groups would be unambiguously determined in the case of one mixed double labelled molecule while it would not in the case of two single labelled molecules.

The current study does not employ any MM force field, but uses the information content from the 2D-IR spectra only. All conformations in the (ϕ,ψ) space are considered to be energetically equivalent. In reality, however, only a small portion of the (ϕ,ψ) space is sterically possible [321]. Hence, the volume of the search space could be reduced significantly by adding the information from a realistic MM force field. In that case, one would compute the potential energy surface on which the peptide moves during the optimization procedure as a weighted sum of the MM potential and the same penalty function used here. This approach is very common also in x-ray and NMR structure analysis [328] and will be discussed in a future work. The robustness of 2D-IR spectroscopy can be significantly improved when combining it with a MM force field.

The intrinsic structure resolving ability of 2D-IR spectroscopy is limited by the accuracy of the models of the coupling Hamiltonian and the line shapes, by the experimental noise of the collected spectra, and by homogeneous and inhomogeneous broadening. The present study circumvents the first three unknowns, and focuses on the loss of information due to blurring the various 2D-IR signals by the strong broadening in the solution phase. When we could resolve each cross peak separately, we could collect of the order of $O(n^2)$ pieces of information for each isotopomer (where n is the number of peptide units). With n isotopomers like in Fig. 5.10, this adds up to the order of $O(n^3)$ pieces of information in total. On the other hand, the coupling Hamiltonian Eq. 5.16 together with the transition dipole matrix ($M_{ij} = \vec{\mu}_i\vec{\mu}_i$) contain only of the order of $O(n^2)$ elements, a parameter space, which has been even further reduced to the order of $O(2n)$ dihedral angles by making use of the molecular structure of the peptide backbone. Hence, in an ideal situation without any homogeneous and inhomogeneous broadening, the problem would be heavily over-determined ($O(n^3)$ versus $O(2n)$). In that case, even the linear absorption spectra (1D-IR spectra) of n isotopomers, providing of the order of $O(2n^2)$ pieces of information, would already define the structure unambiguously.

A significant fraction of the $O(n^3)$ pieces of information of the 2D-IR spectra is lost due to homogeneous and inhomogeneous broadening. It is nevertheless sufficient to reconstruct the structure in an unique way when fitting all five isotopomers simultaneously (Fig. 5.10). In fact we found that the problem is still over-determined and also the linear absorption spectra allow one to determine the structure under this still very idealized circumstances. Nevertheless, 2D-IR spectroscopy adds important additional information (see Sec. 5.2.4 and Fig.5.13), which provides the redundancy needed to make 2D-IR spectroscopy a robust method in a real, non-ideal, experiment with many unknowns, where the underlying coupling models are not necessarily exact. In particular, the angle information contained in the cross peak anisotropy, an information which can be obtained only with 2D-IR spectroscopy and not with linear spectroscopy, is the most direct and model-insensitive structure parameter.

We have recently started to perform transient 2D-IR spectroscopy on a cyclic octa peptide, the conformation of which can be switched on an ultrafast picosecond time scale with the help of a photo-switchable azo-moiety included in the peptide backbone [174]. Since the amide-I band of this peptide is not resolved into individual sub-bands, the discussion of the transient 2D-IR spectrum was limited to effects of homogeneous and inhomogeneous broadening. However, combined with site specific isotope labelling, transient 2D-IR spectroscopy may provide detailed information on the three-dimensional structure of the molecule during the conformational transition and help to construct a molecular movie. The present work provides solid design strategies for isotope labelling to approach this task.

Acknowledgements: We thank Gerhard Stock for carefully reading the manuscript and for illuminating discussions, and the anonymous referee for an important comment. The work has been supported by the Swiss Science Foundation (2100-067573.02/1)

5.2.6 Appendix: First Moment of an Excitonic Absorption Band

Treating the amide-I vibrational spectrum as an excitonic absorption band, the corresponding vibrational eigenstates ψ_k of the peptide can be written in a site basis ϕ_i of amide-I states localized on single peptide units

$$\psi_k = \sum_i \phi_i Q_{ik}. \tag{5.21}$$

The transition dipole moment $\vec{\mu}'_k$ of the k^{th} eigenstate can be expressed in terms of the site transition dipoles $\vec{\mu}_i$

$$\vec{\mu}'_k = \sum_i \vec{\mu}_i Q_{ik}. \tag{5.22}$$

The absolute value of the overall transition dipole moment of the absorption band is

$$\sum_k |\vec{\mu}'_k|^2 = \sum_{ij} \vec{\mu}_i \vec{\mu}_j \underbrace{\sum_k Q_{ik} Q_{jk}}_{\delta_{ij}} = \sum_i |\vec{\mu}_i|^2, \tag{5.23}$$

reflecting its invariance under a basis transformation. The center of gravity of the absorption band, i.e. its first moment, is given by

$$M \equiv \frac{\sum_k |\vec{\mu}'_k|^2 \varepsilon'_k}{\sum_k |\vec{\mu}'_k|^2}, \tag{5.24}$$

which, when inserting Equ. 5.22 and Equ. 5.23, yields

$$M = \frac{\sum_{ij} \vec{\mu}_i \vec{\mu}_j \sum_k Q_{ik} \varepsilon_k Q_{jk}}{\sum_i |\vec{\mu}_i|^2}. \tag{5.25}$$

This can be expressed in terms of the matrix elements β_{ij} and ε_i of the one-exciton Hamiltonian H of Equ. 5.16 to obtain Equ. 5.20

$$M = \frac{\sum_{i\neq j} \vec{\mu}_i \vec{\mu}_j \beta_{ij} + \sum_i |\vec{\mu}_i|^2 \varepsilon_i}{\sum_i |\vec{\mu}_i|^2}. \tag{5.26}$$

Assuming the diagonal elements ε_i being constant under change of structure it is clear from this notation, that the shift ΔM of the absorption band (i.e. the change in the first moment) does not depend on the value of the diagonal elements

$$\Delta M = \frac{\sum_{i\neq j} \vec{\mu}_i \vec{\mu}_j \beta_{ij}}{\sum_i |\vec{\mu}_i|^2}. \tag{5.27}$$

The β_{ij} and, of course, the $\vec{\mu}_i$ depend on the structure of the investigated excitonic system. Within the framework of simple models connecting these parameters to the molecular geometry, like transition charge coupling or transition dipole coupling does, the shift upon structural change can be directly obtained from Equ. 5.27. This relation might also prove useful in the discussion of electronic absorption spectra of delocalized systems like antenna complexes or *J*-aggregates, providing a simple link between molecular structure and position of the absorption band.

5.3 P10 – Transient Two-Dimensional Infrared Spectroscopy: Exploring the Polarization Dependence

Jens Bredenbeck, Jan Helbing, and Peter Hamm,
J. Chem. Phys, 121:5943–5957, 2004.

5.3.1 Abstract

We present a general expression for the polarization dependence of transient two-dimensional IR spectroscopy (T2D-IR), a technique designed to measure 2D-IR spectra of transient species. T2D-IR is a UV-pump narrowband-IR-pump broadband-IR-probe experiment of 5^{th} order in the laser field which involves up to three different transition dipole moments. The UV pulse adds an additional degree of freedom in polarization as compared to 2D-IR spectroscopy and increases the versatility of signal manipulation and the potential structural information content of the signals. The polarization conditions leading to a maximum of structural information are discussed. Important special cases of polarization conditions are formulated. The application of polarization selectivity is demonstrated for different types of T2D-IR experiments on photo triggered metal-to-ligand charge transfer in the model system [Re(CO)$_3$(dmbpy)Cl].

5.3.2 Introduction

Ultrafast two-dimensional infrared spectroscopy (2D-IR) is a promising tool for the investigation of molecular structures [283, 252, 254, 253] and their equilibrium fluctuations [263, 74, 270, 252, 264]. Similar as in 2D-NMR spectroscopy [244] cross-peaks between coupled states emerge in 2D-IR spectra, revealing structural information [252, 306]. The outstanding feature of 2D-IR spectroscopy is the combination of its structure resolution power with an intrinsic sub-picosecond time resolution, freezing in all but the fastest molecular motions. This makes it particularly suited for application to fast dynamical processes, offering means to resolve distributions and dynamics of fast interconverting structures in *equilibrium* [263, 247, 264]. Highly promising is the extension of the 2D-IR technique to the *non-equilibrium* regime, where its high time resolution can be put to full use [174, 302]. Changes of molecular structures on timescales of ms down to sub-ps can be addressed. First steps in this direction have been reported recently for the picosecond conformational transition of a photoswitchable cyclic peptide [125] employing transient 2D-IR spectroscopy (T2D-IR) [174]. T2D-IR spectroscopy allows to record snapshot 2D-IR spectra of transient species in the course of a photo-triggered event like a photo-reaction or a conformational transition. The reaction or transition is triggered by an additional laser pulse, which can be polarized at wish with respect to the IR pulses constituting the 2D-IR part of the experiment.

To fully explore the possibilities of higher order nonlinear spectroscopies like T2D-IR, their polarization dependence has to be well understood [293, 294, 3, 292, 251]. A detailed discussion of orientational effects in 3rd order and 5th order spectroscopies of a single oscillator has been given by Tokmakoff [293, 294]. The polarization dependence of the most general type of a 3rd order 2D-IR experiment – the heterodyne-detected stimulated IR photon echo – has been discussed by Hochstrasser [292], and it has been demonstrated how polarization can be used to manipulate band intensities in a 2D-IR spectrum [3, 292, 251]. The T2D-IR spectroscopy [174] discussed here is of 5th order in the field. Interactions between three laser pulses and up to three different transition dipole moments take place. In this work we present a general expression for the polarization and transition dipole angle dependence of T2D-IR spectra. We show how polarization can be exploited to enhance or suppress different features in the spectra. Magic angle like conditions, that allow to record spectra free of the effects of rotational diffusion are derived. The signals of maximal structural information content are discussed.

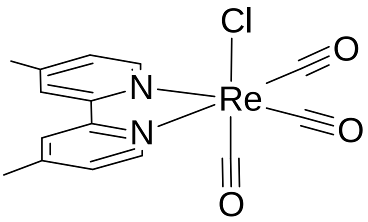

Figure 5.17: [Re(CO)$_3$(dmbpy)Cl].

The polarization effects are illustrated by means of experimental examples. We apply T2D-IR to study metal-to-ligand charge-transfer (MLCT) in [Re(CO)$_3$(dmbpy)Cl] (dmbpy=4,4’-dimethyl-2,2’bipyridine). MLCT in rhenium(I)polypyridyl carbonyls and other metal carbonyls has been studied in considerable detail under various aspects such as solvation dynamics [299], electronic structure [329, 330], photochemistry [331, 332], nonlinear optical properties [333] or the application as luminescent markers [334]. Among many other techniques time-resolved vibrational spectroscopy [335, 299, 331], time-resolved Raman [335], UV-VIS spectroscopy [330] and quantum chemical calculations [329, 330] have been employed. [Re(CO)$_3$(dmbpy)Cl] represents a convenient model system for our prove of principle experiments due to the clear separation of vibrational bands, the long vibrational and the long electronic lifetime.

The paper is organized as follows: Chapter 5.3.3 introduces the basic principles of T2D-IR spectroscopy. An outline of different types of T2D-IR experiments is given in section 5.3.3. Section 5.3.4 briefly describes our experimental setup. In chapter 5.3.5 the theoretical background of the polarization dependence of T2D-IR spectra is explained. We present a general expression for the dependence of the signal on laser polarization and transition dipole angles. It is shown that four linearly independent signals can be obtained to acquire a maximum of structural information (section 5.3.5). We demonstrate that conditions allowing for transient measurements that are unaffected by rotational diffusion - like the magic angle signal in pump-probe spectroscopy - do not exist for the general case of a T2D-IR signal (section 5.3.5). Nevertheless we show how magic angle like conditions can be obtained (i) when only one of the two available delays is scanned at a time (section 5.3.5), (ii) for the case of diagonal peaks (section 5.3.5), and (iii) in the presence of symmetry constraints (section 5.3.5). In section 5.3.6 we introduce our model system [Re(CO)$_3$(dmbpy)Cl] by means of transient IR absorption spectroscopy (T1D-IR) and characterize the molecular structure and the timescales of dynamic effects that are relevant for the T2D-IR experiments discussed subsequently. Section 5.3.6 describes in detail a 2D-IR and a T2D-IR spectrum of [Re(CO)$_3$(dmbpy)Cl] to explain the spectral features we will refer to in our discussion of the polarization dependence of the T2D-IR spectra in chapter 5.3.7. There, two different types of T2D-IR experiments are described in detail with an emphasis on the effects of different polarization conditions.

5.3.3 Principles of T2D-IR Spectroscopy

Outline of the Experiment

The 2D-IR part of the experiment is performed according to our previously described double-resonance scheme [2, 252]: The center frequency of a spectrally tunable, narrow-band IR-pump pulse is tuned across the spectral range of interest. It is followed by a broad-band probe pulse. 2D-IR spectra are constructed as a function of the IR-pump and IR-probe frequency. By addition of a UV pulse preceding the 2D-IR part of the experiment, the 2D-IR spectrum of the electronically excited ensemble can be recorded. Hence, the total T2D-IR experiment consists of 3 pulses: a UV-pump, a narrow-band IR-pump and a broad-band IR-probe pulse.

The T2D-IR experiment as outlined here offers a number of scanning parameters (two delays, two relative polarizations and the IR-pump frequency). It is neither convenient nor desirable to scan the whole parameter space. Instead meaningful experiments representing cuts through this parameter space have to be designed. So far, we could demonstrate three types of T2D-IR experiments [174, 336, 302, 337], each employing one of the three different pulse sequences in Figure 5.18.

The straightforward extension of 2D-IR spectroscopy to the transient regime corresponds to the pulse sequence in Figure 5.18a: After a photo-reaction was initiated by the UV-pump pulse, transient 2D-IR spectra are taken at different UV delay times on the course of the reaction. Information on molecular structure, the anharmonicity of vibrations or the change in homogeneous and inhomogeneous broadening can be accessed for the transient ensemble. This mode of T2D-IR spectroscopy has been applied recently to investigate a photo-isomerizable cyclic octapeptide [174].

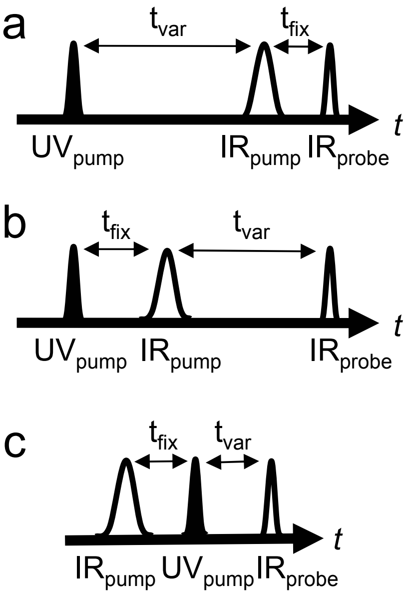

Figure 5.18: Pulse sequences of: a - regular T2D-IR spectroscopy, b - hole burning T2D-IR spectroscopy, c - labelling T2D-IR spectroscopy.

The second scanning mode in Figure 5.18 constitutes a dynamic hole burning experiment on the transient species [336]: At a distinct time after the UV pulse, the narrow-band IR pulse burns a hole into the transient spectrum. The subsequent evolution of the two-dimensional hole in time is then monitored by varying the delay of the broadband probe pulse. In this way ultrafast 2D-IR hole burning experiments can be carried out on a non-equilibrium ensemble that is generated by a trigger pulse [336].

Another useful type of T2D-IR spectroscopy is obtained by exchanging the order of the pulses (pulse sequence Figure 5.18c). The narrow-band IR-pump pulse is now applied before the UV-pump pulse arrives. In this way it is possible to 'label' selectively certain vibrations of the initial state by transferring population from their v=0 to their v=1 state. After triggering a photoreaction with the UV pulse, the subsequent evolution of this label can be monitored. In this way vibrations of the initial and the transient state can be correlated. In a recent work we used this method to achieve an assignment for the MLCT state vibrations of [Re(CO)$_3$(dmbpy)Cl] [302].

5.3.4 Material and Methods

The complex [Re(CO)$_3$(dmbpy)Cl] was prepared according to Ref. [338]. It was dissolved in dimethyl sulfoxide (DMSO) at a concentration of 4 mM. The sample was circulated rapidly through a closed cycle flow cell [182] with an optical path length of 100 μm. MLCT in [Re(CO)$_3$(dmbpy)Cl] was initiated by short (FWHM 400 fs) 390 nm UV-pump pulses (energy 3 μJ/pulse) obtained from a frequency doubled 1 kHz Ti:Sapphire-laser/amplifier system (Spectra-Physics, Spitfire). Intense IR pulses (center frequency between 1960 cm^{-1} and 2050 cm^{-1}, bandwidth 200 cm^{-1} FWHM, duration 150 fs, energy 2.5 μJ) were generated using a white light seeded two-stage BBO optical parametric amplifier, the signal and idler pulses of which were difference frequency mixed in an AgGaS$_2$ crystal [165]. A small fraction of the IR-beam was split off to obtain broadband probe and reference pulses. The remainder was passed through a computer-controlled Fabry-Perot interferometer to generate narrow-band tunable IR-pump pulses (bandwidth $\approx 12\,\text{cm}^{-1}$, tunable between 1860 cm^{-1} and 2070 cm^{-1}). The IR-pump and IR-probe pulses were focused into the sample in spatial overlap with the 390 nm UV-pump pulse (the reference pulse was focused 1 mm upstream in the flow cell). Probe and reference beam were dispersed in a spectrograph and imaged onto a 2 × 32 pixel HgCdTe detector array which enabled us to measure low noise (typically 0.05 mOD rms for 100 shots averaging) transient spectra with spectral resolution between $2\,\text{cm}^{-1}$ and $6\,\text{cm}^{-1}$ depending on the grating used.

With the help of two light choppers, one in the IR-pump beam running at half the repetition rate of the laser system and the other in the UV-pump beam running at a quarter of the repetition rate, four individual data sets were recorded: $I_{\text{UV}_\text{on}\text{IR}_\text{on}}$, $I_{\text{UV}_\text{off}\text{IR}_\text{on}}$, $I_{\text{UV}_\text{on}\text{IR}_\text{off}}$ and $I_{\text{UV}_\text{off}\text{IR}_\text{off}}$. The time-resolved IR absorption spectra (T1D-spectra) (e. g. Figure 5.21) are calculated as

$$\Delta A_{\text{T1D}} = -\log \frac{I_{\text{UV}_\text{on}\text{IR}_\text{off}}}{I_{\text{UV}_\text{off}\text{IR}_\text{off}}}, \tag{5.28}$$

the stationary 2D-IR spectrum (e. g. Figure 5.22a) of the initial state is calculated as

$$\Delta A_{\text{2D,stat}} = -\log \frac{I_{\text{UV}_\text{off}\text{IR}_\text{on}}}{I_{\text{UV}_\text{off}\text{IR}_\text{off}}}, \tag{5.29}$$

and the T2D-IR difference spectra (e. g. Figure 5.22b), which are in fact double-difference spectra, as

$$\Delta A_{\text{T2D}} = -\log \frac{I_{\text{UV}_\text{on}\text{IR}_\text{on}} \cdot I_{\text{UV}_\text{off}\text{IR}_\text{off}}}{I_{\text{UV}_\text{on}\text{IR}_\text{off}} \cdot I_{\text{UV}_\text{off}\text{IR}_\text{on}}}. \tag{5.30}$$

The polarizations of the pulses are set by computer controlled zero order half-wave plates in the IR-pump and the UV-pump beam. The polarization of the IR-probe beam is kept constant to avoid artifacts due to the polarizing properties of the spectrometer. Each half-wave plate can be switched rapidly between two preset positions with high precision. This allows for the quasi-simultaneous measurement of four sets of polarizations by changing the orientation of the plates every few hundred laser pulses. In this way drifts and instabilities in laser intensity are correlated for the measurements with different polarization conditions and linear combinations of the different signals can be calculated without being affected by normalization ambiguities.

5.3.5 Polarization Dependence of the T2D-signal

Derivation of the General Expression

The n^{th} order polarization of a molecule that has interacted n times with an electromagnetic field $\vec{E}(t)$ at times τ_i is given by [310]

$$\begin{aligned}
P^{(n)}(t) &= \left\langle \hat{\mu}(t)\rho(t) \right\rangle \\
&= \left\langle \hat{\mu}_I(t)\rho_I(t) \right\rangle \\
&= \left(-\frac{i}{\hbar}\right)^n \int_{-\infty}^{t} d\tau_n \int_{-\infty}^{\tau_n} d\tau_{n-1} \ldots \int_{-\infty}^{\tau_2} d\tau_1 \\
&\times \mathrm{Tr}\Big(\hat{\mu}_I(t)\big[\vec{E}(\tau_n)\cdot\hat{\mu}_I(\tau_n),\big[\ldots\big[\vec{E}(\tau_2)\cdot\hat{\mu}_I(\tau_2), \\
&\big[\vec{E}(\tau_1)\cdot\hat{\mu}_I(\tau_1),\rho_I(-\infty)\big]\big]\big]\big]\Big),
\end{aligned} \tag{5.31}$$

where ρ is the density matrix, $\hat{\mu}$ is the dipole operator and the subscript I refers to the interaction picture. In pump-probe spectroscopy or heterodyne-detected photon-echo spectroscopy, the field irradiated by this polarization interferes with the electric field of the probe laser or the local oscillator E_{Het} and the detected signal is given by $E_{\text{Het}}(t) \cdot P^{(n)}(t)$. Since both the dipole operators and the electric fields are vector quantities, the signal depends on the relative orientations of light polarizations and transition dipole moments at the times of interaction, and must be averaged over all possible orientations of the molecules of the measured ensemble. Under the usual assumption that frequency fluctuations and dipole orientations are not correlated, the signal is proportional to the product

$$\begin{aligned}
S \propto \Big\langle &\Big(\vec{\mu}^i(\tau_1)\cdot\vec{E}(\tau_1)\Big)\Big(\vec{\mu}^j(\tau_2)\cdot\vec{E}(\tau_2)\Big)\ldots \\
&\Big(\vec{\mu}^n(\tau_n)\cdot\vec{E}(\tau_n)\Big)\Big(\vec{\mu}(t)\cdot\vec{E}_{\text{Het}}(t)\Big)\Big\rangle S^{(n)},
\end{aligned} \tag{5.32}$$

where the brackets indicate the orientational average $\langle\rangle$ of the angle dependent prefactor and $S^{(n)}$ is the polarization angle independent n^th order response function. In the most general case, the response function is a sum of many terms, each characterized by a different time-order of the transition dipole moments, and therefore a different polarization dependence. However, in the three-pulse schemes used for our T2D-IR experiments (Figure 5.18) the pulses are well separated and ordered in time and each laser pulse interacts two times in a row with the same transition dipole. In addition, the UV pulse can only interact with the electronic transition dipole moment $\vec{\mu}^0$, while the narrow-band IR-pump-pulse is tuned to interact with one specific vibrational transition dipole $\vec{\mu}^i$. The broad-band IR-probe-pulse can either interact with the same $\vec{\mu}^i$ or a second vibrational transition $\vec{\mu}^j$. Thus, there are only two types of signals in the T2D-IR spectra: transient *diagonal peaks*, involving one electronic and one vibrational transition dipole, and transient *cross peaks* from the consecutive interaction with one electronic and two different vibrational transition dipoles. The polarization dependence of the signal is therefore given by the the orientational average of the angle dependent prefactor

$$D = \langle(\vec{\mu}^0\cdot\vec{e}_0)(\vec{\mu}^0\cdot\vec{e}_0)(\vec{\mu}^i\cdot\vec{e}_1)(\vec{\mu}^i\cdot\vec{e}_1)(\vec{\mu}^j\cdot\vec{e}_2)(\vec{\mu}^j\cdot\vec{e}_2)\rangle \tag{5.33}$$

where $\vec{\mu}^0$, $\vec{\mu}^i$, $\vec{\mu}^j$ are the transition dipole moments in the laboratory frame interacting with the UV pulse with polarization vector $\vec{e}_0$ and the two IR pulses with polarizations $\vec{e}_1$ and $\vec{e}_2$, respectively.

We define the Z-axis in the laboratory frame in the direction of the UV-pump polarization, and the Y-axis as the direction of light propagation. The IR pulses may then have arbitrary polarization in the ZX-plane:

$$\vec{e}_0 = \hat{Z} \tag{5.34}$$

$$\vec{e}_1 = (\hat{Z}\cos\alpha + \hat{X}\sin\alpha) \tag{5.35}$$

$$\vec{e}_2 = (\hat{Z}\cos\beta + \hat{X}\sin\beta) \tag{5.36}$$

where α and β are the angles formed with the UV-pump beam. Inserting Equations 5.34 to 5.36 in 5.33, the tensor D can be decomposed in the so defined space fixed frame:

$$\begin{aligned}
D(\alpha,\beta) = &\\
&\cos^2\alpha\cos^2\beta & \langle Z^0Z^0Z^iZ^iZ^jZ^j\rangle \quad & \text{(I)}\\
+\; &\cos^2\alpha\sin^2\beta & \langle Z^0Z^0Z^iZ^iX^jX^j\rangle \quad & \text{(II)}\\
+\; &\sin^2\alpha\cos^2\beta & \langle Z^0Z^0X^iX^iZ^jZ^j\rangle \quad & \text{(III)}\\
+\; &\sin^2\alpha\sin^2\beta & \langle Z^0Z^0X^iX^iX^jX^j\rangle \quad & \text{(IV)}\\
+\; &2\sin^2\beta\cos\alpha\sin\alpha & \langle Z^0Z^0X^iZ^iZ^jZ^j\rangle \quad & \text{(V)}\\
+\; &2\cos^2\alpha\cos\beta\sin\beta & \langle Z^0Z^0X^iZ^iX^jX^j\rangle \quad & \text{(VI)}\\
+\; &2\cos^2\alpha\cos\beta\sin\beta & \langle Z^0Z^0Z^iZ^iX^jZ^j\rangle \quad & \text{(VII)}\\
+\; &2\sin^2\alpha\cos\beta\sin\beta & \langle Z^0Z^0X^iX^iX^jZ^j\rangle \quad & \text{(VIII)}\\
+\; &4\sin\alpha\cos\alpha\sin\beta\cos\beta & \langle Z^0Z^0X^iZ^iX^jZ^j\rangle \quad & \text{(IX)}
\end{aligned}$$

where we use the shorthand notation

$$\begin{aligned}
&\langle A^0B^0C^iD^iE^jF^j\rangle\\
&= \langle\mu^0_A(t_1)\mu^0_B(t_1)\mu^i_C(t_2)\mu^i_D(t_2)\mu^j_E(t_3)\mu^j_F(t_3)\rangle,
\end{aligned} \tag{5.37}$$

with space-fixed directions $A,B,C\dots = X,Y,Z$, and labels 0, i and j for the UV and the two IR transition dipole moments in the laboratory frame, respectively. In terms of transition dipole moments in the molecular frame $\vec{m} = R_{\phi,\theta,\chi}\vec{\mu}$, where $R_{\phi,\theta,\chi}$ is the Euler rotation matrix (see Appendix A) these correlation functions can be re-written as

$$\begin{aligned}
&\langle\mu^0_A(t_1)\mu^0_B(t_1)\mu^i_C(t_2)\mu^i_D(t_2)\mu^j_E(t_3)\mu^j_F(t_3)\rangle\\
&= \Big\langle\sum_p m^0_pA_p(t_1)\sum_q m^0_qB_q(t_1)\sum_r m^i_rC_r(t_2)\\
&\quad\times\sum_s m^i_sD_s(t_2)\sum_t m^j_tE_t(t_3)\sum_u m^j_uF_u(t_3)\Big\rangle\\
&= \sum_{pqrstu=x,y,z} m^0_pm^0_qm^i_rm^i_sm^j_tm^j_u\langle A_p(t_1)B_q(t_1)C_r(t_2)\\
&\quad\times D_s(t_2)E_t(t_3)F_u(t_3)\rangle.
\end{aligned} \tag{5.38}$$

The $\langle A_pB_qC_rD_sE_tF_u\rangle$ are correlation functions of direction cosines, which define the angles between laboratory axes $A,B,C,\dots = X,Y,Z$ and molecular axes $p,q,r,\dots = x,y,z$ at the different time-points. Terms V-VIII in equation 5.3.5 vanish identically as they contain an odd number of direction cosines related to one laboratory axis [1]. In the diffusion-free case the brackets $\langle\rangle$ simply stand for the integration over the isotropic distribution of molecular orientations, and can be evaluated directly using the tensor invariants [339]:

$$\begin{aligned}
&\langle A_pA_qA_rA_sA_tA_u\rangle\\
&= \frac{1}{3\cdot5\cdot7}(\delta_{pq}\delta_{rs}\delta_{tu} + \delta_{pq}\delta_{rt}\delta_{su}\\
&\quad+ \delta_{pq}\delta_{ru}\delta_{ts} + \delta_{pr}\delta_{qs}\delta_{tu} + \dots)\ \text{15 terms}
\end{aligned} \tag{5.39}$$

---

[1] See Reference [339] for a didactic and comprehensive introduction on rotational averaging.

$$\begin{aligned}&\langle B_pB_qA_rA_sA_tA_u\rangle\\&=\frac{1}{2\cdot3\cdot5\cdot7}(6\delta_{pq}\delta_{rs}\delta_{tu}+6\delta_{pq}\delta_{rt}\delta_{su}\\&\quad+6\delta_{pq}\delta_{ru}\delta_{ts}-\delta_{pr}\delta_{qs}\delta_{tu}-\dots)\text{ 15 terms}\end{aligned}\tag{5.40}$$

In the presence of orientational motion they can be used to express the dipole correlation functions in equation 5.3.5 in terms of correlation functions of time-dependent cosines of the angles Θ_{i0}, Θ_{j0} between IR and UV transition dipoles and Θ_{ij} between IR transition dipoles *in the laboratory frame* [292]. This leads to an expression of 5 terms:

$$D(\alpha,\beta)=\tfrac{|\mu_0|^2|\mu_i|^2|\mu_j|^2}{2\cdot3\cdot5\cdot7}$$

$$\begin{array}{llllllll}
(& \cos^2\alpha\cos^2\beta & [& 2 & +4\langle\cos^2\Theta_{i0}\rangle & +4\langle\cos^2\Theta_{j0}\rangle & +4\langle\cos^2\Theta_{ij}\rangle & +16\langle\cos\Theta_{i0}\cos\Theta_{j0}\cos\Theta_{ij}\rangle] \\
+ & \cos^2\alpha\sin^2\beta & [& 6 & +12\langle\cos^2\Theta_{i0}\rangle & -2\langle\cos^2\Theta_{j0}\rangle & -2\langle\cos^2\Theta_{ij}\rangle & -8\langle\cos\Theta_{i0}\cos\Theta_{j0}\cos\Theta_{ij}\rangle] \\
+ & \sin^2\alpha\cos^2\beta & [& 6 & -2\langle\cos^2\Theta_{i0}\rangle & +12\langle\cos^2\Theta_{j0}\rangle & -2\langle\cos^2\Theta_{ij}\rangle & -8\langle\cos\Theta_{i0}\cos\Theta_{j0}\cos\Theta_{ij}\rangle] \\
+ & \sin^2\alpha\sin^2\beta & [& 6 & -2\langle\cos^2\Theta_{i0}\rangle & -2\langle\cos^2\Theta_{j0}\rangle & +12\langle\cos^2\Theta_{ij}\rangle & -8\langle\cos\Theta_{i0}\cos\Theta_{j0}\cos\Theta_{ij}\rangle] \\
+ & \sin\alpha\cos\alpha\sin\beta\cos\beta & [& -4 & -8\langle\cos^2\Theta_{i0}\rangle & -8\langle\cos^2\Theta_{j0}\rangle & +20\langle\cos^2\Theta_{ij}\rangle & +24\langle\cos\Theta_{i0}\cos\Theta_{j0}\cos\Theta_{ij}\rangle]\quad)
\end{array}\tag{5.41}$$

Written out explicitly, these correlation functions are:

$$\langle\cos^2\Theta_{ij}\rangle=\langle(\hat{\mu}^i(t_2)\cdot\hat{\mu}^j(t_3))(\hat{\mu}^i(t_2)\cdot\hat{\mu}^j(t_3))\rangle,\tag{5.42}$$

$$\begin{aligned}&\langle\cos\Theta_{i0}\cos\Theta_{j0}\cos\Theta_{ij}\rangle\\&=\quad\langle(\hat{\mu}^0(t_1)\cdot\hat{\mu}^i(t_2))(\hat{\mu}^0(t_1)\cdot\hat{\mu}^j(t_3))(\hat{\mu}^i(t_2)\cdot\hat{\mu}^j(t_3))\rangle.\end{aligned}\tag{5.43}$$

Throughout this paper we use capital symbols Θ to denote angles between transition dipoles in the laboratory frame, and small symbols θ for (diffusion-independent) angles in the molecular frame.

The different terms in equation 5.41 are linearly dependent. The last term in square brackets can be obtained as a linear combination of the first four, or, using the short-hand notation of equation 5.3.5:

$$\begin{aligned}4\langle Z^0Z^0X^iZ^iX^jZ^j\rangle&=\langle Z^0Z^0Z^iZ^iZ^jZ^j\rangle-\langle Z^0Z^0X^iX^iZ^jZ^j\rangle\\&-\langle Z^0Z^0Z^iZ^iX^jX^j\rangle+\langle Z^0Z^0X^iX^iX^jX^j\rangle.\end{aligned}\tag{5.44}$$

The remaining four terms are linearly independent. Therefore 4 linearly independent measurements can be made in a T2D-IR experiment to obtain a maximum of angle-information, employing for example the following polarization conditions for α and β to obtain different $D(\alpha,\beta)$

$$D(0,0)=\langle Z^0Z^0Z^iZ^iZ^jZ^j\rangle\tag{5.45}$$

$$D(0,\frac{\pi}{2})=\langle Z^0Z^0Z^iZ^iX^jX^j\rangle\tag{5.46}$$

$$D(\frac{\pi}{2},0)=\langle Z^0Z^0X^iX^iZ^jZ^j\rangle\tag{5.47}$$

$$D(\frac{\pi}{2},\frac{\pi}{2})=\langle Z^0Z^0X^iX^iX^jX^j\rangle\tag{5.48}$$

These measurements can be carried out quasi-simultaneously using the rapid polarization switches described in the experimental section 5.3.4.

The correlation functions that appear in the equations above are sensitive to all possible types of angular motion. They will decay both due to re-orientation of the molecules as well as due to intramolecular changes in the dipole angles that may be caused by structure fluctuations or a photochemical reaction. They also contain the ensemble averaging over possible distributions of molecular structures. In Appendix A we describe in detail the evaluation of the correlation functions for the case where they only depend on the Debye diffusion of the rigid molecules. To bring out the essential features we assume spherical diffusors, which is often a good approximation even when the molecules are not spherical tops (e.g. for the Rhenium complex discussed in the experimental section). More complicated cases may be readily worked out along the same lines when needed. The final result is given in Table 5.3. Note that the angles (small θ s) that appear in this table are now the diffusion-independent angles in the molecular frame. The time-dependence of the signal due to diffusion is given via the two correlation functions

$$c_{12}=\exp[-6\mathrm{D_R}(\mathrm{t_2}-\mathrm{t_1})]\tag{5.49}$$

$$c_{23}=\exp[-6\mathrm{D_R}(\mathrm{t_3}-\mathrm{t_2})]\tag{5.50}$$

where D_R is the rotational diffusion constant. Although the angular terms in Table 5.3 are no longer explicitly time-dependent, they still depend on *intramolecular* motion and must be regarded as averages over structure distributions, i.e. they contain all the molecular properties of the system that we may want to investigate with T2D-IR spectroscopy.

The equivalence of the signal in Table 5.3 and equation 5.41 in the absence of rotational diffusion can be easily verified, by letting $c_{12},c_{23}\to1$ and noting that for short times the correlation functions of dipole angles in the laboratory frame approach the molecule-fixed angles, e. g. $\langle\cos^2\Theta_{ij}\rangle \rightarrow \cos^2\theta_{ij}$.

Magic Angle Like Conditions

To illustrate the concepts of magic angle measurements we will briefly review the case of pump-probe spectroscopy. In a two-pulse experiment like pump-probe spectroscopy or our implementation of 2D-IR spectroscopy [252], the signal depends on the relative polarization of pump and probe pulse α, the delay time $t_2 - t_1$ and the molecular angle Θ_{ij} between the transition dipoles interacting with the pump pulse and the the probe pulse, respectively. This gives rise to a fourth rank tensor for the polarization dependent prefactor

$$\begin{aligned} D_{\mathrm{pp}}(\alpha) &= \langle a_i a_i b_j b_j\rangle = \tfrac{|\mu_i|^2|\mu_j|^2}{45} \\ &\big(\quad \cos^2\alpha \quad [\quad 5 \quad + \quad 4\langle P_2(\cos\Theta_{ij})\rangle] \\ &+ \quad \sin^2\alpha \quad [\quad 5 \quad - \quad 2\langle P_2(\cos\Theta_{ij})\rangle] \quad \big) \end{aligned} \tag{5.51}$$

where $P_2(x) = (3\cos^2 x - 1)/2$ is the second Legendre polynomial, and $\langle P_2(\cos\Theta_{ij})\rangle = \langle P_2(\hat{\mu}_i(t_2)\cdot\hat{\mu}_j(t_1))\rangle$ is equal to $P_2(\cos\theta_{ij})\exp[-6D_R(t_2 - t_1)]$ in the spherical diffusor approximation. The first term in equation 5.51 arises from the tensor element $\langle Z^i Z^i Z^j Z^j\rangle$ and the second term from $\langle Z^i Z^i X^j X^j\rangle$. The signal is sensitive to rotational diffusion of the molecules as the angle between pumped and probed transition dipole moments $\vec{\mu}_i$ and $\vec{\mu}_j$ in the laboratory frame becomes time dependent due to the motion of the molecules. To suppress rotational diffusion effects in the signal, the linear combination $D(0) + 2D(\frac{\pi}{2})$ can be calculated from two independent measurements. The same can be achieved directly by setting α to the magic angle, $\mathrm{M} = \arctan\sqrt{2} \approx 54.74^\circ$ (because $\sin^2\mathrm{M} = 2\cos^2\mathrm{M}$). The angle between dipoles Θ_{ij} can be inferred from the anisotropy, which is the difference of the signals measured with parallel and perpendicular polarization divided by the magic angle signal:

$$r = \frac{D_{\mathrm{pp}}(0) - D_{\mathrm{pp}}(\frac{\pi}{2})}{D_{\mathrm{pp}}(0) + 2D_{\mathrm{pp}}(\frac{\pi}{2})} = \frac{2}{5}\langle P_2(\cos\Theta_{ij})\rangle \tag{5.52}$$

By this operation, the dependence on the magnitudes of the transition dipole moments is normalized out. The anisotropy ranges from $r = -\frac{1}{5}$ for perpendicular dipoles to $r = \frac{2}{5}$ for parallel dipoles. As r decays under the influence of rotational diffusion it represents an unambiguous measure of the molecular angle θ_{ij} only at times that are short compared to the timescale of rotational diffusion.

It would be desirable to find a magic angle like signal for T2D-IR spectroscopy as well. To this end an appropriate linear combination of tensor elements has to be generated, where the dependence on the correlation functions $\langle\cos\Theta_{i0}^2\rangle$, $\langle\cos\Theta_{j0}^2\rangle$, $\langle\cos\Theta_{ij}^2\rangle$ and $\langle\cos\Theta_{i0}\cos\Theta_{j0}\cos\Theta_{ij}\rangle$ cancels. Only the linearly independent contributions in equation 5.41 need to be considered:

$$\begin{aligned} S &\propto c_1 D(0,0) + c_2 D(0,\frac{\pi}{2}) + c_3 D(\frac{\pi}{2},0) + c_4 D(\frac{\pi}{2},\frac{\pi}{2}) \\ &= \underbrace{(c_1,c_2,c_3,c_4)\begin{pmatrix} 4 & 4 & 4 & 16 \\ 12 & -2 & -2 & -8 \\ -2 & 12 & -2 & -8 \\ -2 & -2 & 12 & -8 \end{pmatrix}}_{\overset{!}{=}0} \\ &\times \begin{pmatrix} \langle\cos^2\Theta_{i0}\rangle \\ \langle\cos^2\Theta_{j0}\rangle \\ \langle\cos^2\Theta_{ij}\rangle \\ \langle\cos\Theta_{i0}\cos\Theta_{j0}\cos\Theta_{ij}\rangle \end{pmatrix} + (c_1,c_2,c_3,c_4)\begin{pmatrix} 2 \\ 6 \\ 6 \\ 6 \end{pmatrix}. \end{aligned} \tag{5.53}$$

In order to cancel the time-dependence of the signal S, the underbraced product has to vanish. In other words: the vector (c_1,c_2,c_3,c_4) has to belong to the nullspace of the coefficient matrix to its right. As the matrix has full rank, a nullspace does not exist and the condition cannot be fulfilled. Or to put it differently: whereas in pump-probe spectroscopy we have one angle and one polarization degree of freedom, we now have three angles but only two independent polarization degrees of freedom to control. A magic angle like condition therefore does not exist for the T2D-IR experiment, when three arbitrarily oriented transition dipoles are involved. The nonexistence of a magic angle signal was already described for the general case of coherent higher order spectroscopies of a two level system (or a single vibrational mode) by Tokmakoff [293]. However, in Reference [293] the absence of a magic angle signal was due to a different reason, namely the propagation of the system in a coherent state during certain time intervals. In T2D-IR spectroscopy the system propagates in a population state during the scanned delays. Although magic angle like conditions for the general T2D-IR signal cannot be found, they exist in important special cases, as discussed in the next section.

Table 5.3: Dependence of the T2D-signal on the angles between dipoles in the molecular frame θ_{0i}, θ_{0j},θ_{ij}, polarization angles α, β, and the delay between the three pulses in the spherical diffusor approximation. The time-correlation functions are given by $c_{12} = \exp[-6\mathrm{D_R}(\mathrm{t_2} - \mathrm{t_1})]$ and $c_{23} = \exp[-6\mathrm{D_R}(\mathrm{t_3} - \mathrm{t_2})]$. All terms must be divided by 945.

	1	$\cos^2\theta_{i0}$	$\cos^2\theta_{j0}$	$\cos^2\theta_{ij}$	$\cos\theta_{i0}\cos\theta_{j0}\cos\theta_{ij}$
$\cos^2\alpha\cos^2\beta$	$(35-14c_{23}-14c_{12}+2c_{12}c_{23})$	$6(7-4c_{23})c_{12}$	$18c_{12}c_{23}$	$6(7-4c_{12})c_{23}$	$72c_{12}c_{23}$
$\cos^2\alpha\sin^2\beta$	$(35+7c_{23}-14c_{12}-c_{12}c_{23})$	$6(7+2c_{23})c_{12}$	$-9c_{12}c_{23}$	$-3(7-4c_{12})c_{23}$	$-36c_{12}c_{23}$
$\sin^2\alpha\cos^2\beta$	$(35+7c_{23}+7c_{12}-22c_{12}c_{23})$	$-3(7-4c_{23})c_{12}$	$54c_{12}c_{23}$	$-3(7-4c_{12})c_{23}$	$-36c_{12}c_{23}$
$\sin^2\alpha\sin^2\beta$	$(35-14c_{23}+7c_{12}-c_{12}c_{23})$	$-3(7-4c_{23})c_{12}$	$-9c_{12}c_{23}$	$6(7+2c_{12})c_{23}$	$-36c_{12}c_{23}$
$\cos\alpha\cos\beta\sin\alpha\sin\beta$	$-6(7-4c_{12})c_{23}$	$-36c_{12}c_{23}$	$-36c_{12}c_{23}$	$18(7-2c_{12})c_{23}$	$108c_{12}c_{23}$

Special Cases

Partial Magic Angle Like Conditions The T2D-IR experiments described by the pulse sequences in Figure 5.18 typically involve the scanning of only one of the two time delays. It is therefore usually sufficient to eliminate the rotational diffusion dependence of the signal during this scanned delay. In the regular T2D-IR experiment for example (Figure 5.18a), where one is interested in 2D-IR snapshots at different UV delays, the UV delay t_{12} is varied and the IR delay t_{23} is made as short as possible. This is often necessary, because the lifetimes of vibrational modes during which the 2D-IR measurement must be performed, is usually only of the order of a few picoseconds and therefore much shorter than typical rotational diffusion times. It is in fact always possible to eliminate all but one of the the four correlation functions that appear in the most general signal of equation 5.41, by finding appropriate linear combinations of the four basis spectra (equations 5.45-5.48) with the help of equations such as,

$$\begin{aligned} S &\propto c_1 D(0,0) + c_2 D(0,\frac{\pi}{2}) + c_3 D(\frac{\pi}{2},0) + c_4 D(\frac{\pi}{2},\frac{\pi}{2}) \\ &= \underbrace{(c_1,c_2,c_3,c_4)\cdot\begin{pmatrix} 4 & 4 & 16 \\ 12 & -2 & -8 \\ -2 & 12 & -8 \\ -2 & -2 & -8 \end{pmatrix}}_{\overset{!}{=}0} \\ &\times \begin{pmatrix} \langle\cos^2\theta_{i0}\rangle \\ \langle\cos^2\theta_{j0}\rangle \\ \langle\cos\theta_{i0}\cos\theta_{j0}\cos\theta_{ij}\rangle \end{pmatrix} + (c_1,c_2,c_3,c_4) \\ &\times \begin{pmatrix} 2 & 4 \\ 6 & -2 \\ 6 & -2 \\ 6 & 12 \end{pmatrix}\cdot\begin{pmatrix} 1 \\ \langle\cos^2\theta_{ij}\rangle \end{pmatrix}. \end{aligned} \tag{5.54}$$

The underbraced product vanishes for $(c_1,c_2,c_3,c_4) = (1,0,0,2)$. As a result, the signal

$$\begin{aligned} 2D(\frac{\pi}{2},\frac{\pi}{2}) + D(0,0) &= \frac{1}{15}(1 + 2\langle\cos^2\Theta_{ij}\rangle) \\ &= \frac{1}{45}[5 + 4\langle P_2(\cos\Theta_{ij})\rangle] \end{aligned} \tag{5.55}$$

only depends on the correlation function $\langle\cos\Theta_{ij}\rangle$ and is no longer influenced by rotational diffusion during the UV-IR delay t_{12} (the dipole amplitudes $|\mu_0|^2|\mu_i|^2|\mu_j|^2$ are omitted here for better legibility). In a similar way two more correlation functions may be isolated

$$2D(\frac{\pi}{2},0) + D(0,0) = \frac{1}{45}[5 + 4\langle P_2(\cos\Theta_{i0})\rangle], \tag{5.56}$$

$$2D(0,\frac{\pi}{2}) + D(0,0) = \frac{1}{45}[5 + 4\langle P_2(\cos\Theta_{j0})\rangle]. \tag{5.57}$$

The first expression is independent of rotational diffusion during the IR-IR delay, which is scanned in transient dynamic hole-burning spectroscopy (Figure 5.18b). The significance of signal 5.57 is best seen in the spherical diffusor approximation, where $\langle P_2(\cos\Theta_{j0})\rangle = \mathrm{Exp}[-\mathrm{D_R}(\mathrm{t_3}-\mathrm{t_1})]\mathrm{P_2}(\cos\theta_{\mathrm{j0}})$. When first and third pulse are held at a fixed delay $t_3 - t_1$ and the second pulse is scanned in between, this linear combination signal is not affected by rotational diffusion. This can be useful in a T2D-IR labelling experiment.

Just like in third order pump-probe spectroscopy, signals 5.55-5.57 may also be obtained in a single measurement, using the magic angle M. In the spherical diffusor approximation (Table 5.3) we find explicitly:

$$D(\mathrm{M},\mathrm{M}) = \frac{1}{135}[5 + 4c_{23}P_2(\cos\theta_{ij})] \tag{5.58}$$

$$D(\mathrm{M},0) = \frac{1}{135}[5 + 4c_{12}P_2(\cos\theta_{i0})] \tag{5.59}$$

$$D(0,\mathrm{M}) = \frac{1}{135}[5 + 4c_{12}c_{23}P_2(\cos\theta_{j0})] \tag{5.60}$$

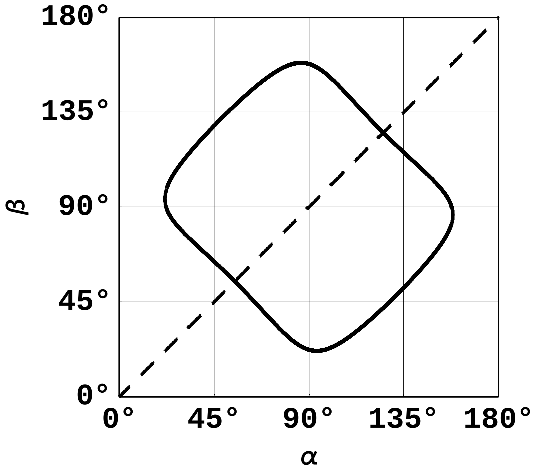

Figure 5.19: Combinations of polarization angles α and β that yield quasi-magic angle conditions for diagonal peaks for arbitrary UV-IR delays in the limit of short IR-IR delays.

Diagonal Peaks The diagonal peaks in the T2D-IR spectrum arise, when the same transition dipole μ^i interacts with the IR-pump and IR-probe pulse. In the molecular frame we then have $\theta_{i0} = \theta_{j0}$ and $\theta_{ij} = 0$. However, since rotational diffusion will usually change the orientation of the IR-transition dipole between the IR-pump and the IR-probe pulse we may (approximately) write $\langle\cos^2\Theta_{i0}\rangle = \langle\cos^2\Theta_{j0}\rangle$, $\langle\cos^2\Theta_{ij}\rangle = 1$, and $\langle\cos\Theta_{i0}\cos\Theta_{j0}\cos\Theta_{ij}\rangle = \langle\cos^2\Theta_{i0}\rangle$ only if rotational diffusion is slow compared to the IR-IR delay in the T2D-IR probe process. Under this assumption we then obtain an infinite number of quasi-magic angle polarization conditions (α,β), which eliminate the remaining correlation function $\langle\cos^2\Theta_{i0}\rangle$ from the signal, i.e. make it independent of rotational diffusion during any UV-IR delay. They can be represented by a closed path in the α,β-plane as shown in Figure 5.19. It can be seen, that for a given α there are usually two possible 'quasi-magic' polarizations β. For example, choosing the magic angle $\alpha = \arctan\sqrt{2} \approx 54.7°$ allows for $\beta = \alpha$ as well as for $\beta = \arccos\frac{-11}{\sqrt{219}} \approx 138.0°$. Therefore magic angle-like conditions for the diagonal peaks can be obtained for different polarization conditions. This offers the possibility to manipulate cross peak intensities while keeping the diagonal peak intensities free from rotational diffusion effects.

Symmetry Constraints Due to molecular symmetry it is sometimes possible to express one of the three angles θ_{i0}, θ_{j0} and θ_{ij} that enter the T2D-IR signal as a function of the other two. This is demonstrated for the case of a planar molecule or a planar unit of a more complicated molecule. The complex [Re(CO)$_3$(dmbpy)Cl] for example (Figure 5.17), that is investigated in the experimental sections of this paper possesses a mirror plane (it has C_s-symmetry). The transition dipole moments of the electronic transition as well as the transition dipole moments of the a'(2) and a'(1) vibrations lie in the mirror plane. One of the angles $\theta_{\mathrm{a}'(2)\,\mathrm{UV}}$, $\theta_{a'(1)\,UV}$ and
$\theta_{a'(2)\,a'(1)}$ can therefore be expressed by the other two ($\cos\theta_{ij} = \cos(\theta_{i0} - \theta_{j0})$). For quasi-instantaneous measurements, i. e. when the correlation functions in equation 5.41 can all be replaced by the corresponding functions of angles in the molecular frame, we can completely eliminate any angle dependence from the T2D-IR signal by taking the linear combination

$$D_\mathrm{m} = D(0,0) + 3D(0,\frac{\pi}{2}) + 3D(\frac{\pi}{2},0) + 3D(\frac{\pi}{2},\frac{\pi}{2}) \tag{5.61}$$

It is then straightforward to define expressions similar to the anisotropy signal r in pump probe spectroscopy, where the dependence on transition dipole magnitudes is normalized out:

$$\frac{D(0,0) + 2D(0,\frac{\pi}{2})}{D_\mathrm{m}} = \frac{1}{6}(1 + 2\cos^2\theta_{i0}), \tag{5.62}$$

$$\frac{D(0,0) + 2D(\frac{\pi}{2},0)}{D_\mathrm{m}} = \frac{1}{6}(1 + 2\cos^2\theta_{j0}), \tag{5.63}$$

$$\frac{D(0,0) + 2D(\frac{\pi}{2},\frac{\pi}{2})}{D_\mathrm{m}} = \frac{1}{6}(1 + 2\cos^2\theta_{ij}). \tag{5.64}$$

From these linear combination signals the angles θ_{i0}, θ_{j0} and θ_{ij} can be calculated. They remain useful even if rotational diffusion can only be neglected during one of the two delays between pulses. For example, as long as the delay time between the two IR pulses is sufficiently short to assure $c_{23} = 1$ we obtain in the spherical diffusor case:

$$\frac{D(0,0) + 2D(\frac{\pi}{2},\frac{\pi}{2})}{D_\mathrm{m}} = \frac{3(5 + 4P_2(\cos\theta_{ij})}{50 + 4c_{12} + (1 - c_{12})P_2(\cos\theta_{ij})} \approx \frac{1}{6}(1 + 2\cos^2\theta_{ij}) \tag{5.65}$$

The denominator in this expression changes only very little as c_{12} decays from 1 to 0 as a result of rotational diffusion, and equation 5.64 is actually a very good approximation for determining the IR-IR angle θ_{ij} at arbitrary UV-IR delays.

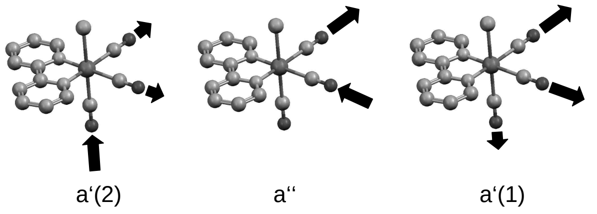

Figure 5.20: C_s symmetric CO normal modes of [Re(CO)$_3$(dmbpy)CL].

5.3.6 Model Photoreaction: Charge Transfer in [Re(CO)$_3$(dmbpy)Cl]

T1D Spectroscopy of [Re(CO)$_3$(dmbpy)Cl]

Before entering the discussion of the T2D-IR spectra, we briefly introduce our model system [Re(CO)$_3$(dmbpy)Cl]. The complex is expected to have C_s symmetry [329]. Its different CO vibration modes are depicted in Figure 5.20. The top panel of Figure 5.21 shows the absorption spectrum of the electronic ground state. The ground state bands at 1889 cm^{-1}, 1910 cm^{-1} and 2018 cm^{-1} have been assigned to a'(2) (antisymmetric stretching of axial CO and equatorial COs), a" (antisymmetric stretching of equatorial COs) and a'(1) (symmetric stretching of all COs) modes respectively. This assignment is based on the different anisotropy values in the UV-pump IR-probe spectrum (Figure 5.21) and is in agreement with Ref. [299] as well as in agreement with the assignment based on absorption spectra of samples containing different ratios of ^{12}C/^{13}C [340].

Upon excitation at 390 nm metal-to-ligand charge transfer (MLCT) occurs and a large blue-shift of the vibrational frequencies is observed (second panel in Figure 5.21). The instantaneous change of the electronic structure and the subsequent slower shift due to solvation have been identified as the effects responsible for the change in vibrational frequency. For a more detailed discussion of these effects see References [299, 329, 302]. The vibrations in the MLCT state can be assigned employing T2D-IR spectroscopy in the band labeling mode [302] as a" (1946 cm^{-1}), a'(2) (1989 cm^{-1}) and a'(1) (2061 cm^{-1}) (see section 5.3.7). The order of vibrational levels thus is interchanged in the MLCT state as compared to the electronic ground state. The lower graph in Figure 5.21 shows the anisotropy decay of the three ground state modes. Despite the fact the three IR transition dipole moments are almost perpendicular and the molecule is not a spherical top, all three decay curves can be simultaneously fit by a single exponential function with time constant of 140 ps. This shows that the spherical diffusor approximation works very well in this case. From the anisotropies at short delays the angles between IR and UV transition dipoles in the ground state are found to be 65° for a'(2) (anisotropy r=-0.10), 73° for a" (r=-0.15), and 28° for a'(1) (r=+0.27).

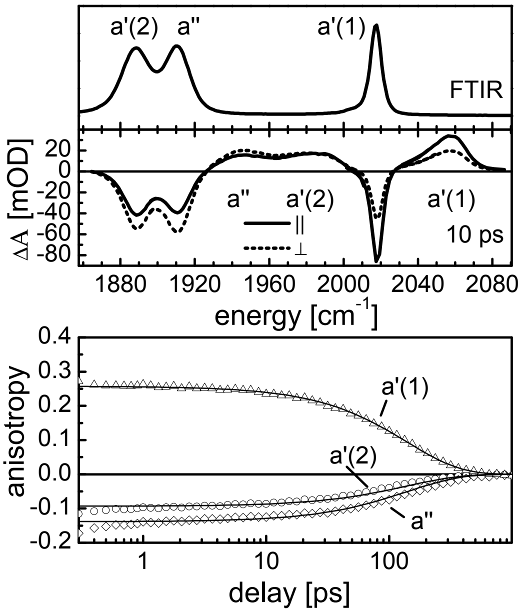

Figure 5.21: Top: Absorption spectrum of the electronic ground state and time-resolved polarization-dependent IR spectrum of [Re(CO)$_3$(dmbpy)Cl] after 10 ps. Note the interchanged order of the modes in the excited state. Bottom: Anisotropy decay of the three ground state CO modes as a function of UV-IR delay. The solid lines show an exponential fit with 140 ps time constant.

Features of the T2D-IR Spectrum of [Re(CO)$_3$Cl(dmbpy)]

In the following we give an overview of the features in the 2D-IR and T2D-IR spectra of [Re(CO)$_3$(dmbpy)Cl]. The T2D-IR spectrum was recorded employing the regular pulse sequence in Figure 5.18a. The polarization conditions in Figure 5.22 where selected to bring out all features in the spectrum simultaneously.

Figure 5.22a shows the absorption spectrum of the electronic ground state. Figure 5.22b displays the corresponding 2D-IR spectrum recorded with perpendicular polarization of the IR-pump and IR-probe pulse. This polarization condition reduces the size of the di-

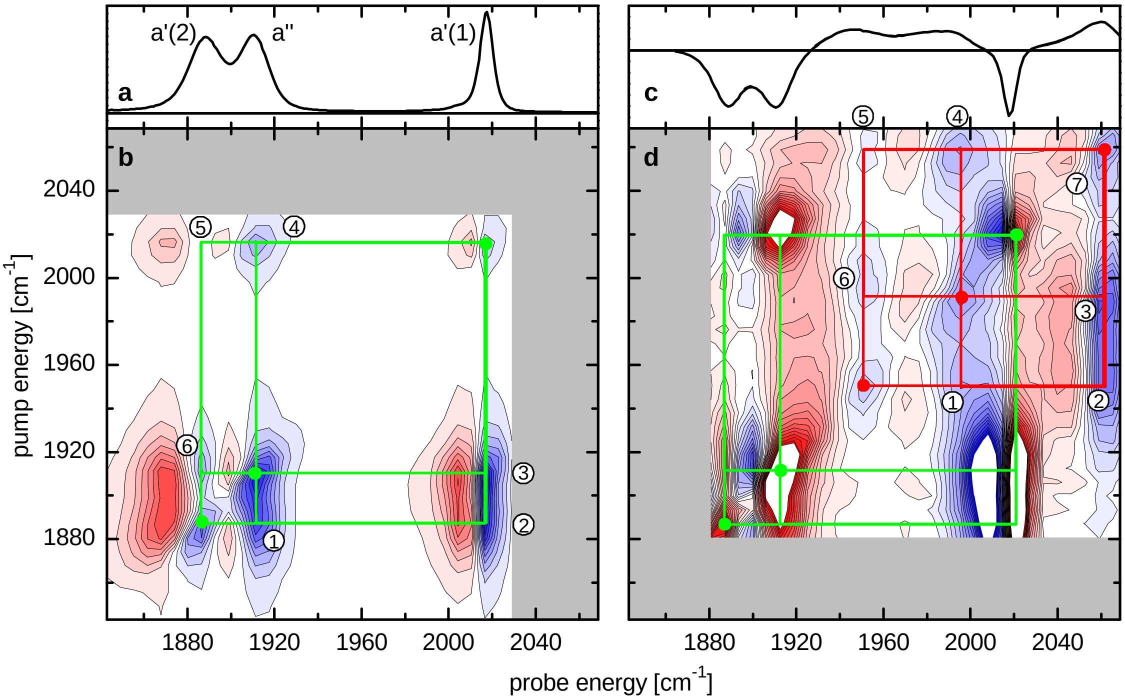

Figure 5.22: a – Absorption spectrum of the electronic ground state of [Re(CO)$_3$(dmbpy)Cl]. b – 2D-IR spectrum of the electronic ground state recorded with perpendicular polarization of the pump and probe pulse at t_{IR}=1.5 ps. c – T1D spectrum after 20 ps. d – T2D-IR spectrum recorded at t_{UV}=20 ps, t_{IR}=1.5 ps, UV-pump-IR-pump polarization $\alpha = 35°$ and UV-pump- IR-probe polarization $\beta = 55°$.

agonal peaks where IR-pump and IR-probe pulse interact with the same transition dipole moment μ^i. The cross peaks originate from interactions of the IR-pump and IR-probe pulse with two different transition dipole moments μ^i and μ^j. Therefore they are intensified with respect to the diagonal peaks if μ^i and μ^j are not parallel. This holds for IR transition dipole moments in [Re(CO)$_3$(dmbpy)Cl]. The diagonal peaks in Figure 5.22b are marked by green dots. The respective cross peaks that indicate coupling between the transitions are connected by green lines. Each peak in the 2D-IR spectrum in fact is a double-peak, due to contributions from the transition between v=0 and v=1 as well as from the transition between v=1 and v=2. To keep the graph clear, the grids in Figure 5.22 connect only the fundamental contributions of the double-peaks. The corresponding v=1 → v=2 contribution is shifted to the left (lower energy) side of the respective fundamental contribution as a result of vibrational anharmonicity. The cross peaks between all transitions are nicely resolved (Figure 5.22b, Pos. 1: cross peak between a'(2)/a'', Pos. 2: a'(2)/a'(1), Pos. 3: a''/a'(1), Pos. 4: a'(1)/a'', Pos. 5: a'(1)/a'(2), Pos. 6: a''/a'(2)). In the case of the cross peak at Pos. 5 the negative part is cancelled by the positive part of the cross peak at Pos. 4.

Figure 5.22c displays the T1D-IR spectrum taken after a UV-delay of 20 ps. As customary in pump-probe spectroscopy the T1D-IR spectrum is a difference spectrum. Negative contributions arise from the depleted ground state, whereas positive contributions are due to the transient MLCT state. In the T2D-IR experiment the IR-probe pulse is replaced by the IR-pump-probe sequence (pulse sequence in Figure 5.18a). Figure 5.22d shows the T2D-IR spectrum taken after the same UV delay time as the T1D-IR spectrum in the upper panel. The T2D-IR spectrum is a difference spectrum in the same fashion as the T1D-IR spectrum. It features signals from the depleted ground state as well as the signals of the transient MLCT state that have opposite sign. The diagonal peaks arising from the electronic ground state are marked by green dots and the respective cross-peaks are connected by green lines, leading to the same grid as in Figure 5.22b. (Figure 5.22d captures a slightly different frequency region than the 2D-IR spectrum in Figure 5.22b to fully include the peaks originating from the

MLCT state.) The MLCT state signals that are shifted along the diagonal are marked in red. The interchange of the sign going from electronic ground state to the excited state can be nicely seen for the a’(1) peak in the upper right corner (Pos. 7) of the 2D representation. The ground state double-peak marked by a green dot has the colors blue and red. The blue-shifted excited state double-peak marked by a red dot has its sign interchanged as indicated by the colors red and blue. The most intriguing features of Figure 5.22d are the well resolved cross peaks in the excited state (Pos. 1: cross peak between a”/a’(2), Pos. 2: a”/a’(1), Pos. 3: a’(2)/a’(1), Pos. 4: a’(1)/a’(2), Pos. 5: a’(1)/a”, Pos. 6: a’(2)/a” - recall the interchanged order of a”, a’(2), a’(1) in the MLCT state as compared to the ground state). The same information as contained in the regular 2D-IR spectra can be now be inferred from T2D-IR spectra for transient species: relative intensities of the cross-peaks and their polarization-dependence provide structural information [252]; homogeneous and inhomogeneous contributions to the line widths can be resolved and reveal dynamical effects and distributions of structures [310, 252, 174, 253]; the anharmonicity of ground and excited state vibrations can be determined [2]. Additional angular information can be inferred from the T2D-IR spectra due to the UV transition dipole that is also involved. For longer delays between the UV pulse and the IR-pump-probe part, the memory of the UV polarization is of course blurred by rotational diffusion. In this case the polarization dependence of the T2D-IR signal approaches that of a normal 2D-IR experiment. Whereas rotational diffusion forbids the determination of dipole orientations in regular UV-pump IR-probe spectroscopy at UV-delays comparable to time scales of rotational diffusion and longer, T2D-IR spectroscopy can access structural information via the relative orientation of the IR dipoles at any time after the UV pulse was applied.

5.3.7 Experimental Examples for the Utilization of Polarization Effects

Regular T2D-IR — Linearly Independent Spectra

The effect of polarization on the T2D-IR spectra is exemplified best by the four linearly independent signals corresponding to the four different tensor elements $D(0,0)$, $D(\frac{\pi}{2},\frac{\pi}{2})$, $D(\frac{\pi}{2},0)$ and $D(0,\frac{\pi}{2})$ that have been introduced in section 5.3.5. Figures 5.23a–d show the four linearly independent spectra obtained with the above polarization settings. The UV-pump-IR-pump delay was set to 20 ps, the IR-pump-IR-probe delay was 1.5 ps. In the following we will discuss the polarization dependence by means of the vibrations of the electronic ground state as their T2D-IR signal is more intense than the signal from the MLCT state (Pos. 6 in Figure 5.23 is the strongest MLCT state signal). Therefore the frequency range in the measurement in Figure 5.23 was adjusted similarly as in Figure 5.22b to capture all peaks from the electronic ground state. Figure 5.23 shows how different features (Pos. 1 to 5) can be selectively enhanced or suppressed by choosing different polarization conditions. This is predicted by our analytic expression for the polarization dependence (Equation 5.41): We calculated model spectra for an idealized C_s symmetric [Re(CO)$_3$(dmbpy)Cl] molecule, where all IR transition dipoles are assumed to be perpendicular to each other and the UV transition dipole to be parallel to the a’(1) transition dipole. The oscillator strengths of the transitions in the model spectra were chosen equal so that differences in the amplitude of the different peaks originate from their polarization dependence only. This model is actually not too far from the true situation. Therefore the model spectra in Figure 5.23e–h agree well with the experimental data. In particular the enhancement or suppression of the different peaks is reproduced well.

In contrast to 2D-IR spectroscopy, the corresponding cross peaks on both sides of the diagonal do not need to show equal polarization dependence in T2D-IR spectroscopy. Instead one peak out of a pair of cross peaks can be selectively enhanced. Consider for example the cross peak between the a’(2) and the a’(1) mode in the lower right corner and the corresponding cross peak between the a’(1) and the a’(2) mode on the other side of the diagonal in the upper left corner. The orientation of the respective transition dipole moments in the idealized molecule is depicted in Figure 5.24. In a 2D-IR spectrum the two cross peaks show the same polarization dependence. This is not the case in the T2D-IR spectra. In Figure 5.23c (corresponding to $D(\frac{\pi}{2},0)$) the lower right peak (Pos. 3) is stronger while the upper left peak (Pos. 4) is strongly reduced. The UV-pump pulse initially selects an oriented sub-ensemble of molecules. In the polarization condition of $D(\frac{\pi}{2},0)$ the IR-pump pulse now arrives with perpendicular polarization which fits well for selecting the a’(2) transition, which is nearly perpendicular to the UV transition dipole. The the IR-probe pulse then arrives with a polarization that

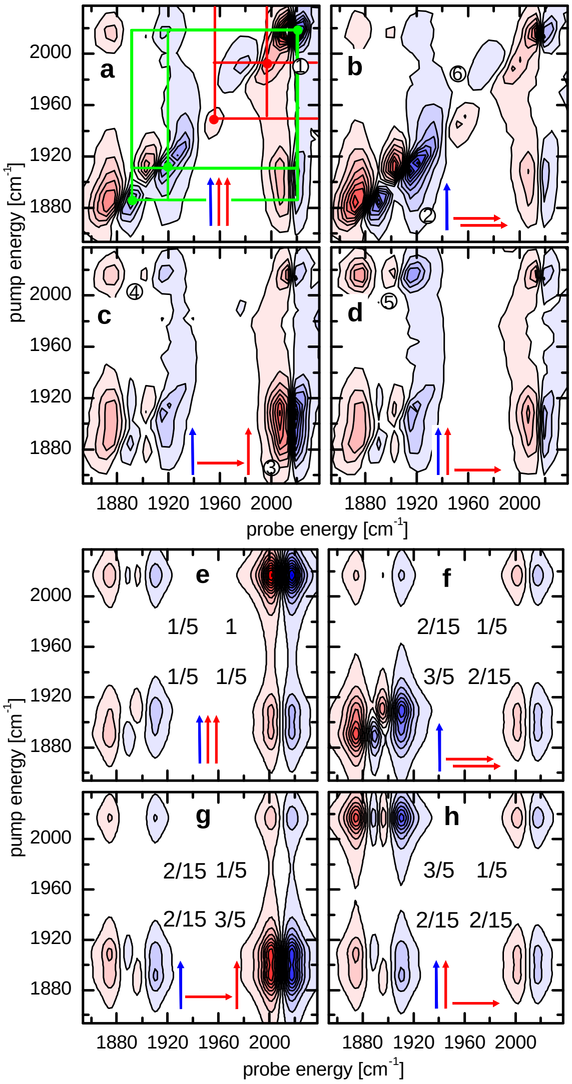

Figure 5.23: a–d: Measurement of the four independent tensor elements, t_{UV}=20 ps, t_{IR}=1.5 ps. The green and red grid connecting the diagonal peaks with the respective cross peaks are identical to the grids in Figure 5.22 and mark the contributions from the electronic ground state and the MLCT state, respectively. a – $D(0,0)$; b – $D(\frac{\pi}{2},\frac{\pi}{2})$; c – $D(\frac{\pi}{2},0)$; d – $D(0,\frac{\pi}{2})$. —– e–f: Schematic spectrum of an idealized C_s symmetric $[Re(CO)_3(dmbpy)Cl]$ molecule. e – $D(0,0)$; f – $D(\frac{\pi}{2},\frac{\pi}{2})$; g – $D(\frac{\pi}{2},0)$; h – $D(0,\frac{\pi}{2})$. The numbers give the relative intensity of the peaks where the a'(1) mode measured with $D(0,0)$ was set 1. The blue and red arrows indicate the relative polarizations of the UV pulse and the two IR pulses.

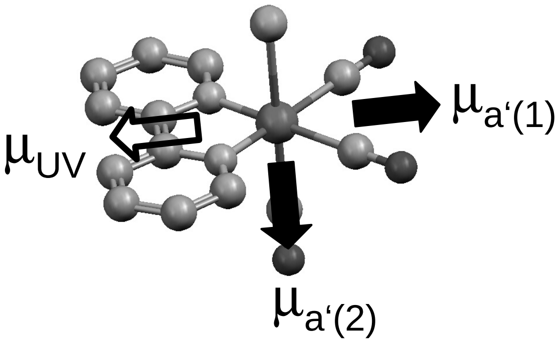

Figure 5.24: a'(1), a'(2) and UV transition dipole moments in the idealized C_s symmetric $[Re(CO)_3(dmbpy)Cl]$ molecule.

is again parallel to the UV-pump pulse now preferring the a'(1) transition. Thus the a'(2)/a'(1) cross peak is favored by this polarization conditions whereas the generation of the a'(1)/a'(2) cross peak proceeds via an unfavorable order of excitations: first, the IR-pump pulse which is perpendicular to the UV-pump pulse has to select the a'(1) mode which is parallel to the UV transition dipole. Then the IR-probe pulse which is parallel to the UV-pump pulse has to select the a'(2) mode which is perpendicular to the UV transition dipole. In the idealized case of perfectly perpendicular or parallel transition dipole moments the contrast ratio of the peaks in the different tensor spectra is largest (5:1 comparing strongest enhancement and strongest suppression). The relative intensities for the idealized case are written next to the bands in Figure 5.23e-h. The actual experiment displays qualitatively the same behavior, whereas the real contrast ratios are somewhat smaller due to the deviations from the idealized transition dipole angles.

For longer UV-delays the molecules selected by the UV pulse undergo rotational diffusion. The polarization dependence of the T2D-IR spectra should therefore approach the polarization dependence of a normal 2D-IR spectrum. Rotational diffusion of $[Re(CO)_3(dmbpy)Cl]$ in DMSO was found to occur on a timescale of 120 ps (see section 5.3.6). We therefore repeated the measurement shown in Figure 5.23 with a UV-delay of 2 ns to be sure that the anisotropy induced by the UV pulse has decayed. The results are shown in Figure 5.25. The two measurements $D(0,0)$ and $D(\frac{\pi}{2},\frac{\pi}{2})$ employing parallel IR pulses have become perfectly equal now as well as the measurements $D(\frac{\pi}{2},0)$ and $D(0,\frac{\pi}{2})$ for perpendicular IR pulses. Like in a normal 2D-IR spectrum, perpendicular IR pulses now emphasize cross peaks on both sides of the diagonal and reduce all diagonal peaks simulta-

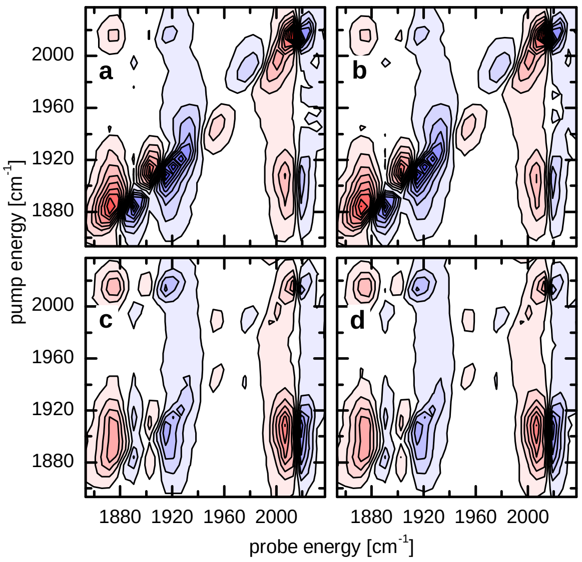

Figure 5.25: Measurement of the four independent tensor elements at a UV delay, which is long compared to the rotational diffusion time, t_{UV}=2 ns, t_{IR}=1.5 ps. a – $D(0,0)$; b – $D(\frac{\pi}{2},\frac{\pi}{2})$; c – $D(\frac{\pi}{2},0)$; d – $D(0,\frac{\pi}{2})$.

neously. The excellent agreement of the two respective measurements demonstrates the reproducibility that can be achieved.

Labeling T2D-IR — Application of Polarization Dependence for Selective Signal Suppression

The labeling technique was already introduced briefly in section 5.3.3. Compared to the regular T2D-IR pulse sequence, the order of pulses is now interchanged: the narrow-band IR-pump pulse is applied before the UV-pump pulse arrives (pulse sequence Figure 5.18c). The IR-pump pulse 'labels' selectively certain vibrations of the initial state by transferring population from the v=0 to the v=1 state. After triggering the MLCT by the UV-pump pulse, the subsequent evolution of this label can be monitored. In this way vibrations of the initial and the MLCT state can be correlated. In a recent work we demonstrated the use of this method to achieve an assignment for the MLCT state vibrations of [Re(CO)$_3$(dmbpy)Cl] [302]. To facilitate the discussion of the polarization effects, we repeat some of the explanations given there.

In the regular T2D-IR spectrum described in section 5.3.6 the peaks where shifted along the diagonal upon photo-excitation (Figure 5.22d). In the labeling T2D-IR spectrum (Figure 5.26b), the shift between ground and excited state now occurs no longer along the diagonal but parallel to the x-axis, since the IR-pump excitation takes place in the electronic ground state before the UV pulse arrives. After UV excitation the IR-probe

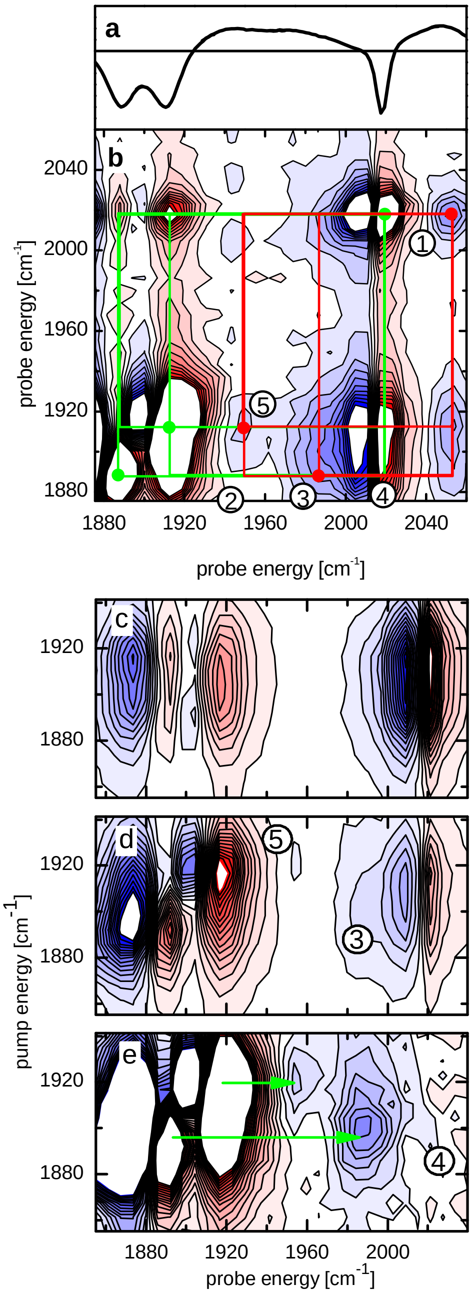

Figure 5.26: a – T1D-IR spectrum at t_{UV}=2 ps; b to e – labeling T2D-IR spectra recorded with a delay of 2 ps between IR-pump and UV-pump and 2.5 ps between UV-pump and IR-probe; b – $D(\frac{\pi}{4},\frac{\pi}{4})$; c – $D(\frac{\pi}{2},0)$; d – $D(\frac{\pi}{2},\frac{\pi}{2})$; e – Difference $D(\frac{\pi}{2},\frac{\pi}{2})$ - 0.29 $D(\frac{\pi}{2},0)$

pulse interacts with the electronically excited state. This means: the y-position (pump frequency axis) of the peak does not change upon excitation, staying at the value of the electronic ground state. On the x-axis (probe frequency axis), the frequency in the transient excited state can be read off. Therefore excited state and ground state vibrations are correlated by the labeling pulse sequence. This can be nicely seen in the case of the a'(1) vibration in the upper right corner of the T2D-IR spectrum (Figure 5.26b, Pos. 1). The peak shifts from its ground state position at 2017 cm^{-1} (green dot) to 2048 cm^{-1} (red dot) within 2 ps after the UV pulse. To our surprise, however, in the case of the a'(2) band at 1888 cm^{-1} we did not find any corresponding excited state signal at 1944 cm^{-1} (Pos. 2) where we had expected it based on the assignment commonly used in literature [299, 335]. Instead of a parallel shift of the a" peak and the a'(2) peak we find that the two peaks change their order in the MLCT state: the a" peak is shifted to 1944 cm^{-1} (Pos. 5), whereas the a'(2) band is shifted to 1985 cm^{-1} (Pos. 3) where it is hidden by the strong ground state cross peaks (Pos. 4) between both the a'(2) and a" modes and the a'(1) mode.

To bring out the effect more clearly, it is desirable to suppress the ground state cross peaks (Pos. 4), while maintaining the MLCT state peaks (Pos. 3 and 5), that have been shifted off the diagonal now. This can be achieved utilizing the different polarization dependence of the various peaks. The peaks at Pos. 3 and Pos. 5 have been shifted off the diagonal. Nevertheless they still behave like diagonal peaks as far as their polarization dependence is concerned, because IR-pump and IR-probe pulse interact twice with the same transition dipole [2]. Investigation of Figure 5.23 suggests the following strategy to bring out the shifted peaks more clearly: measure the tensor element $D(\frac{\pi}{2},\frac{\pi}{2})$, where the diagonal peaks of the a"(2) and a' vibrations are most pronounced and subtract from this the appropriately scaled element $D(\frac{\pi}{2},0)$, where the diagonal peaks are weak and the disturbing cross peaks are enhanced. For the idealized geometry of [Re(CO)$_3$(dmbpy)Cl] the scaling factor is $\frac{2}{9} \approx 0.22$, as can be inferred from the relative intensities given in Figure 5.23f and g. In the real case it is found to be 0.29. Figure 5.26 shows the respective T2D-IR spectra for $D(\frac{\pi}{2},0)$ (Figure 5.26c) and $D(\frac{\pi}{2},\frac{\pi}{2})$ (Figure 5.26d) of the frequency region of interest as well as their difference $D(\frac{\pi}{2},0) - 0.29D(\frac{\pi}{2},\frac{\pi}{2})$ (Figure 5.26e). The strong cross peak (Pos. 4) is completely suppressed and the excited state bands are now well resolved. In particular the a'(2) band (Pos. 3) that overlapped with the cross peak can now be clearly identified. The shift along the x-axis is indicated by green arrows. Figure 5.26 provides direct evidence for the new assignment of the excited state bands. This new assignment agrees well with the findings of Dattelbaum *et al.* [329], who carried out time-dependent DFT calculations for the very similar complex [Re(CO)$_3$(dmbpy)(4-Etpy)]$^+$ (4-Etpy = 4-ethylpyridine). In their quantum chemical calculations Dattelbaum *et al.* also obtain a small shift for the a" band compared to the a'(2) band. It may sometimes be necessary to suppress the cross peaks on both sides of the diagonal simultaneously. For this purpose the difference between signals with the same polarization dependent prefactor for the cross peaks in the upper and lower half of the T2D-IR spectrum is needed. Such symmetric cross peaks are obtained for $|\alpha| = |\beta|$. Therefore the difference between $D(\alpha,\alpha)$ and $D(\alpha,-\alpha)$ has to be taken. The strongest contrast is then obtained by changing the relative polarization of the IR pulses by $\frac{\pi}{2}$. In Reference [302] we have therefore used the polarization condition $D(\frac{\pi}{4},\frac{\pi}{4}) - 0.5D(\frac{\pi}{4},-\frac{\pi}{4})$. For the idealized angles a scaling factor of $\frac{5}{11} \approx 0.45$ would have to be used instead.

5.3.8 Summary and Conclusions

We have derived a general equation for the polarization dependence of T2D-IR spectroscopy which is of 5th order in the laser field and involves up to three transition dipole moments. The polarization conditions leading to a maximum of structural information where discussed. Magic angle like conditions where found to exist in important cases in this three pulse - three dipole experiment. Useful special cases of polarization conditions where formulated. In comparison to pump-probe spectroscopy the additional pulse and transition dipole moment in T2D-IR lead to a much more involved polarization dependence. However, this additional degree of freedom in polarization strongly enhances the versatility of signal manipulation and the potential structural information content of the signals. The utilization of various polarization conditions was demonstrated for different types of T2D-IR experiments on the model compound [Re(CO)$_3$(dmbpy)Cl]. Employing the polarization de-

---

[2] If the photo-triggered process were to cause a substantial change in the orientation of the IR-transition dipole moments, this statement would not hold any longer. Even in this case, however, different peaks often posses different polarization dependence and could be separated.

grees of freedom it is possible to selectively enhance or diminish different features in the spectrum. By taking appropriate linear combinations of signals the complete suppression of selected peaks can be achieved. The need to form linear combinations of signals calls for the reliable measurement of the different tensor elements under equal experimental conditions. This is ensured by the use of rapid polarization switches that allow for a quasi simultaneous measurement of different tensor elements by changing the polarizations every few hundred laser pulses. The influence of rotational diffusion on the regular T2D-IR signal was shown. Whereas rotational diffusion forbids the determination of dipole orientations in UV-pump IR-probe spectroscopy at UV-delays on the timescale of rotational diffusion and longer, T2D-IR spectroscopy can access information on molecular geometry via the IR transitions at any time after the UV pulse was applied. Furthermore T2D-IR experiments are conceivable, where the trigger pulse does not interact with a transition dipole of the investigated molecule at all but initiates a process by a T-jump or a pH-jump. In this case the T2D-IR experiment would retain the polarization dependence of 2D-IR and the tools developed for structure determination by 2D-IR [283, 254, 252, 253] could be applied directly. With the experimental methods and the detailed understanding of the polarization dependence developed in this work the structure resolution potential of 2D-IR [283, 254, 252, 253] is now available for the transient regime.

Acknowledgements. We would like to thank the anonymous referee for pointing out an error in our argumentation in the first version of this manuscript. This work was supported by the Swiss National Science Foundation under contract 21-67573.02.

5.3.9 Appendix: Evaluation of the Correlation Functions

The method followed here is well-described for example in ref. [291] and [341], where the influence of rotational diffusion on the fluorescence-depolarization signal of arbitrarily-shaped molecules was presented. The dipole correlation functions in equation 5.3.5 are of the form $\langle \mu_A^0(t_1)\mu_A^0(t_1)\mu_B^i(t_2)\mu_B^i(t_2)\mu_C^j(t_3)\mu_C^j(t_3)\rangle$. For their evaluation we first express the time-dependent transition dipole moments $\vec{\mu}$ in the laboratory frame in terms of the time-independent components of the dipole moments $\vec{m}$ in the molecule-fixed frame

$$\mu_\alpha(t) = (R^{-1}_{\phi,\theta,\chi}(t)\vec{m})_\alpha \tag{5.66}$$

where $R_{\phi,\theta,\chi}(t)$ is the Euler rotation or direction cosine matrix [342]:

$$R_{\phi,\theta,\chi} \equiv \begin{pmatrix} X_x & X_y & X_z \\ Y_x & Y_y & Y_z \\ Z_x & Z_y & Z_z \end{pmatrix} = \begin{pmatrix} \cos\phi\cos\theta\cos\chi - \sin\phi\sin\chi & -\cos\phi\sin\theta\cos\chi - \sin\phi\cos\chi & \cos\phi\sin\theta \\ \sin\phi\cos\theta\cos\chi + \cos\phi\sin\chi & -\sin\phi\cos\theta\sin\chi + \cos\phi\cos\chi & \sin\phi\sin\theta \\ -\sin\theta\cos\chi & \sin\theta\sin\chi & \cos\theta \end{pmatrix} \tag{5.67}$$

which changes in time as the molecule diffuses. $R_{\phi,\theta,\chi}$ can be expressed in terms of Wigner rotation matrix elements $\mathfrak{D}^J_{MN}$ [342]:

$$R_{\phi,\theta,\chi} = \begin{pmatrix} \frac{1}{2}(\mathfrak{D}^1_{-1-1} - \mathfrak{D}^1_{1-1} - \mathfrak{D}^1_{-11} + \mathfrak{D}^1_{11}) & -\frac{i}{2}(-\mathfrak{D}^1_{-1-1} - \mathfrak{D}^1_{1-1} + \mathfrak{D}^1_{-11} - +\mathfrak{D}^1_{11}) & \frac{1}{\sqrt{2}}(\mathfrak{D}^1_{0-1} - \mathfrak{D}^1_{01}) \\ \frac{i}{2}(-\mathfrak{D}^1_{-1-1} + \mathfrak{D}^1_{1-1} - \mathfrak{D}^1_{-11} + \mathfrak{D}^1_{11}) & \frac{1}{2}(\mathfrak{D}^1_{-1-1} + \mathfrak{D}^1_{1-1} + \mathfrak{D}^1_{-11} + \mathfrak{D}^1_{11}) & -\frac{i}{\sqrt{2}}(\mathfrak{D}^1_{0-1} + \mathfrak{D}^1_{01}) \\ \frac{1}{\sqrt{2}}(\mathfrak{D}^1_{-10} - \mathfrak{D}^1_{10}) & \frac{i}{\sqrt{2}}(\mathfrak{D}^1_{-10} + \mathfrak{D}^1_{10}) & \mathfrak{D}^1_{00} \end{pmatrix} \tag{5.68}$$

This leads to sums of correlation functions like

$$\begin{aligned} & \langle \mathfrak{D}^1_{MN}(\Omega_1,t_1)\mathfrak{D}^1_{M'N'}(\Omega_1,t_1)\mathfrak{D}^1_{M''N''}(\Omega_2,t_2)\mathfrak{D}^1_{M'''N'''}(\Omega_2,t_2)\mathfrak{D}^1_{M^{iv}N^{iv}}(\Omega_3,t_3)\mathfrak{D}^1_{M^vN^v}(\Omega_3,t_3)\rangle & (5.69) \\ = & \frac{1}{8\pi^2}\int d\Omega_1 \int d\Omega_2 \int d\Omega_3 \mathfrak{D}^1_{MN}(\Omega_1,t_1)\mathfrak{D}^1_{M'N'}(\Omega_1,t_1)G(\Omega_1,t_1|\Omega_2,t_2)\mathfrak{D}^1_{M''N''}(\Omega_2,t_2)\mathfrak{D}^1_{M'''N'''}(\Omega_2,t_2) & \\ & \times G(\Omega_2,t_2|\Omega_3,t_3)\mathfrak{D}^1_{M^{iv}N^{iv}}(\Omega_3,t_3)\mathfrak{D}^1_{M^vN^v}(\Omega_3,t_3), & (5.70) \end{aligned}$$

where Ω_i denotes the Euler angles $(\phi_i, \theta_i, \chi_i)$ which define the rotation from the molecular frame to the laboratory frame at time-point t_i and $\int d\Omega = \int_0^{2\pi} d\chi \int_0^{2\pi} d\phi \int_0^{\pi} \sin\theta d\theta$. The correlation functions of rotation matrix elements can now be evaluated by inserting the Green's function of the Debye diffusion equation for symmetric or spherical diffusors [291]

$$G(\Omega_1, t_1|\Omega_0, t_0) = \frac{2J+1}{8\pi^2} \sum_{JMN} \mathfrak{D}^J_{MN}(\Omega_0, t_0) \mathfrak{D}^{J*}_{MN}(\Omega_1, t_1) \times e^{-[D_R^{\perp} J(J+1) + (D_R^{\parallel} - D_R^{\perp}) N^2](t_1 - t_0)}, \tag{5.71}$$

The products of rotation matrix elements at equal times can then be written as sums of matrix elements of different order and we can make use of the closure relation

$$\int d\Omega \mathfrak{D}^{J*}_{MN}(\Omega) \mathfrak{D}^{j}_{mn}(\Omega) = \frac{8\pi^2}{2J+1} \delta_{Jj} \delta_{Mm} \delta_{Nn}. \tag{5.72}$$

Here we evaluate the correlation functions in the spherical diffusor approximation, which considerably simplifies the algebra involved. Since all diffusion directions are then equivalent, we can let the UV transition dipole define the *z*-axis in the molecular frame. The first IR transition dipole may be chosen to lie in the *xz*-plane, and the second IR transition dipole has arbitrary orientation in the molecular frame:

$$\vec{m}^0 = \begin{pmatrix} 0 \\ 0 \\ 1 \end{pmatrix}, \quad \vec{m}^i = \begin{pmatrix} \sin\theta_{i0} \\ 0 \\ \cos\theta_{i0} \end{pmatrix}, \quad \vec{m}^j = \begin{pmatrix} \sin\theta_{j0}\cos\eta_{j0} \\ \sin\theta_{j0}\sin\eta_{j0} \\ \cos\theta_{j0} \end{pmatrix}. \tag{5.73}$$

While the generalization to asymmetric diffusors is much more involved, (up to five time constants appear already in third order pump-probe ore fluorescence-depolarization spectroscopy [341], the treatment of symmetric diffusors can follow exactly the same line. An example was recently given for the third order heterodyne-detected photon echo signal of a symmetric diffusor with arbitrary dipole orientations relative to the main diffusion axes [343].

The dependence of the fifth order response function for T2D pump-pump-probe spectroscopy on polarization and internal molecular angles is summarized in Table 5.4. This table still contains the azimuthal angle η_{j0} in the molecular frame, which depends on our particular choice of coordinates. To obtain the final result given in Table 5.3 it was replaced by the relative angle θ_{ij} between transition dipoles *i* and *j* using the relation:

$$\cos\eta_{j0}\sin\theta_{i0}\sin\theta_{j0} = \cos\theta_{ij} - \cos\theta_{i0}\cos\theta_{j0}. \tag{5.74}$$

The method above may also be used to evaluate the correlation functions in equation 5.41. Except for $\langle\cos\Theta_{i0}\cos\Theta_{j0}\cos\Theta_{ij}\rangle$ these are already well known from third order spectroscopy [292]. For spherical diffusors we have

$$\begin{aligned} \langle\cos^2\Theta_{ij}\rangle &= \frac{1}{3}(1 + 2\langle P_2(\cos\Theta_{ij})\rangle) \\ &= \frac{1}{3}(1 + 2c_{23}P_2(\cos\theta_{ij})) && (5.75) \\ \langle\cos^2\Theta_{i0}\rangle &= \frac{1}{3}(1 + 2c_{12}P_2(\cos\theta_{i0})) && (5.76) \\ \langle\cos^2\Theta_{j0}\rangle &= \frac{1}{3}(1 + 2c_{12}c_{23}P_2(\cos\theta_{j0})) && (5.77) \end{aligned}$$

Expansion of $\langle\cos\Theta_{i0}\cos\Theta_{j0}\cos\Theta_{ij}\rangle$ in direction cosine correlation functions leads to 270 non-vanishing terms and the final expression in the spherical diffusor approximation:

$$\begin{aligned} &\langle\cos\Theta_{i0}\cos\Theta_{j0}\cos\Theta_{ij}\rangle = \\ &\quad \frac{1}{9}(1 - c_{12}c_{23} + 2(1 - c_{23})c_{12}P_2(\cos\theta_{i0}) \\ &\quad + 2(1 - c_{12})c_{23}P_2(\cos\theta_{ij}) \\ &\quad + 9c_{12}c_{23}\cos\theta_{i0}\cos\theta_{j0}\cos\theta_{ij}) \end{aligned} \tag{5.78}$$

is more easily obtained by comparing equation 5.41 with the results in Table 5.3.

Table 5.4: Evaluation of the direction cosine correlation functions that contribute to the the T2D signal in the spherical diffusor approximation. All terms must be divided by 27. Terms marked by an asterisk (*) correspond to those derived in ref. [294] for a single dipole orientation and are denoted there by R^{μ}_{ZZZZZZ}, R^{μ}_{YYZZZZ}, R^{μ}_{ZZYYZZ}, R^{μ}_{ZZZZYY}, R^{μ}_{ZYYZZZ}.

polarization angle dependence	molecular angle dependence	1	$\frac{e^{-6D_R t_{23}}}{5}$ $\equiv c_{23}/5$	$\frac{e^{-6D_R t_{12}}}{5}$ $\equiv c_{12}/5$	$\frac{e^{-6D_R(t_{12}+t_{23})}}{35}$	direction cosine correlation function
$\cos^2\alpha\cos^2\beta$						
	$\sin^2\theta_{i0}\sin^2\theta_{j0}\cos^2\eta_{j0}$	1	4	-2	-22	$\langle Z_z^2(t_1)Z_x^2(t_2)Z_x^2(t_3)\rangle$
	$\sin^2\theta_{i0}\sin^2\theta_{j0}\sin^2\eta_{j0}$	1	-2	-2	2	$\langle Z_z^2(t_1)X_x^2(t_2)Z_y^2(t_3)\rangle$
	$\cos^2\theta_{i0}\sin^2\theta_{j0}\cos^2\eta_{j0}$	1	-2	4	-22	$\langle Z_z^2(t_1)Z_z^2(t_2)Z_x^2(t_3)\rangle$
	$\cos^2\theta_{i0}\sin^2\theta_{j0}\sin^2\eta_{j0}$	1	-2	4	-22	$\langle Z_z^2(t_1)Z_z^2(t_2)Z_y^2(t_3)\rangle$
	$\sin^2\theta_{i0}\cos^2\theta_{j0}$	1	-2	-2	-20	$\langle Z_z^2(t_1)Z_x^2(t_2)Z_z^2(t_3)\rangle$
	$\cos^2\theta_{i0}\cos^2\theta_{j0}$	1	4	4	44	$\langle Z_z^2(t_1)Z_z^2(t_2)Z_z^2(t_3)\rangle^*$
	$\cos\theta_{i0}\sin\theta_{i0}\cos\theta_{j0}\sin\theta_{j0}\cos\eta_{j0}$	0	12	0	24	$\langle Z_z^2(t_1)Z_zZ_x(t_2)Z_zZ_x(t_3)\rangle$
$\cos^2\alpha\sin^2\beta$						
	$\sin^2\theta_{i0}\sin^2\theta_{j0}\cos^2\eta_{j0}$	1	-2	-2	11	$\langle Z_z^2(t_1)Z_x^2(t_2)X_x^2(t_3)\rangle$
	$\sin^2\theta_{i0}\sin^2\theta_{j0}\sin^2\eta_{j0}$	1	1	-2	-1	$\langle Z_z^2(t_1)Z_x^2(t_2)X_y^2(t_3)\rangle$
	$\cos^2\theta_{i0}\sin^2\theta_{j0}\cos^2\eta_{j0}$	1	1	4	11	$\langle Z_z^2(t_1)Z_z^2(t_2)X_x^2(t_3)\rangle$
	$\cos^2\theta_{i0}\sin^2\theta_{j0}\sin^2\eta_{j0}$	1	1	4	11	$\langle Z_z^2(t_1)Z_z^2(t_2)X_y^2(t_3)\rangle$
	$\sin^2\theta_{i0}\cos^2\theta_{j0}$	1	1	-2	-10	$\langle Z_z^2(t_1)Z_x^2(t_2)X_z^2(t_3)\rangle$
	$\cos^2\theta_{i0}\cos^2\theta_{j0}$	1	-2	4	-22	$\langle Z_z^2(t_1)Z_z^2(t_2)X_z^2(t_3)\rangle^*$
	$\cos\theta_{i0}\sin\theta_{i0}\cos\theta_{j0}\sin\theta_{j0}\cos\eta_{j0}$	0	-6	0	-12	$\langle Z_z^2(t_1)Z_xZ_z(t_2)X_xX_z(t_3)\rangle$
$\sin^2\alpha\cos^2\beta$						
	$\sin^2\theta_{i0}\sin^2\theta_{j0}\cos^2\eta_{j0}$	1	-2	1	-10	$\langle Z_z^2(t_1)X_x^2(t_2)Z_x^2(t_3)\rangle$
	$\sin^2\theta_{i0}\sin^2\theta_{j0}\sin^2\eta_{j0}$	1	1	1	-22	$\langle Z_z^2(t_1)X_x^2(t_2)Z_y^2(t_3)\rangle$
	$\cos^2\theta_{i0}\sin^2\theta_{j0}\cos^2\eta_{j0}$	1	1	-2	-10	$\langle Z_z^2(t_1)X_z^2(t_2)Z_x^2(t_3)\rangle$
	$\cos^2\theta_{i0}\sin^2\theta_{j0}\sin^2\eta_{j0}$	1	1	-2	-10	$\langle Z_z^2(t_1)X_z^2(t_2)Z_y^2(t_3)\rangle$
	$\sin^2\theta_{i0}\cos^2\theta_{j0}$	1	1	1	32	$\langle Z_z^2(t_1)X_x^2(t_2)Z_z^2(t_3)\rangle$
	$\cos^2\theta_{i0}\cos^2\theta_{j0}$	1	-2	-2	20	$\langle Z_z^2(t_1)X_z^2(t_2)Z_z^2(t_3)\rangle^*$
	$\cos\theta_{i0}\sin\theta_{i0}\cos\theta_{j0}\sin\theta_{j0}\cos\eta_{j0}$	0	-6	0	-12	$\langle Z_z^2(t_1)X_xX_z(t_2)Z_xZ_z(t_3)\rangle$
$\sin^2\alpha\sin^2\beta$						
	$\sin^2\theta_{i0}\sin^2\theta_{j0}\cos^2\eta_{j0}$	1	4	1	11	$\langle Z_z^2(t_1)X_x^2(t_2)X_x^2(t_3)\rangle$
	$\sin^2\theta_{i0}\sin^2\theta_{j0}\sin^2\eta_{j0}$	1	-2	1	-1	$\langle Z_z^2(t_1)X_x^2(t_2)X_y^2(t_3)\rangle$
	$\cos^2\theta_{i0}\sin^2\theta_{j0}\cos^2\eta_{j0}$	1	-2	-2	11	$\langle Z_z^2(t_1)X_z^2(t_2)X_x^2(t_3)\rangle$
	$\cos^2\theta_{i0}\sin^2\theta_{j0}\sin^2\eta_{j0}$	1	-2	-2	11	$\langle Z_z^2(t_1)X_z^2(t_2)X_y^2(t_3)\rangle$
	$\sin^2\theta_{i0}\cos^2\theta_{j0}$	1	-2	1	-10	$\langle Z_z^2(t_1)X_x^2(t_2)X_z^2(t_3)\rangle$
	$\cos^2\theta_{i0}\cos^2\theta_{j0}$	1	4	-2	-22	$\langle Z_z^2(t_1)X_z^2(t_2)X_z^2(t_3)\rangle^*$
	$\cos\theta_{i0}\sin\theta_{i0}\cos\theta_{j0}\sin\theta_{j0}\cos\eta_{j0}$	0	12	0	-12	$\langle Z_z^2(t_1)X_xX_z(t_2)X_xX_z(t_3)\rangle$
$\sin\alpha\cos\alpha\sin\beta\cos\beta$						
	$\sin^2\theta_{i0}\sin^2\theta_{j0}\cos^2\eta_{j0}$	0	12	0	-12	$\langle Z_z^2(t_1)X_xZ_x(t_2)X_xZ_x(t_3)\rangle$
	$\sin^2\theta_{i0}\sin^2\theta_{j0}\sin^2\eta_{j0}$	0	-6	0	24	$\langle Z_z^2(t_1)X_xZ_x(t_2)X_yZ_y(t_3)\rangle$
	$\cos^2\theta_{i0}\sin^2\theta_{j0}\cos^2\eta_{j0}$	0	-6	0	-12	$\langle Z_z^2(t_1)X_zZ_z(t_2)X_xZ_x(t_3)\rangle$
	$\cos^2\theta_{i0}\sin^2\theta_{j0}\sin^2\eta_{j0}$	0	-6	0	-12	$\langle Z_z^2(t_1)X_zZ_z(t_2)X_yZ_y(t_3)\rangle$
	$\sin^2\theta_{i0}\cos^2\theta_{j0}$	0	-6	0	-12	$\langle Z_z^2(t_1)X_xZ_x(t_2)X_zZ_z(t_3)\rangle$
	$\cos^2\theta_{i0}\cos^2\theta_{j0}$	0	12	0	24	$\langle Z_z^2(t_1)X_zZ_z(t_2)X_zZ_z(t_3)\rangle^*$
	$\cos\theta_{i0}\sin\theta_{i0}\cos\theta_{j0}\sin\theta_{j0}\cos\eta_{j0}$	0	36	0	36	$\langle Z_z^2(t_1)X_zZ_x(t_2)X_zZ_x(t_3)\rangle$ $+\langle Z_z^2(t_1)X_xZ_z(t_2)X_zZ_x(t_3)\rangle$ $+\langle Z_z^2(t_1)X_zZ_x(t_2)X_xZ_z(t_3)\rangle$ $+\langle Z_z^2(t_1)X_xZ_z(t_2)X_xZ_z(t_3)\rangle$

5.4 P14 –Solvation beyond the Linear Response Regime

Jens Bredenbeck, Jan Helbing and Peter Hamm,
Phys Rev. Lett., submitted.

5.4.1 abstract

Transient two-dimensional infrared spectroscopy (T2D-IR) on a charge transfer model system is used as a non-linear probe of solvation dynamics. Unlike expected in the linear response case, non-equilibrium relaxation and equilibrium spectral diffusion occur on different timescales. Transient 2D-IR spectroscopy is shown to be sensitive to higher order frequency fluctuation correlation functions, and provides evidence for correlation between commonly observed fast and slow solvation processes.

In the solution phase, the quantum-mechanical states of a solute molecule are coupled to - and perturbed by - a continuum of low-frequency modes of the solvent, which may qualitatively and quantitatively change the mechanism and outcome of any liquid phase reaction in chemistry and biology. Solvation experiments are used to investigate the strength and dynamics of solute-solvent interactions. In such an experiment, a non-equilibrium configuration is first prepared, and it's relaxation to equilibrium is then sensed by means of a particular spectroscopic transition, which can be either electronic or vibrational. Spectroscopy of solvation modes is particularly challenging since the band typically is very broad and essentially structureless. It is well established that only non-linear spectroscopy can 'look underneath' a spectroscopic transition and resolve the mechanisms and interactions giving rise to its broadening. Dynamic Stokes shift [168, 344] photon echo peak shift [345, 301, 346, 347, 348, 308] and 2D spectroscopy [320, 261, 247, 303] have been used to measure solvent-solute interactions. They all are 3rd-order nonlinear spectroscopies and reveal the spectral density of the solvation modes [310]. However, concerning the solvation degrees of freedoms, these experiments are linear spectroscopies, and contain no more information than a far-IR absorption or a low frequency Raman spectrum (except that different techniques couple with different strength to different low frequency modes). Furthermore, essentially all solvation experiments so far have been discussed in the framework of linear response theory. The reason for this is not that linear response has been *proven* to be valid for solute-solvent systems, but that experiments so far didn't provide the information needed to *look beyond* the linear response hypothesis.

Along the lines of Onsager's regression hypothesis [211], a *non-equilibrium* solvation experiments can be described in terms of an *equilibrium* two-point frequency fluctuation correlation function (FFCF) $c_2(t) = \langle \omega(0)\omega(t) \rangle$ The instantaneous deviation $\omega(t)$ of the test molecule's transition frequency from its mean value is a direct measure of the interaction of the surrounding solvent with that transition. The two-point FFCF is related to the spectral density of solvation modes through a Fourier transformation [310]. In the linear response regime, the two-point FFCF is sufficient to fully characterize the solvation process, since higher order correlation functions would factorize into two-point FFCF's. In the present paper, we show that transient 2D (T2D) spectroscopy, which is a 5th-order technique, is nonlinear with respect to solvation modes, and hence, provides information which is similar to that potentially obtained from 2D-Raman spectroscopy [295, 298]. Unlike 3rd-order spectroscopy, T2D spectroscopy offers a glance at the nonlinear dynamics of solvation. In particular, we demonstrate that T2D spectroscopy is a sensitive probe of higher order FFCF's, such as the three-point FFCF $c_3(t_1,t_2) = \langle \omega(0)\omega(t_1)\omega(t_2) \rangle$.

Experiment: Transient 2D (T2D) IR spectroscopy extends conventional 2D spectroscopy to the non-equilibrium regime [174, 349]. An $\mathrm{UV_{pump}}$-pulse photo-excites a molecule, and a subsequent pair of IR pulses ($\mathrm{IR_{pump}}$ and $\mathrm{IR_{probe}}$) - acting as a probe process - measures a snapshot 2D spectrum. We apply transient 2D (T2D) spectroscopy to investigate solvation of the photo-induced metal-to-ligand charge transfer (MLCT) of $[\mathrm{Re(CO)_3Cl(dmbpy)}]$ (dmbpy=4,4'-dimethyl-2,2'bi-pyridine) dissolved in DMSO. Photo-excitation of $[\mathrm{Re(CO)_3Cl(dmbpy)}]$ changes the electronic structure of the molecule, causing an instantaneous blue shift of all C=O modes. The sudden change of the electronic dipole moment, in turn, triggers a reorientation of the surrounding solvent molecules and the new charge distribution is solvated. Since the solvent molecules are coupled to the molecule's C=O groups, the solvation process can be observed as a further blue-shift of the C=O modes on a 5.5 ps timescale (Fig. 5.27b, top row) [299].

We focus on the highest frequency C=O vibration (symmetric stretch of all three CO's), which shifts from 2018 $\mathrm{cm^{-1}}$ in the electronic ground state to 2060 $\mathrm{cm^{-1}}$ in the completely solvated charge transfer state. Fig. 5.27a shows a 2D spectrum of the 2060 $\mathrm{cm^{-1}}$ band with an $\mathrm{UV_{pump}}$-$\mathrm{IR_{pump}}$ delay time of 100 ps and an $\mathrm{IR_{pump}}$-$\mathrm{IR_{probe}}$ delay time of 1.5 ps (see Refs. [174, 349] for experimental details). Since the system is equilibrated in the electronically excited state 100 ps after excitation, we refer to this spectrum as the equilibrium 2D spectrum. In a 2D spectrum, a broad band $\mathrm{IR_{probe}}$ pulse measures the response of the sample as a function of a tunable, narrow band $\mathrm{IR_{pump}}$ pulse (dynamic hole burning). The spectrum consists of the negative bleach and stimulated emission signal (depicted in blue) and the anharmonically red-shifted excited state absorption signal (in red). Since the 2D spectrum of the 2060 $\mathrm{cm^{-1}}$ band is superimposed in the lower-left corner by the contribution from the electronic ground state at 2018 $\mathrm{cm^{-1}}$, we concentrate our discussion on the negative (blue) band, which is well separated from any perturbing sig-

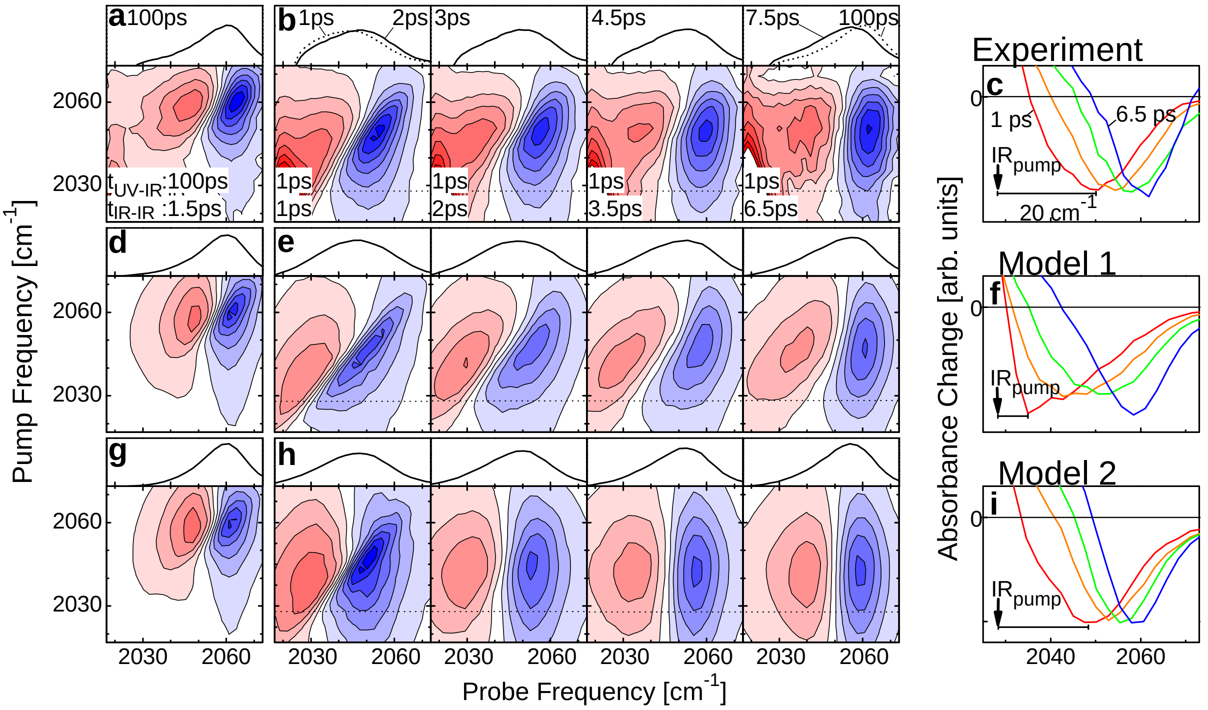

Figure 5.27: (a) Equilibrium 2D spectra with $t_{UV_{\text{pump}},IR_{\text{pump}}}$=100 ps and $t_{IR_{\text{pump}},IR_{\text{probe}}}$=1.5 ps. (b) T2D spectra with $t_{UV_{\text{pump}},IR_{\text{pump}}}$=1 ps and $t_{IR_{\text{pump}},IR_{\text{probe}}}$ varied from 1 ps to 6.5 ps. The signal decay due to vibrational relaxation is normalized out. Negative signals are depicted in blue, positive in red, on a linear scale. Top row: T1D spectra at corresponding delay times $t_{UV_{\text{pump}},IR_{\text{pobe}}}$. Dashed lines: 1ps T1D and equilibrium 1D spectra for comparison. (c) Cuts through the T2D spectra with pump frequency 2028 cm^{-1} (marked by the arrow in (c) and the dotted line in (b)). (d-i) Corresponding results from model **1** and **2**.

nals. The equilibrium 2D spectrum shows a characteristic tilt, which is a signature of inhomogeneity on the picosecond time scale [247, 303].

Fig. 5.27b shows T2D spectra with short UV$_{\text{pump}}$-IR$_{\text{pump}}$ delay time of 1 ps and IR$_{\text{pump}}$-IR$_{\text{probe}}$ delay times varied between 1 ps and 6.5 ps. At a first sight, the T2D spectra evolve in time as one would intuitively expect: At early times, the T2D spectrum is broad and tilted, reflecting a strong inhomogeneity of the band. With increasing IR$_{\text{pump}}$-IR$_{\text{probe}}$ delay time, the band orients more vertically as a result of the loss of memory of the IR$_{\text{pump}}$ frequency that initially labelled the molecules. At the same time, the 2D band center shifts towards the right and away from the diagonal, in parallel with the solvation shift also seen in the T1D spectra (Fig. 5.27b, top row). In other words, the molecules are vibrationally labelled and keep their tag as solvation shifts the absorption band to higher frequencies.

A closer inspection, however, reveals a couple of nontrivial details: Firstly, the spectral hole burned by the IR$_{\text{pump}}$-pulse shifts surprisingly fast within the first 1 ps IR$_{\text{pump}}$-IR$_{\text{probe}}$ delay time. This is best seen in horizontal cuts through the red wing of the T2D spectrum at an IR$_{\text{pump}}$-frequency of 2028 cm^{-1} (Fig. 5.27c), which reveal a shift of about 20 cm^{-1} from the pump pulse position within 1 ps. Secondly, the 2D lineshape is essentially vertical already after 6.5 ps IR$_{\text{pump}}$-IR$_{\text{probe}}$ delay time, although the system has not yet reached equilibrium (compare with dashed line in Fig. 5.27b, top at 6.5 ps). Scanning the IR$_{\text{pump}}$-IR$_{\text{probe}}$ delay time reveals spectral diffusion [320, 247, 303]. Hence, spectral diffusion within the ensemble appears to be faster than relaxation of the non-equilibrium ensemble to the equilibrium state and the system is outside the linear response regime. Thirdly, the transient hole narrows with time. Since the hole width represents the homogeneous width of the absorption band, this result seems to suggest that the homogeneous width decreases as the system approaches equilibrium. None of these observations could be explained in a linear response regime where fast (homogeneous) and slow (spectral diffusion) dephasing processes decouple.

Theory: Strictly speaking, the T2D experiment is a 5th-order experiment with two field interactions form the $\mathrm{UV_{pump}}$-pulse and three from the two IR pulses. However, we can also model the experiment as a 3rd-order process (i.e. 3 field interactions from the IR pulses) on a *non-equilibrium* ensemble, where the $\mathrm{UV_{pump}}$-pulse prepares the non-equilibrium state. In this case, we have to express the 3rd-order response functions of a weakly anharmonic oscillator (anharmonicity δ) in their most general forms [310, 301, 346]:

$$R^{(3)}_{1,2}(t_3,t_2,t_1) = e^{i\omega_0(-t_3\mp t_1)}\left(1-e^{i\delta t_3}\right) \times \left\langle \exp\left(-i\int_{t_2+t_1}^{t_3+t_2+t_1}\omega(\tau)d\tau \mp i\int_0^{t_1}\omega(\tau)d\tau\right)\right\rangle, \tag{5.79}$$

where $\omega(t)$ is the fluctuating transition frequency with the average frequency ω_0 subtracted and $\langle\ldots\rangle$ denotes an ensemble average. T2D spectra are calculated by convolution of the response functions with the laser fields with the appropriate time orderings and subsequent Fourier transformation.

Equilibrium and nonequilibrium frequency trajectories $\omega(t)$ are obtained by integrating a Langevin equation:

$$\ddot{\vec{x}} = -\vec{\nabla}V(\vec{x}) - \gamma\dot{\vec{x}} + \vec{R}(t) \tag{5.80}$$

where $\vec{x}$ is a unitless generalized solvation coordinate, $V(\vec{x})$ a potential of mean force, γ a friction term and $\vec{R}(t)$ an isotropic Gaussian δ-correlated random force with $\langle R(0)R(t)\rangle = \gamma k_B T\delta(t)$.

It is commonly found in solvation experiments that the FFCF decays on (at least) two times scales [168, 345, 301, 261, 247]: (i) an inertial component on a 100 fs time scale, giving rise to homogeneous broadening in the motional narrowing limit (in most cases), and (ii) a slower picosecond component giving rise to spectral diffusion. This complex behavior cannot be reproduced using Equ. 5.80 in one dimension. We therefore interpret $V(x_f,x_s)$ as a two-dimensional potential of mean force with $\vec{x} = (x_f,x_s)$ a fast and a slow generalized solvation coordinate, respectively. The frequency shift is calculated as a linear combination of these two coordinates with $\omega(t) = \Delta_f\sqrt{k_f/k_BT}x_f(t) + \Delta_s\sqrt{k_s/k_BT}x_s(t)$.

The ω-distribution will be Gaussian for a harmonic potential of mean force, $V_{harm}(x_f,x_s) = k_f x_f 2/2 + k_s x_s 2/2$. The Gaussian assumption, which eventually leads to the linear response regime, is implicitly made in almost any modelling of nonlinear spectroscopic experiments when truncating the cumulant expansion of Equ. 5.79 after second order. In the Gaussian case, higher order FFCF's either vanish (odd FFCF's) or factorize into two-point FFCF's and hence, do not contain any additional information. This changes dramatically when considering non-Gaussian ω-distributions. The equilibrium 1D spectrum in Fig. 5.27a, top, is strongly asymmetric. In contrast to the electronic case, the lineshape function $g(t)$ is a real function to a very good approximation in vibrational spectroscopy [346], which is why a non-symmetric lineshape is an unequivocal indication of non-Gaussian dynamics. Vibrational probes often interact very locally with only a few solute molecules, while the electrostatic interaction of an electronic probe with its surrounding is long-ranged. Therefore, in the case of vibrational transitions, the central limit theorem does not necessarily apply and ω-distributions may deviate very strongly from Gaussian statistics.

We may generate a non-Gaussian ω-distribution by either explicitly introducing an asymmetric potential (model **1**)

$$V_1(x_f,x_s) = k_f/2\cdot x_f^2 + k_s/2\cdot x_s^2 + A_{sss}/6\cdot x_s^3, \tag{5.81}$$

or by non-linearly coupling both coordinates (model **2**):

$$V_2(x_f,x_s) = k_f/2\cdot x_f^2 + k_s/2\cdot x_s^2 + A_{ffs}/2\cdot x_f^2 x_s. \tag{5.82}$$

In model **1**, the two coordinates decouple since $V_1(x_f,x_s)$ $=V_{1,f}(x_f)+V_{1,s}(x_s)$, and hence are uncorrelated. In model **2**, in contrast, the two coordinates are inherently correlated. Interestingly, model **2** yields a nonsymmetric x_s-distribution although a cut through $V_2(x_f=0,x_s)$ is symmetric. This is because the two-dimensional potential widens for negative x_s.

Provided that a non-equilibrium disturbance is not too large, its relaxation is governed by the same laws as the regression of spontaneous fluctuations in an equilibrium ensemble (Onsager's regression hypothesis [211]). Since the 1 ps T1D spectrum (Fig. 5.27b, top) significantly overlaps spectrally with the equilibrium 1D spectrum (Fig. 5.27a, top), the non-equilibrium disturbance lies within k_BT, and we may use the same potential of mean force to describe both an equilibrium and a non-equilibrium experiment. The linear response assumption, however, is not valid since already thermal fluctuations sample regions of the potential of mean force that deviates notably from harmonic, as seen in the asymmetry of the equilibrium 1D spectrum.

Model spectra were calculated according to models **1** and **2** by averaging Eq. 5.79 over 200.000 trajectories (Fig. 5.27d-i). We chose a critically damped fast process with a correlation time τ_c =200 fs (i.e. $\gamma =$ 20 ps^{-1}, $k_f/k_BT = 100$), which is a typical value for the solvent DMSO [168]. The remaining parameters were fit to simultaneously reproduce the equilibrium 1D spectrum (Fig. 5.27a, top), the equilibrium 2D spectrum (Fig. 5.27a, bottom) and the T1D spectra (Fig. 5.27b, top). We obtained for model **1**: k_s/k_BT=7.3, A_{sss}/k_BT=20, Δ_f=2.3 ps^{-1}, Δ_s=1.3 ps^{-1} and for model **2**: k_s/k_BT=3.6, A_{ffs}/k_BT=60, Δ_f=2.4 ps^{-1}, Δ_s=1.0 ps^{-1}. Note that we did not include the T2D data in the fit to determine these parameters. The resulting potentials of mean force are plotted in Fig. 5.28a,b as insert. Non-equilibrium trajectories were obtained by choosing starting values for the slow solvation coordinate from a Gaussian distribution which was shifted with respect to the equilibrium value.

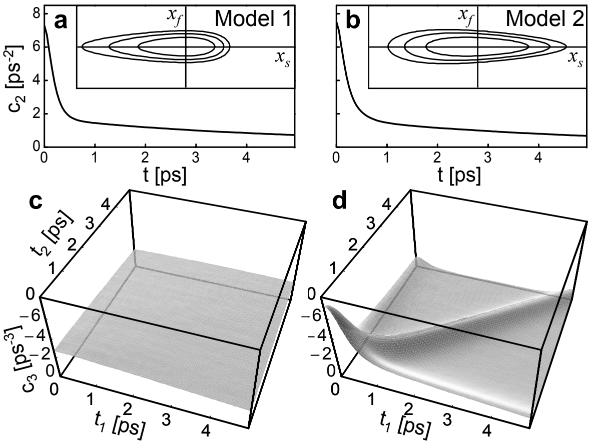

Figure 5.28: Two-point (a,b) and three-point (c,d) FFCF's of model **1** and **2**. The inserts in (a,b) show contour plots of the corresponding potentials of mean force in units of k_BT.

Both models render excellent fits of the equilibrium 1D spectrum (Fig. 5.27a, top), the equilibrium 2D spectrum (Fig. 5.27a, bottom) and the T1D spectra (Fig. 5.27b, top). One could not distinguish between both models with the help of this forms of first and 3$^{\text{rd}}$-order spectroscopies. For the T2D spectra, however, the two models yield distinctively different results, proving that the information content of T2D spectroscopy is higher than that of the equilibrium 1D, 2D and T1D spectra alone. Model **2** (Fig. 5.27h) works significantly better in reproducing the large initial shift of the spectral hole, highlighted by the horizontal cuts through the T2D spectra (Fig. 5.27i). Model **1** completely fails to explain this feature (Fig. 5.27f). Also the narrowing of the hole with time, as well as the faster turning of the 2D band into a vertical lineshape is reproduced by model **2**. Model **2** actually exaggerates the latter feature significantly. We thus consider both models as limiting cases and a realistic potential of mean force might contain both anharmonic terms.

Fig. 5.28 compares the equilibrium two-point and three-point FFCF's of model **1** and **2**. The three-point FFCF's are remarkably different although the corresponding two-point FFCF's are virtually identical. In particular, the fast component is not visible in the three-point FFCF's of model **1**, while it appears as a sharp ridge along the diagonal (i.e. $t_1 = t_2$) in model **2**. In case of model **1**, the fast and slow processes are uncorrelated, which is why the three-point FFCF separates into a sum:

$$c_3(t_1,t_2) = \langle \omega_f(0)\omega_f(t_1)\omega_f(t_2)\rangle + \langle \omega_s(0)\omega_s(t_1)\omega_s(t_2)\rangle \tag{5.83}$$

Since the fast process was assumed to be Gaussian, its three-point FFCF vanishes. In contrast, fast and slow process are *correlated*, or '*entangled*', in model **2**, which is why the fast process is 'present' even for large times t_1 and t_2. The force constant of the fast coordinate linearly depends on the excursion of the slow solvation coordinate. Since the fast component is in the motional narrowing limit, the effective T_2 varies as equilibration along the slow coordinate progresses, yielding a line narrowing as a function of IR$_{\text{pump}}$-IR$_{\text{probe}}$ delay time.

In contrast, the effective T_2 dephasing time is frequency independent in model **1** since both coordinates decouple. The sharp ridge along the diagonal of the three-point FFCF of model **2** causes the fast initial shift of the hole from the pump pulse position, even after a relatively long UV$_{\text{pump}}$-IR$_{\text{pump}}$ delay time of 1 ps (Fig. 5.27i). No such shift is obtained in model **1** since the fast process has long decayed away at $t_{UV\text{pump}-IR_{\text{pump}}}$=1 ps (Fig. 5.27f).

Discussion: The different orders of nonlinear spectroscopy are typically classified in terms of multipoint dipole-dipole correlation functions (DDCF): the two-point DDCF $\langle \mu(0)\mu(t)\rangle$ for linear spectroscopy, the four-point DDCF $\langle \mu(0)\mu(t_1)\mu(t_2)\mu(t_3)\rangle$ for 3$^{\text{rd}}$-order spectroscopy, etc. However, in particular in the context of solvation experiments, the dipole operator is not a very intuitive quantity. We rather like to think about the experiment in terms of a vibrational transition of a test molecule, the frequency $\omega(t)$ of which directly mirrors the fluctuating surrounding. The high-dimensional spatial motion of the surrounding is thought to be projected onto a one-dimensional spectroscopic coordinate, $\omega(t)$. The dipole operator $\mu(t)$ and the instantaneous frequency $\omega(t)$ are connected through an exponential function [310], the expansion of which leads to infinite terms in the general, non-Gaussian case. Hence, mathematically speaking, any order of spectroscopy, linear or nonlinear, depends on *all* orders of FFCF's, and a rigorous classification of nonlinear spectroscopy in terms of FFCF's is not possible.

Nevertheless, in terms of sensitivity, we may still use such a classification in a loose sense. For example, linear spectroscopy is a measure of the center frequency $\langle\omega\rangle$ and width $\langle\omega 2\rangle$ of a transition. Yet, it is an extremely *in*sensitive probe of the two-point FFCF, despite the fact that the linear spectrum $I(\omega) = \Re \int_0^\infty e^{i\omega t} e^{-g(t)} dt$ is expressed explicitly in terms of the two-point FFCF through the lineshape function $g(t) = \int_0^t d\tau_1 \int_0^{\tau_1} d\tau_2 \langle\omega(0)\omega(\tau_2)\rangle$. Yet, the inversion of these equations is ill-conditioned and not feasible [301]. Likewise, we have demonstrated here that 3^{rd}-order spectroscopy is not sensitive to higher order correlation functions. The three-point FFCF's of models **1** and **2** differ distinctively, and yet, the linear (Fig. 5.27dg, top) and 3^{rd}-order (Fig. 5.27dg, bottom and Fig. 5.27eh, top) spectra are virtually identical. On the other hand, the 5^{th}-order T2D spectra (Fig. 5.27fi) are different, although the two-point FFCF's are essentially the same in both cases.

The commonly observed biphasic decay of the two-point FFCF implies that at least two generalized coordinates are needed to describe solvation. However, with the help of 3^{rd}-order spectroscopy, nothing can be learned about possible couplings between these solvation modes. Only 5^{th}-order spectroscopy can distinguish model **1**, where both modes are uncoupled, from model **2** with an anharmonic coupling term. A frequency trajectory from a molecular dynamics simulation would contain the information about all orders of FFCF's. However, only the two-point FFCF is usually extracted for comparison with experiment, throwing away significant part of the information. The two-point FFCF does *not* characterize a random process unequivocally, unless it is Gaussian. T2D spectroscopy suggested here allows one to determine higher order FFCF's to more completely characterize the random process of solvation. Hence, the work not only presents a experiment that demonstrably is nonlinear with respect to solvation modes, but also proposes a language of how to characterize nonlinear dynamics with the help of higher order frequency fluctuation correlation functions.

Acknowledgement: We thank Gerhard Stock for illuminating discussions and the Swiss National Science Foundation for financial support (contract 2100-067573/1).

5.5 P5 – Labeling Vibrations by Light — Ultrafast Transient 2D-IR Spectroscopy Tracks Vibrational Modes During Photoinduced Charge Transfer

Jens Bredenbeck, Jan Helbing and Peter Hamm,
J. Am. Chem. Soc., 126:990–991, 2004.

Ultrafast 2D infrared spectroscopy (2D-IR) is a promising tool to investigate molecular structure [3, 252, 254] and its equilibrium fluctuations [74, 252] with subpicosecond time resolution. These experiments can be regarded as IR analogues of COSY and NOESY in NMR [252, 350]. Recently, the method has been extended to the non-equilibrium regime to investigate the conformational transition of a photoswitchable cyclic peptide [173] by transient 2D-IR spectroscopy (T2D-IR) [174]. In this communication we report on a novel T2D-IR laser pulse sequence that allows to 'label' certain vibrational modes in the reactant of a photoreaction by an IR pulse and tracks their evolution on the way to the product. In this way the experiment correlates vibrational bands of reactant and product. The experiment can be regarded as an IR analogue of 2D-NMR exchange spectroscopy under non-equilibrium conditions [244, 290], in that it generates off-diagonal peaks between related vibrations of reactant and product in the T2D-IR spectrum.

We have chosen the photoinduced metal-to-ligand charge-transfer (MLCT) in [Re(CO)$_3$Cl(dmbpy)] (dmbpy = 4,4'-dimethyl-2,2'bipyridine) in DMSO as an interesting application to demonstrate this technique. MLCT in rhenium(I) polypyridyl carbonyls and similar metal carbonyls has been studied in great detail. Various aspects have been investigated, such as solvation dynamics [299], electronic structure [329, 330], photocatalysed CO$_2$ reduction [351], photo-chemistry [331, 332], or use as luminescent markers [334]. Among other techniques, time resolved vibrational [335, 299, 331], Raman [335] and UV-VIS spectroscopy [330], as well as quantum chemical calculations [329, 330] were used. Nevertheless, there is no generally accepted assignment for the CO vibrations in the excited (MLCT) state of [Re(CO)$_3$Cl(dmbpy)] and similar complexes. In this communication we show how an unambiguous assignment can be achieved by T2D-IR spectroscopy.

Figure 5.29a shows the absorption spectrum of the ground state. The bands at 1889, 1910 and 2018 cm^{-1} have been assigned to a'(2) (antisymetric stretching of axial CO and equatorial COs), a" (antisymetric stretching of equatorial COs) and a'(1) (symmetric stretching of all COs) modes, respectively [299]. Upon excitation of [Re(CO)$_3$Cl(dmbpy)] at 390 nm, MLCT induces a large frequency shift of the CO vibrations (Figure 5.29b). An assignment is widely used [299, 335], that maintains the ordering of the bands in the excited state as indicated by the red arrows in Figure 5.29b. To the best of our knowledge this assignment is not based on any direct experimental evidence as also pointed out by Asbury *et al.* [299].

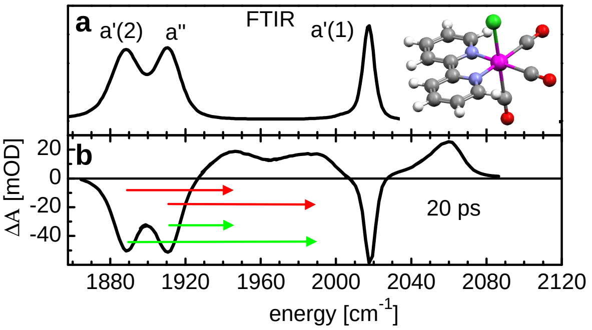

Figure 5.29: Figure 1. a: Ground state absorption spectrum. b: Time resolved IR spectrum recorded 20 ps after excitation. Negative signal originates from the depleted ground state of [Re(CO)$_3$Cl(dmbpy)] (inset, methyl groups of dmbpy omitted) whereas positive signal corresponds to the excited state. Red arrows: band shift according to previous assignment, green arrows: band shift as revealed by T2D-IR.

The instantaneous change of the electronic structure and the subsequent slower vibrational Stokes shift have been identified as the effects responsible for the change in vibrational frequency [299, 329]. DFT calculations for the similar complex [Re(CO)$_3$(4-Etpy)]+ (4-Etpy = 4-ethylpyridine) predict the shift for a'(2) to be twice as large as for a" [329]. Furthermore the contribution of the vibrational Stokes effect is expected to be small for the a" vibration, as its transition dipole moment is perpendicular to the symmetry plane and therefore perpendicular to the permanent dipole moment change upon MLCT [299]. Nevertheless the common assignment [299, 335] attributes the strongest shift to the a" mode (long red arrow in Figure 5.29b). However, in this paper we will show with the help of T2D-IR spectroscopy that the a'(2) and a" modes indeed change their ordering upon excitation, as indicated by the green arrows in Figure 5.29b.

The original T2D-IR experiment was designed to investigate transient structural dynamics of small peptides [174]. It is an UV-pump IR-narrowband-pump IR-broadband-probe scheme (pulse sequence in Figure 5.30c). Common transient IR absorption spectroscopy employs just one IR-probe pulse after UV pumping. In contrast, the T2D-IR spectrum is obtained using a combination of two IR pulses as a probe process, where the narrow-

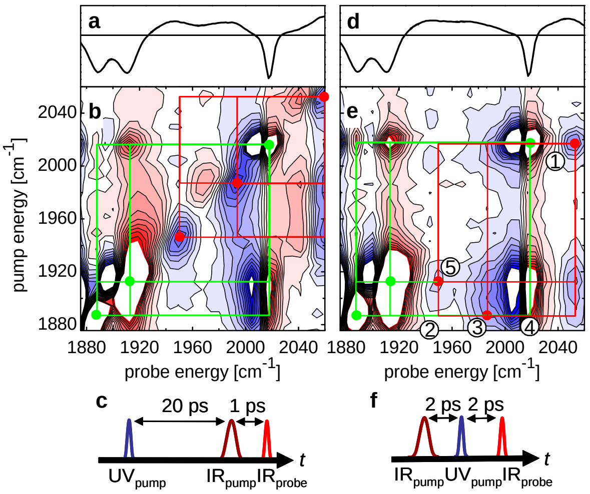

Figure 5.30: Figure 2. a: Time resolved IR spectrum after 20 ps. b: T2D-IR spectrum. c: Pulse sequence for normal T2D-IR. First, the UV-pump pulse arrives, then a 2D-IR measurement is carried out. d: Time resolved IR spectrum after 2 ps. e: Labeling T2D-IR spectrum. f: Pulse sequence for labeling T2D-IR. The narrowband IR-pump pulse arrives first now and labels the electronic ground state. The UV-pump pulse transfers the molecule into the excited state. The IR-probe pulse arrives last.

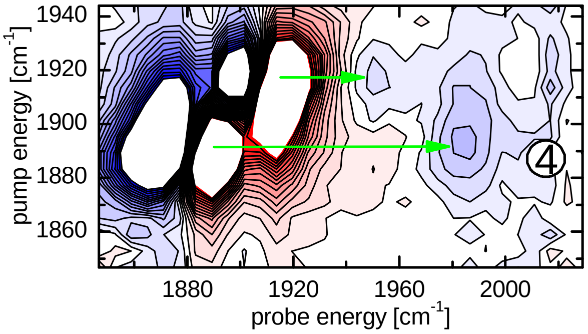

Figure 5.31: Figure 3. Labeling experiment for the a'(2) and a" bands employing special polarization conditions. The green arrows indicate the shift upon excitation.

band pulse is scanned over the spectral range of interest [252]. Figure 5.30b shows such a T2D-IR spectrum of [Re(CO)$_3$Cl(dmbpy)] at a UV delay of 20 ps[3]. Like in a 2D-NMR spectrum, the T2D-IR spectrum features diagonal peaks and cross peaks that report couplings - in this case not between spins but between vibrations. Each 2D-IR peak consists of a negative and positive contribution [252] represented by blue and red colors. The T2D-IR spectrum features signals originating from the ground state which is the 'reactant' of the photoreaction, as well as the signals of the excited MLCT state, which is the 'product'. The ground state diagonal peaks are marked by green dots and are connected to their respective cross peaks by green lines. The excited state signals are shifted along the diagonal relative to the ground state and are marked in red. In the new labeling T2D-IR experiment introduced here, the narrowband IR pulse precedes the UV pulse (pulse sequence in Figure 5.30f). It 'labels' the vibrations by transferring population from the $\nu = 0$ to the $\nu = 1$ state, while the molecule is still in the electronic ground state. The UV-pulse then transfers the molecule into the excited electronic state and induces a frequency shift. In the labeling T2D-IR spectrum (Figure 5.30e), the shift from ground to excited state now occurs no longer along the diagonal but parallel to the x-axis, since the IR excitation takes place in the electronic ground state. This means: the y-position of the peak does not change upon excitation, staying at the ground state value. On the x-axis, the frequency in the transient excited state can be read off. Therefore excited state (product) and ground state (reactant) vibrations are correlated by the pulse sequence. This can be nicely seen in the case of the a'(1) vibration (Pos. 1) in the upper right corner of the T2D-IR spectrum. The peak shifts from its ground state position at 2017 cm^{-1} (green dot) to 2048 cm^{-1} (red dot) within 2 ps after the UV pulse. To our surprise, however, in the case of the a'(2) band at 1888 cm^{-1} we did not find any corresponding excited state signal at 1944 cm^{-1} (Pos. 2) where we had expected it based on the old assignment [299, 335]. Instead the a" peak is shifted to 1944 cm^{-1} (Pos. 5).

The a'(2) band is shifted to 1985 cm^{-1} (Pos. 3) where it is hidden by the strong reactant cross peaks (Pos. 4) between both the a'(2) and a" modes and the a'(1) mode. To bring out the effect more clearly, it is desirable to suppress the reactant cross peaks (Pos. 4), while maintaining the product peaks (Pos. 3 and 5), that have been shifted off the diagonal now. This can be achieved utilizing the different polarization dependences of the various peaks [352]. The experiment offers two polarization degrees of freedom: The angle between UV-pump and IR-pump α and the UV-pump

---

[3] Pulse parameters: UVpump: 390 nm, 5 J, 400 fs; IRpump: 0.1 J, 1 ps, bandwidth 12 cm^{-1}, tunable between 1880 cm^{-1} and 2050 cm^{-1}; IRprobe, 150 fs, 1960 cm^{-1}, bandwidth 200 cm^{-1}; for details of the setup see Reference [174]

IR-probe angle β. Figure 5.31 shows the T2D-IR spectrum of the a'(2) and a" bands measuring $\mathrm{Signal}(\alpha = 45^\circ, \beta = 45^\circ) - \mathrm{Signal}(\alpha = 45^\circ, \beta = -45^\circ)$. This polarization condition suppresses the strong cross peak (Pos. 4) [352]. The excited state bands are now well resolved[4]. Their shift along the x-axis is indicated by green arrows. Figure 5.31 provides direct evidence for the new assignment of the excited state bands, as it was proposed in Figure 1b and predicted by DFT calculations [329].

Apparently, vibrational labeling is robust and survives the photoreaction - despite the abruptly changed electronic structure (i.e. the bond order of the C=O groups) in the electronically excited state. Furthermore, the modes largely maintain their character, i.e. their delocalization among the various C=O groups. Upon photo excitation, the labeled vibrational mode is projected onto the newly generated product normal modes, forming a wavepacket. If remixing of the modes were substantial, the experiment would be difficult to interpret in terms of single vibrations. However, the spectator modes in this proof of principle experiment allow for a straightforward assignment of the excited state spectrum. Future applications of labeling T2D-IR are not limited to CO modes and excited electronic states. The sensitivity of our current setup also allows the investigation of much weaker transitions. A variety of phototriggered reactions including isomerization, rearrangement and dissociation can be addressed.

Acknowledgement This Work has been supported by the Swiss Science Foundation (2100-067573/1).

---

[4] The positive part of the a" band is not visible as it overlaps with the ground state diagonal peak

5.6 P4 – Transient 2D-IR Spectroscopy – Snapshots of the Non-Equilibrium Ensemble During the Picosecond Conformational Transition of a Small Peptide

Jens Bredenbeck, Jan Helbing, Raymond Behrendt, Christian Renner, Luis Moroder, and Peter Hamm,
J. Phys. Chem. B, 107:8654–8660, 2003

5.6.1 Abstract

The technique of transient two dimensional infrared (T2D-IR) spectroscopy is introduced, which extends the advantage of 2D-IR spectroscopy to the investigation of a transient species with picosecond time resolution. The conformational change of a small cyclic peptide in the amide-I spectral range is studied, which is induced by means of a photo-switch integrated into the peptide backbone. Substantial changes are found in the transient 2D-IR spectra at times when the transient 1D spectra only show minor time dependence, illustrating the information gain accessible from 2D-IR spectroscopy. In contrast to 1D spectroscopy, 2D-IR can distinguish between homogeneous and inhomogeneous broadening. The homogeneous contribution to the total width of the amide-I band changes on the course of the conformational transition, a result, which is interpreted in terms of the manner the peptide samples its conformational space.

5.6.2 Introduction

Recent work has shown that nonlinear 2D infrared (2D-IR) spectroscopy might be a valuable experimental complement to 2D-NMR for studying molecular systems [295, 318, 2, 249, 252, 319, 313, 305, 320, 251, 250, 283, 3, 4]. 2D-IR spectroscopy yields much more detailed information on the vibrational Hamiltonian of a molecular system than one-dimensional IR spectroscopy. In the case of small peptides, 2D-IR spectroscopy allows one to measure the coupling between certain vibrational modes of different peptide units within the polypeptide chain. The vibrational modes under study are the so-called amide-I modes (mostly a C=O stretching vibration of the peptide unit) located between 1600 - 1700 cm^{-1}. Since the coupling strength is related to the relative orientation of the peptide units [139, 150, 166], one can obtain structural information from a 2D-IR spectrum. This has been demonstrated recently in the case of Ala-Ala-Ala (trialanine) [3, 4], the smallest conceivable system with only two peptide units. Sub-picosecond equilibrium fluctuations of the peptide backbone around its preferred conformation have been addressed as well by investigating the population transfer between both peptide units [74]. Furthermore, the width of the structural distribution of trialanine has been analyzed by exploring the inhomogeneity of the 2D-IR spectra [247].

The most promising potential of 2D-IR spectroscopy is its intrinsic high time resolution of about 1 ps - many orders of magnitudes faster than what 2D-NMR spectroscopy can achieve - which allows for freezing in all but the fastest sub-picosecond motions of the peptide backbone. Up to now, 2D-IR spectroscopy has only been applied to equilibrium states, in which case the high time resolution helps to distinguish between dynamically coupled sub-conformations [247]. This work reports on our first efforts in *transient* 2D-IR (T2D-IR) spectroscopy of a non-equilibrium ensemble, in which case the high time resolution can be taken full advantage of.

The molecule chosen for this study is a bicyclic octapeptide (bcAMPB) containing a photo-responsive azobenzene moiety [125]. The azobenzene unit can be reversibly switched between the *cis* and *trans* conformation using light of different wavelengths, thereby predetermining the conformation of the peptide backbone. According to NMR investigations [125], the *cis* state is a frustrated system with many close-lying conformational energy minima, while the backbone structure of the *trans* conformation is much more stretched as a result of the larger end-to-end distance of the azobenzene unit. The *cis* → *trans* isomerization of the azobenzene unit itself is completed within less than a picosecond with a quantum efficiency of $\approx$50% [164]. The time scales of the response of the peptide backbone on the changed restraint has been investigated in detail in recent work [173], where we employed conventional UV-pump-IR-probe spectroscopy (transient 1D-IR spectroscopy, T1D-IR) of the amide-I band. Two major phases have been observed during the conformational transition: During a fast driven phase, the peptide backbone is forced into a stretched conformation by the isomerizing azobenzene unit. The stretching is essentially finished after a surprisingly short time of 20 ps and can be imagined as a downhill process on a steep part of the potential energy surface of the peptide. The stretched system is still in non-equilibrium and subsequently relaxes on a discrete hierarchy of time scales that continues for longer than 16 ns. In the present work, we present transient 2D-IR (T2D-IR) snapshots of the peptide ensemble taken during the transition from the *cis* to the *trans* configuration.

5.6.3 Principle of Transient 2D-IR Spectroscopy

The 2D-IR part of the experiment is performed according to our previously described double-resonance scheme [2, 252]: The center frequency ω_{pu} of a spectrally tunable, narrow-band IR pump pulse is tuned across the amide-I band to construct 2D-IR spectra as a function of the IR pump and IR probe frequency, ω_{pu} and ω_{pr}. By addition of a UV pulse preceding the 2D-IR part of the experiment, the 2D-IR spectrum of the photo-switched ensemble is recorded. Hence, the total experiment consists of 3 pulses: a UV-pump, a narrow-band IR-pump and a broad-band IR-probe pulse. Since we cannot convert 100% of the initial species into the product species, the 2D-IR spectrum in the presence of the UV-switch pulse always contains contributions from both. In order to eliminate contributions of molecules that have not absorbed a UV photon, two sets of 2D-IR spectra are recorded simultaneously - one with the UV-switch pulse on and one with the UV-switch pulse off - and subtracted from each other. Hence, just like it is common practice in conventional pump-probe spectroscopy, our T2D-IR spectra are in fact T2D-IR *difference* spectra.

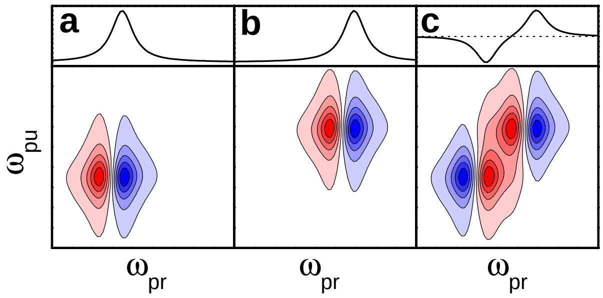

Figure 5.32: Schematic illustration of transient 1D (top) and 2D-IR (bottom) spectroscopy. The absorption frequency shifts from the steady state **a** to **b**, each yielding a characteristic 2D-IR spectrum. In c, difference 1D and 2D-IR spectra are shown. Negative response is depicted in blue, positive response in red.

To facilitate the discussion, we introduce a schematic T2D-IR spectrum of an idealized molecule with one single homogeneously broadened oscillator, the frequency of which shifts upon triggering the photo-reaction. In both the initial and product states, the vibrator would give rise to a 2D-IR spectrum (Fig. 5.32a and b) given by

$$\Delta A_{2D}(\omega_{pu},\omega_{pr}) = n_{ex}(\omega_{pu},\omega_0)\times \left[A_{hom}(\omega_{pr}-\omega_0+\delta)-A_{hom}(\omega_{pr}-\omega_0)\right] \quad (5.84)$$

where the probability $n_{ex}(\omega_{pu},\omega_0)$ of exciting the oscillator with the IR pump pulse is a convolution of the pump-pulse spectrum I_{pu} with center frequency ω_{pu} and the absorption band A with center frequency ω_0 [2]:

$$n_{ex}(\omega_{pu},\omega_0) = \int_{-\infty}^{\infty} I_{pu}(\omega-\omega_{pu})A_{hom}(\omega-\omega_0)d\omega \quad (5.85)$$

Two peaks would be observed in each 2D-IR spectrum, a negative (blue) bleach and stimulated emission signal at the vibrator's original frequency ω_0 and a positive (red) excited state absorption signal, which is slightly red-shifted owing to the intrinsic anharmonicity δ of the oscillator. The T2D-IR spectrum (Fig. 5.32c) is the difference of the 2D-IR spectra of the initial (Fig. 5.32a) and the transient species (Fig. 5.32b). In a transient 1D difference spectrum, negative contributions arise from the depleted initial population, while positive contributions stem from the transient photo-product (Fig. 5.32c, top). Accordingly, the signs of the various 2D-IR peaks (color-coded in Fig. 5.32) of the initial and the product state are interchanged also in the T2D-IR difference spectrum (Fig. 5.32c, bottom). Fig. 5.32c will be used as a guide line to discuss the experimental result. We shall see, however, that the simple-minded picture of Fig. 5.32 is not sufficient to account for the dynamic features observed in T2D-IR spectroscopy.

5.6.4 Material and Methods

The peptide sample (Ala-Cys-Ala-Thr-Cys-Asp-Gly-Phe cyclized by (4-aminomethyl)-phenylazobenzoic acid and oxidized to contain a Cys-Cys disulfide bond [125]) was dissolved in anhydrous dimethylsulfoxide (DMSO) at a concentration of ≈ 12 mM (absorbance of the amide-I band ≈ 0.3 OD) and circulated through a closed cycle flow cell designed for small amounts of liquid [182]. Before the experiment was started, the *cis*-*trans* equilibrium was shifted to about 80% *cis* by continuous UV irradiation of the *trans* $\pi \rightarrow \pi^*$ transition with an Ar-Ion laser (363 nm, 200 mW). The transition from *cis* to *trans* was then initiated by a short 420 nm laser pulse (energy 10 μJ/pulse) obtained from a frequency doubled 1 kHz Ti:Sapphire-laser/amplifier system (Spectra-Physics, Spitfire). In order to allow for a high excitation density (≈ 20%) without inducing nonlinear effects in the sample cell windows (such as white light generation or color center formation), the UV pulses were stretched to 700 fs by guiding them through 25 cm of fused silica.

Intense IR pulses (center frequency 1650 cm^{-1}, bandwidth 240 cm^{-1} FWHM, duration 100 fs, energy 1.7 μJ) were generated using a white light seeded two-stage BBO-optical parametric amplifier, the signal and idler pulses of which were difference frequency mixed in a $AgGaS_2$ crystal [165]. A small fraction of the IR-beam was split off to obtain broadband probe and reference pulses. The remainder, which was used as the IR-pump pulse, was passed through a computer-controlled Fabry-Perot interferometer to generate narrow-band tunable IR pump pulses (bandwidth ≈ 12 cm^{-1}). The IR pump and probe pulses were focused into the sample in spatial overlap with the 420 nm switch pulse (the reference pulse was focused ≈ 1 mm apart). Probe and reference beams were dispersed in a spectrograph and imaged onto a 2 × 32 pixel HgCdTe detector array which enabled us to measure low noise (typically 0.003 mOD rms) transient spectra with spectral resolution of 4 cm^{-1}.

With the help of two light choppers, one in the IR-pump beam running at half the repetition rate of the laser system and the other in the UV-pump beam running at a quarter of the repetition rate, four individual data sets were recorded: $I_{\mathrm{UV_{on}IR_{on}}}$, $I_{\mathrm{UV_{off}IR_{on}}}$, $I_{\mathrm{UV_{on}IR_{off}}}$

and $I_{\mathrm{UV_{off}IR_{off}}}$. The stationary 2D-IR spectrum of the initial state is calculated as (Fig. 5.33b):

$$\Delta A_{\mathrm{2D,stat}} = -\log \frac{I_{\mathrm{UV_{off}IR_{on}}}}{I_{\mathrm{UV_{off}IR_{off}}}}, \tag{5.86}$$

the T1D-spectra as (Fig. 5.34, top in each panel):

$$\Delta A_{\mathrm{T1D}} = -\log \frac{I_{\mathrm{UV_{on}IR_{off}}}}{I_{\mathrm{UV_{off}IR_{off}}}}, \tag{5.87}$$

and the T2D-IR difference spectra as (Fig. 5.34, middle in each panel):

$$\Delta A_{\mathrm{T2D}} = -\log \frac{I_{\mathrm{UV_{on}IR_{on}}} \cdot I_{\mathrm{UV_{off}IR_{off}}}}{I_{\mathrm{UV_{on}IR_{off}}} \cdot I_{\mathrm{UV_{off}IR_{on}}}}. \tag{5.88}$$

The IR-pump-IR-probe delay time t_{IR} was set fixed to 800 fs (to avoid non-time ordered pump-probe interactions) in the present study, while the UV-pump-2D-IR-probe delay time t_{uv} was varied between 3 ps and 1.7 ns. All 3 pulses were polarized parallel.

5.6.5 Results

Stationary Spectroscopy: The stationary FTIR absorption spectra of the amide-I band of the *cis* (solid line) and the *trans* (dotted line) species are shown in Fig. 5.33a. They consist of 9 amide-I oscillators which are not resolved due to strong broadening mechanisms in the solvent environment. The small wing at $\omega_{\mathrm{pr}} = 1720\,\mathrm{cm}^{-1}$ originates from the carboxyl group in the aspartic acid.

The stationary 2D-IR spectrum of the *cis*-configuration is displayed in Fig. 5.33b. It can be imagined as a stack of 1D pump-probe spectra recorded for different IR-pump frequencies ω_{pu}. Each pump-probe signal consists of a negative bleach and stimulated emission (blue) and a positive excited state absorption (red) contribution, which is slightly red-shifted owing to the intrinsic anharmonicity of the C=O vibrators [2]. When scanning the frequency of the narrow-band pump pulse across the amide-I absorption band, the frequency position of the pump-probe response follows directly. In other words, the narrow-band pump pulse burns holes into the absorption band. The 2D-IR signal is elongated along the diagonal of the 2D-IR spectrum, reflecting the strong inhomogeneity of the amide-I band. This inhomogeneity has to be attributed to two effects: (a) The presence of 9 individual amide-I states, which are centered at different frequencies, and (b) the spectral inhomogeneity of the individual amide-I vibrators as a result of structural heterogeneity [247]. Cross peaks between the various amide-I states are relatively weak in this type of experiment as a result of the parallel polarization of IR-pump and IR-probe pulse [283, 251].

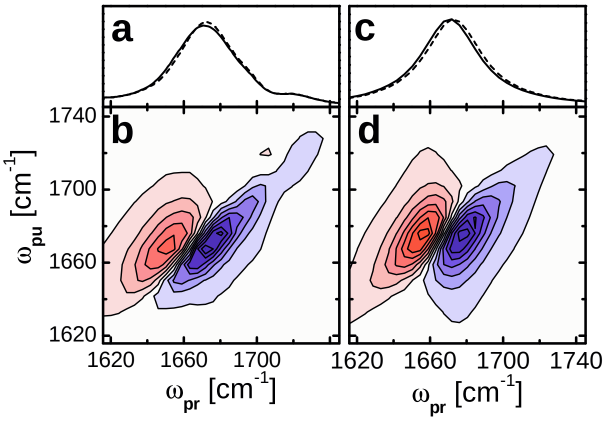

Figure 5.33: (a) Stationary FTIR spectra of the *cis* (solid line) and the *trans* (dotted line) state of the cyclic peptide. (b) Stationary 2D-IR spectrum of the *cis* state for parallel polarization of pump and probe beam. (c) and (d) represent the corresponding spectra from the model calculation. Negative response is depicted in blue, positive response in red.

Transient 2D-IR Spectroscopy: Based on the results of our recent T1D-IR experiments [173], we have chosen four characteristic delays t_{uv} between the UV-switch pulse and the 2D-IR probe: 3 ps, 20 ps, 200 ps and 1.7 ns. The red-shift of the amide-I band at 3 ps has been attributed to (thermal or non-thermal) excitation of low frequency modes which anharmonically couple to the amide-I modes [173]. Hence, the peptide backbone is still hot after 3 ps and contains a significant fraction of the large excess energy absorbed by the photo-switch. The T2D-IR spectrum recorded at 3 ps (Fig. 5.34) is very similar to the stationary 2D-IR spectrum of the initial *cis* state, except for the sign (Fig. 5.33b). This is in strong contrast to the schematic example described in Fig. 5.32c. Despite the strong red-shifted absorption band in the T1D-IR spectrum, we do not observe any distinct contribution from the transient photo-product in the T2D-IR spectrum (expected at arrow 1 in Fig. 5.34). If the transient photo-product were to contribute to the T2D-IR spectrum to the same extend as it does in the T1D-IR spectrum, one would expect the T2D-IR spectrum look similar to Fig. 5.32c (except for the overall sign, since the shift is in the opposite direction).

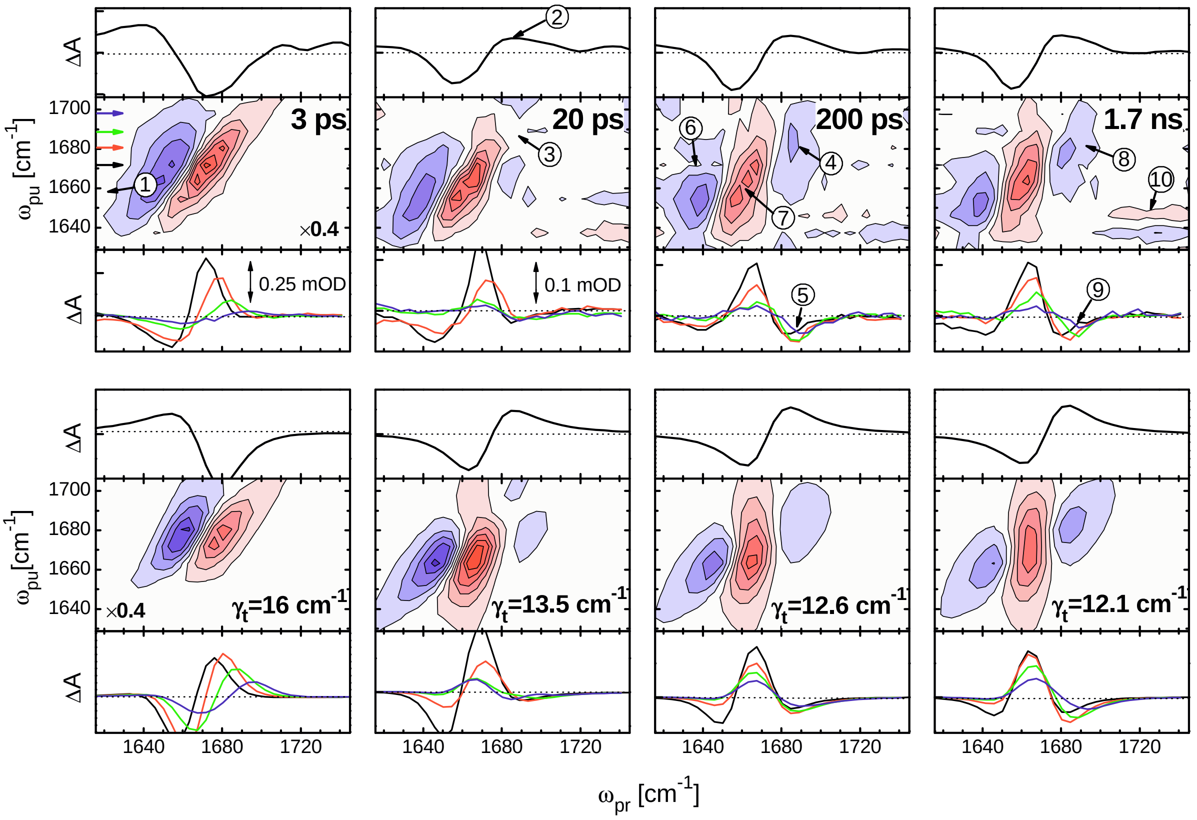

Figure 5.34: T1D and T2D spectra at UV-pump-2D-IR-probe delay times of experimental results, the lower row the result of the model calculation. Each panel consists of a T1D spectrum (top), a T2D spectrum (middle), and cuts through the T2D spectra (bottom) at pump frequencies 1672 cm^{-1} (black), 1689 cm^{-1} (red), 1680 cm^{-1} (green) and 1689 cm^{-1} (blue, see colored arrows in the 3 ps T2D spectrum). The amplitude of the 3 ps T2D spectrum is larger and has been scaled. All other spectra are on the same linear scale and can be compared directly. In the T2D-spectra, negative signals are depicted in blue, positive signals in red. The labelled arrows refer to features described in the text.

After 20 ps, the stretching of the backbone conformation is almost finished, leaving the system highly in non-equilibrium [173]. The molecules have essentially cooled down. The T1D-IR spectrum at $t_{uv} = 20\,\text{ps}$ shows a blue-shifted contribution from the transient photo-product at $\omega_{pr} = 1685\,\text{cm}^{-1}$ (Fig. 5.34, arrow 2). Again, hardly any signal is observed in the T2D-IR spectrum from the transient photo-product (Fig. 5.34, arrow 3). Furthermore, while the amplitude of the T1D-IR spectrum at 20 ps is 0.63 of the 3 ps signal, the ratio of the respective T2D-IR spectra is only 0.35.

The dynamics at delays larger than 20 ps is due to the peptide backbone adjusting to the stretched conformation [173]. After 200 ps the T1D-IR spectrum has changed very little compared to that at 20 ps. In the T2D-IR spectrum, however, we now observe a negative (blue) band resulting from the transient photo-product at $\omega_{pr} = 1685\,\text{cm}^{-1}$ (Fig. 5.34, arrow 4 and 5). Furthermore, the negative (blue) band at $\omega_{pr} = 1635\,\text{cm}^{-1}$ is less elongated at 200 ps (Fig. 5.34, arrow 6) and the positive (red) band in the center of the T2D-IR spectrum is oriented more vertically at longer delays (Fig. 5.34, arrow 7).

After 1.7 ns, the negative band (blue) around $\omega_{pr} = 1685\,\text{cm}^{-1}$ is twisted towards the diagonal compared to the 200 ps spectrum (Fig. 5.34, arrow 8). This effect is better seen in the cuts through the T2D-IR spectrum: At 1.7 ns the minima of the signals at different pump frequencies are shifted apart (Fig. 5.34, arrow 9). The T2D-IR spectrum after 1.7 ns looks very much like the schematic T2D-IR spectrum shown in Fig. 5.32c.

5.6.6 Modelling of the Data

The most striking result of our T2D-IR experiment is the absence of an observable signal from the transient photo-product at 3 ps and 20 ps delay time, although such a signal is clearly present in the T1D-IR spectra. To gain an understanding for this observation, we have to recall that a 2D-IR measurement can be viewed as a dynamic hole burning experiment. As such, 2D-IR spectroscopy - in contrast to 1D spectroscopy - can distinguish between homogeneous and inhomogeneous broadening. For each pump frequency (i.e. for each horizonal cut through the 2D-IR spectra), we observe a hole with the *homogeneous* line width of the transition resonant with the pump frequency (convoluted with the laser bandwidth) together with a red-shifted excited state absorption (Equ. 5.84). However, since the anharmonic shift δ is roughly of the same size as the homogeneous width, both signals partially cancel, and the amplitude of the measured signal decreases with increasing homogeneous width. The second key for understanding the outcome of the experiment is the small shift of the photo-product absorption relative to that of the initial state. As a result, the 2D-IR spectra of both species also strongly overlap and tend to cancel each other yet another time; the T2D-IR spectra are in fact *double*-difference spectra. Hence, a T2D-IR spectrum of the photo-product with an enlarged homogeneous width, and hence a smaller overall amplitude, will be almost invisible in the double-difference spectrum, in which case the latter looks similar to the stationary 2D-IR spectrum of the initial state with interchanged sign.

To verify this working hypothesis we used a very simple approach. We modelled the amide-I band as one single transition, which is inhomogeneously broadened:

$$A_{\text{inh}}(\omega) = \int_{-\infty}^{\infty} G(\omega_0) A_{\text{hom}}(\omega - \omega_0) d\omega_0 \qquad (5.89)$$

The inhomogeneous distribution function $G(\omega_0)$ took into account both the presence of the (quasi-continuous) nine individual amide-I states as well as structural heterogeneity. We found that a Lorentzian distribution function $G(\omega_0)$ fits the linear absorption spectra better than a Gaussian distribution function. A total width of $\approx 38\,\text{cm}^{-1}$ (FWHM) in both the *cis* and *trans* state and a 2 cm^{-1} blue-shift upon *cis* → *trans* isomerization reproduced well the FTIR spectrum (Fig. 5.33c). In agreement with the T1D-IR data, we used this blue-shift for delays of 20 ps and longer. The shift of the center frequency after 3 ps can be estimated from the amplitude of the T1D-IR spectrum under the assumption that the depletion of the initial population is the same at 3 ps and 20 ps. It is set to $-2\,\text{cm}^{-1}$ (which represents a red-shift). Using these ingredients, model 1D difference spectra could readily be calculated (Fig. 5.34). As the frequency shifts are small compared to the total line width of the amide-I band, the negative signal from the initial state and the positive signal from the transient product state cancel strongly and the difference signal has the form of the first derivative of the absorption spectrum.

2D-IR spectra were calculated by weighing the 2D-IR response of a homogeneous line - calculated as in Fig. 5.32 (Equ. 5.84) - with the inhomogeneous distribution function $G(\omega_0)$:

$$\Delta A_{\text{2D}}(\omega_{\text{pu}}, \omega_{\text{pr}}) = \int_{-\infty}^{\infty} G(\omega_0) n_{ex}(\omega_{\text{pu}}, \omega_0) \times \left[A_{\text{hom}}(\omega_{\text{pr}} - \omega_0 + \delta) - A_{\text{hom}}(\omega_{\text{pr}} - \omega_0)\right] d\omega_0 \qquad (5.90)$$

Cross peaks between the various amide-I states were neglected in this approach. The homogeneous width could be deduced from the stationary 2D-IR spectrum (Fig.5.33d) and is $\gamma_{\text{i}} \approx 12\,\text{cm}^{-1}$, in agreement with earlier results [247]. A typical value of $16\,\text{cm}^{-1}$ was used for the anharmonicity δ [2]. To reproduce the time-dependence of the T2D-IR spectra, we slightly varied the homogeneous broadening γ_{t} of the transient photo-product as the only free parameter, keeping all other parameters constant. While the T1D-IR difference spectra at 20 ps, 200 ps and 1.7 ns are almost indistinguishable under these assumptions, the T2D-IR spectra do depend sensitively on the homogeneous line width of the transient species. Good agreement with the experimental data was obtained with a homogeneous width of the photo-product decreasing from $\gamma_{\text{t}} = 16\,\text{cm}^{-1}$ at 3 ps, $\gamma_{\text{t}} = 13.5\,\text{cm}^{-1}$ at 20 ps to $\gamma_{\text{t}} = 12.1\,\text{cm}^{-1}$ at 1.7 ns (Fig.5.34). The model T2D-IR spectrum would be symmetric for $\gamma_{\text{i}} = \gamma_{\text{t}} = 12\,\text{cm}^{-1}$ (as in Fig. 5.32c), a situation which is almost reached after 1.7 ns. We verified that a variation of the homogeneous width γ_{i}, as well as more detailed calculations, that explicitly use the experimental T1D-IR spectra, lead to very similar results [5]. In particular, a

---

[5] Note that in the case of equal homogeneous broadening for initial and transient species, the T2D-IR spectrum is given by the convolution of the T1D-IR response with the 2D-IR signal of a homogeneous line. In contrast to our experimental findings, the T2D-IR spectra at 20 ps and 200 ps would then be almost identical to the spectrum at 1.7 ns. The signal at 3 ps cannot be reproduced at all under this assumption. Indeed, the T1D-IR signals exclude any variations in the relative intensities of the product bands, which could have provided an alternative explanation for the growth of the signal belonging to the product species in the T2D-IR spectra.

$\approx$ 10% change of γ_t between 20 ps and 1.7 ns is always required to reproduce the experimental result.

The simulated T2D-IR spectra can almost quantitatively explain all the experimentally observed features, despite the crudeness of the model. In particular, the lack of an observable transient product band in the 3 ps and 20 ps T2D-IR spectra (Fig. 5.34, arrow 1 and 3) as well as its appearance at $\omega_{pr} = 1685\,\text{cm}^{-1}$ at later times (Fig. 5.34, arrow 4 and 5) are perfectly reproduced. Also the more subtle changes, i.e. tilts and shifts of the various T2D-IR bands (Fig. 5.34, arrows 6-9), are well described. Note, that a minor change of the homogeneous line width of only 10% between 20 ps and 1.7 ns is sufficient to cause appreciable changes in the T2D-IR difference spectra. The reason for this high sensitivity is the small shift of the amide-I band upon *cis-trans* isomerization relative to its total line width (Fig, 5.33a), leading to an almost complete cancellation of the various contributions in the T2D-IR spectra. Hence, even minor changes in the absolute 2D-IR spectra can lead to measurable effects in the T2D-IR spectrum. As a result of the difference measurement, the relative change of the homogeneous width γ_t can be measured much more accurately than its absolute value.

5.6.7 Discussion

Spectral dephasing of a vibrational transition in the condensed phase is commonly related to stochastic fluctuations of its transition frequency [353]. In this approach, both linear and nonlinear spectroscopy are described in terms of the transition frequency fluctuation autocorrelation function $\langle\delta\omega(t)\delta\omega(0)\rangle$, where $\delta\omega(t)$ is the instantaneous deviation of the vibrator's frequency from its average value [310, 301, 249]. The vibrator is coupled to a fluctuating bath, which may include inter- or intramolecular degrees of freedom. As the average transition frequency of the amide-I band is related to the average backbone structure [139], fluctuations of the transition frequency reflect dynamics of the backbone as well as of surrounding solvent molecules.

In this context it is frequently found that the frequency fluctuation correlation function decays on (at least) two times scales [345]: (i) An ultrafast, inertial component on a 100 fs time scale and (ii) a slower, diffusion controlled component on a time scale of many picoseconds. In the case of vibrational transitions, the ultrafast component is typically in the motional narrowing limit, i.e. its correlation time τ_c is faster than or of the same order as the dephasing time $T_2^{-1} \equiv \langle\delta\omega(0)^2\rangle\tau_c$ [301, 249, 247]. Hence, the homogeneous line width γ_t in our experiment is a measure of exclusively the fast (< 1 ps) part of the total fluctuations of the system. The experimental data reveal that this fast contribution is more pronounced when the system is far from equilibrium. In the following, we will discuss four possible explanations for this observation:

Temperature effect: The UV photons of the pump pulse carry an energy of 3 eV ($\hat{=}$290 kJ/mol). We estimate the upper limit of the temperature of the molecule having absorbed a UV photon by Boltzmann-distributing this energy over all normal modes. Normal modes have been calculated on the AM1 level for a geometry generated by an optimization of the *trans*-state, using the Gaussian 98 program package [228]. The UV energy heats the molecule by $\approx$ 220°C. This estimate is considered to be an upper limit, as a significant fraction of the energy is dissipated directly into the solvent during the first few picoseconds of the isomerization (an estimated factor of $\approx$ 0.5) [162]. The temperature jump gives rise to the red-shift of about -2 cm^{-1} in the 3 ps T1D spectrum as a result of (thermal or non-thermal) excitation of anharmonically coupled low frequency modes [173], an effect which has been studied in detail in Refs. [167]. The observed red-shift of -2 cm^{-1} is in agreement with an estimate of $\approx$ 100°C for the temperature jump [354].

A temperature rise of that order of magnitude after 3 ps could certainly cause faster fluctuations of the molecule, and hence the broader homogeneous line width we observe. After 20 ps, however, the red-shifted band, which we may use as a built-in thermometer, has vanished, suggesting that the system has cooled down to the bath temperature. Using the observed cooling rate of (4 ps)$^{-1}$ [173], we conclude that the temperature is elevated by less than 1°C after 20 ps. The temperature dependence of vibrational dephasing in protein environment has been investigated in detail and has revealed an Arrhenius law with an activation energy of $\approx$600 cm^{-1} [355]. If we use this scaling law we find that a temperature rise of 10°C would be required to explain the observed 10% broadening of the homogeneous line width after 20 ps. This discrepancy of one order of magnitude calls for alternative explanations.

Hole-burning in a non-equilibrium ensemble: The 2D-IR part of the experiment is performed on a non-equilibrium ensemble. Strictly speaking, the standard procedure to describe 3$^{\text{rd}}$-order nonlinear IR spectroscopy [310, 301, 249] should break down in this case. One could imagine that a hole burned into a distribution, which evolves in time (i.e. a non-equilibrium distribution), broadens in a different way than a hole burned into a stationary distribution. However, we have performed model calculations which show that this effect is too small to account for the additional 10% homogeneous broadening observed experimentally at 20 ps. Indeed, because of a clear separation of time scales, the 2D-IR experiment is actually performed on a quasi-equilibrium ensemble. A full account of this work will be given elsewhere.

Solvent Effect: A large contribution to the frequency fluctuation correlation function giving rise to dephasing and spectral diffusion originates from solvent fluctuations. This can be seen, for example, from the similar homogeneous dephasing rate of N-methylacetamide (NMA), which contains only a single peptide unit without the flexibility of the peptide backbone around the (ϕ,ψ) degrees of freedom [247]. The temperature argument given above applies in the same way for the solvent, i.e. a temperature jump of the order of 1°C after 20 ps should be too small to account for the observed amount of broadening. In addition, the timescale on which the change of the homogeneous width takes place (an appreciable effect is still observable after 200 ps) is considerably longer than the solvation of DMSO, which contains a small (10%) 10 ps component [168]. Nevertheless, it is possible that the C=O groups are more exposed to the solvent during the early phase due to structural rearrangements, and hence, dephase faster. However, the homogeneous width of the *cis* and the *trans* ensembles in equilibrium are the same despite the very different structural distributions obtained from NMR analysis [125]. This can be deduced from the symmetric pattern of the late 1.7 ns T2D-IR spectrum (well reproduced in the simple model of Fig. 5.32c), which turns out to be an extraordinarily sensitive measure of small differences in the homogeneous width of reactant and transient photoproduct. Hence, it seems unlikely that the solvent alone is responsible for the observed effect between 20 ps and 1.7 ns.

Dimensionality of the potential energy surface: A significant part of homogeneous dephasing can originate directly from fluctuations of the peptide backbone [74]. Hence, its change in time would reflect properties of the part of the potential energy surface the molecules sample at a given UV-pump-2D-IR-probe delay time. The time scale relevant for homogeneous broadening ($<$1 ps) is too fast for the system to cross any significant barrier on the order of $k_B T$. For example, jumps over the barrier between the two preferred conformations of trialanine, the smallest possible peptide with one pair of (ϕ,ψ) dihedral angles, take ten's of picoseconds to nanoseconds [356, 357]. However, there may be regions in the potential energy surface far from equilibrium which are more shallow, and on which the molecule can move almost freely and hence quickly. In fact, it has been shown with the help of time-dependent 2D-IR experiments in combination with molecular dynamic (MD) simulations for trialanine that sampling of the conformational space of a peptide can be very fast (100 fs) when the system is located in a shallow part of the potential energy surface [74]. Along that line, the change of homogeneous width with UV-pump-2D-IR-probe delay time would be an effect of the dimensionality of the accessible conformational space, which certainly becomes more confined when the backbone approaches its global energy minimum.

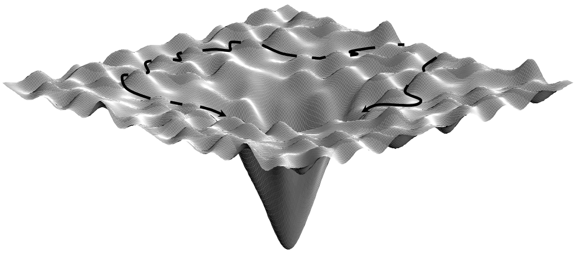

Figure 5.35: Schematic view of the random sampling on a rough potential energy surface.

Fig. 5.35 schematically depicts the search of the system towards its global minimum: Although the potential energy surface is rough, paths exist which do not have to *overcome* any barrier, but may *pass by* barriers in a high dimensional space. The potential energy surface is shallow along these directions, so that sampling of the surface can proceed extremely quickly on time scales faster than < 1 ps. Nevertheless, owing to the large dimensionality of the problem, it may take a much longer time until the system actually finds the global minimum. Once it is trapped, however, the conformational space is confined and the fast fluctuation amplitude is diminished accordingly.

5.6.8 Conclusion

We introduced the technique of transient two dimensional infrared spectroscopy (T2D-IR) and applied it to the ultrafast conformational transition of a photoswitchable cyclic peptide. Substantial changes in the T2D-IR spectra are found at times where the T1D-IR spectra show only little time dependence, illustrating the information boost provided by 2D-IR spectroscopy. In contrast to 1D spectroscopy, 2D-IR can distinguish between homogeneous and inhomogeneous broadening. Transient 2D-IR spectroscopy allows determining these quantities for a non-equilibrium ensemble, evolving on an ultrafast time scale. As the amide-I band reflects the instantaneous conformation of peptides and proteins, homogeneous and inhomogeneous broadening reveals details of the conformational distribution and its dynamics, which cannot be obtained otherwise. We find that the homogeneous contribution to the total width of the amide-I band decreases on the course of the conformational transition. This effect is tentatively attributed to the change of the rate with which the potential energy surface is sampled. However, in order to conclusively distinguish this effect, which would have important consequences in understanding rough energy landscapes, from more trivial explanations (such as solvent fluctuations), the support from MD simulations is clearly needed.

In the present paper, the discussion of the T2D-IR spectrum is limited to the effects of homogeneous and inhomogeneous broadening, since the amide-I spectrum of the peptide investigated is not resolved into individual sub-bands. For the case of spectrally resolved amide-I vibrators, it has been shown that additional structural information is contained in the cross peaks of 2D-IR spectra. We find a transient cross peak between the carboxyl group of the aspartic acid side chain at 1720 cm^{-1} and the amide-I band (Fig. 5.34, arrow 10), which would allow a more site-specific discussion of the conformational transition of that side chain, and which will be addressed in a future work. The possibility of observing transient cross peaks gives rise to the hope, that combined with site specific isotope labelling the present technique may provide detailed pictures of the 3D structure, or structural distribution, of the peptide as it approaches its new equilibrium state and may help to construct a molecular movie.

Acknowedgement. We thank Gerhard Stock and Wolfgang Zinth for illuminating discussions. This work has been supported by the Swiss Science Foundation (2100-067573.02/1) and by the SFB 533 (grant A8) of the Ludwig-Maximilians-Universitaet, Munich.

Chapter 6

Conclusions and Outlook

Ultrafast two-dimensional infrared spectroscopy (2D-IR) measures the vibrational response of a sample as a function of IR excitation frequency, time and polarization. It is a promising tool for the investigation of molecular structures and their equilibrium fluctuations. Similar as in 2D-NMR spectroscopy, cross-peaks between coupled states emerge in 2D-IR spectra, revealing structural information. The 2D-lineshapes and their time dependence allow for conclusions on ensemble inhomogeneity and the timescale of its persistence. The outstanding feature of 2D-IR spectroscopy is the combination of its structure sensitivity with an intrinsic sub-picosecond time resolution, freezing in all but the fastest molecular motions. This makes it particularly suited for application to fast dynamical processes, offering means to resolve distributions and dynamics of fast interconverting states in *equilibrium*. Highly promising is the extension of the 2D-IR technique to the *non-equilibrium* regime, where its high time resolution can be put to full use. Changes of molecular structures on timescales of ms down to sub-ps could be addressed. Transient 2D-IR spectroscopy (T2D-IR), introduced in Part II of this dissertation, realizes this extension of 2D-IR to the non-equilibrium regime.

Besides the IR pulses used for 2D-IR, T2D-IR features an additional UV/Vis pulse that prepares the system in a non-equilibrium state. Different T2D-IR pulse sequences (Figure 6.1) have been introduced in this dissertation. Their information content has been investigated theoretically as well as experimentally. It became clear, that only in certain limits T2D-IR can be understood as a mere extension of 2D-IR to transient species. Only in pulse sequence (a) in Figure 6.1, when the IR delay is short compared to the time scale of the relaxation of the non-equilibrium ensemble prepared by the UV pulse, one can think in terms of 2D-IR snapshots of the transient species. As typical IR delays are on the order of 1 ps, this will be well fulfilled for UV delays on the order of 10 ps and longer. Then, the system can be considered being in quasi-equilibrium during the 2D-IR part of the experiment. This is the limit that will be useful for the determination of transient structure parameters. As soon as we leave the ‘snapshot limit’ by making the IR delay longer compared to relaxation as in sequence (b) or by even exchanging the order of the pulses as in sequence (c), new types of information become accessible. Application of the different pulse

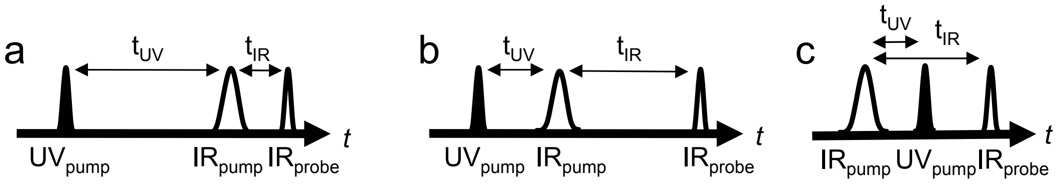

Figure 6.1: T2D-IR pulse sequences: (a) Regular T2D-IR experiment. A UV pulse generates a non-equilibrium situation. Its relaxation is monitored by 2D-IR experiments at variable delays. (b) Holeburning T2D-IR. (c) Labeling T2D-IR.

sequences has been demonstrated for the investigation of metal-to-ligand charge transfer of a metal carbonyl model system and the accompanying solvation dynamics. In a combination of the developments of Part I and II of this dissertation, T2D-IR has been applied to the conformational transition of a photoswitchable peptide

Experiment (b) (*holeburning T2D-IR*) has been applied to the investigation of solvation dynamics. Many molecular processes in the liquid phase are intimately coupled to the dynamics of the surrounding solvent molecules in a variety of ways. The quantum-mechanical states of a solute molecule are coupled to—and perturbed by—a continuum of low-frequency modes of the solvent, which may qualitatively and quantitatively change the mechanism and outcome of any liquid phase reaction in chemistry and biology. At the same time, the fluctuations of the energy levels can be used as an experimental probe for the strength and dynamics of solute-solvent interactions. Previous solvation experiments such as dynamic stokes shift, photon echo peak shift or 2D spectroscopy are primarily sensitive to the two-point frequency fluctuation correlation function (FFCF) of the probed spectroscopic transition. From these experiments it is known that the two-point FFCF is multiphasic or at least biphasic, thus at least two generalized solvation modes coupled to the spectroscopic transition have to be used to describe the process. If solvation would occur in the linear response regime, the two-point FFCF would completely describe the process and coupling of the solvation modes would not play a role. Coupling between solvation modes shows up only in higher order correlation functions. However, the experiments previously used are 3rd order techniques and are linear spectroscopies with respect to the solvation modes. Thus they are not sensitive to their coupling. 5th order Raman spectroscopy has been suggested as a probe of the nonlinear response of solvent modes, however, its experimental realization turned out to be very difficult. In the present dissertation it has been shown that the T2D-IR holeburning experiment can provide similar information on the coupling of solvation modes. Langevin diffusion simulations on model potentials with two (solvation) coordinates showed that processes featuring identical two-point FFCFs but different higher order FFCFs, due to coupling of the coordinates, are virtually indistinguishable by 2D-IR (3rd order) but can be distinguished by holeburning T2D-IR. We applied the holeburning experiment to the solvation of our metal carbonyl model system after metal-to-ligand charge transfer (MLCT) in the solvent DMSO. Its 2D-IR spectra could be explained by a biphasic FFCF using a fast and a slow solvation coordinate. However, to model the T2D-IR spectra a coupling between solvation coordinates had to be introduced which leads to a correlation of the fast and slow fluctuations that shows up in the three-point FFCF. T2D-IR thus provides information that is not accessible with previous techniques and allows to go beyond the linear response hypothesis. Similar information for equilibrium systems could be obtained by an all-IR 5th order experiment, where the UV-pump pulse is replaced by an IR pulse. The sensitivity of the current setup should already allow for such an experiment. Not only solvation but also other processes that modulate the frequency of a vibrational transition, such as conformational fluctuations, can be investigated along the same lines. Investigation of the frequency fluctuations induced by conformational changes along an MD trajectory of trialanine showed a similar correlation between a fast and a slow process as found in the solvation experiment. The information on liquid phase dynamics obtained from such experiments might also help to tune MD force fields for solvents, that up to now mostly rely on thermodynamic observables for calibration, yet are often used to predict dynamics.

The *labeling T2D-IR* experiment is another novel pulse sequence (Figure 6.1(c)). It has been designed for disentangling the vibrational bands during a photoinduced process or reaction. Usually it is not possible to follow the shifts of vibrational bands during a reaction by time resolved absorption spectroscopy. Bands typically overlap and may shift over each other, a situation that is in many cases made even worse by significant broadening after photoexcitation. The labeling pulse sequence introduced here correlates vibrations of a molecule before and after a photoreaction by generating *cross peaks* between the reactant vibrations and the product vibrations into which they are transformed. In this respect labeling T2D-IR could be regarded as an IR version of NMR exchange spectroscopy under non-equilibrium conditions. In the present work the labeling technique was used to track the carbonyl vibrations of $[Re(CO)_3Cl(dmbpy)]$ during photoinduced MLCT and the accompanying solvation process. It was shown that the vibrational levels change their order in the MLCT state. This finding disproves the assignment widely used in literature but is in excellent agreement with a recent theoretical study. This observation allowed to draw conclusions on the electronic structure of the excited state. It suggests that mixing between the π^* orbital of the bipyridyl ligand occupied after MLCT and the π^* orbitals of the equatorial CO ligands takes place and partially compensates the electron transfer to the bipyridyl ligand. Thus the blue shift of the a” mode, that is exclusively centered on the equatorial COs, is smaller then the shift of the other CO modes. Labeling T2D-IR is widely applicable to all kinds of phototriggered events. Studies on similar metal carbonyls with different delocalizations for the $\pi*$ orbitals are envisaged. A labeling study of CO dissociation in myoglobin mutants will hopefully allow to correlate different primary CO binding states with the binding sites that are populated when CO is dissociated from those primary states.

A long-term objective driving the development of T2D-IR spectroscopy is to extend the structure determination approach of 2D-IR spectroscopy to the transient regime, and apply it to the study of peptide and protein dynamics. Samples of particular interest in this context are the photoswitchable peptides discussed in Part I of this dissertation. In a 2D-IR spectrum, cross peaks occur when the two corresponding resonances on the diagonal are coupled. Two important pieces of structure relevant information can be deduced from each cross peak: The coupling strength, related to the cross-peak amplitude, and the angle between corresponding transition dipoles on the diagonal, given by the cross peak anisotropy. Using appropriate models this information can be translated into structure information. With T2D-IR, a series of 2D-IR spectra can be taken at various times after a reaction or a conformational transition has been initialized (experiment (a) in Figure 6.1). The goal is to extract structure information during the transition of the molecules. Important prerequisites for approaching the task of determining transient structure parameters by T2D-IR have been established in this dissertation:

The improvement and extension of 2D-IR structure determination to larger peptides has been discussed. Structure information content of the heterodyne photon echo approach and the double resonance approach have been compared theoretically and experimentally. Additional Feynmann diagramms due to interstate coherences can be obtained by the photon echo as compared to double resonance. However, the information relevant for structure determination obtained from the two approaches is essentially identical. In certain limits, the spectra obtained by double resonance are found to be connected to the photon echo spectra through convolution with the pump pulse spectrum along one frequency axis. As a consequence, spectral resolution of the photon echo approach is superior. The higher resolution as well as the (theoretically) higher signal to noise ratio could turn out as an advantage for congested spectra. However, a big problem in the echo experiment is the determination and stabilization of the phase (and possible chirp of the pulses). This phase sensitivity makes the experiment very susceptible to artifacts. This is often avoided by plotting absolute value spectra, in which case, however, the advantage in spectral resolution is forfeited. To overcome these problems an actively phase stabilized echo setup is currently build in our group.

It was found that the information content of a 2D-IR spectrum would be by far sufficient for polypeptide structure determination if each vibrational transition could be resolved. Unfortunately, severe band overlap due to homogeneous and inhomogeneous broadening blurs this information. In a computational case study of a cyclic pentapeptide the resulting loss of structural information was investigated. It was demonstrated how this loss can be compensated by intelligent isotope labeling strategies. A new algorithm for structure determination taking into account geometrical restrains imposed by the peptide structure has been devised. This approach greatly reduces the search space of the optimization compared to a direct fit of the spectroscopic hamiltonian and allows to approach more complex problems. It could be further improved by the use of a realistic force field like it is commonly done in NMR and X-ray structure determination. Experiments will have to show how far 2D-IR structure determination really can be taken. In many cases, however, one will be interested only in a small subsystem of a larger structure and not try to solve the structure of a whole polypeptide. The 2D-IR signal of an isotope labeled substructure will be comparably strong and easy to observe as the anharmonicity of the labeled amide I band is stronger than the anharmonicity of the more delocalized unlabeled amide I vibrations. The use of other vibrations besides the amide I band should be explored, such as the amide II and amide A band. Also, additional groups could be synthetically introduced into molecules that provide vibrations with large cross-sections and strong coupling.

The measurement of cross peaks in T2D-IR spectra required for the determination of transient structures has been demonstrated for our Rhenium carbonyl model compound. The polarization dependence of transient cross peaks is well understood. A general expression has been derived for the polarization dependence of T2D-IR which is of 5th order in the laser field and involves up to three transition dipole moments. The dependence on rotational diffusion was analyzed. It was shown that a diffusion independent signal like the magic angle signal in pump-probe spectroscopy does not exist. However, magic angle like signals for important special cases where obtained. The polarization conditions leading to a maximum of structural information have been discussed. Important special cases of polarization conditions have been formulated. The validity of the theoretical findings was demonstrated by experiments, again employing the model system of phototriggered MLCT in [Re(CO)$_3$Cl(dmbpy)]. In comparison to pump-probe spectroscopy the additional pulse and transition dipole moment in T2D-IR lead to a much more involved polarization dependence. This additional degree of freedom in polarization was found to strongly enhance the versatility of signal manipulation and the potential structural information content of the signals. The additional versatility can be exploited to enhance or suppress different spectral features to simplify interpretation of the spectra. The utilization of various polarization conditions has been demonstrated for the three different types of T2D-IR experiments that are shown in Figure 6.1.

Part I of this dissertation dealt with the conformational dynamics of polypeptides over a wide range of time-scales. Built-in photoswitches have been used as an ultrafast trigger for peptide dynamics. As a first step in combining these efforts with the development of T2D-IR described in Part II, we applied T2D-IR to the conformational transition of the photoswitchable cyclic peptide cycAMPB. Substantial changes have been found in the T2D-IR spectra at delays where the transient absorption spectra show only little time dependence, illustrating the information gain provided by 2D-IR spectroscopy. The investigated cycAMPB sample does not feature any isotope labels, therefore severe band overlap precluded a measurement of cross peaks. The present discussion therefore focussed on the overall 2D-lineshape. As explained above, 2D-IR is sensitive to homogeneous and inhomogeneous contributions to the lineshape. Transient 2D-IR spectroscopy allows determining these quantities for an evolving non-equilibrium ensemble. As the amide-I band reflects the conformation of peptides, homogeneous and inhomogeneous broadening reveals details of the conformational distribution and its dynamics. We found that the homogeneous contribution to the amide-I lineshape decreases on the course of the conformational transition. This effect has been tentatively attributed to a reduction of the fast (picosecond) part of the conformational fluctuations with which the potential energy surface is sampled. In the beginning of the relaxation, regions higher up on the energy landscape are sampled, while at later times the fluctuations become more and more confined as the system approaches its native conformation at the global minimum of the energy landscape. However, in order to conclusively distinguish this effect from more trivial explanations (such as solvent fluctuations), the support from MD simulations is clearly needed. Such simulations are currently under way in the group of Gerhard Stock.

In the investigation of cycAMPB strong band overlap precluded structure determination from the T2D-IR spectra. However, the present experiment demonstrates the feasibility of T2D-IR spectroscopy of photoswitchable peptides. In future, isotope labeling can help to overcome the problem of band overlap as shown in Paper **P3**. A next step in the investigation of cycAMPB could be the labeling of two peptide units, one by ^{13}C and one by ^{13}C ^{18}O, to obtain a subsystem of two coupled oscillators that can be investigated in presence of the remaining unlabeled amid I band. In this fashion, time dependent structure information could be obtained for pairs of peptide units. In the investigation of more complicated molecules the cross peak emerging from the coupling between two oscillators could be used to just report on their spatial proximity without attempting a detailed structure analysis. Such experiments could provide information about contact formation in a similar fashion as time resolved FRET or triplet-triplet energy transfer [64] but without the need of introducing bulky chromophores that might alter structure and dynamics. An interesting application will be β-sheet or β-hairpin folding, where the appearance of cross peaks between residues of two strands could be measured. Site directed labeling could provide information on the contact formation with unprecedented detail.

The few examples presented in this dissertation show that two-dimensional IR spectroscopy (2D-IR) and the new technique of transient two-dimensional IR spectroscopy (T2D-IR) definitively open up an other dimension to the IR spectroscopist. They provide a wealth of spectroscopic, structural and dynamic information that has not been accessible before. As the techniques are very versatile and not demanding in sample preparation, a wide range of future applications can be foreseen.

Part III

Technical Appendix

Chapter 7

The Transient 2D-IR Spectrometer

7.1 Scope

The transient 2D-IR (T2D-IR) setup is based on the 2D-IR principle described previously by Hamm and coworkers [2, 246]. Thus, the description given here will be brief and focussed on the points relevant for the upgrade from 2D-IR to T2D-IR and on the technical developments required for working with photoswitchable peptides. **Section 7.2** describes the T2D-IR setup, the MIR light generation, as well as the generation of UV light used for triggering of the photoswitchable peptides in Part I and for photo excitation of the metal carbonyl complex in Part II. Capturing all time scales of the dynamics of the photoswitchable peptides requires scanning of the delays over many orders of magnitude one picosecond to microseconds. This is realized by the setup described in Paper **P11** in **Section 7.3** employing two synchronized femtosecond laser systems. Working with specially designed rare or expensive samples—like the photoswitchable peptides—requires a reliable flow cell that allows to recover the sample. The cell has to be designed for microamounts, as the amount of sample available is typically very small (200 μg - 700 μg in the measurements of the photoswitchable α-helix of Paper **P13**). Paper **P2** in **Section 7.4** introduces a flow cell that meets this requirements and can be used for time resolved measurements on sample volumes down to 200 μl. Investigation of peptide dynamics at various temperatures demands thermoregulation of the flow cell. This add-on is described in **Section 7.5**.

7.2 The Transient 2D-IR Experiment

7.2.1 Femtosecond Pulse Generation

The T2D-IR experiment requires tunable femtosecond IR pulses that are generated by a MIR-OPA (Section 7.2.2) and femtosecond UV pulses that are generated by SHG or THG (Section 7.2.3). In the standard configuration used in most experiments reported in this dissertation, MIR-OPA and SHG or THG are pumped by a single Ti:sapphire (Ti:S) oscillator/amplifier femtosecond system. For a description of this commercially available femtosecond system see Paper **P11** in Section 7.3. Its typical working parameters are summarized in Table 7.1.

For the experiments on the photoswitchable α-helix FK11X (Chapter 2, Paper **P13** and **P16**) we used a setup of two electronically synchronized femtosecond laser systems as described in Paper **P11**. In this case one femtosecond system pumps the SHG, while the other pumps the MIR-OPA. This configuration allows to scan the delay between the UV and the MIR pulses continuously in a range up to 50 μs with a jitter of < 2 ps, avoiding the limitations of optical delay lines regarding delay range, beam pointing and scanning speed.

7.2.2 MIR Generation

The setup for MIR generation comprising a white light seeded two stage BBO-OPA and subsequent difference frequency generation (DFG) from signal and idler of the OPA in $AgGaS_2$ was described previously [165].

7.2.3 UV Generation

Pulses in the range of 385 nm to 430 nm are obtained by SHG in a BBO crystal. The UV wavelength is set by tuning the Ti:S oscillator and amplifier. The typical pulse duration is about 200 fs. In some experiments, high UV excitation density is required while high time resolution is not crucial (part of the experiments in Papers **P4**, **P7**, **P8**, **P9**, **P10** and **P15**). In these cases the UV pulses are stretched by guiding them through fused silica rods of 10 cm or 15 cm length. Stretching significantly increases the threshold for the onset of undesired nonlinear effects like white light generation and/or color center formation in the sample cell [104], and allows to excite a larger fraction of the sample. To restore a proper beam profile after the silica rods we use spatial mode filtering by focusing the beam with a 1500 mm lens on a pinhole. To obtain UV pulses at 280 nm or at 259 nm for the experiments on N-Methylthioacetamide (NMTAA) in paper **P9**, we use a collinear time plate tripler for third harmonic generation (THG). The second harmonic or third harmonic is isolated by dielectric mirrors.

7.2.4 Principle of the T2D-IR Measurement

The 2D-IR part of the experiment is performed according to the double-resonance scheme described previously by Hamm and coworkers [2, 252]. A schematic overview of the T2D-IR experiment is given in Figure 7.1. For typical working parameters see table 7.1.

After DFG from the signal and idler of the OPA, the resulting MIR light passes a low pass filter to dump signal and idler. A small fraction of the IR-beam is split off by a BaF_2 wedge to obtain broadband probe and reference pulses (the reference pulse is omitted for clarity in Fig. 7.1). The remainder, which is used as the IR-pump pulse, is send over a delay line and passes through a computer-controlled Fabry-Perot interferometer to generate narrow-band tunable IR-pump pulses [2, 246]. The IR-pump and probe pulses are focused into the sample in spatial overlap (the reference pulse is focused ≈ 1 mm apart and upstream when a flow cell is used). Probe and reference beams are dispersed in a spectrograph and imaged onto a 2×32 pixel HgCdTe detector array which allows to measure single shot IR-pump IR-probe spectra with a resolution of typically $2\,\mathrm{cm}^{-1}$ – $8\,\mathrm{cm}^{-1}$ (depending on grating and wavelength range). 2D-IR spectra are then constructed as a function of the IR-pump frequency ω_{pu} set by the Fabry-Perot interferometer and the IR-probe frequency ω_{pr} resolved by the spectrometer. By addition of a UV pulse preceding the IR-pump and IR-probe pulses, the transient 2D-IR spectrum of the UV excited ensemble is recorded. Hence, the total T2D-IR experiment consists of 3 pulses: a UV-pump, a narrow-band tunable IR-pump and a broad-band IR-probe pulse. The delay between the UV pulse and the IR-probe pulse is controlled by a 15 cm delay stage in the UV branch. A scanning range of up to 7 ns is achieved by quadruple or octuple passage of the stage, as this compensates for most of the beam walkoff induced by scanning. Alternatively a second synchronized and delayable femtosecond system can be used for UV generation as described before.

Since the UV pulse cannot convert 100% of the initial species into the product species, the 2D-IR spectrum in the presence of the UV pulse always contains contributions from both. In order to eliminate contributions of molecules that have not absorbed a UV photon, two sets of 2D-IR spectra are recorded simultaneously - one with the UV-pump pulse on and one with the UV-pump pulse off - and subtracted from each other. Hence, just like it is common practice in conventional pump-probe spectroscopy, our T2D-IR spectra are in fact T2D-IR *difference* spectra.

To collect the required signals we use two light choppers, one in the IR-pump beam running at half the repetition rate of the laser system and the other in the UV-pump beam running at a quarter of the repetition rate. Four

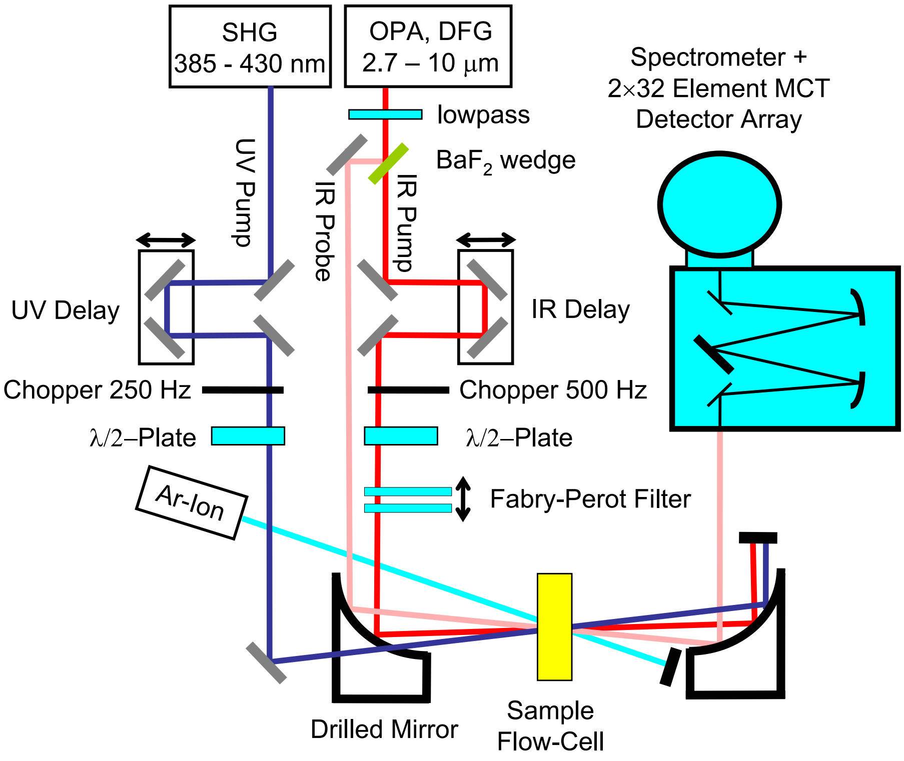

Figure 7.1: Schematic setup for T2D-IR spectroscopy. Not all components are shown, the IR reference beam is omitted for clarity.

individual data sets are recorded: $I_{\mathrm{UV_{on}IR_{on}}}$, $I_{\mathrm{UV_{off}IR_{on}}}$, $I_{\mathrm{UV_{on}IR_{off}}}$ and $I_{\mathrm{UV_{off}IR_{off}}}$. The stationary 2D-IR spectrum of the initial state is calculated as:

$$\Delta A_{\mathrm{2D,stat}} = -\log \frac{I_{\mathrm{UV_{off}IR_{on}}}}{I_{\mathrm{UV_{off}IR_{off}}}}, \tag{7.1}$$

the UV-pump IR-probe spectrum as:

$$\Delta A_{\mathrm{T1D}} = -\log \frac{I_{\mathrm{UV_{on}IR_{off}}}}{I_{\mathrm{UV_{off}IR_{off}}}}, \tag{7.2}$$

and the T2D-IR difference spectrum as:

$$\Delta A_{\mathrm{T2D}} = -\log \frac{I_{\mathrm{UV_{on}IR_{on}}} \cdot I_{\mathrm{UV_{off}IR_{off}}}}{I_{\mathrm{UV_{on}IR_{off}}} \cdot I_{\mathrm{UV_{off}IR_{on}}}}. \tag{7.3}$$

.

If only the UV-pump IR-probe spectra are needed (Papers **P1**, **P6**, **P8**, **P9**, **P13** and **P16**), the same setup is used with the IR-pump pulses blocked and the UV chopper running at 500 Hz. For regular 2D-IR spectroscopy (Papers **P4**, **P12**) the UV-pump branch is blocked.

Due to the very stable MIR source [165], the use of a spectrally dispersed IR reference beam and chopper normalization this setup allows to collect transient spectra with a noise as low as 5 μOD within less then a minute of averaging.

7.2.5 Rapid Control of the Laser Polarization

The polarizations of the pulses are set by computer controlled zero order half-wave plates in the IR-pump and the UV-pump beam (Figure 7.2). The polarization of the IR-probe beam is kept constant to avoid artifacts due to the polarizing properties of the spectrometer. Each half-wave plate can be switched rapidly between two preset

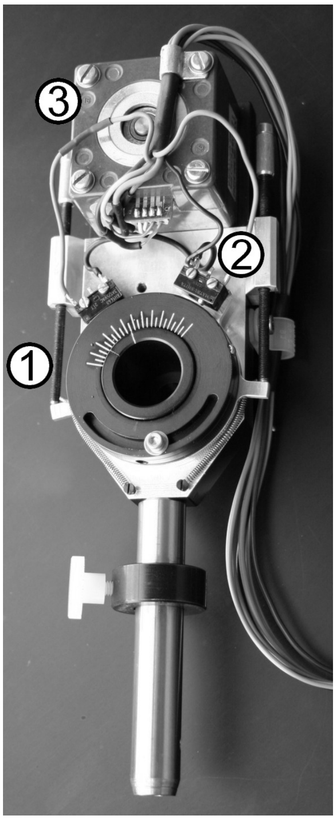

Figure 7.2: Motorized computer controlled mount for the half-wave plates. (1) Fine thread for adjusting the preset polarizations. (2) Position sensor. (3) Stepping motor.

positions with high precision. This allows for the quasi-simultaneous measurement of four sets of polarizations by changing the orientation of the plates every few hundred laser pulses. In this way drifts and instabilities in laser intensity are correlated for the measurements with different polarization conditions and linear combinations of the different signals can be calculated without being affected by normalization ambiguities (Paper **P10**).

7.2.6 CW Irradiation of Photoswitchable Molecules

In most experiments on photoswitchable molecules described in Chapter 2, the molecules have to be prepared in a certain conformation by photoinduced isomerization. In case of the azobenzene based photoswitches investigated in Papers **P1**, **P4**, **P6**, **P13** and **P16**, the *cis* conformation is prepared by irradiating the $\pi\pi^*$ band of the *trans* state with an Argon-Ion laser (Coherent ”Innova 100”) operating at 363 nm (Fig. 7.1). Irradiation is typically done in the flow cell in a small reservoir of the spacer while the sample is circulating to achieve equilibrium before the actual measurement is started (see Fig. 7.8 in paper **P2** for the spacer geometry with the reservoir). During the measurement the cw irradiation is continued to regenerate the initial conformation of the photoswitches.

parameter	value
Mid-IR pulse duration	130 fs
Mid-IR pulse width	240 cm^{-1}
Mid-IR power @ 6μm	1-3 μJ
Fabry-Perot filter width	8 - 16 cm^{-1}
UV pulse duration	150 - 600 fs
UV power @ 400 nm	2 - 8 μJ
UV pump focus	140 - 200 μm
Mid-IR pump focus	100 μm
Mid-IR probe focus	80 μm
Tsunami width @ 800 nm	13 nm
Tsunami power @ 800 nm	400-500 mW
YLF power	8 W
Spitfire power @ 800 nm	500-700 mW
Spitfire pulse duration	90 fs
Spitfire tuning range	770 - 860 nm

Table 7.1: Typical working parameters of the laser setup.

7.3 P11 – Continuous Scanning from Picoseconds to Microseconds in Time Resolved Linear and Nonlinear Spectroscopy

Jens Bredenbeck, Jan Helbing, and Peter Hamm,
Rev. Sci. Instrum., 75:4462–4466, 2004.

7.3.1 Abstract

We describe a setup of two synchronized femtosecond 1 kHz oscillator/regenerative amplifier laser systems that allows to continuously delay the amplified pulses up to 50 μs, with a jitter of $\leqslant 2$ ps. It can be realized by facile modification and combination of equipment that already exists in many femtosecond laser laboratories. It opens up a variety of new experimental possibilities, particularly for the investigation of systems that display dynamics over a wide range of time scales, such as peptides and proteins. As an example we discuss the application of this setup for time resolved IR spectroscopy.

7.3.2 Introduction

There is currently an intense effort to investigate the dynamics of biomolecules such as peptides and proteins in their native environment, be it liquid phase or membrane. The picture beginning to emerge is that a continuum of timescales governs peptide and protein dynamics in a time range over many orders of magnitude from seconds down to the picosecond regime. The setup described in this work offers a great versatility for the design of experiments covering this whole time range. It employs two synchronized and delayable amplified Ti:sapphire (Ti:S) femtosecond laser systems. While synchronization of two laser oscillators has been described previously [358], the objective of this work is to synchronize the amplified pulses and to scan their relative delay continuously over many orders of magnitude in time.

With the nonlinear frequency conversion techniques established today, the 800 nm output of the two Ti:S laser systems can be converted to cover interesting spectral windows for a variety of applications. In the present work we demonstrate this for time resolved IR spectroscopy. The output of one of the two laser systems is frequency doubled to generate 400 nm pulses that are used for photoexcitation. The other laser system is used to pump a mid-IR optical parametric amplifier (OPA) [165] to obtain probe pulses (duration 100 fs, width 240 cm^{-1} FWHM) that are tunable from 1200 to 3800 cm^{-1}. The probe pulses are frequency dispersed in a spectrometer and imaged onto a mercury-cadmium-telluride (MCT) detector array. This setup constitutes an IR spectrometer with $<$ 2 ps time resolution that can be scanned up to 50 μs in the present version. A setup for nanosecond IR spectroscopy that uses the broad bandwidth of a femtosecond Ti:S laser has been described previously [359].

There are three significant advantages of our laser setup compared to a step-scan Fourier transform infrared (FTIR) spectrometer [360] or setups with cw laser probing [45], which is what is commonly used for time resolved IR studies in the nanosecond and microsecond regime:

- The mid-IR light from a femtosecond laser system provides high intensity and a comparably large bandwidth (240 cm^{-}1 FWHM). For the synchronized laser setup the signal-to-noise ratio is constant over the whole time-range and does not scale with the square-root of the time-resolution, like any approach will do that uses the intrinsic time resolution of fast IR detectors. Hence, in particular in the regime $<$ 100 ns, the laser setup is superior to the step-scan FTIR approach in terms of signal to noise. Transient measurements of molecules that are available only in very small amounts, like biological samples or specially designed biomolecules such as the photoswitchable peptides investigated in our group [173, 206], are made possible.

- The time range below 20 ns, that cannot be resolved by the step scan approach but seems to be very important for the dynamics of peptide and protein secondary structures [173], can be easily accessed with our setup. Picosecond and nanosecond data can be measured with one and the same setup, without having to scale data sets originating from different instruments to each other.

- Using femtosecond lasers opens the possibility of applying nonlinear optical techniques, such as two-dimensional IR spectroscopy, as probe processes. Transient 2D-IR has recently been developed in our group [174] and is a promising method to investigate transient molecular structures. Using the synchronizing and scanning setup described here, this technique can be applied to peptides and proteins over all relevant timescales of their dynamics.

- Femtosecond lasers offer a high flexibility concerning the excitation wavelength. In the present version of the setup the output of the Ti:S amplifier is simply frequency doubled. Other well established techniques of nonlinear frequency conversion may be used to generate any wavelength between 200 nm and the mid-IR.

Compared to standard pump-probe techniques that use optical delay lines to generate delays up to about 10 ns, the present setup has the advantage that the delay time is controlled electronically without any moving parts. This allows for faster data acquisition and high beam pointing stability.

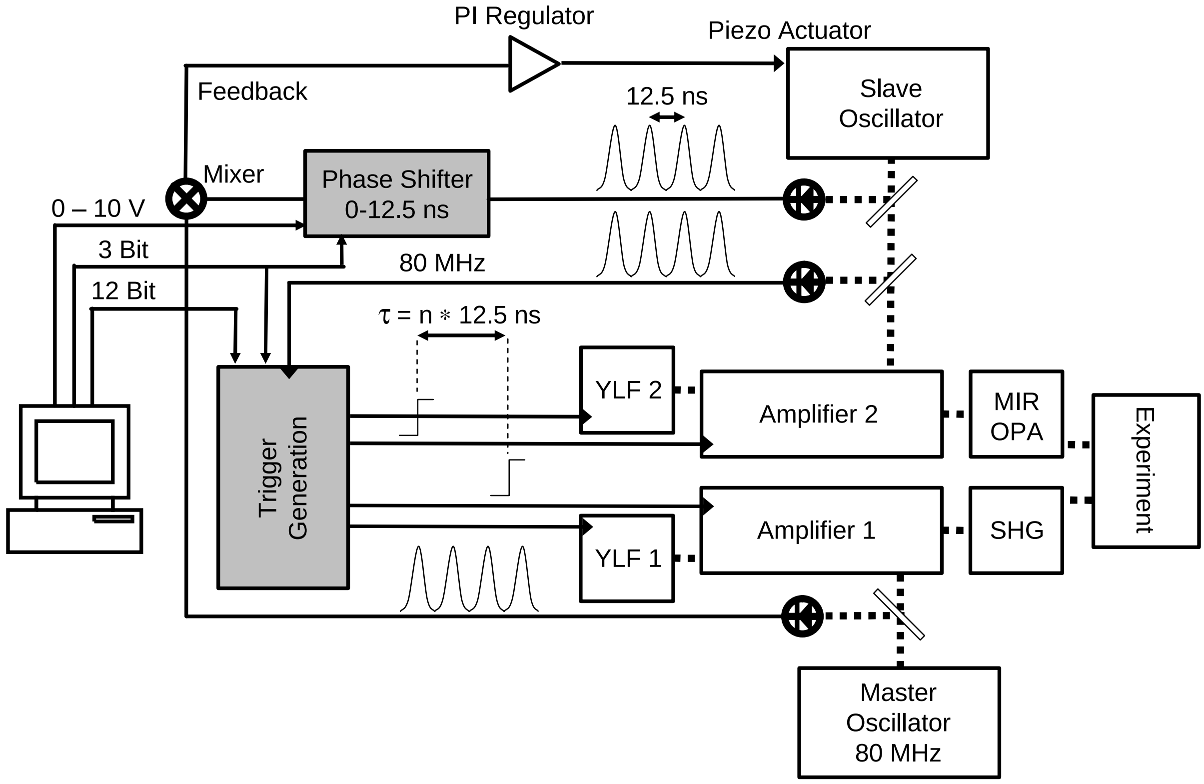

Figure 7.3: Setup of two synchronized and delayable femtosecond laser systems. The trigger generation and the phase shifter are shown in Figures 7.4 and 7.5 in more detail.

7.3.3 Laser Setup

Outline

An overview diagram of the setup is shown in Figure 7.3. It consists of two independent femtosecond laser/amplifier systems. We used Spectra Physics laser/amplifier systems in our implementation, however, the same principle can be applied to almost any femtosecond laser system [1]. Each laser/amplifier system comprises a passively modelocked Ti:S oscillator (Spectra Physics *Tsunami*) pumped by a diode-pumped intracavity doubled Nd:YVO$_4$ cw laser (Spectra Physics *Millenia*) as well as a regenerative Ti:S amplifier (Spectra Physics *Spitfire*), pumped by a diode-pumped Q-switched intracavity doubled Nd:LiYF$_4$ (Nd:YLF) laser (Spectra Physics *Evolution*). One of the Ti:S oscillators serves as a master. The round trip time of the slave oscillator is adjusted by a piezo-actuated mirror to achieve locking to the master oscillator. To this end, the pulse train of each oscillator is monitored by a photodiode, the outputs of which are mixed in a phase detector to generate a feedback signal for the piezoactuator in the slave oscillator. In order to achieve time delays within the oscillator round trip time of 12.5 ns, the photodiode signal of the slave oscillator is phase shifted before mixing in the phase detector. To enable delays spanning more than one oscillator round trip time, the triggers for the regenerative amplifier are shifted by an appropriate integer multiple of the oscillator round trip time. To generate for example a delay of 40 ns, it is decomposed into 3 × 12.5 ns + 2.5 ns. In this way it is possible to achieve long delays, that are in our case limited only by the number of pulses that can be handled by the 12 bit counter in the trigger generator (4096 × 12.5 ns ≈ 50 μs). The maximum delay could easily be extended to even longer times. The various components of Figure 7.3 are described in detail in the following.

---

[1] Product names mentioned are for technical communication only and do not constitute an endorsement by the authors.

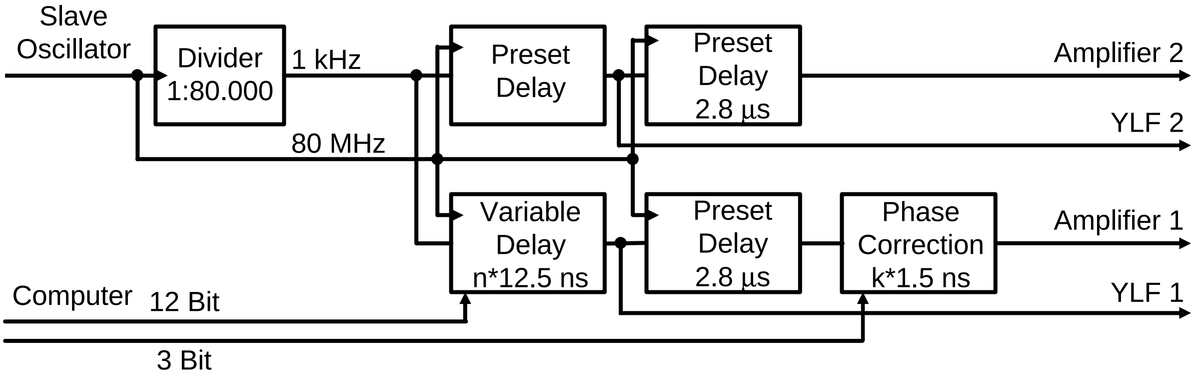

Figure 7.4: Trigger generation for the amplifiers and their pump lasers.

Synchronization of the Ti:S Oscillators

The two locked oscillators constitute a phase locked loop (PLL), where the master oscillator delivers the reference frequency. The length of the cavity of the slave oscillator is controlled by a piezoactuated mirror. Therefore the slave oscillator acts as the voltage controlled oscillator in the PLL. To guarantee stable operation of the PLL and at the same time avoid regulator errors, a PI regulator is used in the loop [361]. The pulse trains of the two oscillators are recorded with two biased silicon photo diodes (Thorlabs DET210), which have been modified to yield a 3 V_{pp} output signal. The output of each photo diode is passed through a 90 MHz low pass filter (Mini-Circuits BLP-90) before they are mixed in a phase detector (Mini-Circuits ZRDP-1). The output of the phase detector serves as the error signal for the PI regulator. The PI regulator drives the piezoactuator in the slave oscillator through a high voltage amplifier, which closes the loop. Note that the high-frequency (rf) part of the electronics (photodiodes, filter, mixer, and phase shifter) is purely passive electronics, which we believe is crucial for a low ($<$ 2 ps) jitter of the two oscillators. Furthermore, the devices are pre-mounted and can be assembled easily using BNC connectors, without any experience in rf electronics.

Modification of the Slave Oscillator

The mount of one cavity mirror (M5 in Spectra Physics design drawings) of the slave oscillator has been redesigned to be movable on a delay stage (Newport M-UMR5.25A). The stage is controlled by a motorized micrometer actuator (Thorlabs Z606) to allow for a coarse matching of the slave oscillator length. The motorized delay stage carries a mirror mount holding a piezo ring actuator (Piezomechanik HPSt 150/14-10/12 VS22, maximum stroke 16 μm, resonance frequency 30 kHz) to which the original 1/2” mirror has been directly attached. The movable masses are kept as small as possible. The resonance frequency of the complete feedback loop is $\approx$ 2 kHz, limiting the settling time to $\approx$ 1 ms.

Triggering the Ti:S Amplifiers and Nd:YLF Pump Lasers

Operation of each amplifier requires a trigger for the pump laser as well as for the Pockels cells in the amplifier. The generation of these trigger signals is shown in Figure 7.4: One master 1 kHz signal is needed to trigger both systems simultaneously, which is derived from a third photodiode monitoring the slave oscillator (80 MHz) and employing a digital 1:80.000 divider. Starting from the 1 kHz signal, four triggers with individual delays are generated for the two Nd:YLF pump lasers and the Pockels cells of the two Ti:S amplifiers. The delay generators are constructed from pre-setable counters (12 bit) that are clocked by the same 80 MHz signal. Hence, the outputs of the electronic delays are automatically synchronized with both oscillators. The delay between the Nd:YLF pump laser and Ti:S amplifier of each system is set to an appropriate fixed value (2.8 μs) using DIP switches. The trigger signals can be feed directly into the original control electronics of the Spectra Physics Nd:YLF pump laser and Ti:S amplifier without any modification thereof [2]. The trigger elec-

---

[2] The delay generated by the pump laser electronics of the Spectra Physics *Evolution* system between an external trigger it receives and

tronics is based on standard TTL electronics using the ’74F’ family.

Time Scanning in Multiples of the Oscillator Round Trip Time of 12.5 ns

Having established the synchronization of the amplified pulses we need to delay them relative to each other. The total delay of system 2 is set to a fixed value close to the maximum delay possible with the 12 bit counter. The delay of system 1 is controlled from the computer using a 12 bit signal from a digital I/O board (KPCI-PIO24, *Keithley*). By changing the preset-value in the counter, delay steps in integer multiples of the oscillator round trip time (12.5 ns) are produced. In that way, large positive (the pump pulse that is generated by system 1 precedes the probe pulse) and small negative delays (the pump pulse arrives after the probe pulse) between both systems can be realized.

Time Scanning Within the Steps of 12.5 ns

Delays within the 12.5 ns steps are generated by phase shifting the photo diode signal of the slave oscillator before mixing it with the master signal in the phase detector. The phase shifting unit is shown in detail in Figure 7.5. It combines two delay methods: A coarse adjustment in steps of ≈1.5 ns is generated with the help of three BNC cables, that have runtimes of ≈1.5 ns, ≈3 ns and ≈6 ns. The cables are combined in a binary manner using six RF coaxial relays (RLC Electronics SR-2 min-H), which are addressed via a 3 bit signal from the computer. Fine tuning in the range between these 1.5 ns steps is accomplished by a voltage controlled phase shifter (Mini-Circuits JSPHS-150) that is controlled via an analog signal (0 - 10 V) from the computer (analog output of the KPCI-1801HC board, *Keithley*, which we also use for data acquisition). The phase shifting unit is calibrated by monitoring the rising edge of two fast photo diodes (Thorlabs DET210) with a 1GHz digital oscilloscope (LeCroy LC564A). The calibration for short delays can be checked with the help of an optical delay line. Calibration was found to be stable during normal operation of the setup, however, when changing cables in the rf part of the electronics, the calibration has to be redone. The error at the positions where jumps occur (i.e. when relays switch) is < 50 ps. The electronic and optical runtimes of the total system are designed such that delay zero at the experiment occurs at the beginning of one of the 1.5 ns windows, so that the switching error occurs at a delay time of ≈+1.5 ns and amounts to a relative error of less than 3 %. The total runtime can be easily adjusted by using BNC cables of appropriate length for the photodiode signals.

The triggers for the Nd:YLF pump lasers and the Pockels cells of system 1 and 2 are derived from the slave oscillator. Despite phase shifting they therefore work fine for system 2. However, as the pulse train of the slave oscillator is shifted with respect to that of the master oscillator, the trigger driving the Pockels cells of amplifier 1 needs to be shifted accordingly in order to cleanly select one master oscillator pulse. This is done in an electronic delay generator ($k \times 1.5$ ns, $k = 0$ - 7, ’Phase Correction’ in Figure 7.4) which is addressed by the same 3 bit signal that also controls the RF coaxial relays in the phase shifter.

7.3.4 Application to Time Resolved IR Spectroscopy

In the following, we demonstrate the use of the setup in time resolved IR spectroscopy. The output of system 1 was frequency doubled to yield 400 nm pump pulses. IR-pulses were generated from the output of system 2 pumping a white light seeded two-stage β-barium-borate (BBO) optical parametric amplifier, the signal and idler pulses of which were difference frequency mixed in an $AgGaS_2$ crystal [165]. They were split into two parts to obtain broadband probe and reference pulses. The IR-probe pulses were focused into the sample in spatial overlap with the 400 nm pump pulse (the reference pulse was focused 1 mm apart). Probe and reference pulse were dispersed in a spectrograph and imaged onto a 2×32 pixel HgCdTe detector array which enabled us to measure low noise transient spectra with spectral resolution between 2 cm^{-1} and 6 cm^{-1} depending on the grating used. Both laser systems were located in different rooms on different optical tables about 20 m apart. The 400 nm pump pulse was guided through an evacuated tube in order to maintain the spatial mode quality. We experienced no problems with beam pointing.

---

the trigger it sends to the Pockels cell drivers of the Ti:S amplifier jitters enough to produce discrepancies between the oscillator pulses selected by the Pockels cell drivers of the two systems. Therefore, also the Pockels cell drivers have to be triggered externally and not as in the unmodified system by the Nd:YLF pump laser via the internal control-electronics.

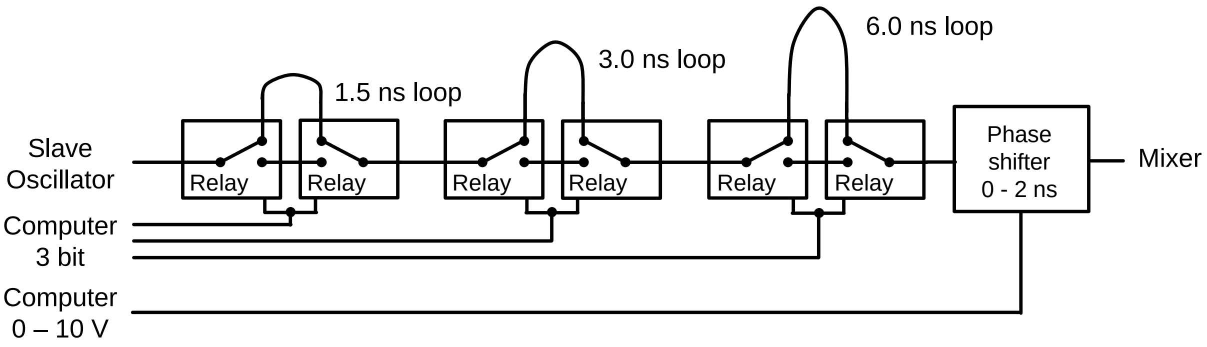

Figure 7.5: Phase-shifter, 0 - 12.5 ns.

We first measured the jitter of the synchronization. To that end, a germanium waver (200 μm) was excited by the 400 nm pulse (150 fs FWHM). Mid-IR pulses (130 fs FWHM) generated from the output of system 1 were used to probe the electrons in the conduction band. The generation of electrons in the conduction band is ultrafast ($<$ 100 fs) and the duration of the laser pulses is short. The rising edge of the signal therefore reflects the jitter of the pulses. The FWHM of the first derivative of the signal provides an upper limit for the jitter of 1.8 ps (see Figure 7.6). The position of time zero was found to be stable within 1 ps over several hours of operation. Synchronization of two oscillators with jitter as low as 20 fs over several hours has been demonstrated by David J. Jones *et. al* [358], locking on higher harmonics of the laser repetition rate. However, this precision is not necessary here, as we are interested in scanning from picoseconds to microseconds.

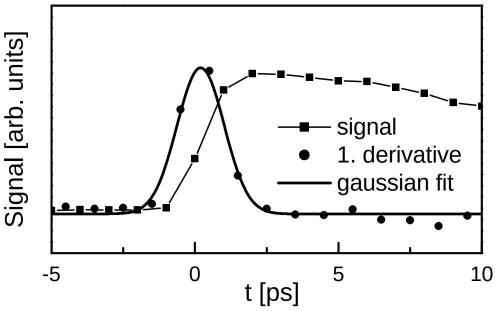

Figure 7.6: Rising edge of IR absorption in a germanium waver after photoexcitation. Its first derivative has a FWHM of 1.8 ps providing an upper limit for the jitter.

In a second step, we measured the effect of photoinduced metal-to-ligand charge transfer (MLCT) on the CO vibrations in [Re(CO)$_3$(dmbpy)Cl] (dmbpy = 4,4'-dimethyl-2,2'bipyridine) [299]. [Re(CO)$_3$(dmbpy)Cl] was prepared according to Ref. [338]. It was dissolved in dimethyl sulfoxide (DMSO) at a concentration of 4 mM. The sample was circulated rapidly through a closed cycle flow cell [182] with an optical path length of 100 μm. MLCT was initiated by short 400 nm pump pulses and the IR-probe pulses monitored the response of the C=O groups of the molecule

Figure 7.7 shows pump-probe difference spectra for delay times up to 400 ns . Negative contributions originate from the depleted electronic ground state, positive contributions arise from the created MLCT state. As can be seen in Figure 7.7, MLCT leads to a large blue shift of the C=O vibrations. At longer delays, the molecule relaxes back into the electronic ground state, and the C=O signal largely disappears. However, a small heat signal remains which stays constant even after complete electronic relaxation.

The data demonstrate the capability to scan continuously over a wide range of timescales. The synchronization jitter allows for a time resolution of $<$ 1.8 ps without any gaps in time up to 50 μs. An application of the system to a photoswitchable peptide undergoing a conformational transition from an unfolded to an α-helical state will be discussed in an upcoming publication [206].

Employing two complete Ti:S laser/amplifier systems for timeresolved IR spectroscopy may appear to be an exaggeration. However, we describe an easy to incorporate modification of equipment which already exists in many research groups engaged in femtosecond spectroscopy. The laser systems can be located in different rooms and on different optical tables. The modification is such that it does not affect the operation of

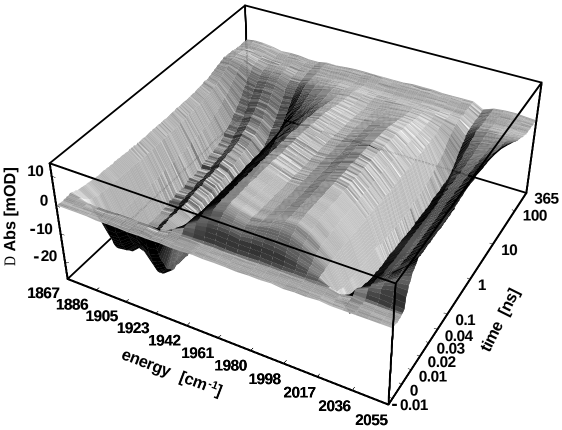

Figure 7.7: Time resolved IR difference spectra of the CO vibrations of [Re(CO)$_3$(dmbpy)Cl] following excitation at 400 nm.

any of the laser systems, when synchronization is not activated. The total price for the parts needed to modify two existing Ti:S femtosecond laser systems amounts less than \$4000. Hence, the modification is a simple and comparatively inexpensive add-on.

Acknowledgement: This work has been supported by the Swiss Science Foundation under Contract 2100-067573.02/1. The competent help of our electronic engineer Herman Schwarz is gratefully acknowledged.

7.4 P2: Versatile Small Volume Closed Cycle Flow Cell System for Transient Spectroscopy at High Repetition Rates

Jens Bredenbeck and Peter Hamm,
Rev. Sci. Instrum., 74:3188–3189, 2003.

7.4.1 Abstract

A closed cycle flow cell system was designed and built for application in ultrafast laser spectroscopy. The system features small cycle volume of down to less than 200 μl, adjustable beam path length and compatibility with a large variety of solvents. The construction principle is simple, reliable and versatile. The window thickness and material can be easily exchanged to meet different demands of femtosecond spectroscopy. The flow rate is sufficient to allow complete sample exchange for measurements with a kHz repetition rate.

7.4.2 Introduction

Ultrafast laser spectroscopy measurements often require high repetition rates of 1kHz or more to enable sufficient averaging. To measure e.g. the time dependence of reactions in the liquid phase that are triggered by a laser pulse, the sample in the measuring spot needs to be exchanged very effectively between subsequent laser pulses. In the case of a measuring spot of a width of $100\,\mu$m this corresponds to a motion of the sample of $> 0.1\,\mathrm{ms}^{-1}$. The need to measure very small absorption changes rules out other approaches like rotating sample cells or liquid jets because the introduced noise is too large. The closed cycle flow cell system presented here was developed particularly with regard to application in transient ultrafast UV pump IR probe spectroscopy[173] and transient 2D-IR spectroscopy[174] of photoisomerizable peptides. However, its features are interesting for a much broader range of spectroscopic applications.

We designed the cell to meet a number of requirements. A large variety of interesting molecules like biological samples or specially designed biomolecules is available only in very small amounts. Here, a *small* overall *volume* of the cycle and the possibility of *recovering the sample* after the measurement becomes crucial. A small volume of the cell and an economical solution for the delivery of the sample to the cell was needed. At the same time *high reliability* with respect to leakage is required, if working with rare or expensive samples. The system should be *compatible with a broad range of solvents*. Solvents like Dimethylsulfoxide (DMSO) and Dimethylformamide (DMF) are often used for peptide samples because of their high dielectric constant. They are very aggressive to the most synthetics commonly used as sealing materials, as glues or for tubings. The materials that come in contact with the sample therefore have to be inert.

7.4.3 Cell Design

The above requirements are met by the design of the cell as shown in Fig. 7.8. The crucial point is the tube-window-connection. Each PTFE (polytetrafluoroethylene) tube (C31140, *Novodirect GmbH, Germany*) is spread to a funnel at its end. A direct contact of PTFE and window would not provide a reliable seal as the PTFE is not resilient enough. We used an o-ring consisting of Chemraz® perfluoroelastomer (obtained from *Greene, Tweed & Co. GmbH, Germany*) as a seal. Just by tightening the screws of the housing, the small o-ring is compressed between the PTFE tube funnel and the window material and seals reliably. No additional parts that would lead to additional weak spots are needed in order to attach the tubing. No connection pieces with additional dead volume are used. The sample only comes in contact with the window material, PTFE and the Chemraz® o-ring. The system therefore is compatible with all common solvents.

As window material we used 2 mm thick CaF_2, that is suitable for a broad range of wavelengths between 200 nm and $9\,\mu$m. Other materials and thicknesses can be chosen depending on the transparency and dispersion properties needed. The spacer sitting between the windows was made of PTFE film whose thickness can be varied to yield different path length. The design of the sample channel in the cell can be easily changed by using specially cut spacers to meet the requirements for different experiments. In this way it is possible to include reservoirs between the sample cell windows as shown in the example in Fig. 7.8. This allows for cw irradiation to prepare a photoactive sample in a certain state or for monitoring the sample quality by additional spectroscopic techniques. The total volume of the cell is determined by the volume between the windows, the volume of the two holes in the window and the volume of the clearances of the o-rings. It amounts to $\approx 5\,\mu$l.

7.4.4 Tubing and Pump

Most measurement schemes require a *steady unidirectional flow* of the sample. We therefore employed the flow cell in combination with a peristaltic pump (ISM444, *Ismatec SA, Switzerland*) driving a pump head featuring 6 rollers (Masterflex® HV-77390-00 for PTFE Tubing, *Cole-Parmer, Illinois, USA*). To preserve compatibility with aggressive solvents like DMSO, we used PTFE for all tubing. A limiting point in the whole closed cycle is the tubing in the pump head of the peristaltic pump. The flow rate is determined by the rotational speed of the pump and the inner diameter of the tubing on which the rollers of the pump head are running. Because of its low resilience PTFE is not very suitable for use as pump head tubing material. Low rotational speed and therefore high inner diameter has to be used, leading to an increased dead volume of the closed cycle. We used the C88006 tubing with rectangular cross section from *Novodirect GmbH, Germany* designed for the Masterflex® HV-77390-00 pump head. This tubing

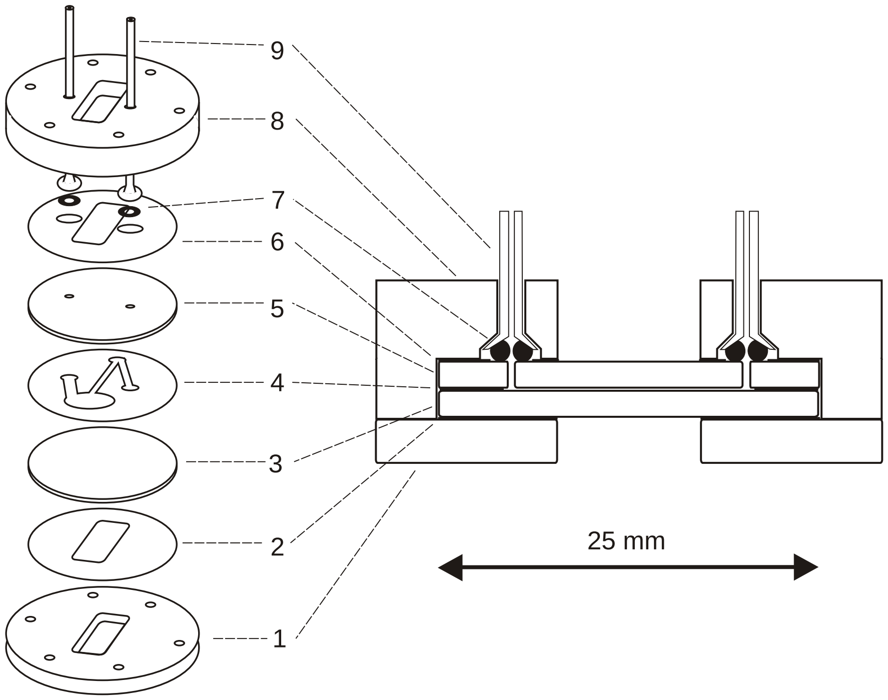

Figure 7.8: Expanded view and cross section of the flow cell. 1: brass baseplate – 2: PTFE cover – 3: CaF_2 window – 4: PTFE spacer featuring reservoir and measurement channel – 5: drilled CaF_2 window – 6: PTFE cover with clearance for o-rings – 7: Chemraz® o-rings – 8: brass housing – 9: PTFE tubes.

has an inner volume of 500 μl if cut as short as possible to still fit into the pump head. For the rest of the cycle we used PTFE tubing with 0.5 mm inner diameter. As connection pieces we used 'cap-type' connectors with PTFE cone fittings (*Omnifit Limited, United Kingdom*), having essentially no dead volume. With this combination we were able to work with sample volumes $< 800\,\mu$l, still having sufficiently high flow rates of up to $2\,\mathrm{ms}^{-1}$ depending on the spacer geometry and the viscosity of the solvent. The flow rate was checked in a pump probe measurement using a test molecule that was photobleached by a laser pulse. Subsequent pulses monitored the transport of the bleached molecule away from the measuring spot.

Other pump head tubing materials like Viton® or Tygon® do not have the same broad solvent compatibility as PTFE but allow for higher rotational speeds and therefore smaller inner diameter. Employing a Masterflex® HV-77201-60 pump head (*Cole-Parmer, Illinois, USA*), Viton® tubing with 0.8 mm inner diameter for the pump head and regular PTFE tubing with 0.3 mm inner diameter for the rest of the cycle, sample volumes of $< 200\,\mu$l where possible.

The flow cell has a high flow resistance compared to the rest of the cyclus. It should be placed behind the peristaltic pump to avoid low pressure leading to bubble formation. We included a solvent reservoir in the cycle, where bubbles can escape from the tubes. A very practical reservoir is an autosampler vial for microsampling as shown in Fig. 7.9. The vials can be used with screw caps featuring PTFE septa. The vial are easily connected to the cycle by pushing the tubing through the septum. After the measurement the sample can be pumped back into the vial and the tubing is removed. This way, the sample can be stored in the vial before and after measurment without ever getting into contact with air.

7.4.5 Other Applications

With a syringe pump the volume limitations of the peristaltic pumps could be overcome at the expense of unsteady flow. One then could approach cycle volumes of 20 μl. The flow cell also proved valuable when no rapid exchange of the sample was desired. Using the flow cell not with a pump in a closed cycle but in com-

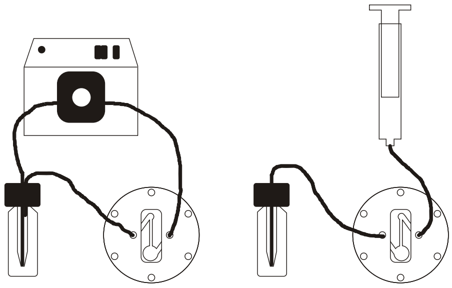

Figure 7.9: Using the flow cell in combination with a pump or with a syringe for spectroscopic measurements with micro amounts of sample.

bination with a syringe (Fig. 7.9), the safe handling and recovering of samples with as little volume as 10 μl for spectroscopic measurements in a laser setup or a regular cw spectrometer is possible.

7.5 Thermoregulation of the Flow Cell

To control the sample temperature, the flow cell is mounted in a thermostated brass holder (Figure 7.10, Position 1). The thin teflon tubings containing the sample (Figure 7.10, Position 2) are guided within the larger diameter tubings of the coolant circuit, where they are surrounded by the coolant (Figure 7.10, Position 3). The reservoir vial (Figure 7.9) is kept in an insulated holder. The coolant temperature is controlled by a minichiller (*ministat*, -25° C to 120° C, Huber Kältemaschinenbau GmbH). The temperature is checked directly in the sample vial as well as in the metal housing of the flow cell using a Fluke 51 thermometer with a suitable thin wire probe. Typically the temperature difference between those two measurement points is found to be smaller than 1° C.

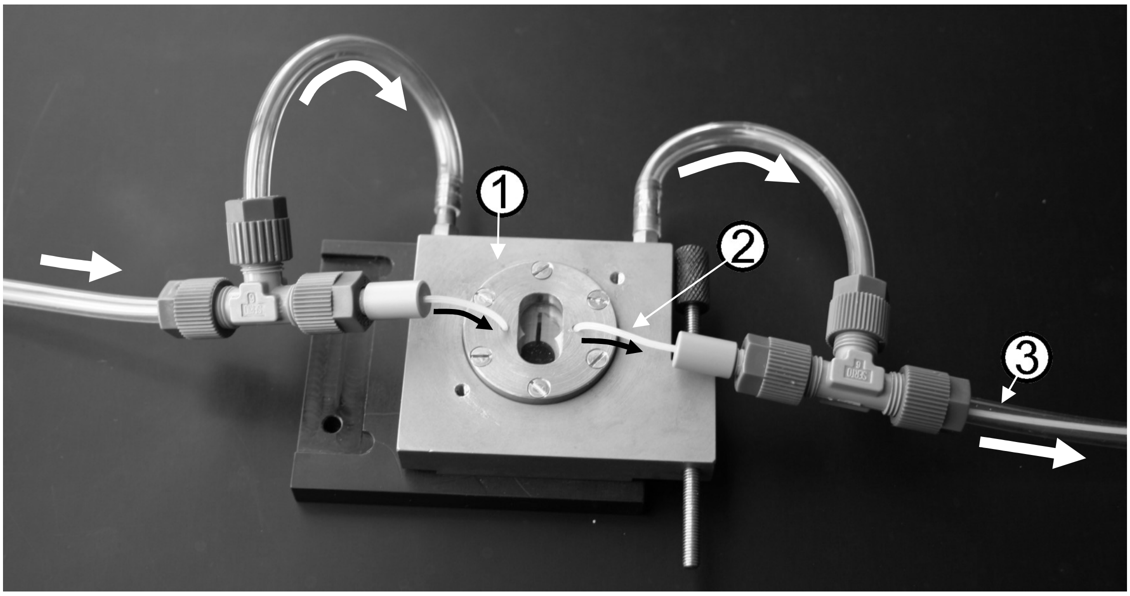

Figure 7.10: Flow cell with part of the coolant circuit. White arrows: coolant flow. Black arrows: sample flow. (1) Thermostated brass block. (2) Tubing containing the sample. (3) Sample tubing guided inside the coolant tubing.

References

[1] W. P. Aue, E. Bartholdi, and R. R. Ernst. Two dimensional spectroscopy. application to nuclear magnetic resonance. *J. Chem. Phys.*, 64(5):2229–2246, 1976.

[2] Peter Hamm, Manho Lim, and Robin M. Hochstrasser. Structure of the amide I band of peptides measured by femtosecond nonlinear-infrared spectroscopy. *J. Phys. Chem. B*, 102:6123–6138, 1998.

[3] Sander Woutersen and Peter Hamm. Structure determination of trialanine in water using polarization sensitive two-dimensional vibrational spectroscopy. *J. Phys. Chem.*, 104:11316–11320, 2000.

[4] Sander Woutersen and Peter Hamm. Isotope-edited two-dimensional vibrational spectroscopy of trialanine in aqueous solution. *J. Chem. Phys.*, 114(6):2727–2737, 2001.

[5] Emil Fischer. Einfluss der Configuration auf die Wirkung der Enzyme. *Ber. Dtsch. Chem. Ges.*, 27:29852993, 1894.

[6] Manfred Schliwa and Günther Woehlke. Molecular motors. *Nature*, 422:759–765, 2003.

[7] Ronald D. Vale and Ronald A. Milligan. The way things move: Looking under the hood of molecular motor proteins. *Science*, 288(5463):88–95, 2000.

[8] R. M. Daniel, R. V. Dunn, J. L. Finney, and J. C. Smith. The role of dynamics in enzyme activity. *Annu. Rev. Biophys. Biomol. Struct.*, 32:69–92, 2003.

[9] Dorothee Kern and Erik RP Zuiderweg. The role of dynamics in allosteric regulation. *Curr. Opin. Struc. Biol.*, 13:748–757, 2003.

[10] Herman J. C. Berendsen and Steven Hayward. Collective protein dynamics in relation to function. *Curr. Opin. Struc. Biol.*, 10:165–169, 2000.

[11] Kurt Wüthrich, editor. *NMR in structural biology*. World Scientific Publishing Company, Incorporated, 1995.

[12] N. Rama Krishna and Lawrence J. Berliner, editors. *Protein NMR for the Millenium (Biological Magnetic Resonance)*. Kluwer Academic Publishers, 2003.

[13] R. John Ellis and F. Ulrich Hartl. Principles of protein folding in the cellular environment. *Curr. Opin. Struc. Biol.*, 9:102–110, 1999.

[14] C. B. Anfinsen, E. Haber, M. Sela, and F. H. White. The kinetics of formation of native ribonuclease during oxidation of the reduced polypeptide chain. *Proc. Natl. Acad. Sci.*, 47(9):1309–1314, 1961.

[15] Christian. B. Anfinsen. Principles that govern the folding of protein chains. *Science*, 181(4096):223–230, 1973.

[16] Cyrus Levinthal. How to fold graciously. In J. T. P. DeBrunner and E. Munck, editors, *Mössbauer Spectroscopy in Biological Systems: Proceedings of a meeting held at Allerton House, Monticello, Illinois.*, volume 67, pages 22–24. Univ. of Illinois Bulletin, Urbana IL 61801, 1969.

[17] Cyrus Levinthal. Are there pathways in protein folding? *J. Chim. Phys.*, 65:44–45, 1968.

[18] Robert L. Baldwin. Matching speed and stability. *Nature*, 369:183–184, 1994.

[19] Andrej Šali, Eugene Shakhnovich, and Martin Karplus. How does a protein fold. *Nature*, 369:248–251, 1994.

[20] Ken A. Dill and Hue Sun Chan. From levinthal to pathways to funnels. *Nat. Struct. Biol.*, 4(1):10–18, 1997.

[21] Martin Karplus. The levinthal paradox: yesterday and today. *Fold. Des.*, 2(4):S69–S75, 1997.

[22] J. N. Onuchic, P. G. Wolynes, Z. Luthey-Schulten, and N. D. Socci. Toward an outline of the topography of a realistic protein folding funnel. *Proc. Natl. Acad. Sci.*, 92:3626–3630, 1995.

[23] J. N. Onuchic, Z. Luthey-Schulten, and P. G. Wolynes. Theory of protein folding: The energy landscape perspective. *Annu. Rev. Phys. Chem.*, 48:545–600, 1997.

[24] Hue Sun Chan and Ken A. Dill. Protein folding in the landscape perspective: Chevron plots and non-arrhenius kinetics. *Proteins*, 30:2–33, 1998.

[25] Joseph D. Bryngelson and Peter G. Wolynes. Spin glasses and the statistical mechanics of protein folding. *Proc. Natl. Acad. Sci.*, 84:7524–7528, 1987.

[26] Richard A. Goldstein, Zaida A. Luthey-Schulten, and Peter G. Wolynes. Optimal protein-folding codes from spin-glass theory. *Proc. Natl. Acad. Sci.*, 89:4918–4922, 1992.

[27] Ken A. Dill. Theory for the folding and stability of globular proteins. *Biochemistry*, 24:1501–1509, 1985.

[28] Carlos J. Camacho and D. Thirumalai. Kinetics and thermodynamics of folding in model proteins. *Proc. Natl. Acad. Sci.*, 90(13):6369–6372, 1993.

[29] Ken A. Dill. Polymer principles and protein folding. *Protein Sci.*, 8:1166–1180, 1999.

[30] Young Duan and Peter A. Kollman. Pathways to a protein folding intermediate observed in a 1-microsecond simulation in aqueous solution. *Science*, 282:740–744, 1998.

[31] S. Banu Ozkan, Ken A. Dill, and Ivet Bahar. Fast-folding protein kinetics, hidden intermediates and the sequential stabilization model. *Protein Sci.*, 11:1958–1970, 2002.

[32] José Nelson Onuchic and Peter G. Wolynes. Theory of protein folding. *Curr. Opin. Struc. Biol.*, 14:70–75, 2004.

[33] Michele Vendruscolo, Emanuele Paci, Christopher M. Dobson, and Martin Karplus. Three key residues form a critical contact network in a protein folding transition state. *Nature*, 409:641–645, 2001.

[34] M. Vendruscolo, N. V. Dokholyan, E. Paci, and M. Karplus. Small-world view of the amino acids that play a key role in protein folding. *Phys. Rev. E*, 65:061910, 2002.

[35] Jae-Hyun Cho, Satoshi Sato, and Daniel P. Raleigh. Thermodynamics and kinetics of non-native interactions in protein folding: A single point mutant significantly stabilizes the N-terminal domain of L9 by modulating non-native interactions in the denatured state. *J. Mol. Biol.*, 338:827–837, 2004.

[36] Martin Volk. Fast initiation of peptide and protein folding processes. *Eur. J. Org. Chem.*, 14:2605–2621, 2001.

[37] Neil Ferguson and Alan R. Fersht. Early events in protein folding. *Curr. Opin. Struc. Biol.*, 13:75–81, 2003.

[38] Heinrich Roder. Stepwise helix formation and chain compaction during protein folding. *Proc. Natl. Acad. Sci.*, 101(7):1793–1794, 2004.

[39] Igor K. Lednev, Anton S. Karnoup, Mark C. Sparrow, and Sanford A. Asher. Transient UV Raman spectroscopy finds no crossing barrier between the peptide α-helix and fully random coil conformation. *J. Am. Chem. Soc.*, 123:2388–2392, 2001.

[40] Efei Chen, Janet R. Kumita, G. Andrew Woolley, and David S. Kliger. The kinetics of helix unfolding of an azobenzene cross-linked peptide probed by nanosecond time-resolved optical rotary dispersion. *J. Am. Chem. Soc.*, 125:12443–12449, 2003.

[41] Ting Wang, Yongjin Zhu, Zelleka Getahun, Deguo Du, Cheng-Yen Huang, William F. DeGrado, and Feng Gai. Length dependent helix—coil transition kinetics of nine alanine-based peptides. *J. Phys. Chem. B*, 108:15301–15310, 2004.

[42] Sarah A. Petty and Martin Volk. Fast folding dynamics of an α-helical peptide with bulky side chains. *Phys. Chem. Chem. Phys.*, 6:1022–1030, 2004.

[43] R. M. Ballew, J. Sabelko, and M. Gruebele. Observation of distinct nanosecond and microsecond protein folding events. *Nat. Struct. Biol.*, 3:923–26, 1996. Fluorescence probe.

[44] Skip Williams, Timothy P. Causgrove, Rudolph Gilmanshin, Karen S. Fang, Robert H. Callender, William H. Woodruff, and R. Brian Dyer. Fast events in protein folding: Helix melting and formation in a small peptide. *Biochemistry*, 35:691–697, 1996.

[45] Rudolf Gilmanshin, Skip Williams, Robert H. Callender, William H. Woodruff, and R. Brian Dyers. Fast events in protein folding: Relaxation dynamics of secondary and tertiary structure in native apomyoglobin. *Proc. Natl. Acad. Sci.*, 94:3709–3713, 1997.

[46] Victor Muñoz, Peggy A. Thompson, James Hofrichter, and William A. Eaton. Folding dynamics and mechanism of β-hairpin formation. *Nature*, 390:196–199, 1997.

[47] Peggy A. Thompson, Victor Muñoz, Gouri S. Jas, Eric R. Henry, William A. Eaton, and James Hofrichter. The helix-coil kinetics of a heteropeptide. *J. Phys. Chem. B*, 104:378–389, 2000.

[48] James H. Werner, R. Brian Dyer, R. Matthew Fesinmeyer, and Niels H. Andersen. Dynamics of the primary processes of protein folding: Helix nucleation. *J. Phys. Chem. B*, 106:487–494, 2002.

[49] Cheng-Yen Huang, Zelleka Getahun, Yongjin Zhu, Jason W. Klemke, William F. DeGrado, and Feng Gai. Helix formation via conformation diffusion search. *Proc. Natl. Acad. Sci.*, 99(5):2788–2793, 2002.

[50] Xavier Daura, Bernhard Jaun, Dieter Seebach, Wilfred F. van Gunsteren, and Alan E. Mark. Reversible peptide folding in solution by molecular dynamics simulation. *J. Mol. Biol.*, 280:925–932, 1998.

[51] Yaoqi Zhou and Martin Karplus. Interpreting the folding kinetics of helical proteins. *Nature*, 401:400–402, 1999.

[52] Gouri S. Jas, William A. Eaton, and James Hofrichter. Effect of viscosity on the kinetics of α-helix and β-hairpin formation. *J. Phys. Chem. B*, 105:261–272, 2001.

[53] Yao Xu, Rolando Oyola, and Feng Gai. Infrared study of the stability and folding kinetics of a 15-residue β-hairpin. *J. Am. Chem. Soc.*, 125:15388–15394, 2003.

[54] R. Brian Dyer, Shelia J. Maness, Eric S. Peterson, Stefan Franzen, R. Matthew Fesinmeyer, and Niels H. Andersen. The mechanism of β-hairpin formation. *Biochemistry*, 43:11560–11566, 2004.

[55] Bengt Nölting and Karl Andert. Mechanism of protein folding. *Proteins*, 41:288–298, 2000.

[56] Yongjin Zhu, Darwin O. V. Alonso, Kosuke Maki, Cheng-Yen Huang, Steven J. Lahr, Valerie Daggett, Heinrich Roder, William F. DeGrado, and Feng Gai. Ultrafast folding of α_3D: A *de novo* designed three-helix bundle protein. *Proc. Natl. Acad. Sci.*, 100(26):15486–15491, 2003.

[57] Wei Yuan Yang and Martin Gruebele. Folding λ-repressor at its speed limit. *Biophys. J.*, 87:596–608, 2004.

[58] Ting Wang, Yongjin Zhu, and Feng Gai. Folding of a three-helix bundle at the folding speed limit. *J. Phys. Chem. B*, page in press, 2004.

[59] Dung M. Vu, Jeffrey K. Myers, Terrence G. Oas, and R. Brian Dyer. Probing the folding and unfolding dynamics of secondary and tertiary structures in a three-helix bundle protein. *Biochemistry*, 43:3582–3589, 2004.

[60] Jan Kubelka, James Hofrichter, and William A. Eaton. The protein folding 'speed limit. *Curr. Opin. Struc. Biol.*, 14:76–88, 2004.

[61] Sergei V. Krivov and Martin Karplus. Hidden complexity of free energy surfaces for peptide (protein) folding. *Proc. Natl. Acad. Sci.*, 101(41):14766–14770, 2004.

[62] S. Gnanakaran, Hugh Nymeyer, John Portman, Kevin Y. Sanbonmatsu, and Angel E. Garcia. Peptide folding simulations. *Curr. Opin. Struc. Biol.*, 13:168–174, 2003.

[63] Xavier Daura, Karl Gademann, Bernhard Jaun, Dieter Seebach, Wilfred F. van Gunsteren, and Alan E. Mark. Peptide folding: When simulation meets experiment. *Angew. Chem. Int. Ed.*, 38(1/2):236–240, 1999.

[64] O. Bieri, J. Wirz, B. Hellrung, M. Schutkowski, M. Drewello, and T. Kiefhaber. The speed limit for protein folding mesured by triplet-triplet energy transfer. *Proc. Natl. Acad. Sci. USA*, 96:9597–9601, 1999.

[65] Igor K. Lednev, Anton S. Karnoup, Mark C. Sparrow, and Sanford A. Asher. α-helix peptide folding and unfolding activation barriers: A nanosecond UV resonance Raman study. *J. Am. Chem. Soc.*, 121:8074–8086, 1999.

[66] Cheng-Yen Huang, Hu She, William F. DeGrado, Dewey G. McCafferty, and Feng Gai. Light-induced helix formation. *J. Am. Chem. Soc.*, 124:12674–12675, 2002.

[67] Cheng-Yen Huang, Zelleka Getahun, Ting Wang, William F. DeGrado, and Feng Gai. Time-resolved infrared study of the helix-coil transition using ^{13}C-labeled helical peptides. *J. Am. Chem. Soc.*, 123:12111–12112, 2001.

[68] Cheng-Yen Huang, Jason W. Klemke, Zelleka Getahun, William F. DeGrado, and Feng Gai. Temperature-dependent helix-coil transition of an alanine based peptide. *J. Am. Chem. Soc.*, 123:9235–9238, 2001.

[69] Lisa J. Lapidus, William A. Eaton, and James Hofrichter. Measuring dynamic flexibility of the coil state of a helix-forming peptide. *J. Mol. Biol.*, 319:19–25, 2002.

[70] Themis Lazaridis and Martin Karplus. 'new view' of protein folding reconciled with the old throug multiple unfolding simulations. *Science*, 278:1928–1930, 1997.

[71] Gerhard Hummer, Angel E. Garcia, and Shekhar Garde. Conformational diffusion and helix formation kinetics. *Phys. Rev. Lett.*, 85(12):2637–2640, 2000.

[72] Gerhard Hummer, Angel E. Garcia, and Shekhar Garde. Helix nucleation kinetics from molecular simulations in explicit solvent. *Proteins*, 42:77–84, 2001.

[73] Xavier Daura, Wilfred F. van Gunsteren, and Alan E. Mark. Folding-unfolding thermodynamics of a β-heptapeptide from equilibrium simulations. *Proteins*, 24:269–280, 1999.

[74] Sander Woutersen, Yuguang Mu, Gerhard Stock, and Peter Hamm. Subpicosecond conformational dynamics of small peptides probed by two-dimensional vibrational spectroscopy. *Proc. Natl. Acad. Sci.*, 98:11254–11258, 2001.

[75] Blake Gillespie and Kevin W. Plaxco. Nonglassy kinetics in the folding of a simple single domain protein. *Proc. Natl. Acad. Sci.*, 97:12014–12019, 2000.

[76] Peggy A. Thompson, William A. Eaton, and James Hofrichter. Laser temperature jump study of the helix $\rightleftharpoons$ coil kinetics of an alanine peptide interpreted with a 'kinetic zipper' model. *Biochemistry*, 36:9200–9210, 1997.

[77] Christopher D. Snow, Linlin Qiu, Deguo Du, Feng Gai, Stephen J. Hagen, and Vijay S. Pande. Trp zipper folding kinetics by molecular dynamics and temperature-jump spectroscopy. *Proc. Natl. Acad. Sci.*, 101(11):4077–4082, 2004.

[78] Martin Karplus. Aspects of protein reaction dynamics: Deviations from simple behaviour. *J. Phys. Chem. B*, 104:11–27, 2000.

[79] P. Hänggi, P. Talkner, and M. Borkovec. Reaktion-rate theory: fifty years after kramers. *Rev. Mod. Phys.*, 62(2):251, 1990.

[80] Alan R. Fersht and Satoshi Sato. Φ-Value analysis and the nature of protein-folding transition states. *Proc. Natl. Acad. Sci.*, 101(21):7976–7981, 2004.

[81] Stephen J. Hagen. Exponential decay kinetics in “downhill” protein folding. *Proteins*, 50:1–4, 2003.

[82] Robert Zwanzig. Diffusion in a rough potential. *Proc. Natl. Acad. Sci.*, 85(7):2029–2030, 1988.

[83] Joseph D. Bryngelson and Peter G. Wolynes. Intermediates and barrier crossing in a random energy model (with applications to protein folding). *J. Phys. Chem.*, 93:6902–6915, 1989.

[84] Dominique J. Bicout and Attila Szabo. Entropic barriers, transition states, funnels, and exponential protein folding kinetics: A simple model. *Protein Sci.*, 9:452–465, 2000.

[85] Robert Zwanzig. Two-state models of protein folding kinetics. *Proc. Natl. Acad. Sci.*, 94:148–150, 1997.

[86] Jack Schonbrun and Ken A. Dill. Fast protein folding kinetics. *Proc. Natl. Acad. Sci.*, 100:12678–12682, 1003.

[87] J. A. Schellman. Factors affecting the stability of hydrogen-bonded polypeptide structure in solution. *J. Phys. Chem.*, 62:1485, 1958.

[88] B. H. Zimm and J. K. Bragg. Theory of the phase transition between helix and random coil in polypeptide chains. *J. Chem. Phys.*, 31(2):526–535, 1959.

[89] Shneior Lifson and A. Roig. On the theory of helix-coil transition in polypeptides. *J. Chem. Phys.*, 34:1963–1974, 1961.

[90] Douglas Poland and Harold A. Scheraga. *Theory of Helix-Coil Transitions in Biopolymers*. Molecular Biology. Academic Press, New York and London, 1970.

[91] Victor Muñoz, Eric R. Henry, James Hofrichter, and William A. Eaton. A statistical mechanical model for β-hairpin kinetics. *Proc. Natl. Acad. Sci.*, 95:5872–5879, 1998.

[92] Wei Yuan Yang, Ryan B. Prince, Jobiah Sabelko, Jeffrey S. Moore, and Martin Gruebele. Transition from exponential to nonexponential kinetics during formation of a nonbiological helix. *J. Am. Chem. Soc.*, 122:3248–3249, 2000.

[93] Urmi R. Doshi and Victor Muñoz. Kinetics of α-helix formation as diffusion on a one-dimensional free energy surface. *Chem. Phys.*, 307:129–136, 2004.

[94] Urmi R. Doshi and Victor Muñoz. The principles of α-helix formation: Explaining complex kinetics with nucleation-elongation theory. *J. Phys. Chem. B*, 108:8497–8506, 2004.

[95] Ralf Metzler, Joseph Klafter, and Joshua Jortner. Hierarchies and logarithmic oscillations in the temporal relaxation patterns of proteins and other complex systems. *Proc. Natl. Acad. Sci.*, 96:11085–11089, 1999.

[96] Oren M. Becker and Martin Karplus. The topology of multidimensional potential energy surfaces: Theory and application to peptide structure and kinetics. *J. Chem. Phys.*, 106(4):1495–1517, 1997.

[97] Sergei V. Krivov and Martin Karplus. Free energy disconnectivity graphs: Application to peptide models. *J. Chem. Phys.*, 117(23):10894–10903, 2002.

[98] Aaron R. Dinner, Themis Lazaridis, and Martin Karplus. Understanding β-hairpin formation. *Proc. Natl. Acad. Sci.*, 96:9068–9073, 1999.

[99] M. Gulotta, R Gilmanshin, T. C. Buscher, R. H. Callender, and R. B. Dyer. Core formation in apomyoglobin: probing the upper reaches of the folding energy landscape. *Biochemistry*, 40:5137–5143, 2001.

[100] Jay R. Winkler. Cytochrome c folding dynamics. *Curr. Opin. Struc. Biol.*, 8:169–174, 2004.

[101] Wei Yuan Yang, Jed W. Pitera, William C. Swope, and Martin Gruebele. Heterogeneous folding of the trpzip hairpin: Full atom simulation and experiment. *J. Mol. Biol.*, 336:241–251, 2004.

[102] Martin Gruebele. Protein folding: the free energy surface. *Curr. Opin. Struc. Biol.*, 12:161–168, 2002.

[103] Christopher M. Dobson and Martin Karplus. The fundamentals of protein folding: bringing together theory and experiment. *Curr. Opin. Struc. Biol.*, 9:92–101, 1999.

[104] Martin Volk, Yuriy Kholodenko, Helen S. M. Lu, Edward A. Gooding, William F. DeGrado, and Robin M. Hochstrasser. Peptide conformational dynamics and vibrational stark effects following photoinitiated disulfide cleavage. *J. Phys. Chem. B*, 101:8607–8616, 1997.

[105] Daniel G. Flint, Janet R. Kumita, Oliver S. Smart, and G. Andrew Woolley. Using an azobenzene cross-linker to either increase or decrease peptide helix content upon *Trans*-to-*Cis* photoisomerization. *Chem. Biol.*, 9:391–397, 2002.

[106] Martin Gruebele. The fast protein folding problem. *Annu. Rev. Phys. Chem.*, 50:485–516, 1999.

[107] Heinrich Roder and MC Ramachandra Shastry. Methods for exploring early events in protein folding. *Curr. Opin. Struc. Biol.*, 9:620–626, 1999.

[108] H. Roder, G. A. Elöve, and S. W. Englander. Structural characterization of folding intermediates in cytochrome C by H-exchange labeling and proton NMR. *Nature*, 335:700–704, 1988.

[109] Mallela M.G. Krishna, Linh Hoang, Yan Lin, and S. Walter Englander. Hydrogen exchange methods to study protein folding. *Methods*, 34:51–64, 2004.

[110] Lars Konermann and Douglas A. Simmons. Protein-folding kinetics and mechanisms studied by pulse-labeling and mass spectrometry. *Mass Spectrom. Rev.*, 22(1):1–26, 2003.

[111] Markus Zeeb and Jochen Balbach. Protein folding studied by real-time NMR spectroscopy. *Methods*, 34:65–74, 2004.

[112] Ken Hun Mok and Peter J. Hore. Photo-CIDNP NMR methods for studying protein folding. *Methods*, 34:75–87, 2004.

[113] Robert A. Goldbeck, Yiren G. Thomas, Eefei Chen, Raymond M. Esquerra, and David S. Kliger. Multiple pathways on a protein-folding energy landscape: Kinetic evidence. *Proc. Natl. Acad. Sci.*, 96:2782–2787, 1999.

[114] Shuji Akiyama, Satoshi Takahashi, Tetsunari Kimura, Koichiro Ishimori, Isao Morishima, Yukihiro Nishikawa, and Tetsuro Fujisawa. Conformational landscape of cytochrome C folding studied by microsecond-resolved small-angle X-ray scattering. *Proc. Natl. Acad. Sci.*, 99(3):13291334, 2002.

[115] Rita P.-Y. Chen, Joseph J. T. Huang, Hsin-Liang Chen, Howard Jan, Marappan Velusamy, Chung-Tien Lee, Wunshain Fann, Randy W. Larsen, and Sunney I. Chan. Measuring the refolding of beta-sheets with different turn sequences on a nanosecond time scale. *Proc. Natl. Acad. Sci.*, 101(19):7305–7310, 2004.

[116] K. Teilum, K. Maki, B. B. Kragelund, F. M. Poulsen, and H. Roder. Early kinetic intermediate in the folding of acyl-CoA binding protein detected by fluorescence labeling and ultrarapid mixing. *Proc. Natl. Acad. Sci.*, 99(15):9807–9812, 2002.

[117] Maik Jacob, Georg Holtermann, Dieter Perl, Jochen Reinstein, Thomas Schindler, Michael A. Geeves, and Franz X. Schmid. Microsecond folding of the cold shock protein measured by a pressure-jump technique. *Biochemistry*, 38:2882–2891, 1999.

[118] Stefania Abbruzzetti, Elisa Crema, Laura Masino, Arnaldo Vecli, Cristiano Viappiani, Jeanne R. Small, Louis J. Libertini, and Enoch W. Small. Fast events in protein folding: Structural volume changes accompanying the early events in the N→I transition of apomyoglobin induced by ultrafast pH jump. *Biophys. J.*, 78:405–415, 2000.

[119] J. Sabelko, J. Ervin, and M.Gruebele. Observations of strange kinetics in protein folding. *Proc. Natl. Acad. Sci.*, 96:6031–6036, 1999.

[120] C. M. Phillips, Y. Mizutani, and R. M. Hochstrasser. Ultrafast thermally induced unfolding of RNAse A. *Proc. Natl. Acad. Sci.*, 92:7292–7296, 1995.

[121] H. S. M. Lu, M. Volk, Y. Kholodenko, E. Gooding, R. M. Hochstrasser, and W. F. DeGrado. Aminothiotyrosine disulfide, an optical trigger for initiation of protein folding. *J. Am. Chem. Soc.*, 119:7173–7180, 1997.

[122] T. Nägele, R. Hoche, W. Zinth, and J. Wachtveitl. Femtosecond photoisomerization of *cis*-azobenzene. *Chem. Phys. Lett.*, 252:489–495, 1997.

[123] Thomas Schultz, Jason Quenneville, Benjamin Levine, Alessandro Toniolo, Todd J. Martínez, Stefan Lochbrunner, Michael Schmitt, James P. Shaffer, Marek Z. Zgierski, and Albert Stolow. Mechanism and dynamics of azobenzene photoisomerization. *J. Am. Chem. Soc.*, 125:8098–8099, 2003.

[124] Christian Renner, Raymond Behrendt, Sebastian Sprlein, Josef Wachtveitl, and Luis Moroder. Photomodulation of conformational states. I. mono- and bicyclic peptides with (4-amino)phenylazobenzoic acid as backbone constituent. *Biopolymers*, 54:489–500, 2000.

[125] Christian Renner, Jörg Cramer, Raymond Behrendt, and Luis Moroder. Photomodulation of conformational states. II. mono- and bicyclic peptides with (4-aminomethyl)phenylazobenzoic acid as backbone constituent. *Biopolymers*, 54:501–514, 2000.

[126] Markus Schütt, Simone S. Krupka, Alexander G. Milbradt, Sebastian Deindl, Eva-Kathrin Sinner, Dieter Oesterhelt, Christian Renner, and Luis Moroder. Photocontrol of cell adhesion processes: Model studies with cyclic azobenzene-RGD peptides. *Chem. Biol.*, 10:487–490, 2003.

[127] L. Ulysse, J. Cubillos, and J. Chmielewski. Photoregulation of cyclic peptide conformation. *J. Am. Chem. Soc.*, 117:8466–8467, 1995.

[128] Janet R. Kumita, Oliver S. Smart, and G. Andrew Woolley. Photo-control of helix content in a short peptide. *Proc. Natl. Acad. Sci.*, 97(8):3803–3808, 2000.

[129] Janet R. Kumita, Daniel G. Flint, Oliver S. Smart, and G. Andrew Woolley. Photo-control of peptide helix content by an azobenzene cross-linker: steric interactions with underlying residues are not critical. *Protein Eng.*, 15(7):561–569, 2002.

[130] Darcy C. Burns, Daniel G. Flint, Janet R. Kumita, Howard J. Feldman, Luis Serrano, Zhihua Zhang, Oliver S. Smart, and G. Andrew Woolley. Origins of conformational switching in a light-sensitive peptide. *Biochemistry*, 43:15329–15338, 2004.

[131] Sunho Song, Sanford A. Asher, Samuel Krimm, and Keith D. Shaw. Ultraviolet resonance Raman studies of trans and cis peptides: Photochemical consequences of the twisted π^* excited state. *J. Am. Chem. Soc.*, 113:1155–1163, 1991.

[132] Julia H. Miwa, Avani K. Patel, Nita Vivatrat, Sarah M. Popek, and Ann M. Meyer. Compatibility of the thioamide functional group with β-sheet secondary structure: Incorporation of a thioamide linkage into a β-hairpin peptide. *Org. Lett.*, 3(21):3373–3375, 2001.

[133] Julia H. Miwa, Letha Pallivathucal, Shyla Gowda, and Katherine E. Lee. Conformational stability of helical peptides containing a thioamide linkage. *Org. Lett.*, 4(26):4655–4657, 2002.

[134] Thierry Sifferlen, Magnus Rueping, Karl Gademann, Bernhard Jaun, and Dieter Seebach. β-thiopeptides: Synthesis, NMR solution structure, CD spectra, and photochemistry. *Helv. Chim. Acta*, 82:2067–2093, 1999.

[135] Robert Frank, Mario Jakob, Frank Thunecke, Gunter Fischer, and Mike Schutkowski. Thioxylation as one-atom-substitution generates a photoswitchable element within the peptide backbone. *Angew. Chem. Int. Ed.*, 39(6):1120–1122, 2000.

[136] G. B. B. M. Sutherland. Infrared analysis of the structure of amino acids: Polypeptides and proteins. *Adv. Protein Chem.*, 5:291318, 1932.

[137] Jose Luis R. Arrondo, Arturo Muga, Jose Castresana, and Felix M. Goñi. Quantitative studies of the structure of proteins in solution by fourier-transform infrared spectroscopy. *Prog. Biophys. Mol. Bio.*, 59:23–56, 1993.

[138] Andreas Barth and Christian Zscherp. What vibrations tell us about proteins. *Q. Rev. Biophys.*, 35(4):369–430, 2002.

[139] Samuel Krimm and Jagdeesh Bandekar. Vibrational spectroscopy of peptides and proteines. *Adv. Protein Chem.*, 38:181, 1986.

[140] Hajime Torii and Mitsuo Tasumi. Model calculations on the amide-I infrared bands of globular proteins. *J. Chem. Phys.*, 96(5):3379–3387, 1992.

[141] Reto Koradi, Martin Billeter, and Kurt Wüthrich. MOLMOL: a program for display and analysis of macromolecular structures. *J. Mol. Graphics*, 14:51–55, 1996.

[142] J. K. Kaupinnen, D. J. Moffat, H. H. Mantsh, and D. G. Cameron. Fourier self-deconvolution: a method for resolving intrinsically overlapped bands. *Appl. Spectrosc.*, 35:271–276, 1981.

[143] Andreas Barth. Fine-structure enhancement - assesment of a simple method to resolve overlapping bands in spectra. *Spectrochim. Acta (A)*, 56:1223–1232, 2000.

[144] Witold. K. Surewicz, Henry. H. Mantsch, and Dennis Chapman. Determination of protein secondary structure by Fourier transform infrared spectroscopy. *Biochemistry*, 32:389–394, 1993.

[145] M. Jackson and H. H. Mantsch. The use and misuse of FTIR spectroscopy in the determination of protein structure. *Crit. Rev. Biochem. Mol.*, 30(2):95–120, 1995.

[146] T. E. Creighton. *Proteins*. W. H. Freeman and Company, New York, 1993.

[147] Tatsuo Miyazawa. Perturbation treatment of the characteristic vibrations of polypeptide chains in various configurations. *J. Chem. Phys.*, 32(6):1647–1652, 1960.

[148] Samuel Krimm and Yasuaki Abe. Intermolecular interaction effects in the amide I vibrations of β polypeptides. *Proc. Natl. Acad. Sci.*, 69(10):2788–2792, 1972.

[149] W. H. Moore and Samuel Krimm. Transition dipole coupling in amide I modes of β polypeptides. *Proc. Natl. Acad. Sci.*, 72(12):4933–4935, 1975.

[150] Hajime Torii and Mitsuo Tasumi. *Ab Initio* molecular orbital study of the amide I vibrational interactions between the peptide groups in di- and tripeptides and considerations on the conformation of the extended helix. *J. Raman Spectrosc.*, 29:81–86, 1998.

[151] Peter Hamm, Manho Lim, William F. DeGrado, and Robin M. Hochstrasser. Pump/probe self heterodynes 2D spectroscopy of vibrational transitions of a small globular peptide. *J. Chem. Phys.*, 112(4):1907–1916, 2000.

[152] Jun-Ho Choi, Sihyun Ham, and Minhaeng Cho. Inter-peptide interaction and delocalization of amide I vibrational excitons in myoglobin and flavodoxin. *J. Chem. Phys.*, 117(14):6821–6832, 2002.

[153] Ralf Moritz, Heinz Fabian, Ulrich Hahn, Max Diem, and Dieter Naumann. Impact of four ^{13}C-proline isotope labels on the infrared spectra of ribonuclease T1. *J. Am. Chem. Soc.*, 124:6259–6264, 2002.

[154] Tim M. Watson and Jonathan D. Hirst. Calculating vibrational frequencies of amides: From formamide to concanavalin A. *Phys. Chem. Chem. Phys.*, 6:998–1005, 2004.

[155] Rong Huang, Jan Kubelka, Wendy Barber-Armstrong, R. A. G. D. Silva, Sean M. Decatur, and Timothy A. Keiderling. Nature of vibrational coupling in helical peptides: An isotopic labeling study. *J. Am. Chem. Soc.*, 126:2346–2354, 2004.

[156] Fatma Eker, Kai Griebenow, Xialin Cao, Laurence A. Nafie, and Reinhard Schweitzer-Stenner. Preferred peptide backbone conformations in the unfolded state revealed by the structure analysis of alanine-based (AXA) tripeptides in aqueous solution. *Proc. Natl. Acad. Sci.*, 101:10054–10059, 2004.

[157] Anna Cattani-Scholz, Christian Renner, Chiara Cabrele, Raymond Behrendt, Dieter Oesterhelt, and Luis Moroder. Photoresponsive cyclic bis(cysteinyl)peptides as catalysts of oxidative protein folding. *Angew. Chem. Int. Ed.*, 41(2):289–292, 2002.

[158] Daan Thorn Leeson, Feng Gai, Hector M. Rodriguez, Lydia M. Gregoret, and R. Brian Dyer. Protein folding and unfolding on a complex energy landscape. *Proc. Natl. Acad. Sci.*, 97(6):2527–2532, 2000.

[159] Robert H. Callender, R. Brian Dyer, Rudolf Gilmanshin, and William H. Woodruff. Fast events in protein folding: The time evolution of primary processes. *Annu. Rev. Phys. Chem.*, 49:173–202, 1998.

[160] William A. Eaton, Victor Muñoz, Stephen J. Hagen, Gouri S. Jas, Lisa J. Lapidus, Eric R. Henry, and James Hofrichter. Fast kinetics and mechanisms in protein folding. *Annu. Rev. Biophys. Biomol. Struct.*, 29:327–359, 2000.

[161] Raymond Behrendt, Christian Renner, Michaela Schenk, Fengqi Wang, Josef Wachtveitl, Dieter Oesterhelt, and Luis Moroder. Photomodulation of the conformation of cyclic peptides with azobenzene moieties in the peptide backbone. *Angew. Chem. Int. Ed.*, 38(18):2771–2774, 1999.

[162] Sebastian Spörlein, Heiko Carstens, Helmut Satzger, Christian Renner, Raymond Behrendt, Luis Moroder, Paul Tavan, Wolfgang Zinth, and Josef Wachtveitl. Ultrafast spectroscopy reveals subnanosecond peptide conformational dynamics and validates molecular dynamics simulation. *Proc. Natl. Acad. Sci.*, 99(12):7998–8002, 2002.

[163] J. Wachtveitl, S. Spörlein, B. Fonrobert, H. Satzger, C. Renner, R. Behrendt, L. Moroder, and W. Zinth. Photonitiated conformational dynamics in cyclic azobenzene peptides. in preparation.

[164] J. Wachtveitl, S. Spörlein, B. Fonrobert, C. Renner, R. Behrendt, L. Moroder, and W. Zinth. *Ultrafast Processes in Spectroscopy XII*. Leo S. Olschki, Firenze, in press.

[165] Peter Hamm, Robert A. Kaindl, and Jens Stenger. Noise suppression in femtosecond mid-infrared light sources. *Opt. Lett.*, 25(24):1798–1800, 2000.

[166] Peter Hamm and Sander Woutersen. Coupling of the amide I modes of the glycine dipeptide. *Bull. Chem. Soc. Jpn.*, 75:985–988, 2002.

[167] P. Hamm, S. M. Ohline, and W. Zinth. Vibrational cooling after ultrafast photoisomerization of azobenzene measured by femtosecond infrared spectroscopy. *J. Chem. Phys.*, 106(2):519–529, 1997.

[168] M. L. Horng, J. A. Gardecki, A. Papazyan, and M. Maroncelli. Subpicosecond measurements of polar solvation dynamics—coumarin-153 revisited. *J. Phys. Chem.*, 99:17311–17337, 1995.

[169] Hans Frauenfelder, Stephen G. Sligar, and Peter G. Wolynes. The energy landscapes and motions of proteins. *Science*, 254:1598–1603, 1991.

[170] R. Metzler, J. Klafter, Joshua Jortner, and Martin Volk. Multiple time scales for dispersive kinetics in early events of peptide folding. *Chem. Phys. Lett.*, 293:477–484, 1998.

[171] William S. Young and Charles L. Brooks III. A microscopic view of helix propagation: N and C-terminal helix growth in alanine helices. *J. Mol. Biol.*, 259:560–572, 1996.

[172] Martin Karplus and David L. Weaver. Protein folding dynamics: The diffusion-collision model and experimental data. *Protein Sci.*, 3:650–668, 1993.

[173] Jens Bredenbeck, Jan Helbing, Arne Sieg, Tobias Schrader, Wolfgang Zinth, Christian Renner, Raymond Behrendt, Luis Moroder, Josef Wachtveitl, and Peter Hamm. Picosecond conformational transition and equilibration of a cyclic peptide. *Proc. Natl. Acad. Sci.*, 100:6452–6457, 2003.

[174] Jens Bredenbeck, Jan Helbing, Raymond Behrendt, Christian Renner, Luis Moroder, and Peter Hamm. Transient 2D-IR spectroscopy – snapshots of the non-equilibrium ensemble during the picosecond conformational transition of a cyclic peptide. *J. Phys. Chem. B*, 107:8654–8660, 2003.

[175] J. Wachtveitl, S. Spörlein, H. Satzger, B. Fonrobert, C. Renner, R. Behrendt, L. Moroder, and W. Zinth. Ultrafast conformational dynamics in cyclic azobenzene peptides of increased flexibility. *Biophys. J.*, 86:2350–2362, 2004.

[176] Jens Bredenbeck, Jan Helbing, and Peter Hamm. Continuous scanning from picoseconds to microseconds in time resolved linear and nonlinear spectroscopy. *Rev. Sci. Instrum.*, in press.

[177] Susan Marqusee and Robert L. Baldwin. Helix stabilization by Glu^{-}...Lys^{+} salt bridges in short peptides of *de novo* design. *Proc. Natl. Acad. Sci.*, 84:8898–8902, 1987.

[178] Susan Marqusee, Virginia H. Robbins, and Robert L. Baldwin. Unusually stable helix formation in short alanine-based peptides. *Proc. Natl. Acad. Sci.*, 86:5286–5290, 1989.

[179] Gene Merutka, William Shalongo, and Earle Stellwagen. A model peptide with enhanced helicity. *Biochemistry*, 30:4245–4248, 1991.

[180] Rajeev Aurora and George D. Rose. Helix capping. *Protein Sci.*, 7:21–28, 1998.

[181] Jun-Ho Choi, Sihyun Ham, and Minhaeng Cho. Local amide I mode frequencies and coupling constants in polypeptides. *J. Phys. Chem. B*, 107(34):9132–9138, 2003.

[182] Jens Bredenbeck and Peter Hamm. Versatile small volume closed cycle flow cell system for transient spectroscopy at high repetition rates. *Rev. Sci. Instrum.*, 74:3188–3189, 2003.

[183] Gary Martinez and Glenn Millhauser. FTIR spectroscopy fo alanine-based peptides: Assignment of the amide I’ modes for random coil and helix. *J. Struct. Biol.*, 114:23–27, 1995.

[184] Andreas Barth. The infrared absorption of amino acids side chains. *Prog. Biophys. Mol. Bio.*, 74:141–173, 2000.

[185] H. Satzger, C. Root, and M. Braun. Excited-state dynamics of *trans*- and *cis*-azobenzene after UV excitation in the $\pi\pi^*$ band. *J. Phys. Chem. A*, 108(30):6265–6271, 2004.

[186] H. Nymeyer, A. E. Garcia, and J. N. Onuchic. Folding funnels and frustration in off-lattice minimalist protein landscapes. *Proc. Natl. Acad. Sci.*, 95:5921–5928, 1998.

[187] Maksim Skorobogatiy, Hong Guo, and Martin Zuckermann. Non-arrhenius modes in the relaxation of model proteins. *J. Chem. Phys.*, 109:2528–2535, 1998.

[188] Yaoqi Zhou, Chi Zhang, George Stell, and Jin Wang. Temperature dependence of the distribution of the first passsage time: Results from discontinuous molecular dynamics simulations of an all-atom model of the second β-hairpin fragment of protein g. *J. Am. Chem. Soc.*, 125:6300–6305, 2003.

[189] Satoshi Saigo and Naoya Shibayama. Highly nonexponential kinetics in the early-phase refolding of proteins at low temperatures. *Biochemistry*, 42:9669–9676, 2003.

[190] Wei Yuan Yang and Martin Gruebele. Folding at the speed limit. *Nature*, 423:193–197, 2003.

[191] Ting Wang, Deguo Du, and Feng Gai. Helix–coil kinetics of two 14-residue peptides. *Chem. Phys. Lett.*, 370:842–848, 2003.

[192] She-Yi Sheu, Dah-Yen Yang, H. L. Selzle, and E. W. Schlag. Energetics of hydrogen bonds in peptides. *Proc. Natl. Acad. Sci.*, 100:12683–12687, 2003.

[193] Robert L. Baldwin. A new perspective on unfolded proteins. *Adv. Protein Chem.*, 62:361–367, 2002.

[194] Zhengshuang Shi, Robert W. Woody, and Neville R. Kallenbach. Is polyproline II a major backbone conformation in unfolded proteins? *Adv. Protein Chem.*, 62:163–240, 2002.

[195] David Shortle. The denatured state (the other half of the folding equation) and its role in protein stability. *FASEB J.*, 10:27–34, 1996.

[196] Xavier Daura, Alice Glättli, Peter Gee, Christine Peter, and Wilfred F. van Gunsteren. Unfolded state of peptides. *Adv. Protein Chem.*, 62:341–360, 2002.

[197] Wilfred F. van Gunsteren, Roland Bürgi, Christine Peter, and Xavier Daura. The key to solving the protein-folding problem lies in an accurate description of the denatured state. *Angew. Chem. Int. Ed.*, 40(2):351–355, 2001.

[198] Angel E. Garcia. Characterization of non-alpha helical conformations in ala peptides. *Proteins*, 45:669–676, 2004.

[199] Yuguang Mu, Phuong Nguyen, and Gerhard Stock. Energy landscape of a small peptide revealed by dihedral angle principle component analysis. *Proteins*, 58(1):45–52, 2005.

[200] Wei Zhang, Hongxing Lei, Shibasish Chowdhury, and Yong Duan. Fs-21 peptides can forma both single helix and helix-turn-helix. *J. Phys. Chem. B*, 108:7479–7489, 2004.

[201] Ruth Ann Bertsch, Nagarajan Vaidehi, Sunney I. Chan, and William A. Goddard III. Kinetic steps for α-helix formation. *Proteins*, 33:343–357, 1998.

[202] Shibasish Chowdhury, Wei Zhang, Chun Wu, Guoming Xiong, and Yong Duan. Breaking non-native hydrophobic clusters is the rate limiting step in the folding of an alanine-based peptide. *Biopolymers*, 68:63–75, 2003.

[203] Charles L. Brooks III, Martin Gruebele, José N. Onuchic, and Peter G. Wolynes. Chemical physics of protein folding. *Proc. Natl. Acad. Sci.*, 95:11037–11038, 1998.

[204] Joseph D. Bryngelson, J. N. Onuchic, N. D. Socci, and Peter G. Wolynes. Funnels, pathways, and the energy landscape of protein folding: a synthesis. *Proteins - Struct. Funct. Genet.*, 21:167, 1995.

[205] R. M. Ballew, J. Sabelko, and M. Gruebele. Direct observation of fast protein folding: The initial collapse of apomyoglobin. *Proc. Natl. Acad. Sci.*, 93:5759–5764, 1996. Fluorescence probe.

[206] Jens Bredenbeck, Jan Helbing, Janet R. Kumita, G. Andrew Woolley, and Peter Hamm. α-Helix formation in a photo-switchable peptide tracked from picoseconds to microseconds by time resolved IR spectroscopy. *Proc. Natl. Acad. Sci.*, 102:2379–2384, 2005.

[207] L. A. Morozova-Roche, J. A. Jones, W. Noppe, and C. M. Dobson. Independent nucleation and heterogeneous assembly of structure during folding of equine lysozyme. *J. Mol. Biol.*, 289:1055–1073, 1999.

[208] E. Rhoades, M. Cohen, B. Schuler, and G. Haran. Two-state folding observed in individual protein molecules. *J. Am. Chem. Soc.*, 126:14686–14687, 2004.

[209] N. G. van Kampen. *Stochastic Processes in Physics and Chemistry*. Elsevier, Amsterdam, 1992.

[210] F. Alvarez, A. Alegria, and J. Colmenero. Relationship between the time-domain Kohlrausch-William-Watts and frequency-domain Havriliak-Negami relaxation functions. *Phys. Rev. B*, 44:7306–7312, 1991.

[211] David Chandler. *Introduction to Modern Statistical Mechanics*. Oxford University Press, Oxford, 1987.

[212] Sunho Song, Sanford A. Asher, Samuel Krimm, and Keith D. Shaw. Ultraviolet resonance Raman studies of trans and cis peptides: Photochemical consequences of the twisted π^* excited state. *J. Am. Chem. Soc.*, 113:1155–1163, 1991.

[213] Eigil B. Nielsen and John A. Schellman. The absorption spectra of simple amides and peptides. *J. Phys. Chem.*, 71:2297, 1967.

[214] Thierry Sifferlen, Magnus Rueping, Karl Gademann, Bernhard Jaun, and Dieter Seebach. β-thiopeptides: Synthesis, NMR solution structure, CD spectra, and photochemistry. *Helv. Chim. Acta*, 82:2067, 1999.

[215] Jianzhang Zhao, Dirk Wildemann, Mario Jakob, Carolyn Vargas, and Cordelia Schiene-Fischer. Direct photomodulation of peptide backbone conformations. *Chem. Commun.*, pages 2810–2811, 2003.

[216] Issei Harada and Mitsuo Tasumi. Formation of transient *cis* N-methylthioacetamide under ultraviolet laser irradiation. *Chem. Phys. Lett.*, 70:279–282, 1980.

[217] Chihiro Kato, Hiro-o Hamaguchi, and Mitsuo Tasumi. Transient resonance Raman study on the trans-cis photoisomerization of *N*-methylthioacetamide. *J. Phys. Chem.*, 89:407, 1985.

[218] Robert Frank, Mario Jakob, Frank Thunecke, Gunter Fischer, and Mike Schutkowski. Gas-phase ^{1}H NMR studies of internal rotation barriers and conformer stabilities of *N*-ethyl,*N*-methylthioamides. *J. Phys. Chem. A*, 104:7957, 2000.

[219] X. G. Chen, Sanford A. Asher, Reinhard Schweitzer-Stenner, Noemi G. Mirkin, and Samuel Krimm. UV Raman determination of the $\pi\pi^*$ excited state geometry of *N*-methylacetamide: Vibrational enhancement pattern. *J. Am. Chem. Soc.*, 117:2884–2895, 1995.

[220] Yi Li, Robin L. Garrell, and K. N. Houk. Mechanism of cis-trans isomerizations of amide and peptide excited states. *J. Am. Chem. Soc.*, 113:5895, 1991.

[221] I. Thomsen, K. Clausen, S. Scheibye, and S.-O. Lawesson. Thiation with 2.4-bis(4-methoxyphenyl)-1,3,2,4-dithiadiphosphetane 2,4-disulfide: N-methylthiopyrrolidone (2-pyrrolidinethione,1-methyl-). *Organic Synthesis*, 62:158–162, 1984.

[222] R. Gonzalez-Luque, M. Garavelli, F. Bernardi, M. Merchn, M. A. Robb, and M. Olivucci. Computational evidence in favor of a two-state, two-mode model of the retinal chromophore photoisomerization. *Proc. Natl. Acad. Sci.*, 97:9379–9384, 2000.

[223] L. De Vico, C. S. Page, M. Garavelli, F. Bernardi, R. Basosi, M. A. Robb, and M. Olivucci. Reaction path analysis of the ”tunable” photoisomerization selectivity of free and locked retinal chromophores. *J. Am. Chem. Soc.*, 124:4124–4134, 2002.

[224] M. J. Bearpark, M. A. Robb, and H. B. Schlegel. A direct method for the location of the lowest energy point on a potential surface crossing. *Chem. Phys. Lett.*, 223:269, 1994.

[225] O. Celani, M. A. Robb, M. Garavelli, F. Bernardi, and M. Olivucci. Geometry optimization on a hypersphere - application to finding reaction paths from a conical intersection. *Chem. Phys. Lett.*, 243:1–8, 1995.

[226] K. Andersson, P.-Å Malmqvist, and B. O. Roos. Second-order perturbation theory with a complete active space self-consistent field reference function. *J. Chem. Phys.*, 96:1218, 1992.

[227] K. Andersson, M. Barysz, A. Bernhardsson, M. R. A. Blomberg, D. L. Cooper, M. P. Fülscher, C. D. Graaf, B. A. Hess, G. Karlström, R. Lindh, P.-Å Malmqvist, T. Nakajima, P. Neogrády, J. Olsen, B. O. Roos, B. Schimmelpfennig, M. Schtz, L. Seijo, L. Serrano-Andrés, P. E. M. Siegbahn, J. Stålring, T. Thorsteinsson, V. Veryazov, and P. O. Widmark. *MOLCAS*, 5.4, 2002.

[228] M. J. Frisch, G. W. Trucks, H. B. Schlegel, G. E. Scuseria, M. A. Robb, J. R. Cheeseman, V. G. Zakrzewski, J. A. Montgomery Jr., R. E. Stratmann, J. C. Burant, S. Dapprich, J. M. Millam, A. D. Daniels, K. N. Kudin, M. C. Strain, O. Farkas, J. Tomasi, V. Barone, M. Cossi, R. Cammi, B. Mennucci, C. Pomelli, C. Adamo, S. Clifford, J. Ochterski, G. A. Petersson, P. Y. Ayala, Q. Cui, K. Morokuma, D. K. Malick, A. D. Rabuck, K. Raghavachari, J. B. Foresman, J. Cioslowski, J. V. Ortiz, B. B. Stefanov, G. Liu, A. Liashenko, P. Piskorz, I. Komaromi, R. Gomperts, R. L. Martin, D. J. Fox, T. Keith, M. A. Al-Laham, C. Y. Peng, A. Nanayakkara, C. Gonzalez, M. Challacombe, P. M. W. Gill, B. Johnson, W. Chen, M. W. Wong, J. L. Andres, C. Gonzalez, M. Head-Gordon, E. S. Replogle, and J. A. Pople. *Gaussian 98, Revision A.5*. Gaussian, Inc., Pittsburgh, PA, 1998.

[229] M. A. Robb, M. Garavelli, M. Olivucci, and F. Bernardi. In K. B. Lipkowitz and D. B. Boyd, editors, *Reviews in Computational Chemistry*, pages 87–146, New York, 2000. Wiley-VCH: John Wiley and Sons Inc.

[230] M. Olivucci, M. A. Robb, and F. Bernardi. In J. Waluk, editor, *Conformational Analysis of Molecules in Excited States*, pages 297–366, New York, 2000. Wiley-VCH: John Wiley and Sons Inc.

[231] G. J. Atchity, S. S. Xantheas, and K. Ruedenberg. Potential energy surfaces near intersections. *J. Chem. Phys.*, 95:1862–1876, 1991.

[232] S. Ataka, H. Takeuchi, I. Harada, and M. Tasumi. Infrared studies of the cis form of N-methylthioacetamide in low-temperature matrices. *J. Phys. Chem.*, 88(3):449–451, 1984.

[233] Edwin J. Hart and J. W. Boag. Absorption spectrum of the hydrated electron in water and in aqueous solutions. *J. Am. Chem. Soc.*, 84(21):4090–4095, 1962.

[234] Joseph C. Alfano, P. K. Walhout, Y. Kimura, and Paul F. Barbara. Ultrafast transient-absorption spectroscopy of the aqueous solvated electron. *J. Chem. Phys.*, 98(7):5996–5998, 1993.

[235] Guido Sieler and Reinhard Schweitzer-Stenner. The amide I mode of peptides in aqueous solution involves vibrational coupling between the peptide group and water molecules of the hydration shell. *J. Am. Chem. Soc.*, 119:1720–1726, 1997.

[236] Wolfgang Walter and Ernst Schaumann. Über die Struktur der Thioamide und ihrer Derivate, XV. Trennung der geometrischen Isomeren und Bestimmung der Rotationsbarrieren bei N-Alkyl-thioamiden. *Chem. Ber.*, 104:3361–3377, 1971.

[237] M. A. El-Sayed. Vanishing first- and second-order intramolecular heavy-atom effects on the ($\pi^* \rightarrow$ n) phosphorescence in carbonyls. *J. Chem. Phys.*, 41:2462, 1964.

[238] A. Gilbert and J. Baggot. Blackwell Scientific Publications, Oxford, 1991.

[239] C. Adamo and V. Barone. A TDDFT study of the electronic spectrum of s-tetrazine in the gas-phase and in aqueous solution. *Chem. Phys. Lett.*, 330:152–160, 2000.

[240] L. M. Markham and B. S. Hudson. *Ab Initio* analysis of the effects of aqueous solvation on the resonance raman intensities of N-methylacetamide. *J. Phys. Chem.*, 100:2731–2737, 1996.

[241] Sanford A. Asher, Zhenhuan Chi, and Pusheng Li. Resonance Raman examination of the two lowest amide $\pi\pi^*$ excited states. *J. Raman Spectrosc.*, 29(10-11):927–931, 1998.

[242] Donald B. Larson an John F. Arnett, Carl J. Selikar, and S. P. McGlynn. Emissive characteristics of amidic molecules. *J. Am. Chem. Soc.*, 96:3370–3380, 1974.

[243] Andreas Aemissegger, Vincent Kräutler, Wilfred F. van Gunsteren, and Donald Hilvert. A photoinducible β-hairpin. *J. Am. Chem. Soc.*, 127(9):2929–2936, 2005.

[244] Richard R. Ernst, Geoffrey Bodenhausen, and Alexander Wokaun. *Principles of Nuclear Magnetic Resonance in One and Two Dimensions*, volume 14 of *International Series of Monographs on Chemistry*. Oxford University Press, 1987.

[245] Kijeong Kwac and Minhaeng Cho. Molecular dynamics simulation study of N-methylacetamide in water. I. Amide I mode frequency fluctuation. *J. Chem. Phys.*, 119(4):2247–2255, 2003.

[246] S. Woutersen, Y. Mu, G. Stock, and P. Hamm. Hydrogen-bond lifetime measured by time resolved 2D-IR spectroscopy: N-methylacetamide in methanol. *Chem. Phys.*, 266:137–147, 2001.

[247] Sander Woutersen, Rolf Pfister, Peter Hamm, Yuguang Mu, Daniel S. Kosov, and Gerhard Stock. Peptide conformational heterogeneity revealed from nonlinear vibrational spectroscopy and molecular-dynamics simulations. *J. Chem. Phys.*, 117(14):6833–6839, 2002.

[248] M. Khalil, N. Demirdöven, and A. Tokmakoff. Coherent 2D IR spectroscopy: Molecular structure and dynamics in solution. *J. Phys. Chem. A*, 107:5258–5279, 2003.

[249] Peter Hamm and Robin M. Hochstrasser. Structure and dynamics of proteins and peptides: Femtosecond two-dimensional infrared spectroscopy in 'ultrafast infrared and Raman spectroscopy'. In Michael D. Fayer, editor, *Ultrafast Infrared and Raman Spectroscopy*. Marcel Dekker, New York, 2001.

[250] Martin T. Zanni, S. Gnanakaran, Jens Stenger, and Robin M. Hochstrasser. Heterodyned two-dimensional infrared spectroscopy of solvent-dependent conformations of acetylproline-NH_2. *J. Phys. Chem. B*, 105:6520–6535, 2001.

[251] M. T. Zanni, N. H. Ge, Y. S. Kim, and R. M. Hochstrasser. 2D-IR can be desinged to eliminate the diagonal peaks and expose only the crosspeaks needed for structure determination. *Proc. Natl. Acad. Sci. USA*, 98:11265–11270, 2001.

[252] Sander Woutersen and Peter Hamm. Nonlinear two-dimensional vibrational spectroscopy of peptides. *J. Phys. Condens. Matter*, 14:R1035–R1062, 2002.

[253] Jens Bredenbeck and Peter Hamm. Peptide structure determination by 2D-IR spectroscopy in the presence of homogeneous and inhomogeneous broadening. *J. Chem. Phys.*, 119:1569 – 1578, 2003.

[254] O. Golonzka, M. Khalil, N. Demirdöven, and A. Tokmakoff. Coupling and orientation between anharmonic vibrations characterized with two-dimensional infrared vibrational echo spectroscopy. *J. Chem. Phys.*, 115(23):10814–10828, 2001.

[255] Hoi Sung Chung, Munira Khalil, and Andrei Tokmakoff. Nonlinear infrared spectroscopy of protein conformational change during thermal unfolding. *J. Phys. Chem. B*, 108:15332–15342, 2004.

[256] Nurettin Demirdöven, Christopher M. Cheatum, Hoi Sung Chung, Munira Khalil, Jasper Knoester, and Andrei Tokmakoff. Two-dimensional infrared spectroscopy of antiparallel β-sheet secondary structure. *J. Am. Chem. Soc.*, 126:7981–7990, 2004.

[257] Igor V. Rubtsov, Jianping Wang, and Robin M. Hochstrasser. Vibrtaional coupling between amide I and amide A modes revealed by femtosecond two color infrared spectroscopy. *J. Phys. Chem. A*, 107:3384–3396, 2003.

[258] Igor V. Rubtsov, Jianping Wang, and Robin M. Hochstrasser. Dual frequency 2D-IR of peptide amide-A and amide-I modes. *J. Chem. Phys.*, 118:7733–7736, 2003.

[259] Sander Woutersen and Peter Hamm. Time-resolved two-dimensional vibrational spectroscopy of a short α-helix in water. *J. Chem. Phys.*, 115(16):7737–7747, 2001.

[260] G. Lipari and A. Szabo. Model-free approach to the interpretation of nuclear magnetic resonance relaxation in macromolecules. 1. theory and range of validity. *J. Am. Chem. Soc.*, 104:4546–4570, 1982.

[261] Martin T. Zanni, Matthew C. Asplund, and Robin M. Hochstrasser. Two-dimensional heterodyned and stimulated infrared photon echoes of *N*-methylacetamide-d. *J. Chem. Phys.*, 114(110):4579–4590, 2001.

[262] Jaehun Park, Jeong-Hyon Ha, and Robin Hochstrasser. Multidimensional infrared spectroscopy of the N-H bond motions in formamide. *J. Chem. Phys.*, 121(15):7281–7291, 2004.

[263] Sander Woutersen, Y. Mu, Gerhard Stock, and Peter Hamm. Hydrogen-bond lifetime measured by time-resolved 2D-IR spectroscopy: *N*-methylacetamide in methanol. *Chem. Phys.*, 266:137–147, 2001.

[264] John B. Asbury, Tobias Steinel, C. Stromberg, K. J. Gafney, I. R. Piletic, Alexi Goun, and M. D. Fayer. Hydrogen bond dynamics probed with ultrafast infrared heterodyne-detected multidimensional vibrational stimulated echoes. *Phys. Rev. Lett.*, 91(23):237402, 2003.

[265] John B. Asbury, Tobias Steinel, C. Stromberg, K. J. Gafney, I. R. Piletic, Alexi Goun, and M. D. Fayer. Ultrafast heterodyne detected infrared multidimensional vibrational stimulated echo studies of hydrogen bond dynamics. *Chem. Phys. Lett.*, 374:362–371, 2003.

[266] John B. Asbury, Tobias Steinel, C. Stromberg, K. J. Gafney, I. R. Piletic, and M. D. Fayer. Hydrogen bond breaking probed with multidimensional stimulated vibrational echo correlation spectroscopy. *J. Chem. Phys.*, 119(24):12981–12997, 2003.

[267] John B. Asbury, Tobias Steinel, and M. D. Fayer. Hydrogen bond networks: Structure and evolution after hydrogen bond breaking. *J. Phys. Chem. B*, 108:6544–6554, 2004.

[268] John B. Asbury, Tobias Steinel, C. Stromberg, S. A. Corcelli, C. P. Lawrence, J. L. Skinner, and M. D. Fayer. Water dynamics: Vibrational echo correlation spectroscopy and comparison to molecular dynamics simulations. *J. Phys. Chem. A*, 108(7):1107–1119, 2004.

[269] N. Demirdöven, M. Khalil, O. Golonzka, and A. Tokmakoff. Correlation effects in the two-dimensional vibrational spectroscopy of coupled vibrations. *J. Phys. Chem. A*, 105:8025–8029, 2001.

[270] N. Demirdöven, M. Khalil, and A. Tokmakoff. Correlated vibrational dynamics revealed by two-dimensional infrared spectroscopy. *Phys. Rev. Lett.*, 89(23):237401, 2002.

[271] Nien-Hui Ge, Martin T. Zanni, and Robin M. Hochstrasser. Effects of vibrational frequency correlations on two-dimensional infrared spectra. *J. Phys. Chem. A*, 106:962–972, 2002.

[272] Igor V. Rubtsov, Jianping Wang, and Robin M. Hochstrasser. Dual frequency 2D-IR spectroscopy heterodyned photon echo of the peptide bond. *Proc. Natl. Acad. Sci.*, 100:5601–5606, 2003.

[273] J. Edler and P. Hamm. Two-dimensional vibrational spectroscopy of the amide I band of crystalline acetanilide: Fermi resonance, conformational substates, or vibrational self-trapping. *J. Chem. Phys.*, 119(5):2709–2715, 2003.

[274] C. Fang, J. Wang, Y. S. Kim, A. K. Charnley, W. Barber-Armstrong, A. B. Smith III, S. M. Decatur, and R. M. Hochstrasser. Two-dimensional infrared spectroscopy of isotopomers of an alanine rich α-helix. *J. Phys. Chem. B*, 108:10415–10427, 2004.

[275] John B. Asbury, Tobias Steinel, and M. D. Fayer. Using ultrafast infrared multidimensional correlation spectroscopy to aid in vibrational spectral peak assignments. *Chem. Phys. Lett.*, 381:139–146, 2003.

[276] M. Khalil, N. Demirdöven, and A. Tokmakoff. Vibrational coherence transfer characterized with Fourier-transform 2D IR spectroscopy. *J. Chem. Phys.*, 121:362–373, 2004.

[277] Victor Volkov and Peter Hamm. A two-dimensional infrared study of localization, structure, and dynamics of a dipeptide in membrane environment. *Biophys. J.*, 87:4213–4225, 2004.

[278] A. T. Krummel, P. Mukherjee, and M. T. Zanni. Inter and intrastrand vibrational coupling in DNA studied with heterodyned 2D-IR spectroscopy. *J. Phys. Chem. B*, 107:9165–9169, 2003.

[279] E. C. Fulmer, P. Mukherjee, A. T. Krummel, and M. T. Zanni. A pulse sequence for directly measuring the anharmonicities of coupled vibrations: Two-quantum two-dimensional infrared spectroscopy. *J. Chem. Phys.*, 120:8067–8078, 2004.

[280] Christoph Scheurer and Shaul Mukamel. Magnetic resonance analogies in multidimensional vibrational spectroscopy. *Bull. Chem. Soc. Jpn.*, 75:989–999, 2002.

[281] Christoph Scheurer and Shaul Mukamel. Infrared analogs of heteronuclear nuclear magnetic resonance coherence transfer experiments in peptides. *J. Chem. Phys.*, 116:6803–6816, 2002.

[282] Yung Sam Kim, Jianping Wang, and Robin M. Hochstrasser. Two-dimensional infrared spectroscopy of the alanine dipeptide in aqueous solution. *J. Phys. Chem. B*, in press.

[283] Peter Hamm, Manho Lim, William F. DeGrado, and Robin M. Hochstrasser. The two-dimensional IR nonlinear spectroscopy of a cyclic penta-peptide in relation to its three-dimensional structure. *Proc. Natl. Acad. Sci.*, 96:2036–2041, 1999.

[284] P. Hamm, S. Woutersen, and M. Rueping. On the thermal stability of β-peptides: A two-dimensional vibrational spectroscopy study. *Helv. Chim. Acta*, 85:3883–3894, 2002.

[285] I. L. Karle. Crystal structure and conformation of *cyclo*-(glycylprolylglycyl-d-alanylprolyl) containing 4→1 and 3→1 intramolecular hydrogen bonds. *J. Am. Chem. Soc.*, 100:1286, 1978.

[286] M. Aumailley, M. Gurrath, G. Müller, J. Calvete, R. Timpl, and H. Kessler. Arg-gly-asp constrained within cyclic pentapeptides - strong and selective inhibitors of cell-adhesion to vitronectin and laminin fragment-p1. *FEBS Lett.*, 291:50–54, 1991.

[287] Gerhard Müller, Marion Gurrath, and Horst Kessler. Pharmacophore refinement of gpIIb/IIIb antagonists based on comparative studies of antiadhesive cyclic and acyclic RGD peptides. *J. Comput.-Aided Mol. Des.*, 8:709–730, 1994.

[288] G. V. Nikiforovich, K. E. Kövér, W.-J. Zhang, and G. R. Marshall. Cyclopentapeptides as flexible conformational templates. *J. Am. Chem. Soc.*, 122:3262–3273, 2000.

[289] D. F. Mierke, M. Kurz, and H. Kessler. Peptide flexibility and calculations of an ensembe of molecules. *J. Am. Chem. Soc.*, 116:1042–1049, 1994.

[290] Juergen Schleucher, Beatrix Schwoerer, Rudolf K. Thauer, and Christian Griesinger. Elucidation of the stereochemical course of chemical reactions by magnetic labeling. *J. Am. Chem. Soc.*, 117:2941–2942, 1995.

[291] Bruce J. Berne and Robert Pecora. *Dynamic Light Scattering: With Applications to Chemistry, Biology, and Physics*. Wiley, New York, 1976.

[292] Robin M. Hochstrasser. Two-dimensional ir-spectroscopy: polarization anisotropy effects. *Chem. Phys.*, 266:273–284, 2001.

[293] Andrei Tokmakoff. Orientational correlation functions and polarization selectivity for nonlinear spectroscopy of isotropic media. I. Third order. *J. Chem. Phys.*, 105(1):1–12, 1996.

[294] Andrei Tokmakoff. Orientational correlation functions and polarization selectivity for nonlinear spectroscopy of isotropic media. II. Fifth order. *J. Chem. Phys.*, 105(1):13–21, 1996.

[295] Y. Tanimura and S. Mukamel. 2-Dimensional femtosecond vibrational spectroscopy of liquids. *J. Chem. Phys.*, 99:9496–9511, 1993.

[296] A. Tokmakoff, M. J. Lang, D. S. Larsen, and G. R: Fleming. Intrinsic optical heterodyne detection of a two-dimensional fifth order raman response. *Chem. Phys. Lett.*, 272(1-2):48–54, 1997.

[297] T. Steffen, S. Nakashima, and K. Duppen. Temporally two-dimensional fifth-order raman scattering on intermolecular vibrations in CS_2/pentane binary mixtures. 19(1-4):91–96, 1999.

[298] Kevin J. Kubarych, C. J. Milne, and R. J. D. Miller. Heterodyne detected fifth order Raman response of liquid CS_2: 'dutch cross' polarization. *Chem. Phys. Lett.*, 369:635–642, 2003.

[299] John B. Asbury, Yongqiang Wang, and Tianquan Lian. Time-dependent vibration stokes shift during solvation: Experiment and theory. *Bull. Chem. Soc. Jpn.*, 75:973–983, 2002.

[300] Karin Nienhaus, Pengchi Deng, John S. Olson, Joshua J. Warren, and G. Ulrich Nienhaus. Structural dynamics of myoglobin. ligand migration and binding in valine 68 mutants. *J. Biol. Chem.*, 278(43):42532–42544, 2003.

[301] Peter Hamm, Manho Lim, and Robin M. Hochstrasser. Non-markovian dynamics of the vibrations of ions in water from femtosecond infrared three-pulse photon echoes. *Phys. Rev. Lett.*, 81(24):5326–5329, 1998.

[302] Jens Bredenbeck, Jan Helbing, and Peter Hamm. Labeling vibrations by light — ultrafast transient 2D-IR spectroscopy tracks vibrational modes during photoinduced charge transfer. *J. Am. Chem. Soc.*, 126:990–991, 2004.

[303] Kijeong Kwac and Minhaeng Cho. Molecular dynamics simulation study of *N*-methylacetamide in water. II. Two-dimensional infrared pump-probe spectra. *J. Chem. Phys.*, 119(4):2256–2263, 2003.

[304] M. C. Asplund, M. T. Zanni, and R. M. Hochstrasser. Two-dimensional infrared spectroscopy of peptides by phase-controlled femtosecond vibrational photon echoes. *Proc. Natl. Acad. Sci. USA*, 97:8219–8224, 2000.

[305] O. Golonzka, M. Khalil, N. Demirdöven, and A. Tokmakoff. Vibrational anharmonicities revealed by coherent two-dimensional infrared spectroscopy. *Phys. Rev. Lett.*, 86:2154–2157, 2001.

[306] Martin T. Zanni and Robin M. Hochstrasser. Two-dimensional infrared spectroscopy: a promising new method for the time resolution of structures. *Curr. Opin. Struc. Biol.*, 11(5):516–522, 2001.

[307] M. Khalil, N. Demirdöven, and A. Tokmakoff. Obtaining absorptive line shapes in two-dimensional infrared vibrational correlation spectra. *Phys. Rev. Lett.*, 90:047401–1–047401–4, 2003.

[308] C. J. Fecko, J. D. Eaves, J. J. Loparo, A. Tokmakoff, and P. L. Geissler. Ultrafast hydrogen-bond dynamics in the infrared spectroscopy of water. *Science*, 301:1698–1702, 2003.

[309] T. Steinel, J. B. Asbury, S. A. Corcelli, C. P. Lawrence, J. L. Skinner, and M. D. Fayer. Water dynamics: dependence on local structure probed with vibrational echo correlation spectroscopy. *Chem. Phys. Lett.*, 386:295–300, 2004.

[310] Shaul Mukamel. *Principles of nonlinear optical spectroscopy*, volume 6 of *Oxford Series in Optical and Imaging Sciences*. Oxford University Press, Inc., 1995.

[311] M. L. Cowan, J. P. Ogilvie, and R. J. D. Miller. Two-dimensional spectroscopy using diffractive optics based phased-locked photon echoes. *Chem. Phys. Lett.*, 386:184–189, 2004.

[312] S. M. Gallagher Faeder and D. M. Jonas. Two-dimensional electronic correlation and relaxation spectra: Theory and model calculations. *J. Phys. Chem. A*, 103:10489–10505, 1999.

[313] Christoph Scheurer and Shaul Mukamel. Design strategies for pulse sequences in multidimensional optical spectroscopies. *J. Chem. Phys.*, 115:4989–5004, 2001.

[314] K. A. Meyer, D. M. Besemann, and J. C. Wright. Coherent two dimensional spectroscopy with triply vibrationally enhanced infrared four-wave mixing. *Chem. Phys. Lett.*, 381:642–649, 2003.

[315] S. Yeremenko, M. S. Pschenichnikov, and D. A. Wiersma. Hydrogen-bond dynamics in water explored by heterodyne-detected photon echo. *Chem. Phys. Lett.*, 369:107–113, 2003.

[316] Andrei Tokmakoff. *private communication*.

[317] Christoph Scheurer, Andrei Piryatinski, and Shaul Mukamel. Signatures of β-peptide unfolding in two-dimensional vibrational echo spectroscopy: A simulation study. *J. Am. Chem. Soc.*, 123:3114–3124, 2001.

[318] J. D. Hybl, A. W. Albrecht, S. M. Gallagher Faeder, and D. M. Jonas. Two-dimensional electronic spectroscopy. *Chem. Phys. Lett.*, 297:307–313, 1998.

[319] W. Zhao and J. C. Wright. Doubly vibrationally enhanced four wave mixing: The optical analog to 2D-NMR. *Phys. Rev. Lett.*, 84:1411–1414, 2000.

[320] K. A. Merchant, David E. Thompson, and M. D. Fayer. Two-dimensional time-frequency ultrafast infrared vibrational echo spectroscopy. *Phys. Rev. Lett.*, 86:3899–3902, 2001.

[321] G. N. Ramachandran and V. Sasisekharan. Conformation of polypeptides and proteins. *Adv. Protein Chem.*, 23:283–438, 1968.

[322] Xavier Daura, Ires Antes, Wilfred F. van Gunsteren, Walter Thiel, and Alan E. Mark. The effect of motional averaging on the calculation of NMR-derived structural properties. *Proteins*, 36:542–555, 1999.

[323] R. Bürgi, J. Pitera, and W. F. van Gunsteren. Assessing the effect of conformational averaging on the measured values of observables. *J. Biomol. NMR*, 19:305–320, 2001.

[324] S. M. Decatur and J. Antonic. Isotope-edited infrared spectroscopy of helical peptides. *J. Am. Chem. Soc.*, 121:11914–11915, 1999.

[325] J. Torres, A. Kukol, J. N. Goodman, and I. T. Arkin. Site-specific examination of secondary structure and orientation determination in membrane proteins: The peptidic $^{13}C^{18}O$ group as a novel infrared probe. *Biopolymers*, 59:396–401, 2001.

[326] Jean-Paul Ryckaert. Special geometrical constraints in the molecular-dynamics of chain molecules. *Molec. Phys.*, 55:549–556, 1985.

[327] W. H. Press, S. A. Teukolsky, W. T. Vetterling, and B. P. Flannery. *Numerical Recipes in C*. Cambridge University Press, Cambridge, 1992.

[328] M. J. Karplus and G. A. Petsko. Molecular-dynamics simulations in biology. *Nature*, 347(6294):631–639, 1990.

[329] Dana M. Dattelbaum, Kristin M. Omberg, Jon R. Schoonover, Richard L. Martin, and Thomas J. Meyer. Application of time-resolved infrared spectroscopy to electronic structure in metal-to-ligand charge-transfer excited states. *Inorg. Chem.*, 41:6071–6079, 2002.

[330] Stanislav Záliš, Ian R. Farrell, and Antonin Vlček. The involvement of metal-to-CO charge transfer and ligand-field excited states in the spectroscopy and photochemistry of mixed-ligand metal carbonyls. a theoretical and spectroscopic study of $[W(CO)_4$(1,2-ethylenediamine)] and $[W(CO)_4$(*N*,*N*’-Bis-alkyl-1,4-diazabutadiene)]. *J. Am. Chem. Soc.*, 125:4580–4592, 2003.

[331] Kazuhide Koike, Nobuaki Okoshi, Hisao Hori, Koji Takeuchi, Osamu Ishitani, Hideaki Tsubaki, Ian P. Clark, Michael W. George, Frank P. A. Johnson, and James J. Turner. Mechanism of the photochemical ligand substitution reactions of *fac*-$[Re(bpy)(CO)_3(PR_3)]^+$ complexes and the properties of their triplet ligand-field excited states. *J. Am. Chem. Soc.*, 124:11448–11455, 2002.

[332] Ian R. Farrell, Pavel Matousek, Michael Towrie, Anthony W. Parker, David C. Grills, Michael W. George, , and Jr. Antonin Vlček. Direct observation of competitive ultrafast co dissociation and relaxation of an mlct excited state: Picosecond time-resolved infrared spectroscopic study of $[Cr(CO)_4$(2,2’-bipyridine)]. *Inorg. Chem.*, 41:4318–4323, 2002.

[333] Maddalena Pizzotti, Renato Ugo, Dominique Roberto, and Silvia Bruni. Organometallic counterparts of push-pull aromatic chromophores for nonlinear optics: Push-pull heteronuclear bimetallic complexes with pyrazine and *trans*-1,2-bis(4-pyridyl)ethylene as linkers. *Organometallics*, 21:5830–5840, 2002.

[334] Kenneth Kam-Wing Lo, Wai-Ki Hui, and Dominic Chun-Ming Ng. Novel rhenium(I) polypyridine biotin complexes that show luminescence enhancement and lifetime elongation upon binding to avidin. *J. Am. Chem. Soc.*, 124:9344–9345, 2002.

[335] Jon. R. Schoonover and Geoffrey F. Strouse. Time-resolved vibrational spectroscopy of electronically excited inorganic complexes in solution. *Chem. Rev.*, 98:1335–1355, 1998.

[336] Jens Bredenbeck, Jan Helbing, and Peter Hamm. Solvation dynamics: Beyond the two-point frequency fluctuation correlation function. *Phys. Rev. Lett.*, in preparation.

[337] Jens Bredenbeck, Jan Helbing, and Peter Hamm. Transient two-dimensional infrared spectroscopy - towards measuring ultrafast structural dynamics. In Monique M. Martin and James. T. Hynes, editors, *Femtochemistry and Femtobiology*, Ultrafast Events in Molecular Science, pages 387–390. Elsevier, 2004.

[338] Laura A. Worl, Rich Duesing, Pingyun Chen, Leopold Della Ciana, and Thomas J. Meyer. Photophysical properties of polypyridyl carbonyl complexes of rhenium(I). *J. Chem. Soc. Dalton Trans.*, S:849–858, 1991.

[339] Steven S. Andrews. Using rotational averaging to calculate the bulk response of isotropic and anisotropic samples from molecular parameters. *J. Chem. Ed.*, in press.

[340] Daniel R. Gamelin, Michael W. George, Paul Glyn, Friedrich-Wilhelm Grevels, Frank P. A. Johnson, Werner Klotzbücher, Sara L. Morrison, Graham Russell, Kurt Schaffner, and James J. Turner. Structural investigation of the ground and excited states of $ClRe(CO)_3$(4,4'-bipyridyl$)_2$ using vibrational spectroscopy. *Inorg. Chem.*, 33:3246–3250, 1994.

[341] Terence Tao. Time-dependent fluorescence depolarization and brownian rotational diffusion coefficients of macromolecules. *Biopolymers*, 8:609–632, 1969.

[342] Richard N. Zare. *Angular Momentum — Understanding Spatial Aspects in Chemistry and Physics*. Wiley Interscience, New York, 1986.

[343] Manho Lim and Robin M. Hochstrasser. Unusual vibrational dynamics of the acetic acid dimer. *J. Chem. Phys.*, 115(16):7629–7643, 2001.

[344] Sander Woutersen and Huib Bakker. Hydrogen bond in liquid water as a brownian oscillator. *Phys. Rev. Lett.*, 83(10):2077–2080, 1999.

[345] G. R. Fleming and M. Cho. Chromophore-solvent dynamics. *Annu. Rev. Phys. Chem.*, 47:109–134, 1996.

[346] A. Piryatinski and J. L. Skinner. Determining vibrational solvation-correlation functions from three-pulse infrared photon echoes. *J. Phys. Chem. B*, 106:8055–8063, 2002.

[347] Jens Stenger, Dorte Madsen, Peter Hamm, Erik T. J. Nibbering, and Thomas Elsaesser. Ultrafast vibrational dephasing of liquid water. *Phys. Rev. Lett.*, 87(2):027401–1–027401–4, 2001.

[348] Michel F. Emde, Andrius Baltuska, Andreas Kummrow, Maxim S. Pshenichnikov, and Douwe A. Wiersma. Ultrafast librational dynamics of the hydrated electron. *Phys. Rev. Lett.*, 80(21):4645–4648, 1998.

[349] Jens Bredenbeck, Jan Helbing, and Peter Hamm. Transient two-dimensional IR spectroscopy: exploring the polarization dependence. *J. Chem. Phys.*, 121(12):5943–5957, 2004.

[350] Nien-Hui Ge and Robin M. Hochstrasser. Femtosecond two-dimensional infrared spectroscopy: IR-COSY and THIRSTY. *PhysChemComm*, 5:17–26, 2002.

[351] Kazuhide Koike, Hisao Hori, Masakazu Ishizuka, Jeremy R. Westwell, Koji Takeuchi, Takashi Ibusuki, Kengo Enjouji, Hideo Konno, Kazuhiko Sakamoto, and Osamu Ishitani. Key process of the photocatalytic reduction of CO_2 using $[Re(4,4'\text{-}X_2\text{-bipyridine})(CO)_3PR_3]^+$ ($X = CH_3$, H, CF_3; PR_3 = phosphorus ligands): Dark reaction of the one-electron-reduced complexes with CO_2. *Organometallics*, 16:5724–5729, 1997.

[352] Jens Bredenbeck, Jan Helbing, and Peter Hamm. Transient two-dimensional IR spectroscopy - exploring the polarization dependence. *J. Chem. Phys.*, submitted.

[353] R. Kubo, M. Toda, and N. Hashitsume. *Statistical Physics II. Nonequilibrium Statistical Mechanics*. Springer, Berlin, 1985.

[354] P. Hamm, M. Zureck, T. Röschinger, H. Patzelt, D. Oesterhelt, and W. Zinth. Subpicosecond infrared spectroscopy on the photoisomerisation of the protonated schiff base of all-trans retinal. *Chem. Phys. Lett*, 268:180–186, 1997.

[355] K. D. Rector, J. R. Engholm, C. W. Rella, J. R. Hill, D. D. Dlott, and M. D. Fayer. A dynamical transition in the protein myoglobin observed by infrared vibrational experiments. *J. Phys. Chem. A*, 103:2381–2387, 1999.

[356] P. E. Smith. The alanine dipeptide free energy surface in solution. *J. Chem. Phys.*, 111:5568–5579, 1999.

[357] Y. Mu and G. Stock. Confortmational dynamics of trialanine in water: A molecular dynamics study. *J. Phys. Chem. B*, 106:5294–5301, 2002.

[358] David J. Jones, Eric O. Potma, Ji xin Cheng, Berndt Burfeindt, Yang Pang, Jun Ye, and X. Sunney Xie. Synchronization of two passively mode-locked, picosecond lasers within 20 fs for coherent anti-stokes Raman scattering microscopy. *Rev. Sci. Instrum.*, 73(8):2843–2848, 2002.

[359] Hairong Ma, John Ervin, and Martin Gruebele. Single-sweep detection of relaxation kinetics by submicrosecond midinfrared spectroscopy. *Rev. Sci. Instrum.*, 75(2):486–491, 2004.

[360] C. Rödig, O. Weidlich, C. Hackmann, and F. Siebert. Nanosecond step-scan FTIR spectroscopy applied to photobiological systems. *AIP conference proceedings*, 430(1):361–366, 1998.

[361] Paul Horowitz and Winfried Hill. *The Art of Electronics*. Cambridge University Press, 1989.

Abbreviations

2D-IR — two-dimensional infrared spectroscopy
ACAC — acetylacetone
BBO — β barium borate
BLYP — Becke-Lee-Yang-Parr
CASPT2 — complete active space second-order Møller-Plesset perturbation theory
CASSCF — complete active space self-consistent-field
CD — circular dichroism
CI — conical intersection
CPA — chirped pulse amplification
DABCODO — 2,5-diazabicyclo[2,2,2]octane-3,6-dione
DFG — difference frequency generation
DMSO — dimethylsulfoxide
FFCF — frequency fluctuation correlation function
FMOC — fluorenylmethoxycarbonyl
FT — Fourier transform
FTIR — Fourier transform infrared spectroscopy
FRET — flourescence resonant energy transfer
IR — infrared
ISC — inter system crossing
MCT — mercury cadmium telluride
MD — molecular dynamics
MEP — minimum energy path
MIR — mid-infrared
NMA — N-methylacetamide
NMR — nuclear magnetic resonance
NMTAA — N-methylthioacetamide
OPA — optical parametric amplifier
rmsd — root mean square deviation
SHG — second harmonic generation
T2D-IR — transient two-dimensional infrared spectroscopy
TC — transition charges
TDC — transition dipole coupling
TDDD — transition density derivative distribution
THG — third harmonic generation
Ti:S — Ti:sapphire, titanium-doped sapphire
TFE — Trifluoroethanol
T-jump — temperature jump
UV — ultraviolet

List of Figures

List of Tables

Curriculum Vitae

Personal

Name: BREDENBECK

First name: Jens

Date of birth: 19th of April, 1975

Citizenship: German

Education and Training

Oct. 01 – June 05:	*PhD Program in Physical Chemistry* **Universität Zürich**, Switzerland Dissertation: Transient 2D-IR Spectroscopy – Towards Ultrafast Structural Dynamics of Peptides and Proteins
May 00:	*Diploma in Chemistry* **Georg-August-Universität Göttingen**, Germany
May 99 – Mar. 00:	*Diploma Research* **Max-Planck-Institut für Strömungsforschung**, Göttingen, Germany Diploma Thesis: Quantum-Mechanical Investigation of HCN Isomerization
Oct. 97 – May 00:	*Main Studies in Chemistry* **Georg-August-Universität Göttingen**, Germany
Oct. 95 – Sept. 97:	*Basic Studies in Chemistry* **Technische Hochschule Darmstadt**, Germany
July 94 – June 95:	*Military Service* **Sportschule der Bundeswehr**, Warendorf, Germany Sportfördergruppe für Spitzensportler
July 94:	*Abitur* **Adolf-Reichwein-Gymnasium**, Heusenstamm, Germany

Research Experience

Oct. 01 – pres.:	*Graduate Research Assistant* **Universität Zürich**, Switzerland Group for Femtosecond Vibrational Spectroscopy, Prof. Dr. Peter Hamm
May 01 – Sept. 01:	*Graduate Research Assistant* **Max-Born-Institut**, Berlin, Germany Group for Femtosecond Dynamics of Molecular Systems, Dr. Peter Hamm

Jan. 01 – Mar. 01: *Graduate Research Assistant*
Technische Universität München, Garching, Germany
Group for NMR Theory and Experiment, Prof. Dr. Steffen Glaser

Oct. 00 – Dec. 00: *Graduate Research Assistant*
Johann Wolfgang Goethe Universität, Frankfurt am Main, Germany
Group for NMR-based Structural Biology, Prof. Dr. Christian Griesinger

Feb. 99 – Sept. 00: *Student Research Assistant*
Max-Planck-Institut für Strömungsforschung, Göttingen, Germany
Group for Theoretical Molecular Physics, Dr. habil. Reinhard Schinke

Feb. 98 – Apr. 99: *Student Research Assistant*
Georg-August-Universität Göttingen, Germany
Theoretical Chemistry Group, Prof. Dr. Peter Botschwina

Acknowledgements

I wish to thank:

Prof. Dr. Peter Hamm, for giving me, endangered to become a theoretician, the chance to start a new life as an experimentalist. My PhD-research in his group was characterized by an ideal combination of freedom to develop and realize own projects and his continuous enthusiasm, support and guidance during this work. In particular during the early phase in Zurich, after our relocation from Berlin, when the new labs and facilities had to be set up, I benefited from his extensive practical and technical knowledge, he took the time to share with us despite his numerous commitments as a new faculty member. With his esteem for the ideas and opinions of his group members that encouraged our discussions, Peter created an inspiring and lively research atmosphere here in Zurich.

Prof. Dr. Shaul Mukamel, *University of California, Irvine*, for agreeing to act as a referee for this dissertation, for his kind and steady interest in this work, for encouraging and forward-looking conversations and advice at various conferences.

Prof. Dr. Majed Chergui, *École Politechnique Fédérale De Lausanne*, for refereeing this dissertation, for acting as an external member of the *Promotionskomitee*.

Prof. Dr. Stefan Seeger and Prof. Dr. Jürg Hutter, *Universität Zürich*, for refereeing and serving on the *Promotionskomitee*.

Prof. Dr. Gerhard Stock, *Johann Wolfgang Goethe-Universität, Frankfurt am Main*, for providing results on amide I coupling calculations prior to publication, for providing the trialanine trajectory discussed in the context of holeburning T2D-IR spectroscopy and for reading several of the manuscripts.

Cyclic Peptide - Collaboration

Prof. Dr. Luis Moroder, *Max-Planck-Institute of Biochemistry, Martinsried*, for the continuous interest and support for this project, for making it possible for us to do research on these unique samples, not having to starve on analytic amounts but enjoying supply on an almost industrial scale.

Dr. Christian Renner, *Max-Planck-Institute of Biochemistry, Martinsried*, for sharing his view on the structures of the photoswitchable cyclic peptides, for providing and explaining his results of NMR structure analysis, for supporting the project by acting as a mediator between the world of bioorganic synthesis and the world of spectroscopy.

Prof. Dr. Josef Wachtveitl, *Johann Wolfgang Goethe-Universität, Frankfurt am Main*, and Prof. Dr. Wolfgang Zinth, *Ludwigs-Maximilian-Universität, Munich*, and their group members Arne Sieg and Tobias Schrader for collaboration on the cyclic peptide, for sharing their experience and knowledge on photoswitchable peptides gained through years of investigation in the UV-Vis spectral region.

Photoswitchable α-Helix - Collaboration

Prof. Dr. G. Andrew Woolley, *University of Toronto*, and his former PhD student Dr. Janet Kumita (now with Prof. Chris Dobson, *University of Cambridge*), for their enthusiasm to get this project on phototriggered secondary structure formation started, for providing us with high quality samples of the fantastic molecules they designed, for continuous discussion and support during the data evaluation and writing.

N-Methylthioacetamide - Collaboration

Prof. Dr. Massimo Olivucci and his PhD student Luca De Vico, *Università degli Studi di Siena*, for creating the theoretical picture of NMTAA isomerization in great detail.

Prof. Dr. Josef Wachtveitl and his Post-Doc Dr. Robert Huber, *Johann Wolfgang Goethe-Universität, Frankfurt am Main*, for strong support from the visible side.

Hamm Group

Julian Edler for good company all the way from Berlin to where we are now and for surviving our chaotic office, for uncomplicated reliable collaboration and sharing of tasks particularly in the early phase of construction at the PCI.

Dr. Jan Helbing for the productive collaboration in many of the projects in this dissertation, for attacking dear ideas and for lively discussions.

Dr. Victor Volkov for adding a spiritual component to the live in the PCI, for sharing his creative ideas concerning science and live in general.

Dr. Hiroyuki Katsuki(-san) for guiding us through dazzling Japan.

Rolf Pfister for advice and support concerning chemical synthesis, for organizing the SOLA-competition, for developing 4D-Tetris and for ”you just have to edit the postscript file a little”-software support.

Maja Gossweiler, our secretary, for creating a good atmosphere, for keeping away the administrative troubles.

And the other members of the Group, Paul Kocian, Dr. Roland Schanz, Harry Bregy, Valentina Cervetto, Virgiliu Boţan, Dr. Christoph Kolano, for making the time being here a pleasant one.

Workshops and Support

Many thanks to Horst Blasi, Roland Zehnder and Armin Kühne in our mechanics workshop who took care about the biggest and the smallest projects with the same precision, speed, creativity and longsightedness (”Do you really want us to build it like THIS!?”).

I also wish to thank our electronic engineer Hermann Schwarz and his co-worker Andreas Knecht - several ideas would not have been realized without them.

Our computer-technician, Ueli Feusi, for keeping computer-problems well under control. I never worked at an institute before, where the computers did so well, what they where supposed to.

People at the Max-Born-Institute in Berlin

Before moving to Zurich and starting the PhD program there, I had the chance to work for a few months period at the Max-Born-Institute in Berlin. I also wish to express my thanks to Prof. Dr. Thomas Elsässer for making this stay possible, Dr. Erik T. J. Nibbering for sharing his knowledge and his excellent collection of scientific publications, as well as Dr. Matteo Rini, Dr. Jens Stenger, Dr. Tobias Günther, Dr. Jens Dreyer and Dr. Felix Eickemeyer for a good start in ultrafast spectroscopy.